



UNIVERSITAT POLITÈCNICA
DE CATALUNYA
BARCELONATECH

Advanced adaptive compensation system for free-space optical communications

by
Carlos E. Carrizo

ADVERTIMENT La consulta d'aquesta tesi queda condicionada a l'acceptació de les següents condicions d'ús: La difusió d'aquesta tesi per mitjà del repositori institucional UPCommons (<http://upcommons.upc.edu/tesis>) i el repositori cooperatiu TDX (<http://www.tdx.cat/>) ha estat autoritzada pels titulars dels drets de propietat intel·lectual **únicament per a usos privats** emmarcats en activitats d'investigació i docència. No s'autoritza la seva reproducció amb finalitats de lucre ni la seva difusió i posada a disposició des d'un lloc aliè al servei UPCommons o TDX. No s'autoritza la presentació del seu contingut en una finestra o marc aliè a UPCommons (*framing*). Aquesta reserva de drets afecta tant al resum de presentació de la tesi com als seus continguts. En la utilització o cita de parts de la tesi és obligat indicar el nom de la persona autora.

ADVERTENCIA La consulta de esta tesis queda condicionada a la aceptación de las siguientes condiciones de uso: La difusión de esta tesis por medio del repositorio institucional UPCommons (<http://upcommons.upc.edu/tesis>) y el repositorio cooperativo TDR (<http://www.tdx.cat/?locale-attribute=es>) ha sido autorizada por los titulares de los derechos de propiedad intelectual **únicamente para usos privados enmarcados** en actividades de investigación y docencia. No se autoriza su reproducción con finalidades de lucro ni su difusión y puesta a disposición desde un sitio ajeno al servicio UPCommons No se autoriza la presentación de su contenido en una ventana o marco ajeno a UPCommons (*framing*). Esta reserva de derechos afecta tanto al resumen de presentación de la tesis como a sus contenidos. En la utilización o cita de partes de la tesis es obligado indicar el nombre de la persona autora.

WARNING On having consulted this thesis you're accepting the following use conditions: Spreading this thesis by the institutional repository UPCommons (<http://upcommons.upc.edu/tesis>) and the cooperative repository TDX (<http://www.tdx.cat/?locale-attribute=en>) has been authorized by the titular of the intellectual property rights **only for private uses** placed in investigation and teaching activities. Reproduction with lucrative aims is not authorized neither its spreading nor availability from a site foreign to the UPCommons service. Introducing its content in a window or frame foreign to the UPCommons service is not authorized (*framing*). These rights affect to the presentation summary of the thesis as well as to its contents. In the using or citation of parts of the thesis it's obliged to indicate the name of the author.

ADVANCED ADAPTIVE COMPENSATION SYSTEM FOR FREE-SPACE OPTICAL COMMUNICATIONS

Thesis by
Carlos E. Carrizo

Supervised by
Prof. Dr. Aniceto Belmonte
Dr. Ramon Mata Calvo

In Partial Fulfillment of the Requirements for the
Degree of
Doctor of Philosophy



UNIVERSITAT POLITÈCNICA DE CATALUNYA
BARCELONATECH
DEPARTMENT OF SIGNAL THEORY AND COMMUNICATIONS

Barcelona, Spain
Defended []

ERRATA

ABSTRACT

MASSIVE amounts of information are created daily in commercial fields like earth observation, that must be downloaded to earth ground stations in the short time of a satellite pass. Today, much of the collected information must be dropped due to lack of bandwidth, and laser downlinks can offer tenths of gigabits throughput solving this bottleneck limitation. In a down-link scenario, the performance of laser satellite communications is limited due to atmospheric turbulence, which causes fluctuations in the intensity and the phase of the received signal leading to an increase in bit error probability. In principle, a single-aperture phase-compensated receiver, based on adaptive optics, can overcome atmospheric limitations by adaptive tracking and correction of atmospherically induced aberrations. However, under strong-turbulence situations, the effectiveness of traditional adaptive optics systems is severely compromised. In such scenarios, sensor-less techniques offer robustness, hardware simplicity, and easiness of implementation and integration at a reduced cost, but the state-of-the-art approaches still require too many iterations to perform the correction, exceeding the temporal coherence of the field and thus falling behind the field evolution.

This thesis proposes a new iterative AO technique for strong turbulence compensation that reduces the correction time, bridging the limitation of similar systems in lasercom applications. It is based on the standard sensor-less system design, but it additionally uses a short-exposure focal intensity image to accelerate the correction. The technique combines basic principles of Fourier optics, image processing, and quadratic signal optimization to correct the wave-front. This novel approach directly updates the phases of the most intense focal-plane speckles, maximizing the power coupled into a single-mode fiber convexly.

Numerical analyses show that this method has a robust and excellent performance under very strong turbulence. Laboratory results confirm that a focal speckle pattern can be used to accelerate the iterative compensation. This technique delivers nearly twofold bandwidth reduction compared with standard methods, and sufficient signal gain and stability to allow high throughput data transmission with nearly error-free performance in emulated satellite downlink scenarios. A property highlight is the in-advance knowledge of the required number of iterations, allowing on-demand management of the loop bandwidth in different turbulent regimes. Besides remaining conceptually and technically simple, it opens a new insight to iterative solutions that may lead to the development of new methods.

A specific challenge remains to be the real-time functioning of the technique. A first approach for the dynamic wave-front correction was proposed and partially validated, but several potential alternatives are on the table. A dedicated control algorithm must be developed accordingly. With further refinement, this technique can surely contribute to making possible the use of iterative solutions in laser communications.

PROLOGUE

FREE-SPACE optical communications (FSOC) is the solution to today's and future bandwidth requirements in several civil and military telecommunications areas. This claim was arguably twenty years ago when the technology and methods were not mature enough to confidently assure the viability of this technology against the robust performance of RF systems. Since then, and especially in the last decade, free-space laser communications (Lasercomm) has evolved at a very fast paced. Nowadays, it orients to be complementary with RF systems, using laser wireless for backbone applications and RF as a backup hybrid system and end-user links, especially in remote areas.

Commercial applications like earth observation demand very high throughput channels to download the massive amount of information collected by different satellite payloads. Radio channels are limited in bandwidth; thus several satellite passes are required which results in the necessity of onboard large storage capacity. A huge operational and economical benefit may result from the possibility of solving this bandwidth limitation. The use of laser links can provide sufficient bandwidth, but it also faces natural-imposed constraints. This limitation is associated with strong turbulence, particularly at lower satellite elevations. Establishing a robust laser link under such conditions is important because most of the flying time of a satellite occurs below 30° (or 60° Zenith angle). At such elevations, the laser beam travels long distances and the cumulative effect of the turbulence induces strong amplitude and phase distortion in the wave-front. These distortions affect the beam focusing leading to signal fading. High data throughput above 10 Gbps, require a stable and efficient single-mode fiber coupling that allows the integration of fiber-based components, like optical amplifiers and coherent receivers. By integrating coherent systems advance modulation formats can be used, further increasing the transmission data rates. Undoubtedly, beam wave-front correction is required to improve the power coupling, reduce the signal variance, and benefit from the satellite seeing and downloading time. Consequently, technologies like adaptive optics become relevant.

Adaptive optics (AO) is a technique that corrects the wave-front distortions induced by the atmosphere. It essentially senses the distortion with a wave-front sensor and corrects it with a wave-front compensator. The state of the art systems are generally a heritage from astronomy; thus they are designed for more friendly turbulence regimes and suffer performance deterioration when facing strong turbulence. Alternatively, sensor-less systems do not use complex and expensive wave-front sensors and iteratively optimize a performance metric, like power coupled into the fiber. This technology is attractive for laser communications because it adaptatively maintain high quality signal coupling, while being technically robust and simple. The principal problem is related to the number of iterations required, which imply wave-front correction times that exceed the field coherence time.

The German Aerospace Center (DLR), and particularly the optical communications group at the Institute of Communications and navigation (IKN), has been involved for more than two decades in the study and solutions of problems related to free-space optical propagation and communications. My doctoral work originates from a DLR project linked with the need to compensate the phase wave-front distortions induced by strong turbulence in satellite-to-earth laser downlinks, and benefits from the extensive gathered experimental experience of this group. This institution offers me unique facilities and laboratories to evaluate my findings and allow me to gain technical expertise in the field. The doctorate program of the Department of Signal Theory and Communications

of the Polytechnic University of Catalonia (UPC), under the supervision of Prof. Belmonte, gives me the ideal scientific background and guidance in line with my project interest. This group has vast experience in optical communications through the atmosphere, and Prof. Belmonte has experience developing alternatives adaptive optics concepts for laser communications.

Framed within the above-described problem, previous attempts of strong turbulence compensation with existing AO systems, have been addressed with partial success. In particular, iterative solutions have not really evolved further from known approaches. Consequently, this thesis engages in the challenge of proposing a new iterative adaptive optics method capable of solving the intrinsic time constraints of similar state of the art solutions. It seeks to demonstrate that with reduced bandwidth, sufficient signal enhancement allows high throughput data transmission. By doing so, this work tries to contribute with the possibility of establishing robust laser links at lower satellite elevations. Last but not least, this work intends to offer a new insight to iterative solutions, hopefully encouraging further development in the field.

ACKNOWLEDGMENTS

The work presented in this thesis was carried out in the Advanced Optical Technologies Group of the Institute of Communications and Navigation (IKN) at the German Aerospace Center (DLR), in collaboration with the Optical Communications Research Group within the Signal Theory and Communications department at the Polytechnic University of Barcelona (UPC). The work was funded by the German Aerospace Center and the German Academic Exchange Service (DAAD), both which I gratefully acknowledged.

I want to thank my thesis supervisors Prof. Dr. Aniceto Belmonte and Dr. Ramon Mata Calvo, for their guidance, advice, and continuous support, helping me to develop as a researcher and a better professional. I also want to thank the director of the Institute of Communications and Navigation Prof. Dr. Christoph Günther and the head of the Satellite Networks Department, Dr. Sandro Scalise, for their support to my research.

I want to thank my colleagues in DLR for the discussions and collaboration, which helped me to enrich my work.

I especially thank my parents and sisters for their constant support over all these years, and my friends which are my second family far from home, all of which understood and supported my ups and downs during this journey.

DECLARATION

I declare that this thesis and the work presented in it are my own and has been generated by me as the result of my own original research.

A handwritten signature in blue ink, appearing to read 'Carlos E. Carrizo'.

Carlos E. Carrizo
June 13, 2019

CONTENTS

Errata	iii
Abstract	iv
Prologue	v
Acknowledgments	vii
Declaration	viii
Contents	ix
List of Figures	xii
List of Tables	xviii
Abbreviations	xix
Symbols and Notations	xx
Published content and contributions	xxii
Dedication	xxiii
Chapter I: Introduction	1
1.1 The need for free-space optical communications	2
1.2 Atmospheric channel limitations for lasercoms	3
1.3 Communication systems in free-space optics	5
1.4 Adaptive turbulence compensation in lasercoms	8
1.5 Thesis objectives	9
1.6 Thesis outline	12
Chapter II: Free-space laser downlinks	14
2.1 Atmospheric channel effects	15
2.1.1 Absorption and scattering	16
2.1.2 Refractive index structure parameter	17
2.1.3 Propagation effects	19
2.1.3.1 Atmospheric coherence width - Fried parameter	19
2.1.3.2 Greenwood time constant - Coherence time	21
2.1.3.3 Scintillation	22
2.1.3.4 Irradiance probability density function	23
2.1.3.5 Phase piston	25
2.1.4 Emulation of the beam wave-front in a turbulent channel	25
2.2 Lasercom system in free-space	26
2.2.1 Modulator	28
2.2.2 Demodulator	31
2.2.2.1 Direct detection	31
2.2.2.2 Coherent detection	34
2.2.3 Detection Signal-to-Noise ratio	35
2.3 Communications performance	36
2.3.1 Strehl ratio	37
2.3.2 Signal to noise ratio in a turbulent channel	37
2.3.3 Receiver sensitivity and atmospheric impact	38
2.3.4 Fiber coupling	41

2.3.4.1	Single-mode fiber coupling efficiency	42
2.3.4.2	Mixing efficiency and fading statistics	44
2.4	Conclusion of the chapter	47
Chapter III:	Adaptive optics systems	48
3.1	Adaptive optics	49
3.1.1	Tip-tilt mirror	50
3.1.2	Deformable mirror	51
3.1.3	Wave-front sensing methods	53
3.2	Direct methods	54
3.2.1	Shack-Hartmann sensor	55
3.2.2	Curvature Sensor	57
3.2.3	Pyramid Sensor	57
3.2.4	Interferometric sensor	58
3.3	Indirect methods	59
3.3.1	Sensor-less stochastic technique	60
3.3.2	Speckle imaging technique	62
3.3.3	Image sharpening	63
3.4	Comparison of AO techniques	64
3.5	Conclusion of the chapter	66
Chapter IV:	Speckle-based adaptation	67
4.1	The focal speckle pattern	69
4.1.1	Speckle intensity distribution	71
4.1.2	Focal speckle phase	74
4.2	Speckle-based sequential technique	74
4.2.1	The turbulence compensation system	75
4.2.2	Mathematical framework	76
4.2.2.1	Fourier Optics representation	76
4.2.2.2	Angular wave spectrum representation	78
4.2.3	The method	79
4.2.4	Parabolic optimization	82
4.2.5	Optimization process	85
4.2.5.1	First step	85
4.2.5.2	Second step	85
4.2.5.3	Third step	85
4.3	Numerical analysis of the adaptation method	87
4.3.1	Numerical wave-front generation	88
4.3.2	Algorithm performance under the effect of signal noise	91
4.3.3	Overall performance and bandwidth utilization	93
4.3.4	Considerations for a closed-loop operation	95
4.4	Conclusion of the chapter	98
Chapter V:	Experimental validation	100
5.1	Experimental setup	101
5.2	Hardware limitations	103
5.2.1	Spatial Light Modulator	103
5.2.2	Tip Tilt Mirror	105
5.2.3	Deformable Mirror	106
5.2.4	Single-mode Fiber coupling	107
5.2.5	Avalanche Photodetector	109

5.2.6	Focal Camera	110
5.3	Channel emulation	111
5.4	Proof of concept	111
5.4.1	Algorithm performance under the effect of signal noise	112
5.4.2	Overall performance	113
5.4.3	Algorithm performance under very strong turbulence	114
5.4.4	Correction of correlated fields	115
5.5	Conclusion of the chapter	118
Chapter VI:	Experimental validation with transmission system	120
6.1	Coherent QPSK modulation	121
6.1.1	QPSK modulator	121
6.1.2	QPSK demodulator	122
6.2	Coherent data communication test	128
6.2.1	Description of the transmission system	128
6.2.2	Power requirements - Communication vs. AO system	129
6.2.3	Evaluation of the AO system in a communication scenario	131
6.3	Conclusion of the chapter	134
Chapter VII:	Conclusions and Future work	135
7.1	Summary	135
7.2	Conclusions	136
7.3	Future work	139
References	141

LIST OF FIGURES

<i>Number</i>	<i>Page</i>
1.1 Representation of the atmospheric effects in an optical uplink/downlink.	4
1.2 Standard AO solutions employed in FSOC perform efficiently in weak and moderate turbulence, which tends to occur above the 30° elevations of a beam downlink. At lower elevations, the turbulence effect are stronger and an alternative AO system is required.	10
2.1 Representation of a free-space laser beam affected by the atmosphere. Design based on [1]. . .	15
2.2 Representation of the transmitter, channel, and receiver in an FSOC system.	15
2.3 Transmittance for the wavelength range of interest	16
2.4 Turbulence strength profile $HV_{5/7}$	18
2.5 Fried parameter and normalized aperture for different LEO-downlink elevations, considering a laser wavelength $\lambda = 1.55 \mu\text{m}$, $D = 40 \text{ cm}$, and the $HV_{5/7} C_n^2$ profiles of Fig. 2.4.	21
2.6 Coherence time for a range of LEO-downlink elevations, considering a laser wavelength $\lambda = 1.55 \mu\text{m}$ and the change in the rms wind due to beam slew rate.	21
2.7 Scintillation index for different LEO-downlink elevations, considering a laser wavelength $\lambda = 1.55 \mu\text{m}$, and rms wind $v_0 = 21 \text{ [m/s]}$. A comparison with the Rytov variance shows the overestimation below 30° elevations.	23
2.8 Scintillation index variation with the aperture size D , and for LEO-downlink elevations spanning weak to strong turbulence. The simulation considers a laser wavelength $\lambda = 1.55 \mu\text{m}$, and rms wind $v_0 = 21 \text{ [m/s]}$	24
2.9 Block diagram of a free-space optical system and main subsystems, including the transmitter, channel, and receiver, as well as main subsystems.	26
2.10 schematic of a Pockels cell and representation of the π phase shift with U_π	29
2.11 Schematic of Mach-Zehnder modulator and Field/Power transfer functions. Biased operating points allow amplitude and phase modulations in push-pull and push-push modes, respectively.	30
2.12 Constellation diagram, bits per symbol, and modulator configuration for the modulation formats OOK, BPSK, and QPSK.	31
2.13 Block diagram of the direct detection receiver.	32
2.14 Reversed-biased photodiode configuration for optical detection. Incident light power generates free charges which are drawn from the p-n junction producing an electric current. In absence of light, a small dark current is present.	32
2.15 Voltage signal after the TIA is sampled at intervals t_s , defined by the timing recovery performed within the DSP. The digitized signal is processed in the DSP and thresholding is applied to decide between received 1's and 0's.	34
2.16 Block diagram of the coherent receiver.	34
2.17 Strehl ratio vs. Fried parameter for different telescope aperture diameter D	38

2.18	Signal generated at the receiver, and probability densities associated to received ones's and zeros's. The dashed regions highlight the probability of incorrect detection. Graphic inspired from [2].	39
2.19	Mean BER in function of the mean SNR affected by the turbulence at 70° and 10° laser downlink elevations and considering a telescope aperture of 40 cm. The BER is calculated for a receiver working with (a) OOK direct detection and (b) QPSK coherent reception. The curves show the BER improvement in the absence of correction $m=1$, after tilt correction $m=3$, and after higher order compensation $m=100$ of the phase wave-front.	42
2.20	Coupling efficiency vs. corrected modes for $D/r_0 = [3, 6, 10]$ and a telescope aperture $D = 40$ cm.	44
3.1	The received beam is captured with the telescope and guided to the AO system, which corrects the high order phase distortions and couples the light into a SMF fiber. The resultant optical signal represents the modulated signal.	49
3.2	Typical adaptive optic setup with the principal hardware components. The tilt stage is not shown.	50
3.3	Representation of a DM compensating a distorted phase wave-front.	51
3.4	Working principle of the Boston Micromachines membrane-based and segmented DM. Square plates are connected to a negative potential and experience electrostatic attraction to the bottom positive electrodes. The displacement deflects the attached reflective membrane or the individual reflective segments.	52
3.5	(a) Branch points in the phase wave-front. (b) 3D view of the branch cut phase jump between branch points.	53
3.6	Working principle of the Shack-Hartmann wave-front sensor. An array of small lenses capture a portion of the distorted wave-front, which get focused at different positions in the image plane. Each focal displacement in X-Y can be translated into a phase slope at the lenslet position. All the phase slopes are used to approximate the overall wave-front phase.	55
3.7	Curvature wave-front sensor working principle.	57
3.8	Pyramid wave-front sensor working principle.	58
3.9	Interferometer wave-front sensor working principle.	59
3.10	Setup for sensor-less iterative AO system with SPGD blind phase optimization algorithm. . . .	60
3.11	Speckle imaging technique block diagram of principal processing stages.	62
3.12	Image sharpening parabolic optimization process [3].	64
4.1	(a) Short exposure PSF and (b) long exposure PSF. Turbulent scenario $D/r_0 = 6$, with $D = 40$ [cm]	69
4.2	Representation of the pupil field loss of coherence and autocorrelation process [4].	70
4.3	Probability distribution of the on-axis intensity of a large set of speckle pattern.	71
4.4	(a) Airy pattern. (b) Representation of the image processing steps applied to each focal image. The table classifies the speckles based on their peak intensities and shows the total intensity contained on their respective speckle areas.	72
4.5	Mean intensity distribution per speckle for different turbulent scenarios. The markers indicate the optimum number of processed speckles equivalent to 81% of the total focal intensity. . . .	72

4.6	Comparison between the distribution of the mean normalized intensity per speckle between measured focal images (markers) of a GEO downlink and the analytic fitting based on simulations (continuous curve) of table 4.1.	73
4.7	Simplified scheme of the optical receiver. The incoming beam is corrected in tilt, reflected in the deformable mirror, and focused on an infrared camera and single mode fiber. The speckle image and the coupled signal are used to sequentially compensate the distorted phase-front via the iterative control of the deformable mirror.	75
4.8	Representation of a pupil harmonic (plane wave) propagating in the direction of the wave vector k to the focal point of coordinates c , with an angle β_y proportional to the harmonic frequency ν_y	77
4.9	(a) Object plane and image plane representation. A plane wave originates from a point source in the object plane and propagates in the direction of the k vector to a unique point c in the image plane. (b) A plane wave propagates in the direction of the k vector which has (k_x, k_y, k_z) components. In the far field and paraxial limit, the angle β_y is small, thus, the condition of propagating plane wave ($k_x^2 + k_y^2 < k^2$) is fulfilled.	78
4.10	(a) Representation of the coherent regions of phase in the pupil plane. (b) Representation of the focal intensity image with M main speckles. (c) Simplification with the M peak intensities.	79
4.11	Representation of a distorted phase wave-front reaching the focusing lens. Each coherent region in the wave-front can be considered a source of plane waves propagating to a particular point c of the focal plane. The ensemble contribution of each focused set of plane waves results in the formation of a speckle.	80
4.12	Representation of harmonic term with spatial frequency ν_x , amplitude b , and phase shift θ	81
4.13	Description of the optimization of the phase shift of a plane wave.	82
4.14	(a) Real components of a combined set of four plane waves of different amplitudes, propagation directions, and spatial frequencies. (b) Focal image resulted of the Fourier transform of the combined plane wave set. (c) Resultant phase map of the combined set of plane waves.	83
4.15	(a) Representation of the coupled power behavior after the 3π phase shift variations of each plane wave in Fig. 4.14 (a). Markers indicate the three registered power values after three applied phase shifts, required for parabolic fitting. Black markers show the final calculated points of maximum coupling and optimum phase shift for each plane wave. (b) Ensemble average of intensity patterns before and after correction of alike randomly generated pupil fields.	84
4.16	Adaptation algorithm. The captured intensity image is used to create a set of pupil plane waves, each one associated with a main focal speckle. The plane waves are sequentially combined after the optimization of their respective phase shifts, which is done using the feedback power coupling. The argument of the optimized plane wave summation is applied to the DM and represents the estimated distorted phase-front.	86
4.17	A process to create the lookup table. The DM scans the camera sensor applying phase tilts to the reflected beam. The position of the speckle peak in the sensor is registered. During the correction of the distorted field, every speckle inside the active area can be assigned to a plane wave. Speckles outside the area are neglected	87

4.18	Comparison between the reference Fried parameter $r_{0 \text{ ref}}$ used to create sets of 1000 fields for different turbulent conditions, and the estimated Fried $r_{0 \text{ calc}}$ calculated from these fields. Each field is created with 256×256 pixels and 600 Zernike polynomials.	90
4.19	(a) Mean SMF coupling efficiency and (b) normalized variance of the received signal as a function of the number of corrected speckle spots and the signal to noise ratio of the optimization signal (SNR). (c) Normalized histogram at the maximum of each curve. (d) Optimum number of corrected speckles for different SNR values of the optimization signal. All the analyses correspond to an scenario $D/r_0 = 10$ with a $D = 40$ cm.	92
4.20	Percentage of total focal intensity per speckle. Comparison between single-screen and multiple-screen method. Markers indicate the required speckles to reach 81% of the total focal intensity .	93
4.21	(a) Required number of corrected speckles for different turbulent scenarios considering maximum performance M_1 and a penalty of 1 dB from the maximum M_2 . (b) Mean SMF coupling efficiency for different turbulent scenarios with M_1 and M_2 corrected speckles	94
4.22	Coupling efficiency distribution for (a) $D/r_0 = [5, 10]$ and (b) $D/r_0 = [15, 21]$, after the correction of the fields with M_1 (continuous plot) and M_2 (dashed plots) speckles.	94
4.23	Coupling penalty of correlated fields being corrected with their previous field states, considering a dynamic time gap of a fraction of t_0 between fields.	95
4.24	Optical receiver adapted for a dynamic implementation of the method. The camera is positioned before the DM. No change in the algorithm, neither implementation of the method is required. The nomenclature follows the description of Fig. 4.7.	96
4.25	Graphical representation of the dynamic processing of the speckle pattern. The image realization I^h is captured after a time t from the previously captured image I^{h-1} . The process is performed within the coherence time of the field τ_0 . The coordinates r_l of the speckles are compared as described in the algorithm 1.	97
4.26	(a) Numerical simulation of the proposed algorithm for the dynamic correction of correlated field. (b) PDF of the two different types of correction. The scenario corresponds to a 30° elevation link with $D/r_0 \approx 4$	98
5.1	(a) Block diagram of the laser downlink emulator, highlighting the transmitter, turbulent channel, and receiver sections, as well as the involved hardware. (b) Optical setup design to emulate the free-space link affected by the turbulence and corrected with the proposed iterative AO method.	101
5.2	Optical setup of the free-space laser downlink emulator.	102
5.3	(a) Structure of the LCOS SLM chip. Design based on the model Hamamatsu X10468-LCOS [5]. (b) Transfer function of the SLM.	104
5.4	Laboratory examples of SLM phases and their profiles for different turbulent regimes. The measured focal intensity patterns are compared. Higher D/r_0 are not well resolved by the SLM (dashed box), showing a single stable central intensity spot in all tested phase screens.	104
5.5	Comparison between simulated (continuous line) and measured (markers) focal speckle patterns. Analysis of the intensity distribution per speckle for different turbulent regimes. (a) Normalized mean intensity per speckle. (b) Mean intensity variance per speckle.	105

5.6	Maximum angular deflection of the TTM mirror for a 12 [mm] beam diameter and different turbulent regimes.	106
5.7	Comparison between the required peak-to-valley (P2V) DM stroke, and the numerical estimation of the P2V phase excursion of a set of phase screens generated for different turbulent regimes.	106
5.8	Laboratory measurement of the DM scanning process. Different tilts are applied to the illuminated area of the DM, producing a displacement of the focal speckle. The dimensions of the scanned area define the maximum DM stroke.	107
5.9	Free-space beam being focused into a single mode fiber.	108
5.10	Beam profile before the SLM.	108
5.11	(a) Measured Intensity beam profile and simulated back propagated Gaussian profile of the fiber. (b) Focal intensity profiles.	109
5.12	Signal-to-Noise ratio characterization of the APD.	110
5.13	(a) Camera signal-to-noise ratio in function of the input power.	110
5.14	Normalized single-mode fiber coupling efficiency comparison between the laboratory measurements (markers) and the simulations, considering a different set of phase-screens for varying turbulence regimes.	111
5.15	(a) Normalized coupling efficiency vs. number of corrected speckles. The inset shows the PDFs for the final coupling. (b) Evolution of the coupled signal and SNR distribution.	112
5.16	(a) Overall performance for different turbulent scenarios. (b) Ensemble of normalized intensity patterns before and after correction.	113
5.17	Experimental PDF of the coupling penalty for the scenarios (a) $D/r_0 = 5$ and (b) $D/r_0 = 6$. Comparison between the correction with 36 and 20 speckles.	114
5.18	(a) Experimental normalized coupling efficiency versus number of corrected speckles for the scenario $D/r_0 = 10$. Comparison against the curve associated with $D/r_0 = 6$. (b) PDF of the tilt corrected fields and full correction with 36 speckles. (c) Ensemble of normalized intensity patterns before and after correction.	115
5.19	Cross-correlation between pupil phase wave-fronts	116
5.20	Laboratory performance of the dynamical compensation of correlated fields ($D/r_0 = 6$, $\tau_0 = 2.1$ msec). The correction time per field AO_{loop} of the algorithm increases from (a) $AO_{loop} = 0.3\tau_0$, to (b) $AO_{loop} = 0.7\tau_0$, and (c) $AO_{loop} = \tau_0$	117
6.1	Configuration of an IQ modulator based on two $\pi/2$ phase shifted MZM operating in Push-pull mode.	121
6.2	General schematic of an optical transmitter based on the IQ-modulator.	122
6.3	Representation of the effect of the laser phase noise and amplitude in the constellation diagram of a QPSK modulation.	122
6.4	Block diagram of the coherent receiver.	123
6.5	Main blocks of the 90°-hybrid and balanced detectors.	124
6.6	Digital signal processing stages.	126
6.7	Visualization of the signal after each DSP stage for QPSK demodulation.	127

6.8	AO setup with integrated coherent transmission system.	128
6.9	Block diagram of the experimental coherent transmitter and receiver.	129
6.10	Camera input power distribution between the speckles for different turbulent regimes. The cumulative power of the speckles sum up 80% of the total input power. The minimum input power to assure a 3 dB SNR in the less intense speckle of each scenario is $P_{cam} = -54$ dBm.	129
6.11	(a) Receiver sensitivity measurement for a 40 Gbaud QPSK data transmission corrected by the AO system. (b) PDF of the BER when the AO system is set on/off. The dashed curve represents the shot-noise limited ideal performance and the dotted curve. The blue curve represents the back-to-back reference of the receiver. The green and red dots are the mean BER calculated after DSP processing of the received 50×10^6 bits per field when the AO system is ON and OFF, respectively.	132
6.12	(a) Continues BER curves are calculated with Eq. (2.99) and consider the measured power vectors for the scenarios $D/r_0 = [3, 5, 10]$ assuming constant shot noise. The dashed curve represents the shot-noise limited ideal performance and the dotted curve the back-to-back reference curve of the receiver. The green and red dots are the mean BER calculated after DSP processing of the received 50×10^6 bits per field when the AO system is ON and OFF, respectively.	133
6.13	(a) Receiver sensitivity measurement for a 40 Gbaud QPSK data transmission corrected by the AO system ON and considering correlated fields. The data measurement is performed on each iteration. The dashed curve represents the shot-noise limited ideal performance and the blue curve the back-to-back reference of the receiver. The green circles are the mean BER calculated after DSP processing of the received 58×10^6 bits (10^6 bits per iteration) per field. (b) Coupling signal penalty for each iteration of the optimization process. Normalized histogram of the coupling penalty.	134

LIST OF TABLES

<i>Number</i>	<i>Page</i>
1.1 List of satellite mission equipped with laser links, highlighting the modulation format and data rate.	7
3.1 Classification of wave-front sensor types.	54
3.2 Summary comparison of wave-front sensors characteristics.	65
4.1 Range of D/r_0 and formulae for the main coefficients of Eq. (4.1).	73
5.1 List of hardware components of the optical setup.	102
5.2 APD characteristics for the Thorlabs PDA20CS-EC set to 60 dB gain.	110
6.1 Comparison between the power requirements of the AO system and the communication system for a QPSK modulation format and $\text{BER} = 10^{-6}$	130
6.2 Comparison between the power requirements of the AO system and the communication system for a QPSK modulation format and $\text{BER} \approx 10^{-3}$. This BER is considered the limit for the error correction system to deliver error-free data transmission.	131

ABBREVIATIONS

AO	Adaptive Optics
AWS	Angular Wave Spectrum
BER	Bit Error Ratio
BPSK	Binary Phase Shift Keying
DOC	Degree of Coherence
DM	Deformable Mirror
DLR	German Aerospace Center
DSP	Digital Signal Processing
DAC	Digital-to-Analog Converter
ADC	Analog-to-Digital Converter
EO	Earth Observation
ESA	European Space Agency
FFT	Fast Fourier Transform
FSOC	Free-Space Optical Communications
GEO	Geostationary
IFFT	Inverse Fast Fourier Transform
IMDD	Intensity Modulation/Direct Detection
ISL	Inter-satellite link
JAXA	Japan Aerospace Exploration Agency
LEO	Low Earth Orbit
MZM	Mach-Zehnder Modulator
MCF	Mutual Coherence Function
OGS	Optical Ground Station
OFL	Optical Feeder Link
OCT	Optical Communication Terminal
OOK	On-Off keying
QPSK	Quadrature Phase Shift keying
RMS	Root Mean Square
SMF	Single-Mode Fiber
SNR	Signal-to-Noise Ratio
SVD	Singular Value Decomposition
SGL	Space-to-ground link
SAR	Synthetic Aperture Radar
TTM	Tip-tilt Mirror
TIA	Transimpedance amplifier
MCF	Mutual Coherence Function
WFS	Wave-front sensor

SYMBOLS AND NOTATIONS

A_s	Area of a single speckle	r	Spatial coordinate
A	Amplitude complex pupil field	r	Radial distance object plane
A_{RX}	Receiver aperture size	r_n	Radius of n ring of airy pattern
B	Amplitude complex focal field	r_0	Fried parameter
b	Amplitude plane wave	R_b	Data rate
c	Velocity of light	SR_s	Short exposure Strehl ratio
c_l	Zernike coefficient	\Re	Real term complex function
$C_n^2(h)$	Index of refraction structure parameter	$R_n^{ m }$	Zernike radial
D	Aperture diameter	U_0	Back-propagated mode SMF
D/r_0	Normalized aperture	v_g	Wind speed ground level
$D(\rho)$	Wave structure function	v_0	RMS wind speed
D_{be}	Beam diameter	v_{sr}	Slew rate
$D_n(\rho)$	Refractive index structure function	V_{sat}	Satellite velocity
$D_x(\rho)$	log-amplitude structure function	V_{\perp}	Transversal wind speed
$D_S(\rho)$	phase structure function	w_0	Fiber mode field radius
d_0	Mode field diameter	w_b	Beam waist radius Beat frequency
E_p	Photon energy	w_a	Back-propagated mode field radius
$E_{TX}(t)$	Transmitted data signal	W	Wave-front
$E_{RX}(t)$	Received data signal	Z	Zernike polynomial
f	Lens focal length	z	Propagation distance
F	Complex focal field	ρ	Field vector position
H_{sat}	Satellite altitude	θ	Phase complex focal field
H_{se}	Avg. Short-exposure Atmospheric OTF	λ	Laser wavelength
\mathfrak{F}	Fourier transform	ϕ_{pt}	Phase piston
I	Focal intensity image	θ	Scalar phase shift
I_0	Maximum normalized intensity	Φ_b	Beam divergence angle
I_t	Total focal intensity	φ	Phase complex pupil field
$j\Re$	Imaginary term complex function	η	SMF coupling efficiency
J_0	Zero-order Bessel function first kind	η_{norm}	Normalized SMF coupling
$J_{1,2}$	1st, 2nd, order Bessel funct. first kind	Φ	Single speckle phase
k	Plane wave propagation vector	Φ_n	Kolmogorov power law distribution
k	Wave number	α	Elevation angle
l_0	Small scale turbulent cell	α_{div}	Geometrical attenuation
L_0	Large scale turbulent cell	α_e	Extinction coefficient
M	Number considered/corrected speckles	$\alpha_{atm}(t)$	Atmospheric attenuation
m	Azimuthal freq. Zernike polynomial	ψ	Azimuthal angle object plane
N	Number of fields	Δ_j	Phase residual error
N_p	Number photons per bit	ρ	Radial distance focal plane
N_0	Number coherent cells within aperture	ϑ	Azimuthal angle focal plane
n	Radial frequency Zernike polynomial	\circ	Angle degree
$n(\rho)$	Spatial media refractive index	$\langle \rangle$	Ensemble average
p_I	Irradiance probability density function	τ	Atmospheric transmittance
P_s	Communication input power	τ_0	Atmospheric coherence time
P_{in}	Communication input power	ζ	Zenith angle
P_{AO}	Adaptive optic input power	δ_{DM}	Maximum DM stroke
P_{cam}	Camera input power	σ_I^2	Scintillation index
P	Complex pupil field	σ_R^2	Rytov variance

σ_{res}^2	DM Residual phase variance
σ_{fit}^2	DM Fitting error
σ_t^2	DM Temporal error
σ_S^2	Wave-front variance
$\Gamma_2(\rho)$	Mutual coherence function

PUBLISHED CONTENT AND CONTRIBUTIONS

JOURNALS

- **C. E. Carrizo**, R. Mata-Calvo, and A. Belmonte, “Intensity-based adaptive optics with sequential optimization for laser communications,” *Opt. Express*, vol. 26, no. 13, pp. 16044–16053, 2018
- **C. E. Carrizo**, R. Mata-Calvo, and A. Belmonte, “Proof of concept for adaptive sequential optimization of free-space communication receivers,” *App. Optics*, (Accepted 10.6.2019)
- **C. E. Carrizo**, R. Mata-Calvo, A. Belmonte, and J. Surof, “Multi-gigabit coherent transmission over turbulent channels compensated with speckle-based adaptive optics,” *App. Optics*, (In preparation)

CONFERENCES

- **C. E. Carrizo**, R. Mata-Calvo, and A. Belmonte, “Speckle-based sequential optimization of adaptive receivers in downlink laser communications,” in *SPIE Environmental Effects on Light Propagation and Adaptive Systems*, 2018, no. 107870C, p. 10
- R. Mata-Calvo, J. Poliak, J. Surof, A. Reeves, M. Richerzhagen, H. Kelemu, R. Barrios, **C. E. Carrizo**, R. Wolf, F. Rein, A. Dochhan, K. Saucke, W. Luetke, “Optical technologies for very high throughput satellite communications,” in *SPIE Free-Space Laser Communications XXXI*, 2019, no. 10910, p. 31
- **C. E. Carrizo**, R. Mata-Calvo, and A. Belmonte, “Application of Lasers for Sensing and Free Space Communication,” in *OSA* (submitted for presentation)

PATENT

- **C. E. Carrizo**, R. Mata-Calvo, and A. Belmonte, “Method for determining altering parameters for altering the optical features of an optical element for compensation of distortions in a beam for optical free-space communications (EU patent - Accepted, not yet published)

DEDICATION

To Mirta and Carlos, Carina and Daniela

Chapter 1

INTRODUCTION

THIS chapter introduces the topic of this doctoral thesis and gives a conceptual overview of the effects of the turbulence in a propagating beam, the turbulence compensation methods, and communication systems involved in FSOC. The objective of this chapter is to introduce the reader to the topic and the main areas addressed in detail in the following chapters. This chapter also presents the thesis objectives and outline.

1.1 The need for free-space optical communications

Free-space optical communications (FSOC) is rapidly becoming a key enabling technology for terrestrial, aerial, and space communication networks. The fast progress of FSOC in the last decade and the recent boost in research and commercialization of this technology has been driven by the rising demand in satellite communication bandwidth and security.

The field of earth observation (EO) is nowadays experiencing a rocketing demand in the communication bandwidth. Advanced payloads, like high-resolution cameras and synthetic aperture radar (SAR) systems, generate massive amounts of information with daily volumes of 8 Tbps (Terabits per day); estimating an increment to 20 Tbps by 2020 [6]. The download of such amount of information is limited by the short contact time between the satellite and the ground station, and the radio channel capacity. Today, the most mature and stable technology to download remote sensing information is radio link in X-band reaching up to 500 Mbps per channel, or even 1 Gbps using orthogonal channels. Here, Quadrature Phase Shift Keying (QPSK) is a robust, often adopted, carrier modulation scheme [6]. To fulfill future demand, the International Telecommunications Union has allocated the K_a band (1500 MHz bandwidth) to provide up to 3.5 Gbps downstream with orthogonal channels [7]. However, the K_a band is affected more by the atmosphere and special care has to be taken with the interference between flying platforms within the same spectrum. Because of the steady increase in the generated data volume, this technology will soon be reaching its limits. Consequently, earth observation may certainly benefit from stable and efficient laser downlinks between satellites and earth optical ground stations.

Optical systems work at frequency ranges four orders of magnitude above the highest practical radio frequency used in satellite communications. This terahertz-wide bandwidth offers the possibility of huge throughputs and the capacity of multiplexing several gigahertz channels. Additionally, if one compares with the RF counterpart, the short optical wavelength (typically 1064 and 1550 nanometers) allows equal signal gain with reduced optical antenna size (i.e. telescope diameter) which saves weight in satellite payloads [8]. Optical systems also require less transmission power, extending the life span of the satellite. The use of narrow beams results in better power efficiency over long distances and minimum risk of interference, making it attractive for security sensitive applications. The later also implies that no standardization is required, except for power safety concerns [9].

A huge operational and economical benefit may result from the possibility of using laser links instead of the RF counterpart. The increment in bandwidth can minimize the storage requirements in the satellite and extend its life span. This approach faces an important limitation that reduces the link availability. This limitation is related to the strong turbulence at low LEO satellite elevations. Establishing a robust laser link under such conditions is important because most of the flying time of LEO satellite occurs below 30° (or 60° Zenith angle). At such elevations, the laser beam travels long distances and the cumulative effect of the turbulence induces strong amplitude and phase distortion in the wave-front. Because of wave-front distortions, the focusing of the beam results affected, leading to signal fading. High data throughput requires a stable and efficient single-mode fiber (SMF) coupling that allows the integration of fiber based components, like optical amplifiers and coherent receivers. Consequently, beam wave-front correction is required to improve the power coupling, reduce the signal variance, and thus benefit from the satellite seeing and downloading time.

The following sections give a brief conceptual overview of the involved challenges and possible solutions,

leading to the main objectives of this thesis.

1.2 Atmospheric channel limitations for lasercoms

A laser beam propagating from ground-to-satellite (uplink) or satellite-to-ground (downlink) through the atmosphere face unique constraints associated with cloud blockade, absorption and scattering losses, and mainly due to turbulence induced wave-front distortions.

Clouds attenuate the power of a laser downlink reducing the link availability. Ice clouds attenuate up to 15 dB/Km [10], while water clouds represent between 30 and 600 dB/km link power attenuation [11, 12]. This phenomenon varies by region and geographical position, thus Optical Ground Stations (OGS) should preferably be located on a mountain top or in the Mediterranean and sub-tropic latitudes where clear skies are more frequent [13]. To assure 100% availability, ground station diversity is used [14]. This concept implies the distribution of the OGS in different locations, ensuring that when clouds block some stations, others are available.

Atmospheric absorption and scattering occur when the laser beam interacts with various gas molecules and aerosols particles. Beer's law describes the losses due to these factors being wavelength dependent [15], from which the atmosphere has the so-called atmospheric transmission windows. For the particular field of FSOC, the preferred wavelengths span 780 - 850 nm (nanometer) and 1520 - 1600 nm. Today's widely adopted wavelength is 1550 nm due to the synergy with available transponders, amplifier, and detectors used in terrestrial fibered networks. Luckily, 1550 nm coincides with a low atmospheric absorption region (0.2 dB/Km). More details are given in chapter. 2.

The atmospheric turbulence represents the main limitation in free-space optical communications (FSOC), and can be considered significative from ground level until the Tropopause (20 Km height), see Fig. 1.1. The turbulence originates from heating and cooling of the earth's surface during the day and the consequent energy transfer to the air that eventually acquires motion [16]. Large spatial scale motion gradually breaks up into smaller pockets of air of random sizes and temperature, called eddies. The differences in temperature alter the air refractive index thus when a wave-front propagates through these eddies it suffers from localized alterations in amplitude and phase. A *laser uplink* experiences the effect of the turbulence at the very moment it is emitted from the OGS, thus it starts to spread and accumulate distortions from the beginning leading to larger losses compared with the downlink case. As the source of distortion is close to the emitter, uplinks wave-fronts are modeled as spherical waves [17]. The *downlink beam* propagates from the satellite with minimal losses until the 20 Km height. Alongside this path, the beam diverges as it propagates and the wave-front can be considered as a plane wave by the time it reaches the Tropopause. From this point onward, until reaching the OGS, the beam downlink experiences losses and distortions. These perturbations in the wave-front can be physically described by Kolmogorov model [18]. The size difference between the eddies and the beam results in different effects on the beam wave-front.

Beam wander σ_{BW}^2 occurs when eddies are larger than the beam size, having a net effect of random deflection of the propagation direction. This phenomenon is a major problem in uplinks since deviations of the beam trajectory at the beginning of the path results in several hundred meters displacements at the receiver satellite position.

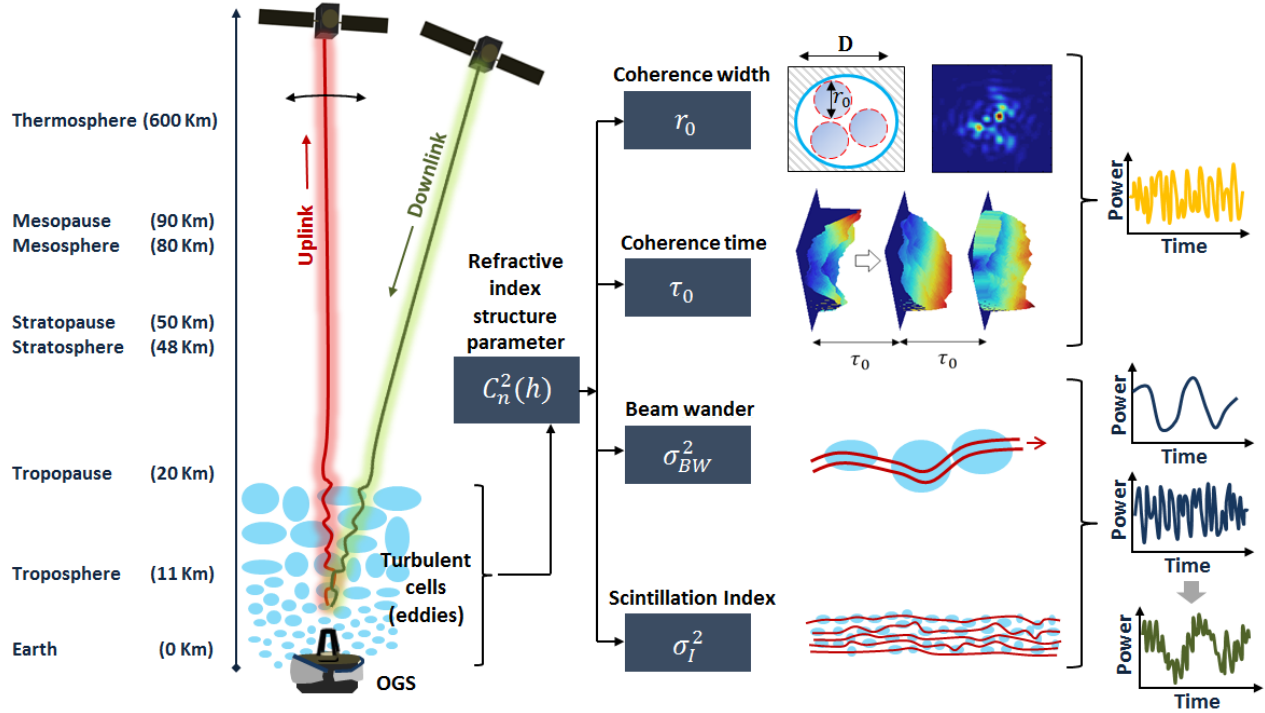


Fig. 1.1: Representation of the atmospheric effects in an optical uplink/downlink.

Considering that a receiver aperture diameter is generally small and assumed as point source receiver, this wandering of the beam produces slowly varying large dynamic range of the acquired signal power, see Fig. 1.1.

Beam spreading occurs when the eddies are smaller than the beam size, inducing diffraction and scattering that distort the received wave-front.

Beam scintillation σ_I^2 happens when the eddies have sizes in the order of the beam dimensions. As mentioned before, the eddies will act as lenses that will redistribute the beam energy, resulting in temporal and spatial irradiance fluctuations of the received signal. This atmospheric effect is critical in FSOC uplinks where it gets combined with the beam wander effects, impairing the communication performance. A method to mitigate the scintillation effects and reduce the signal fading is called aperture averaging. This method is beneficial in FSOC downlinks scenarios where OGS apertures are large, typically between 40 cm and 1 meter; thus the aperture acts as a spatial filter of the irradiance and reduces the induced signal fluctuations. Uplinks use small receiver apertures (≤ 10 cm) with little averaging effects; hence scintillation becomes a problem to solve.

Loss of spatial coherence of the beam also occurs when eddies have sizes in the order of the beam dimensions. The beam experiences localized phase delays that alter the coherence of the propagating field. To quantify this effect, Fried derived one of the most used parameters in atmospheric optics, the atmospheric coherent width r_0 (Fried parameter). This metric describes the long-term turbulence impact on imaging systems [19]. Wave-front distortions result from the cumulative effect of the turbulence, which is particularly strong at low elevations since the laser beam must travel long distances. Consequently, the spatial coherence of the wave-front near the zenith of an OGS will be larger (large r_0) than near the horizon (small r_0). By comparing r_0 with the diameter of the receiver telescope aperture D , the metric D/r_0 indicates the degree of decorrelated regions embraced by

the aperture, which is proportional to the degree of energy dispersion of the focused beam (speckled intensity pattern). This particularly important and critical factor in laser communications downlinks induces variations of the sensed power signal with a large dynamic range, which fluctuates in a time scale of a couple of milliseconds quantified with the atmospheric coherent time τ_0 (time between fully decorrelated field). This power fluctuation develops into severe signal fading that impair the performance of the data transmission [16, 20]. The averaging effect that benefits ground reception against scintillated fields comes at the expense of having larger portions of the spatially distorted beam wave-front embraced by the aperture. This means that larger D/r_0 are representatives of stronger turbulence effects in the received downlink signal. Instead, laser uplinks are very little affected by the decoherence of the wave-front, since the receiver apertures are smaller than the coherence width of the wave-front and only tilt angle of incidence is present.

All of these different metrics can be calculated from the refractive index structure parameter C_n^2 , which quantifies the strength of the index of refraction fluctuation of the atmosphere at different heights. This profile must be measured for the particular conditions of the OGS locations and different models are generally used, like the Hufnagel-Valley. Details of the calculation and derivation of these parameters are given in chapter. 2.

The achievement of an efficient FSOC uplink and downlink involves different technical challenges and these cases must be treated independently. This work focuses on the downlink case.

1.3 Communication systems in free-space optics

The optical communication systems employed in FSOC are the same to those used in fibered networks, and the main difference rests on the free-space channel. In every communication system, the transmitter modulates the information on a carrier whose properties are optimal for the transmission channel. The channel induces unwanted effects in the signal which, once received, is demodulated to retrieve the information. The performance of the communication depends on the right selection of the modulation/detection technique, based on the channel characteristics. Detection techniques are vast, but they can be categorized into two main groups: Direct detection (incoherent) and coherent detection.

Direct detection (DD) systems collect and focus the received beam to a photodetector, which directly reacts to the received signal power and converts it into an electrical signal. The principal advantage of direct detection is its simplicity and the possibility of using larger photodetectors, so fiber coupling or adaptive compensation systems are not required. The modulation format generally adopted is intensity modulation (IM), where the carrier is switched on and off based on the digital data '0' and '1' (On-Off keying OOK), respectively. Due to this, this type of scheme is known as intensity modulation/direct detection (IMDD). The detection of one and zeros is performed in the electrical domain using thresholding; details are presented in Sec. 2.2.2.1. This is the simplest modulation format, yet the most widely implemented in FSOC. As mentioned before, the turbulence induces amplitude modulation (scintillation) and phase distortions (spatial field decoherence). The IMDD scheme is insensitive to phase distortions since it only reacts to the changes on the beam wave-front intensity, hence it is affected by strong scintillation. Because phase distortions do not impact on this communication scheme, the receiver aperture can be enlarged to benefit from aperture averaging.

The IMDD scheme is generally employed for data rates up to 10 Gbps where larger photodetectors can

still be used [21]. This data rate is not uniform in LEO downlinks scenarios. Typically, a LEO downlink to an OGS starts the acquisition process at 5° elevation from the horizon and the communication process from the 10° elevation towards the zenith. From the total seeing time of the satellite, 64% of the time occurs at elevations between 5° and 20° , where longer optical paths imply higher power losses and stronger impact of the atmospheric turbulence (strong scintillation). A conservative estimation of the use of IMDD for LEO downlinks, only considering atmospheric attenuation effects, limits the data rates below 1 Gbps during 64% of the seeing time, reaching the 10 Gbps at around 70° of elevation [21].

Higher data rates and better spectral efficiency can be achieved with coherent systems. These systems modulate the amplitude, frequency, phase, and polarization of the carrier with the so-called IQ-modulator, composed of two Mach-Zehnder modulators (MZM) operating in different configurations. The signal carrier (laser) is split and delayed, sent to each MZM, and modulated with the information signal. After that, the modulated carrier is combined, amplified and sent to the free-space channel; details in Sec. 2.2.1. In reception, the received signal is combined with that of a local oscillator (LO). After combining both signals, the carrier is down-converted to baseband (homodyne), or to an intermediate frequency (Heterodyne-Intradyn) from which further signal processing is performed to extract the information. One of the main advantages of coherent reception is that the power of the local oscillator signal can be incremented to improve the detection of weak signals. In addition, the fact of being able to combine modulation states like amplitude and phase simultaneously, allows to encode several bits within few symbols, thus the spectral efficiency is drastically increased [22, 23]. Two very efficient modulation formats are BPSK and QPSK, where 2 and 4 states of the carrier phase (symbols) are changed to represent 1 and 2 bits per symbol, respectively.

In the absence of turbulence, like inter-satellite links, homodyne detection is possible since the precise synchronization of the received and LO signal can be performed with a fine Phase Locked Loop (PLL) stage. In the presence of turbulence, the wave-front phase distortions make this task increasingly difficult, and practically impossible under strong turbulence regimes. Consequently, heterodyne and mainly intradyne receivers are adopted. Here, the downconversion of the carrier frequency to a lower intermediate frequency allows the use of digital signal processing for the correction of the atmospherically induced phase distortions in the data signal [24]. However, an efficient single mode fiber (SMF) coupling is required for the implementation of such coherent schemes. Due to this, phase wave-front distortions become relevant as they affect the efficiency of fiber coupling, especially in regimes of strong turbulence. This has been one of the main factors limiting the use of such high-efficient schemes in FSOC.

The table 1.1 shows different satellite missions of Asia, USA, and Europe employing lasercoms. Clearly, IMDD has been the preferred scheme in most of the missions. Paying attention to the data rates, most of them perform below 1 Gbps, except for the OSIRISv3 (DLR) mission that reached 10 Gbps data downstream. TerraSAR-X (DLR) and EDRS/Copernicus (ESA) are the very few mission testing BPSK coherent transmission, mostly for inter-satellite links. Other modulation schemes are Pulse Position Modulation (PPM) [25, 26] and Differential Phase Shift Keying (DPSK) [27], not discussed here.

To fully benefit from the spectral efficiency of coherent BPSK or QPSK schemes in all the flying path of a LEO satellite downlink, the adaptive compensation of the turbulence-induced wave-front distortions needs to be addressed.

	ASIA		USA		EUROPA	
FSOC Satellite Missions	1994: ETS-VI (NICT) GEO-GND 0.8-0.5 μ m, 1Mbps	IMDD	1995: GOLD (NASA JPL) GEO-GND 0.8/0.5 μ m, 1Mbps	IMDD	2001: SILEX (ESA) GEO-LEO, GEO-GND GEO-Air 0.8 μ m, 50Mbps	IMDD
	2006: OICETS (JAXA/NICT) LEO-GEO, LEO-GND 0.8 μ m, 50 Mbps	IMDD	2000: STRV-2 (BMDO), LEO-GND, Failure 0.8 μ m, 1.2Gbps	IMDD	2008: TerraSAR-X (DLR) LEO-LEO, LEO-GND 1.06 μ m, 5.6Gbps	Homd. BPSK
	2011: HY-2 (China) LEO-GND 1.5 μ m, 504Mbps	IMDD	2008: NFIRE (MDA) LEO-LEO 1.06 μ m 5.6Gbps	Homd. BPSK	2011: BTLS (Russia) ISS-GND 1.55 μ m/0.85 μ m, 125Mbps	IMDD
	2014: SOCRATES/SOTA (NICT) LEO-GND 0.98/1.5 μ m, 10Mbps	IMDD	2013: LLCD (NASA GSFC) Lunar-GND 1.5 μ m, 622Mbps	PPM	2013-2016: EDRS/Copernicus (ESA) GEO-LEO, GEO-GND 1.06 μ m, 1.8Gbps	Homd. BPSK
	2016: QKD satellite (China) BB84 0.85/0.532/0.671 μ m		2014: OPALS (NASA JPL) ISS-GND 1.5 μ m, 30-50Mbps	IMDD	2016-2019: OSIRISv1-3 (DLR) LEO-GND 1.5 μ m, 20M-10Gbps	IMDD
	2017: RISESAT/VSOTA (NICT) LEO-GND 0.98/1.5 μ m, 1kbps	IMDD	2015: OCSD-A (Aero. Corp.) LEO-GND, Failure 1.5 μ m, 5-50Mbps	IMDD		
	2019: JDRS (JAXA) GEO-GND 1.5 μ m, 1.8Gbps	DPSK	2016: OCSD-B&C (Aero. Corp.) LEO-LEO, LEO-GND 1.5 μ m, 5-200Mbps	IMDD	2017: EDRS-C (ESA) GEO-LEO 1.06 μ m, 1.8Gbps	Homd. BPSK
		2018: LCRD (NASA GSFC) GEO-LEO, GEO-GND 1.5 μ m, 2.8G/622Mbps	DPSK /PPM			

Table 1.1: List of satellite mission equipped with laser links, highlighting the modulation format and data rate.

1.4 Adaptive turbulence compensation in lasercoms

The main challenge to establish a high-performance optical link is the atmospheric turbulence. As mentioned before, when the propagating laser beam passes through a region affected by turbulence, changes in the index of refraction distort the phase-front leading to intensity fluctuations (focal speckles). Ideally, a plane phase-front passing through the focusing optics of the receiver telescope results in a perfect airy pattern, and coupling into a single-mode fiber is achieved with a theoretical coupling efficiency of $\approx 81\%$. When the turbulence distorts the phase-front, the focused light results in a spreading spot, the power fluctuates randomly every millisecond, and an efficient focusing cannot be achieved. This randomly varying speckle limits the use of higher modulation schemes like BPSK and QPSK, which require an efficient single mode fiber (SMF) coupling.

Adaptive optics (AO) techniques can be used to improve the performance of laser communication links. Its main task involves sensing the phase wave-front of the received beam and controlling the shape of a deformable mirror (DM), where the beam is reflected, in order to compensate and minimize the phase distortions. This allows the focusing of the beam energy at the fiber core position. The DM is a micro-mechanical device composed of a flexible membrane and an array of actuators that deform the membrane to mimic the distorted phase. The distorted phase is estimated after capturing the beam with a wave-front sensor (WFS), and post-processing the intensity information. Direct measurement of the phase is not possible and has to be estimated through intensity measurements. As the field evolves in time, these systems run in a real-time closed-loop following the field evolution dynamically. An AO system typically consists of a wave-front sensor, a separated tilt mirror to correct for the angle of incidence of the beam, a deformable mirror to correct the higher order phase distortions, and a control algorithm running in a PC or similar platform.

In FSOC, a perfect wave-front correction is not required, like in imaging applications or astronomy. Instead, a partial phase correction seeks to overcome coupling losses that may limit the feasibility of communication due to link budget limitations and strong fading. The partial correction of the wave-front distortions needs to consider a trade-off between power coupled into a SMF and complexity of the AO system. The received beam from LEO satellite downlink shows various degrees of phase distortions, phase singularities (abrupt 2π phase dislocation), and scintillation levels during the satellite pass. The time required for the wave-front correction is defined by the coherence time of the field τ_0 , and it ranges between 2 and 0.5 milliseconds for elevation between 5 and 60 degrees, respectively [28]. These values include the effect of the slew rate of the satellite and the atmospheric wind. For a geostationary (GEO) satellite communications an important limiting factor is the low received power. Thus, an AO system for satellite optical communications must be efficient in all turbulent regimes, particularly robust under strong wave-front fluctuations, and able to work with low received power.

Adaptive optics systems applied in astronomy, the closest comparable scenario, use traditional WFS like Shack-Hartmann (SH) and interferometers. Both approaches fall within the category of direct methods and perform satisfactorily as long as the turbulence level is moderate (up to 30 degrees elevation). The low beam elevation involved in FSOC makes the phase sensing process very difficult due to the strong scintillation and the occurrence of branch points. When a SH system is used in such scenarios, the phase estimation leads to errors and the performance deteriorates [29], this is because branch points deviate the focusing of the lenslet array to the CCD region corresponding to a neighboring lenslet, leading to a wrong estimation of the local tilt [30–33].

A system based on an interferometer usually involves complex hardware that needs to be carefully adjusted and also has difficulties with scenarios of low received power, like GEO-earth downlinks. Both approaches are seriously limited by phase singularities and/or strong scintillation. Another approach involves working on the focal plane, one method is called phase diversity and curvature sensors, where images in focus and defocus are combined to recover the phase distribution [34–36]. This involves the capture of more than one image during the correlation time, which happens to be in the order of milliseconds, and implies the use of very fast infrared cameras which need to be able to work in the kilohertz range. Details of these sensors are given in Sec. 3.1.3.

Alternatively, the WFS can be suppressed by driving the DM using a direct system performance metric optimization, also known as sensor-less adaptive optics. Here, the control of the wave-front corrector is performed by a blind (model-free) optimization of a system performance metric, e.g., power in the bucket, the Strehl ratio, or the power coupled in the fiber. Two different blind search approaches are generally considered. The zonal approach randomly changes the states of single DM actuators in searching for optimal power coupling; the modal approach shapes all actuators at once, following an orthogonal modal basis (e.g., Zernike polynomials) [37]. Because of the development of efficient control algorithms such as stochastic parallel gradient descent (SPGD) [38,39], and their implementation using parallel processing hardware based on very-large-scale integration (VLSI) micro-electronics, plus the progress in the development of high-bandwidth wave-front phase controllers such as micro-mechanical systems (MEMS)-based deformable mirrors, it is now feasible to develop AO systems for FSOC without a WFS [40,41]. These methods have as a main drawback the longer response time for convergence, since each actuator of the DM is randomly moved until the convergence is reached [42]. Typical iteration numbers for a good coupling efficiency range from 500 to 1000 and even 3000, which are not suitable for scenarios of high turbulence with time constraints in the millisecond range. Recent progress has reduced the number of iterations to around 100 [37], but still, the system must have effective loop bandwidths above 100 kHz. These bandwidths requirements are limited by the capacities of today's DM and the complexity of control systems running at such frequencies.

To the present, the SH-based solution remains to be the preferred WFS adopted by the FSOC community, mainly due to its technological maturity and relative hardware complexity. Using this technique, successful optical downlinks achieving Gigabits data rates under weak to moderate turbulence have been recently demonstrated [43–47]. However, **the sensor-less approach is attractive for free-space optical communications due to its robustness under all levels of turbulence strengths. It also offers hardware simplicity, power efficiency, and easy integration in existing AO systems. A reduction in the convergence time may bridge this fundamental limitation making possible its use in FSOC systems.**

1.5 Thesis objectives

The German Aerospace Center (DLR), and particularly the optical communications group at the Institute of Communications and navigation (IKN), has been involved for more than two decades in the study and solution of problems related to free-space optical propagation and communications. My doctoral work originates from a DLR project seeking to establish a robust laser downlink from LEO satellites used for applications like earth observation (EO), as well as Aircraft-to-Ground and GEO-to-Ground links. Taking a direct-to-earth downlink

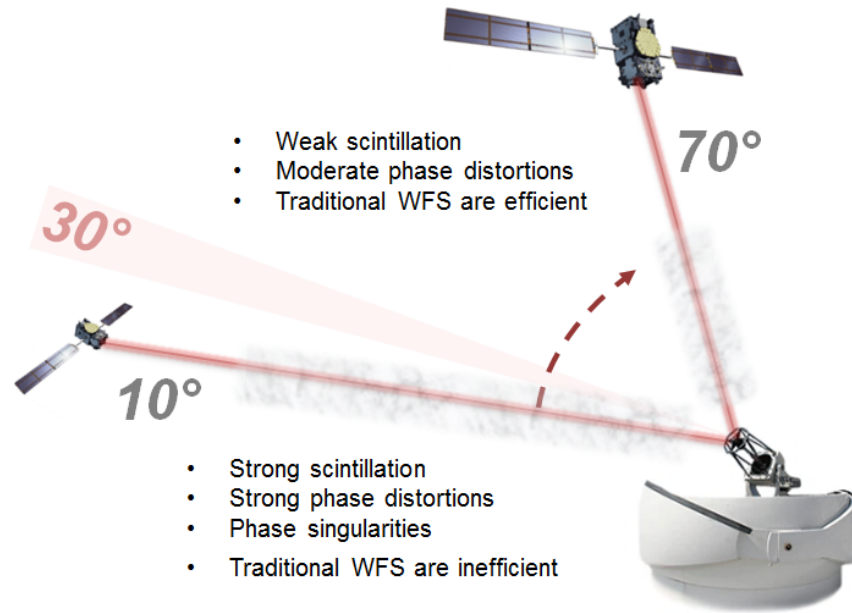


Fig. 1.2: Standard AO solutions employed in FSOC perform efficiently in weak and moderate turbulence, which tends to occur above the 30° elevations of a beam downlink. At lower elevations, the turbulence effects are stronger and an alternative AO system is required.

from LEO satellites as an example, it involves different link elevations with varying distances and turbulence regimes. As introduced in the previous sections, the main limitation is represented by the scenarios of strong turbulence at lower elevations ($<30^\circ$) where the turbulence is considered strong. Under such turbulence regimes, the degree of amplitude and phase distortions in the beam wave-front seriously impair the communication performance. Considering that LEO satellites remain approximately 64% of the flying time below 20° , the full potential of laser communications cannot be used unless the problem of wave-front correction is effectively addressed. By improving the quality of the received beam, focusing of the light into a single mode fiber and the consequent implementation of advanced modulation schemes, like BPSK and QPSK, is entirely feasible. The possibility of using such modulation schemes allows transmission rates higher than 10 Gbps. Knowing that the amount of generated information in applications like EO is expected to reach 20 Tb/day by 2020, and that RF systems are reaching their limits, the necessity of a robust optical solution is evident.

As introduced before, adaptive optics is used in many fields to correct wave-front distortion, but the standard techniques, like Hartmann-based AO systems, were designed for scenarios of moderate turbulence and more relaxed time constraints. The level of scintillation, wave-front distortion, and phase singularities present in FSOC impose limitations on those systems. Alternatively, iterative AO systems offer a good set of characteristics like robustness in all turbulent regimes, hardware simplicity, easiness of integration and calibration, and low cost. The principal limitation here is the long convergence time of the iterative process, which typically follows a blind optimization of the power coupled in the fiber and thus it requires AO loops running at 100 KHz or more; definitively non-practical with the state-of-the-art DM's. Existing AO systems still are not fully reliable under strong turbulence conditions. In particular, iterative solutions have not really evolved further and instead they have been combined with conventional wave-front sensors, increasing the hardware complexity.

The general objective of this thesis is to develop an adaptive optics solution for weak to strong turbulence compensation focused on scenarios of laser downlinks between satellite/aircraft and earth ground stations. The goal is to achieve SMF coupling with sufficient efficiency, meaning an improved gain and reduced signal variance, allowing the use of advanced coherent modulation formats to achieve very high data throughput. The solution needs to fulfill the requirements of an optical ground stations (OGS) for communications, which requires a simple, robust, cost-effective, easy to integrate and calibrate AO system.

In line with these requirements, the proposed method does not use costly and complex wave-front sensors. Instead, it benefits from the image information of the existing OGS tracking camera (speckled intensity pattern) and the power coupled in the fiber, to perform a modal iterative correction of the distorted wave-front. The proposed technique uses the spatial information of the speckle pattern and quadratic optimization of the coupled power to reduce the convergence time of the iterative process within today's DM capabilities. The final algorithm can be classified as non-stochastic, non-blind but well-defined, resulting in a flexible and tractable AO method.

This thesis seeks to demonstrate the above-mentioned claims and intends to offer a new insight to iterative solutions, hopefully encouraging further development in the field. The individual objectives to be addressed in this work are described as follow:

- *Analysis and modeling of the proposed speckle-based compensation method:* First, the short-exposure focal speckle pattern needs to be understood from the point of view of its intensity distribution. The standard literature provides vast information of the speckle statistics treated as a whole, but there is less information on the behavior of each single speckle, thus information of how the total intensity distributes on each spot is needed. It is assumed that only the most intense speckle spots need to be treated to achieve sufficient wave-front compensation [48,49]. The new technique departs from this assumption and it is modeled and mathematically detailed, explaining the processes behind the possibility of using the speckled intensity image to accelerate an iterative wave-front correction. The goal here is to show that the unknown phase field in the pupil plane and the measured focal plane intensity pattern can be directly linked, thus the speckle information can be used for the compensation of the field. Most importantly, this work seeks to demonstrate that, in this model, the compensation process fulfill conditions of a convex problem and each speckle can be adjusted with the quadratic optimization of the coupled power in the fiber.
- *Numerical analysis of the technique:* A key characteristic of the technique is the optimization of each speckle phase with only three power measurements (three iterations per speckle); this allows reducing the total number of iterations proportionally to the number of treated speckles. The first objective here is to verify this assumption and quantify the SMF coupling efficiency improvement with each corrected speckle. As initially mentioned, efficient and stable fiber coupling allows the use of coherent modulation formats to achieve very high data transmission throughput. The second objective seeks to estimate the performance of the method in typical turbulent scenarios. The technique needs to be tested in scenarios of weak to strong turbulence evaluating the signal gain and reduction in the signal variance within the pre-established number of iterations.
- *Experimental evaluation of the adaptation technique:* The main objective in the experimental evaluation

of the technique is to validate the assumptions and simulations previously made. A real-time working prototype is out of the scope of this thesis. The laboratory work tries to demonstrate that the speckle pattern can be used to iteratively compensate the distorted field in different turbulent regimes, following a well-defined, tractable, and non-blind approach. Mostly, it is intended to confirm that the model is technically feasible and the system performance follows the expected trend with the correction of each focal speckle. Additionally, the experiments try to quantify the impact of the noise and laboratory hardware constraints in the method, generally associated with technical limitations in the system implementation. Finally, it is expected to obtain a better understanding of the processes involved to help in future developments and the improvement of the technique and model.

- *Experimental validation in a communication scenario:* The final objective of this thesis involves the validation of the AO system in a communication scenario. A coherent QPSK transmitter and receiver is integrated with the AO system and the improvement in the channel quality is quantified through measurements of BER. The main goal is to verify that, in the presence of turbulence, the AO system can sufficiently correct the induced wave-front distortion allowing a better SMF coupling and the consequent multi-gigabit transmission. An in-depth investigation of coherent communications with adaptive optics is out of the scope of this thesis; instead it is intended to demonstrate that the technique can, in principle, cope with similar turbulent scenarios.

1.6 Thesis outline

This thesis is organized in seven chapters, including this introductory chapter. The general theoretical background needed for this work is presented in Chapter 2. A discussion of different adaptive optics systems for FSOC is given in Chapter 3. Each one of the objectives mentioned above is addressed in chapters 4 to 6, respectively. The final conclusions are discussed in chapter 7. The main content of each chapter is detailed as follows:

- Chapter 2 provides a detailed theoretical background of the atmospheric effects on a propagating laser beam. Here, all the relevant atmospheric parameters, conceptually introduced in chapter 1, are mathematically detailed and explained. The communication scenario and the building blocks of a typical system are introduced. A description of the signal evolution from the transmission to the reception stage, as well as the noise sources, is given. The incoherent and coherent modulator are presented, as well as their correspondent demodulator. The standard metrics of BER, Strehl ratio, SNR, SMF coupling efficiency are mathematically introduced, including the induced effect of the turbulent channel.
- Chapter 3 describes the standard adaptive optic system and main components. It gives an overview of the relevant direct and indirect AO systems, describing their working principle and limitations in a FSOC scenario. Finally, this chapter provides a comparison of these systems from the perspective of lasercoms.
- Chapter 4 presents the proposed speckle-based sequential iterative method for phase wave-front compensation. First, an analysis of the speckled intensity pattern is performed, focusing on the intensity distribution among the individual speckles. Then, the mathematical framework and processes of the

adaptation technique and system are described. The main stages of the method for a plausible implementation are detailed. A numerical analysis of the performance is also presented in this chapter. The technique is evaluated in terms of the SMF coupling efficiency versus loop bandwidth utilization (number of required iterations), considering different turbulent scenarios typical of FSOC. Finally, a preliminary concept for the dynamic correction of correlated fields is proposed and numerically evaluated.

- Chapter 5 presents the laboratory proof of concept. The optical setup, built to emulate a LEO downlink scenario, is described. A characterization of the main hardware components is performed to define the constraints and turbulence range for the experiments. The system is evaluated with decorrelated and correlated fields in a non-real time regime, and the experiments target the validation of the numerical analyses and the working principle presented in chapter 4, thus the same type of analyses are performed. This includes an analysis of the loop bandwidth utilization of the method, and the performance against signal noise. Finally, the proposed concept for the dynamic correction of correlated fields is experimentally evaluated.
- Chapter 6 focuses on the integration of the AO system with a QPSK transmission system to test the method in a communication scenario. First, an overview of the coherent QPSK transmitter and receiver is presented, describing the main processes involved. Then, the integration of both system is explained and the main building blocks of the coherent transmitter and receiver are described. Measurements of BER are carried out considering a non-real time functioning of the system, and performing the correction of uncorrelated and correlated fields. An analysis of the power requirements of the AO system versus the communication system is also presented. Finally, an estimation of the BER performance in scenarios of strong turbulence is carried out.
- Chapter 7 presents the final conclusions for each one of the initial objectives and the future work required to improve the results obtained in this thesis.

Chapter 2

FREE-SPACE LASER DOWNLINKS

LASER beams propagating through the atmosphere are affected by different phenomena that alter the characteristics of the received wave-front. As introduced in the previous chapter, the impact of the atmosphere on the beam wave-front can be quantified through several metrics, and the understanding of them contributes to the development of an efficient solution.

When high data rates are intended in satellite-to-ground downlinks scenarios, an efficient and stable single-mode fiber coupling is required. These wave-front amplitude and phase distortions induce strong fading in the coupled signal, resulting in unacceptable bit error rates.

This chapter presents the challenges of free-space laser communications focusing on satellite-to-ground links. It details the relevant turbulent effects affecting the laser beam wave-front, and it provides an overview of the state-of-the-art optical transmission and reception systems employed in FSOC. The chapter also discusses the benefits of beam wave-front compensation by quantifying the potential performance improvement through communications metrics like SMF coupling efficiency, SNR, and BER.

2.1 Atmospheric channel effects

The earth atmosphere is composed of a variety of gases, molecules, and particles trapped by its gravitational field. It extends up to 700 Km stratified in several layers. The heaviest concentration of particles occurs up to 20 Km, which covers the Troposphere (≈ 11 Km) and the Tropopause (≈ 20 Km). When an infrared laser beam travels through the atmosphere towards an optical ground station (OGS), it is affected by the linear phenomenon of absorption, scattering, and refractive-index fluctuations due to atmospheric turbulence. Figure 2.2 represents a propagating laser beam from the source to the optical detector, affected by the atmosphere.

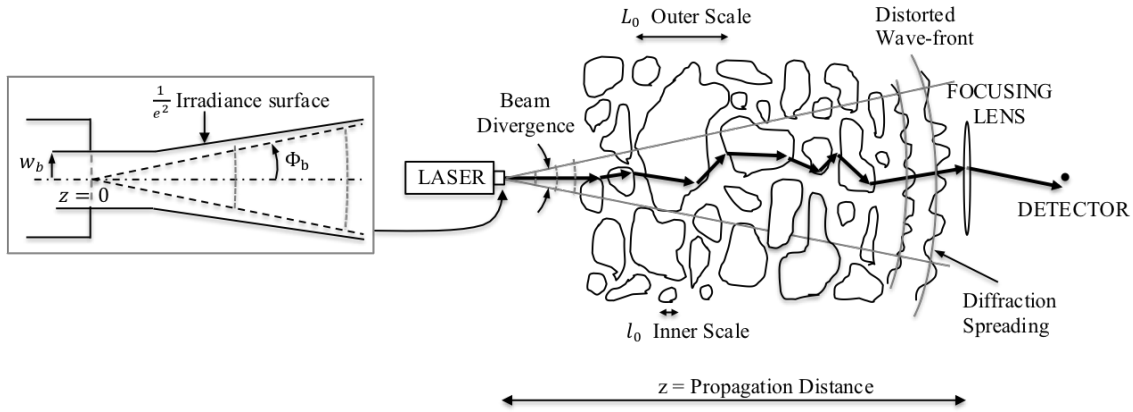


Fig. 2.1: Representation of a free-space laser beam affected by the atmosphere. Design based on [1].

In a laser communication scenario, absorption and scattering as well as beam divergence attenuate the received laser beam power, but the stronger deterioration of the performance of the communication is produced by the atmospheric turbulence, inducing phase wave-front distortions and intensity scintillation that evolve into signal fading.

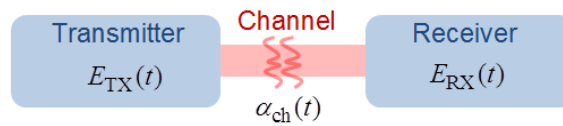


Fig. 2.2: Representation of the transmitter, channel, and receiver in an FSOC system.

Figure 2.2 depicts a transmitted modulated signal $E_{TX}(t)$, being affected in amplitude and phase $\alpha_{ch}(t)$ by the channel, leading to a received signal

$$E_{RX}(t) = E_{TX}(t)\alpha_{ch}(t) \quad (2.1)$$

$$\alpha_{ch}(t) = \alpha_{atm}(t)\exp(j\phi_{pt}(t)) \quad (2.2)$$

where the term $\phi_{pt}(t)$ represents a slowly varying phase offset of the signal induced by the so-called phase wave-front piston. The combined effects of constant power attenuation due to absorption, scattering, and beam divergence, together with the temporal amplitude fluctuations originated by scintillation effects and phase wave-front distortions, are represented in $\alpha_{atm}(t)$. The following sections further detail these concepts.

2.1.1 Absorption and scattering

Absorption occurs when the energy of the photon is transferred to a gaseous molecule inducing kinetic energy. Scattering is produced by certain air molecules and particles that are smaller (*Rayleigh scattering*) or of similar size (*Mie scattering*) to the laser wavelength. The later affects the forward propagation direction of the beam, and both phenomena are strongly dependent on the wavelength [20]. The overall effect produces the attenuation of the beam and induces its divergence increasing the phase-front radius of curvature.

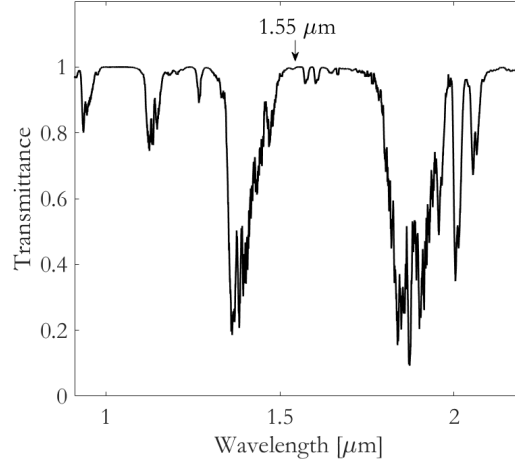


Fig. 2.3: Transmittance for the wavelength range of interest

Both phenomena are generally grouped as *transmittance* representing the atmospheric transmission over a distance z . The transmittance τ is described by Beer's law as

$$\tau = \exp[-\alpha_e(\lambda)z], \quad (2.3)$$

where $\alpha_e(\lambda)$ is the extinction coefficient composed of the absorption and scattering coefficients. Figure 2.3 shows the transmittance curve for the wavelength range 0.9-2.6 μm . The infrared spectra of the atmospheric transmission was acquired with the Gemini observatory above the two identical 8 m telescopes at Mauna Kea (Hawaii) and Cerro Pachon (Chile), thus providing full coverage over the two hemispheres [50]. The transmittance is high for the $\lambda = 1.55 \mu\text{m}$ and $\lambda = 1.064 \mu\text{m}$ wavelengths of interest.

The power loss at the position of the receiver is related, among other factors, to the beam divergence. The divergence of the beam increases with the propagation distance resulting in an illuminated area larger than the telescope aperture. The power loss can be quantified through the geometrical attenuation as

$$\alpha_{\text{div}} = 10 \log_{10} \left(\frac{\pi \Phi_b^2 z^2}{4 A_{\text{rx}}} \right) \text{ [dB]} \quad (2.4)$$

where $\Phi_b \approx \lambda/(\pi w_b)$ is the beam divergence angle, the term w_b is the beam waist radius, and A_{rx} is the receiver aperture size [51]. Note that this attenuation can be reasonably assumed as constant for a given link distance.

2.1.2 Refractive index structure parameter

Random microscopic temperature fluctuations at different altitudes modify the refractive index of the media, introducing changes in the wave-front characteristics. Temperature fluctuations are originated by air motion due to winds and convection [20], where layers of air with different temperature and density are mixed, creating continuous screens of spatially and temporally varying refractive index. Kolmogorov's theory described these effects in terms of large L_0 and small l_0 scale turbulent cells (eddies), see Fig. 2.2, from where energy is cascaded and finally dissipated [18]. These cells act as a series of lenses that deflect regions of the beam alongside the transmission path. When a wave-front propagates through these turbulent layers, it experiences localized delays distorting its phase. The degree of the wave-front deterioration is related to the cumulative effect of the different refractive indices along the optical trajectory and thus longer paths represent the worst scenario. Tatarskii employed Kolmogorov's model to completely define the wave propagation through a turbulent medium [52].

The refractive index structure function $D_n(\boldsymbol{\rho}_1, \boldsymbol{\rho}_2)$ characterizes the fluctuation of the refractive index $n(\boldsymbol{\rho})$ at different vector locations $\boldsymbol{\rho}$ [53]

$$D_n(\boldsymbol{\rho}_1, \boldsymbol{\rho}_2) = \langle |n(\boldsymbol{\rho}_1) - n(\boldsymbol{\rho}_2)|^2 \rangle, \quad (2.5)$$

where $\langle \rangle$ represents the statistical average. Kolmogorov suggested that within the inertial sub-range $l_0 < \rho < L_0$ point separated a certain scale size exhibit statistical homogeneity and isotropy. Therefore, the refractive index structure function depends only on the separation between points $\rho = \rho_2 - \rho_1$, and $D_n(\boldsymbol{\rho}_1, \boldsymbol{\rho}_2) = D_n(\rho)$. Within the range defined by the large L_0 and small l_0 scale turbulent cells, the $D_n(\rho)$ is described by Kolmogorov's two-thirds power law

$$D_n(\rho) = C_n^2(h)\rho^{2/3}, \quad l_0 < \rho < L_0 \quad (2.6)$$

where $C_n^2(h)$ is known as the refractive index structure parameter and indicates the strength of the turbulence at a height h . Kolmogorov predicted turbulent power law distribution as

$$\Phi_n(\kappa) = 0.033C_n^2\kappa^{-11/3}, \quad \kappa_0 < \kappa < \kappa_l \quad (2.7)$$

with spatial frequency $\kappa^{11/3}$, being $\kappa = 2\pi/l$ and l the size of the turbulent eddy. Here, $\kappa_0 = 2\pi/L_0$ and $\kappa_l = 2\pi/l_0$ are the boundaries of the spatial spectrum. Roddier defined the phase power spectrum $\Phi_n(\kappa)$ as [54]

$$\Phi_n(\kappa) = 9.7 \times 10^{-3} k^2 C_n^2(h) dh \kappa^{-11/3} \quad (2.8)$$

with $k = 2\pi/\lambda$ being the wave number, and dh the turbulent layer width. The $\Phi_n(\kappa)$ can be related to the statistical long term coherence width r_0 of the distorted wave-front, which is of great practical utility when it comes to evaluating the impact of the atmosphere in a propagating laser beam. Details are presented in Sec. 2.1.3.1.

A measure of the amount of local refractive index inhomogeneities is represented with the index of refraction structure parameter $C_n^2(h)$, which quantifies the turbulence strength over the height h . This parameter is measured alongside the optical path based upon the location of the optical ground station (OGS), resulting in several models adapted to the particular conditions of the place. The most popular model is the Hufnagel-Valley

(HV) model

$$C_n^2(h) = 0.00594(v_0/27)^2(10^{-5}h)^{10}\exp(-h/1000) + 2.7 \times 10^{-16}\exp(-h/1500) + A\exp(-h/100), \quad (2.9)$$

where h is in meters, v_0 is the rms wind speed in meters per second, and A is the nominal value of $C_n^2(0)$ at the ground in $\text{m}^{-2/3}$. The v_0 is calculated as

$$v_0 = \left[\frac{1}{15 \times 10^3} \int_{5 \times 10^3}^{20 \times 10^3} V^2(h)dh \right]^{1/2}, \quad (2.10)$$

where $V^2(h)$ is described by the modified Bufton wind model, which includes the term for the satellite slew rate

$$V(h) = v_{\text{sr}}h + v_{\text{g}} + 30\exp\left[-\left(\frac{h-9400}{4800}\right)^2\right]. \quad (2.11)$$

Here, v_{g} is the wind speed at ground level, and v_{sr} represents the slew rate due to satellite displacement respect to the ground station,

$$v_{\text{sr}} = \frac{V_{\text{sat}}}{L} \frac{L^2 + H_{\text{sat}}^2 + 2R_{\text{e}}H_{\text{sat}}}{2L(H_{\text{sat}} + R_{\text{e}})} \quad (2.12)$$

$$L = \left[(H_{\text{sat}} + R_{\text{e}})^2 - R_{\text{e}}^2 \cos^2(\alpha) \right]^{1/2} - R_{\text{e}} \sin(\alpha) \quad (2.13)$$

The calculation of v_{sr} requires the satellite velocity V_{sat} , satellite altitude above the ground station H_{sat} , and the earth radius $R_{\text{e}} = 6378$ Km. Based on the link elevation α [rad], the satellite distance L is approximated. Figure 2.4 shows the turbulence strength profile $\text{HV}_{5/7}$ for a satellite-to-ground link. The simulation assumes daylight conditions $A = 1.7 \times 10^{-14}$, and rms wind $v_0 = 21$ m/s.

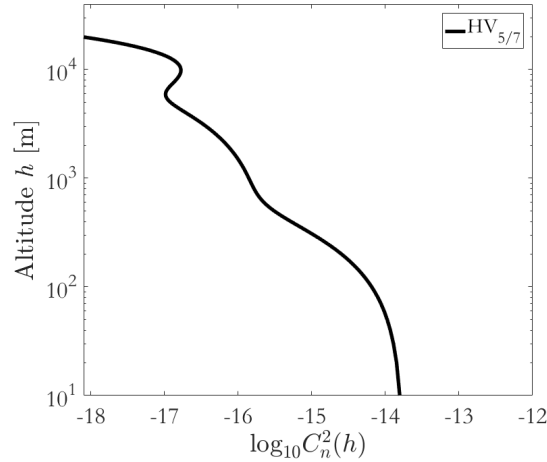


Fig. 2.4: Turbulence strength profile $\text{HV}_{5/7}$.

The behavior of the $C_n^2(h)$ varies during the day. The strongest optical turbulence happens near the ground with values of 10^{-13} (nighttime) or 10^{-14} (daytime) $\text{m}^{-2/3}$. The general behavior of $C_n^2(h)$ involves a decrease with h above uniform ground at a rate $h^{-4/3}$, and $h^{-1/3}$ above complex terrain (mountains). At night the $C_n^2(h)$ decreases at a rate $h^{-2/3}$. Sunrise and Sunset experience absence of temperature gradient thus minimum values of $C_n^2(h)$.

2.1.3 Propagation effects

Turbulence-induced refractive index fluctuations are the primary phenomena affecting laser communications by induced signal attenuation and fluctuation. The $C_n^2(h)$ parameter is crucial to characterize the effects of the atmospheric turbulence in a propagating beam. The atmospheric coherence width r_0 indicates the degree of coherence of an aberrated phase wave-front. The coherence time τ_0 quantifies how rapid the wave-front decorrelates, which is required to design a compensation system. The beam scintillation index σ_I^2 indicates the degree of irradiance fluctuation at the receiver plane. The phase piston ϕ_{pt} occur spatially in the wave-front at a slower rate, and it induces signal phase shifts that may affect coherent communications. These concepts were introduced in Sec. 1.2 and the following sections offer further details.

2.1.3.1 Atmospheric coherence width - Fried parameter

The atmospheric coherence width, commonly known as Fried parameter r_0 , it is a widely adopted metric to evaluate the degree of distortion of the wave-front. It measures the coherence of the beam transversely and it has units of length usually expressed in centimeters. In practice, it defines the diameter of a circular area over which the rms wave-front aberration is equal to 1 radian.

Considering an optical field $P(\boldsymbol{\rho}, L)$ after propagating a distance L to the receiver plane, with $\boldsymbol{\rho}$ being a vector position in the traverse plane, the mutual coherence function (MCF) of the field can be defined as

$$\Gamma_2(\boldsymbol{\rho}_1, \boldsymbol{\rho}_2, L) = \langle P(\boldsymbol{\rho}_1, L)P^*(\boldsymbol{\rho}_2, L) \rangle, \quad (2.14)$$

where $\boldsymbol{\rho}_1$ and $\boldsymbol{\rho}_2$ are points in the receiver transverse plane, and $*$ denotes complex conjugate. For identical point $\boldsymbol{\rho}_1 = \boldsymbol{\rho}_2$, the MCF determines the mean irradiance of the received field. The loss of spatial coherence of the field can also be estimated from the MCF. The modulus of the complex degree of coherence (DOC) can be calculated as

$$\text{DOC}(\boldsymbol{\rho}_1, \boldsymbol{\rho}_2, L) = C(\boldsymbol{\rho}_1, \boldsymbol{\rho}_2, L) = \frac{|\Gamma_2(\boldsymbol{\rho}_1, \boldsymbol{\rho}_2, L)|}{\sqrt{\Gamma_2(\boldsymbol{\rho}_1, \boldsymbol{\rho}_1, L)\Gamma_2(\boldsymbol{\rho}_2, \boldsymbol{\rho}_2, L)}} \quad (2.15)$$

$$C(\boldsymbol{\rho}_1, \boldsymbol{\rho}_2, L) = \exp\left[-\frac{1}{2}D(\boldsymbol{\rho}_1, \boldsymbol{\rho}_2, L)\right], \quad (2.16)$$

where $D(\boldsymbol{\rho}_1, \boldsymbol{\rho}_2, L)$ is the wave structure function that, in a similar manner to the refractive index structure function of Eq. (2.5), it quantifies the variance of the wave amplitude and phase at different points, represented independently as

$$D(\boldsymbol{\rho}_1, \boldsymbol{\rho}_2, L) = D_X(\boldsymbol{\rho}_1, \boldsymbol{\rho}_2, L) + D_S(\boldsymbol{\rho}_1, \boldsymbol{\rho}_2, L). \quad (2.17)$$

In Eq. (2.17) the first term $D_X(\boldsymbol{\rho}_1, \boldsymbol{\rho}_2, L)$ is the log-amplitude structure function due to scintillation, and $D_S(\boldsymbol{\rho}_1, \boldsymbol{\rho}_2, L)$ is the phase structure function, which becomes dominant. Due to Kolmogorov assumptions of isotropy and homogeneity, the structure function depends only on the separation between points $\boldsymbol{\rho} = \boldsymbol{\rho}_2 - \boldsymbol{\rho}_1$, and $D(\boldsymbol{\rho}_1, \boldsymbol{\rho}_2, L) = D(\boldsymbol{\rho}, L)$. From Eq. (2.16), the spatial coherence radius ρ_0 is defined by the $1/e$ point of the DOC or $D(\rho_0, L) = 2$ [20].

Considering that an optical wave propagating from a satellite at an altitude $H \gg 20 \text{ Km}$, enters the atmospheric layer (at $\approx 20 \text{ Km}$) closely resembling a plane wave, the plane wave model is often assumed for

laser downlinks. With this, the wave structure function can be expressed as [20]

$$D(\rho, L) = 2.91k^2\rho^{5/3}\sec(\zeta) \int_{h_0}^H C_n^2(h)dh \quad (2.18)$$

where ρ is the separation between observation point, $\zeta = \pi/2 - \alpha$ [rad] is the zenith angle, the satellite altitude $H = L(\alpha)\cos(\zeta)$, and the wavelength of the light source λ is implicit in the wave number $k = 2\pi/\lambda$. To have a $D(\rho_0, L) = 2$, the coherence radius can be derived from Eq. (2.18) as

$$\rho_0 = \left(\frac{\cos(\zeta)}{1.45k^2 \int_{h_0}^H C_n^2(h)dh} \right)^{3/5}. \quad (2.19)$$

The atmospheric coherence width r_0 is equal to $r_0 = 2.1\rho_0$ and results from the integration over the $C_n^2(h)$ profile for a particular distance between the ground station altitude h_0 and the satellite altitude H ,

$$r_0 = \left[0.423k^2\sec(\zeta) \int_{h_0}^H C_n^2(h)dh \right]^{-3/5} \quad (2.20)$$

In Eq. (2.20), the r_0 increases proportionally to $\lambda^{6/5}$ of the laser beam and decreases with the zenith angle. From the initial definition of the phase power spectrum, Eq. (2.8) can be written in as

$$\Phi_n(\kappa) = 0.023r_0^{-5/3}\kappa^{-11/3} \quad (2.21)$$

recalling $\kappa^{11/3}$ as a spatial frequency with $\kappa = 2\pi/l$ and l the size of the turbulent eddy. Since phase distortions are dominant over log-amplitude fluctuations, $D_S(\rho)$ in Eq. (2.17) can be expressed as [55]

$$D_S(\rho) = 2 \int_0^\infty \Phi_n(\kappa) (1 - \cos(2\pi\kappa\rho)) d\kappa \quad (2.22)$$

Fried simplified this expression for small ρ as [19]

$$D_S(\rho \ll L_0) = 6.88 \left(\frac{\rho}{r_0} \right)^{5/3}, \quad (2.23)$$

which converges for larger ρ to twice the wave-front phase variance σ_S^2

$$D_S(\rho \gg L_0) = 2\sigma_S^2. \quad (2.24)$$

In laser communications, a widely used metric relates the telescope aperture diameter D with the r_0 in the so-called normalized aperture D/r_0 , which indicates the number of uncorrelated zones within the aperture size in the pupil plane. At the focal plane of the optical system, this metric can be used to approximate the number of dispersed focal intensity speckles $M \approx (D/r_0)^2$ of the focused beam, due to atmospheric phase distortion. The higher the D/r_0 , the more disperse the focal energy and thus it is more difficult to couple the light into a fiber. A value for the r_0 and D/r_0 for a LEO downlink at different satellite elevations is shown in Fig. 2.5. Considering a standard OGS telescope aperture $D = 40$ cm for LEO optical ground stations, the expected values of normalized aperture for satellite elevations from 10° to 90° range between $D/r_0 = 6$ and $D/r_0 = 2$, respectively. For GEO satellites, the telescope apertures are typically $D \geq 1$ m, the link elevations are above 30° , and turbulence is weak, hence large r_0 are expected.

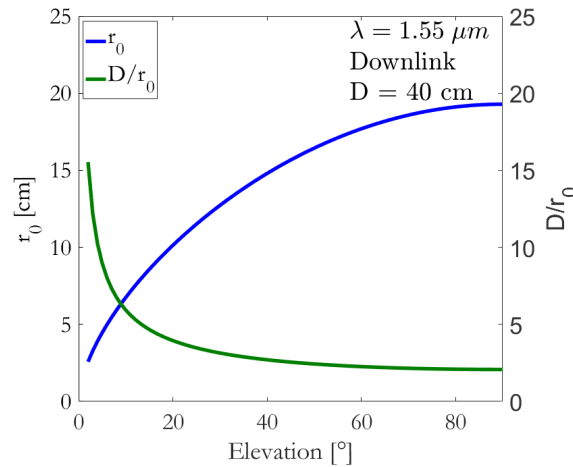


Fig. 2.5: Fried parameter and normalized aperture for different LEO-downlink elevations, considering a laser wavelength $\lambda = 1.55 \mu\text{m}$, $D = 40 \text{ cm}$, and the $HV_{5/7} C_n^2$ profiles of Fig. 2.4.

2.1.3.2 Greenwood time constant - Coherence time

The coherence time of the field τ_0 is an important design parameter of a wave-front compensation system. This parameter represents the time scale over which the phase wave-front can be considered to remain correlated, with tolerable changes. Thus, the parameter τ_0 defines the available time for the system to compensate for the distorted beam. The field can be considered partially coherent within τ_0 and uncorrelated for a time $t > \tau_0$. Taylor’s frozen turbulence hypothesis considers a static field within this time frame, and this assumption is used in wave-front compensation systems to define the required correction bandwidth. The reciprocal of τ_0 is the Greenwood frequency or bandwidth required for the compensation system. Likewise the r_0 , the coherence time

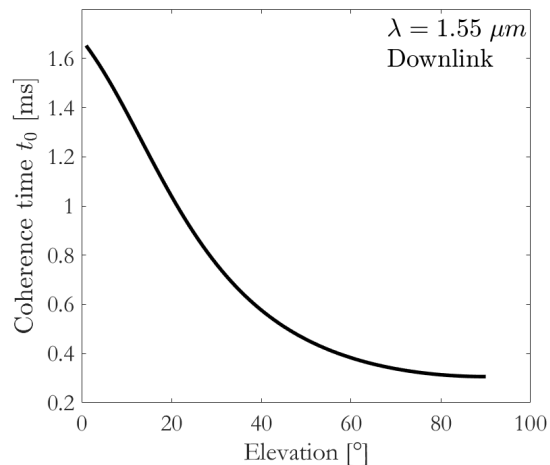


Fig. 2.6: Coherence time for a range of LEO-downlink elevations, considering a laser wavelength $\lambda = 1.55 \mu\text{m}$ and the change in the rms wind due to beam slew rate.

is calculated with the turbulence profile as,

$$\tau_0 = \left[2.91k^2 \int_0^L C_n^2(h)V^{5/3}(h)dh \right]^{-3/5}, \quad (2.25)$$

where k is the wave number, L is calculated with Eq. (2.13), and $V(h)$ is the transverse wind speed as a function of the propagation distance to the satellite. Alternatively, the τ_0 can be approximated with the r_0 and the rms wind speed v_0 as [56]

$$\tau_0 = \frac{0.314r_0}{v_0}. \quad (2.26)$$

As shown in Fig. 2.6, the expected time scale of τ_0 for laser downlinks in a moving satellite, ranges between 1.5 and 0.5 milliseconds for an increasing link elevation [28]. Note that the τ_0 reduces towards the zenith due to the increment in the slew rate of the beam.

2.1.3.3 Scintillation

Irradiance fluctuations (scintillation) in the receiver photodetector affects a communication link since the receiver needs to cope with a large dynamic range of the received power. The scintillation index defines the normalized irradiance variance of the optical wave,

$$\sigma_I^2 = \frac{\langle I^2 \rangle - \langle I \rangle^2}{\langle I \rangle^2} = \frac{\langle I^2 \rangle}{\langle I \rangle^2 - 1} \quad (2.27)$$

where I [W/m^2] is the irradiance of the optical wave or the intensity at the entrance pupil of the measurement system [57], and $\langle \rangle$ indicates the ensemble average. Note that the ensemble average is also the long-time average for ergodic processes. The scintillation index for a plane wave under weak turbulence is equal to the Rytov variance σ_R^2 , which defines the turbulence regime as weak ($\sigma_R^2 \ll 1$) and strong ($\sigma_R^2 > 1$)

$$\sigma_I^2 = \sigma_R^2 = 2.25k^{7/6}\text{sec}^{11/6}(\zeta) \int_{h_0}^H C_n^2(h)(h - h_0)^{5/6}dh. \quad (2.28)$$

In Eq. (2.28), k is the wave number, and ζ is the zenith angle. The weak fluctuation theory is applicable for elevations above 30 degrees where turbulence moves towards the weak regime. The σ_R^2 can also be written as [58]

$$\sigma_R^2 \approx 1.23C_n^2k^{(7/6)}L^{(11/6)} \quad (2.29)$$

where L is the path length between the transmitter and receiver, given by Eq. (2.13). Scintillation develops faster at lower elevations (below 30°) due to the long path and more accumulated turbulence effects. Here, the Rytov approximation overestimates the scintillation index and the model must be extended. The scintillation index σ_I^2 for all turbulence regimes, considering plane wave propagation and Kolmogorov turbulence ($l_0 = 0$ and $L_0 = \infty$), is calculated as

$$\sigma_I^2 = \exp \left[\frac{0.49\sigma_R^2}{\left(1 + 1.11\sigma_R^{12/5}\right)^{7/6}} + \frac{0.51\sigma_R^2}{\left(1 + 0.69\sigma_R^{12/5}\right)^{5/6}} \right] - 1 \quad (2.30)$$

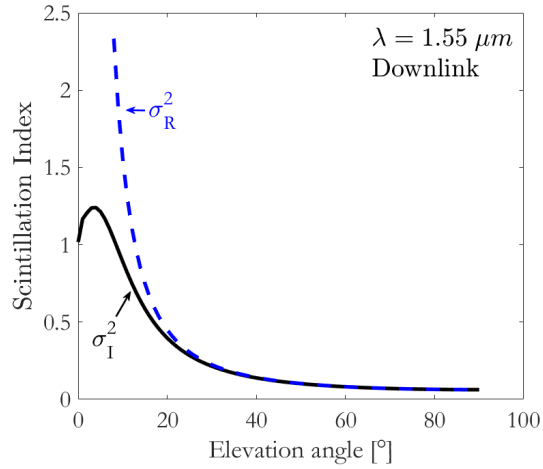


Fig. 2.7: Scintillation index for different LEO-downlink elevations, considering a laser wavelength $\lambda = 1.55 \mu\text{m}$, and rms wind $v_0 = 21$ [m/s]. A comparison with the Rytov variance shows the overestimation below 30° elevations.

Figure 2.7 depicts the scintillation index for a laser downlink of $\lambda = 1.55 \mu\text{m}$, at different satellite elevations, considering the C_n^2 profile with a $v_0 = 21$ [m/s]. Scintillation is particularly important in uplinks, since a satellite receivers use smaller apertures. Larger OGS apertures produce an averaging effect that attenuates the effects of the scintillation in laser downlinks. The reduction in the scintillation with the increment in the aperture size can be calculated as [20]

$$\begin{aligned} \sigma_I^2(D) &= 8.70k^{7/6}(H - h_0)^{5/6}\text{sec}^{11/6}(\zeta) \\ &\times \text{Re} \int_{h_0}^H C_n^2(h) \left[\left(\frac{kD^2}{16L} + i \frac{h - h_0}{H - h_0} \right)^{5/6} - \left(\frac{kD^2}{16L} \right)^{5/6} \right] dh, \end{aligned} \quad (2.31)$$

where the ground station height $h_0 = 0$, L is calculated with Eq. (2.13), and $H = L\cos(\zeta)$. A simpler expression [58], extended from Eq. (2.30) and valid for plane wave propagation in horizontal and slant path, is written as follows

$$\sigma_I^2(D) = \exp \left[\frac{0.49\sigma_R^2}{\left(1 + 0.65d^2 + 1.11\sigma_R^{12/5}\right)^{7/6}} + \frac{0.51\sigma_R^2 \left(1 + 0.69\sigma_R^{12/5}\right)^{-5/6}}{1 + 0.90d^2 + 0.62d^2\sigma_R^{12/5}} \right] - 1 \quad (2.32)$$

where d is related to the aperture diameter as

$$d = \sqrt{kD^2/4L} \quad (2.33)$$

Figure 2.8 shows the reduction in the scintillation with the increment in D for weak, moderate, and strong turbulence, associated to link elevations of 70° , 30° , and 10° , respectively. The curves are calculated with Eq. (2.31) and the C_n^2 considers a rms wind $v_0 = 21$ [m/s].

2.1.3.4 Irradiance probability density function

An important parameter for the design of a free-space communication system is not only the variance of the irradiance σ_I^2 but also its distribution. Scintillation produces signal losses that may lead to fading and ultimate

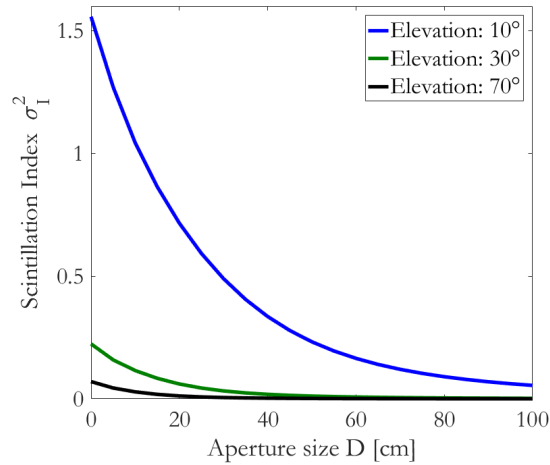


Fig. 2.8: Scintillation index variation with the aperture size D , and for LEO-downlink elevations spanning weak to strong turbulence. The simulation considers a laser wavelength $\lambda = 1.55 \mu\text{m}$, and rms wind $v_0 = 21 \text{ [m/s]}$.

interrupt the communication. The shape of the irradiance probability density function (PDF) indicates, to some extent, the reliability of the communication system which is directly associated with the tail of the distribution. For communication systems, underestimating this region has a negative impact on the performance as more errors occur in the detection process [58].

Depending on the turbulence regime, the log-normal or the gamma-gamma distribution represents the irradiance fluctuations. Log-normal distribution is used for weak turbulent regimes and it is defined as

$$p_I(I) = \frac{1}{I\sigma_I^2(D)\sqrt{2\pi}} \exp\left[-\frac{\left(\ln\left(\frac{I}{\langle I \rangle}\right) + \frac{1}{2}\sigma_I^2(D)\right)^2}{2\sigma_I^2(D)}\right], \quad I > 0 \quad (2.34)$$

where $\sigma_I^2(D)$ is the above-described aperture averaged scintillation index, and $\langle I \rangle$ is the mean intensity. When the strength of turbulence increases, log-normal PDF underestimates the behavior of the tail as compared with experimental data. The gamma-gamma distribution is used under weak and strong turbulence conditions [59–61]. It assumes that small-scale irradiance fluctuations are modulated by large-scale irradiance fluctuations of the propagating wave, each one represented as an independent gamma distribution [58].

$$p_I(I) = \frac{2(\alpha_1\beta_1)^{(\alpha_1+\beta_1)/2}}{\Gamma(\alpha_1)\Gamma(\beta_1)} I^{(\alpha_1+\beta_1)/2-1} K_{\alpha_1-\beta_1}\left(2\sqrt{\alpha_1\beta_1}I\right), \quad I \geq 0 \quad (2.35)$$

In Eq. (2.35), $\Gamma(x)$ is the Gamma function and K_a denotes the modified Bessel function of the second kind and order "a". Note that the parameters α_1 and β_1 indicates the number of small/large scale eddies of the turbulent environment and are directly related to the atmospheric turbulence conditions as [59]

$$\alpha_1 = \left[\exp\left(\frac{0.49\sigma_R^2}{\left(1 + 0.65d^2 + 1.11\sigma_R^{12/5}\right)^{7/6}}\right) - 1 \right]^{-1} \quad (2.36)$$

$$\beta_1 = \left[\exp \left(\frac{0.51\sigma_R^2 \left(1 + 0.69\sigma_R^{12/5}\right)^{-5/6}}{1 + 0.90d^2 + 0.62d^2\sigma_R^{12/5}} \right) - 1 \right]^{-1} \quad (2.37)$$

where d stands for the averaging effect of the aperture, Eq. (2.33), and the Rytov variance σ_R^2 can be calculated with Eq. (2.28). The $p_I(I)$ is used to estimate the bit-error-ratio (BER) in a communication system affected by the turbulence, see Sec. 2.3.3.

2.1.3.5 Phase piston

Besides the high order transverse phase distortions in the beam wave-front, an additional phase fluctuation alongside the propagation path is present. These phase changes are constant in the transverse plane, and thus they do not alter the energy distribution of a focused beam. Instead, these phase changes are translated into the signal affecting its phase, requiring some degree of compensation when working with coherent communication systems.

The impact of the phase piston ϕ_{pt} in coherent data transmission during a Lasercom downlink was evaluated by [62]. Here, the one-dimensional temporal power spectrum $L_{pst}(f)$ for a single turbulent layer is derived considering Taylor frozen turbulence hypothesis, resulting in

$$L_{pst}(f) \approx \frac{0.055(2\pi)^{-2/3} \left(\frac{2\pi}{\lambda}\right)^2 C_n^2 \Delta h V^{5/3} f^{-8/3}}{1 + 37.5D^3 \left(\frac{f}{V}\right)^3} \quad (2.38)$$

where Δh represents the thickness of the turbulent layer, f is the piston frequency, V is the wind velocity, and D is the aperture diameter. **In agreement with [63], the authors in [62] concluded that, in an scenario of FSO downlink working with coherent reception, the induced phase due to atmospheric piston is negligible since laser phase noise dominates.** However, coherent receivers perform digital signal processing to compensate the slow (≈ 4 Hz) and constant phase noise induced by atmospheric piston effects.

2.1.4 Emulation of the beam wave-front in a turbulent channel

To emulate the effects of the turbulent channel in the beam wave-front, the thin screen turbulent model is widely used. Regarding the dynamic range of the irradiance fluctuations of a focused beam in a Laser downlink scenario, the phase wave-front variance is considered to be the dominant factor over wave-front scintillation [58]. The reason is that laser downlinks require larger telescope apertures that produce an averaging of the intensity scintillation, but exposes the optical system to a larger amount of field phase decoherence. Consequently, the emulation of the turbulent channel effects can be done assuming a complex field with unitary amplitude $A(\mathbf{r}) = 1$ and an aberrated phase $\varphi(\mathbf{r})$ as

$$P(\mathbf{r}) = A(\mathbf{r})\exp(j\varphi(\mathbf{r})), \quad (2.39)$$

where \mathbf{r} indicates a spatial coordinate. In this model, the aberrated phase can be created with the single-screen phase method [54] which is well-suited for horizontal beam propagation. It is also widely used in slant-path scenarios to approximate the effects of the turbulence in the wave-front. It is generally adopted because it

gives more control over the type and magnitude of the aberrations involved, as it is purely based on the Zernike polynomials orthogonal basis [64]. Also, it is simple to implement and allows fast generation of a large number of uncorrelated fields. The general idea for the generation of single-phase screens is that a phase wave-front $\varphi(\mathbf{r})$ in the pupil plane can be modeled as a sum of n_z Zernike polynomials $\mathbf{Z}_l(\mathbf{r})$, each one weighted with a Zernike coefficient c_l , and pondered for the scenario D/r_0 under test as

$$\varphi(\mathbf{r}) = \left(\frac{D}{r_0}\right)^{5/6} \sum_{l=0}^{n_z} (c_l \mathbf{Z}_l(\mathbf{r})). \quad (2.40)$$

In Eq. 4.35 the weights are represented by a set of Karhunen-Loève coefficients, generated using the diagonalized covariance matrix of the Zernike polynomials. Details are given in Sec. 4.3.1 for the numerical analyses.

2.2 Lasercom system in free-space

The transmission and reception of digital information over a free-space optical channel, requires the encoding of the data in a suitable carrier (modulation), transfer of the signal through the channel, and finally reception, demodulation, and decoding of the data. The modulation formats can be broadly classified in binary and multilevel (M-ary) schemes. Binary modulation refers to the encoding of the intended transmit signal, i.e. zeros and ones, only in two level states of the wave carrier. The resultant modulation schemes can be differentiated based on the modified carrier property, namely the amplitude (amplitude-shift keying ASK), frequency (frequency-shift keying FSK), phase (phase-shift keying PSK), and polarization (polarization-mode-shift keying PMSK). In addition, M-ary schemes use more than two carrier states to encode several bits into the so-called symbols, e.g. two bits can be encoded in four phase states of the wave carrier (Quadrature phase-shift keying QPSK). In FSOC, the transmitter and receiver systems use the same well-known methods adopted in fibered communications, but atmospheric channel effects induce unwanted fluctuations in the received signal. As explained in Sec. 1.3, the preferred scheme in FSOC is IMDD-OOK, but BPSK and QPSK can deliver substantial benefit in terms of spectral efficiency, provided the sufficient mitigation of the atmospheric channel effects. The following sections explain only the mentioned schemes. Figure 2.9 shows the main building block of a laser communication system in free-space.

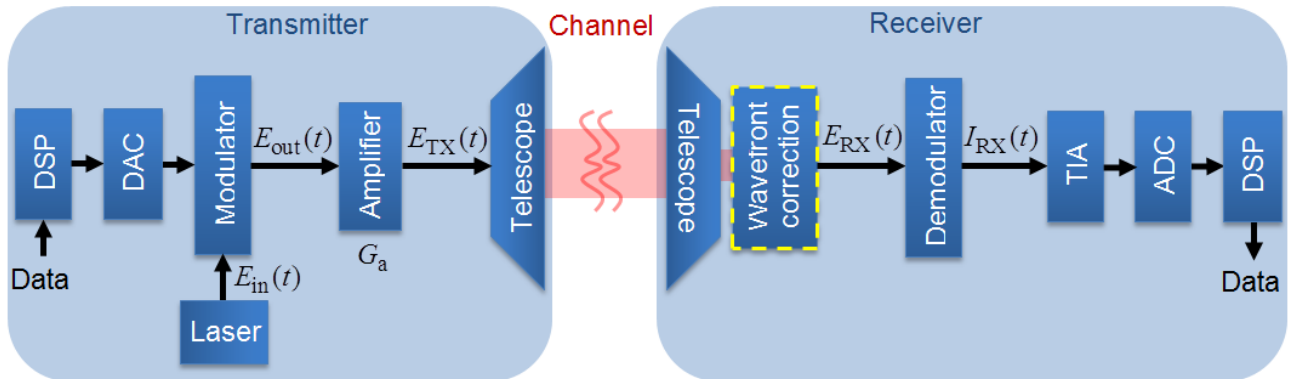


Fig. 2.9: Block diagram of a free-space optical system and main subsystems, including the transmitter, channel, and receiver, as well as main subsystems.

The data is mapped and prepared for the constellation of the intended modulation format using a Digital Signal Processing (DSP) stage. To drive the modulator, the digital signal is converted into the analog domain using a digital-to-analog converter (DAC). The modulator is fed with a laser carrier $E_{\text{in}}(t)$, on which it encodes the digital information by altering the carrier amplitude, phase, frequency, polarization, or a combination of them. Then, the modulated carrier signal $E_{\text{out}}(t)$ is amplified $E_{\text{TX}}(t)$ and transmitted through the free-space using a telescope-based optical system. While the beam propagates over the free-space channel, it results affected in amplitude and phase by the atmospheric phenomena introduced in Sec. 2.1. The receiver system captures the incoming beam with another telescope-based optical system; if necessary, it adapts and corrects beam distortions using a wave-front correction stage, and delivers the received signal $E_{\text{RX}}(t)$ to the demodulator. The demodulator retrieves the encoded signal $I_{\text{RX}}(t)$ which is then amplified with a transimpedance amplifier (TIA) and converted into the digital domain using a analog-to-digital (ADC). Finally, and depending on the modulation format, a DSP processes the signal to recover the synchronization, compensate for additional signal imbalances, and correct induced phase and amplitude variations to retrieve the data.

The most adopted binary modulation scheme in FSOC is the intensity modulation and direct detection (IMDD). The standard technique is known as on-off Keying (OOK), where the carrier is modulated on and off based on the transmitted 1's and 0's, respectively. The received optical signal is then converted into the electrical domain with a front-end photodetector and, after sampling, the bits are recovered using a threshold-based decision circuit. Recently, coherent systems have been deployed and are being considered to achieve higher data transmission rates. For example, binary PSK (BPSK) and quadrature PSK (QPSK) are coherent modulation techniques that require the superposition of the received signal with the one of a local oscillator (LO) for demodulation. These systems have more spectral efficiency and sensitivity than IMDD, at the expense of higher complexity.

Before describing the modulation and demodulation processes of the carrier, let's present the signals involved in the whole transmission chain. The signal carried fed into the modulator, shown in Fig. 2.9, can be defined as

$$E_{\text{in}}(t) = \sqrt{P_s} \exp(j [w_s t + \phi_{\text{ls}}(t)]) \quad (2.41)$$

with signal input power P_s and frequency $w_s = 2\pi\nu_s$. A laser does not have a pure spectrum at the desired frequency but instead there exist phase noise that widens it. This effect is characterized by the laser linewidth $\Delta\nu$ (at full width half maximum) and can be modeled as a laser phase variation $\phi_{\text{ls}}(t)$ represented by Gaussian random process of zero mean and variance defined by $\sigma_{\text{ls}}^2 = 2\pi\Delta\nu(t)$. In this work, it is only considered a carrier modulated in amplitude $a(t)$ and/or in phase $\phi_s(t)$, thus the output signal from the modulator $E_{\text{out}}(t)$ can be written as

$$E_{\text{out}}(t) = a(t)\sqrt{P_s} \exp(j [w_s t + \phi_s(t) + \phi_{\text{ls}}(t)]) \quad (2.42)$$

Amplification is required to deal with the expected signal losses, particularly the ones associated with the atmospheric channel. A widely used amplifier is the Erbium-Doped Fiber Amplifier (EDFA), which amplifies the C-band ($\lambda = 1530 \text{ nm} - 1565 \text{ nm}$) and it is well suited for the transmission wavelength $\lambda = 1550 \text{ nm}$ used in fibered optical communications. The amplification process provides a signal gain G_a but also introduces noise n_{ase} due to the spontaneous emission process of the laser. Assuming $G_a = 1$ for mathematical simplicity, the

output signal from the transmitter toward the free-space channel can be written as

$$E_{\text{TX}}(t) = a(t)\sqrt{P_s}\exp(j[w_s t + \phi_s(t) + \phi_{\text{ls}}(t)]) + n_{\text{ase}} \quad (2.43)$$

As initially introduced in Eq. 2.1, the received signal $E_{\text{RX}}(t)$ must consider the effects of the atmosphere in the beam propagation

$$E_{\text{RX}}(t) = E_{\text{TX}}(t)\alpha_{\text{atm}}(t)\exp(j\phi_{\text{pt}}(t)) \quad (2.44)$$

where $\alpha_{\text{atm}}(t)$ represents the signal attenuation and temporal fluctuations induced by the beam divergence, atmosphere scintillation, and higher order phase distortion; where $\exp(j\phi_{\text{pt}}(t))$ considers the atmospheric piston effects in the signal phase. The induced signal fading due to scintillation can be mitigated using aperture averaging. The wave-front phase piston becomes relevant in coherent transmission, as it induces a slow change of the signal phase easily corrected with digital signal processing. **The signal deterioration due to wave-front phase aberrations represents the main limitation in laser downlinks, particularly in scenarios of strong turbulence, and require the use of a wave-front compensation system. This work focuses on this particular challenge.**

The demodulation process introduces additional noise originated mainly in the photodetectors and amplification stages. These additive noise sources are mainly thermal noise n_{T} (dominant in direct detection) and shot noise n_{ns} (dominant in coherent detection), which will combine with n_{ase} as

$$n_{\text{AG}} = n_{\text{ase}} + n_{\text{T}} + n_{\text{ns}} \quad (2.45)$$

In addition, when considered a coherent system, a local oscillator signal is combined with the received signal. This adds a complex term $I_{\text{lo}}(t) = \sqrt{P_{\text{lo}}}\exp(-j(w_{\text{lo}}t + \phi_{\text{lo}}))$ where P_{lo} , w_{lo} , and ϕ_{lo} are the power, angular frequency, and phase of the LO signal. The resultant signal current previous the ADC process is

$$I_{\text{RX}}(t) \propto \alpha_{\text{atm}}(t)a(t)\sqrt{P_s P_{\text{lo}}}\exp(j[w_{\text{b}}t + \Delta\phi(t) + \phi_{\text{ls}}(t) + \phi_{\text{pt}}(t)]) + n_{\text{AG}}, \quad (2.46)$$

where $w_{\text{b}} = (w_{\text{s}} - w_{\text{lo}})$ represents the beat frequency in a synchronous receiver, and $\Delta\phi = (\phi_{\text{s}} - \phi_{\text{lo}})$ the correspondent phase shift between both signals. Then, as mentioned above, the overall signal needs to be amplified with the TIA, sampled with an ADC, and sent to the DSP for data recovery. The following subsections detail the generation of these signals in the transmission/reception process. Amplification and sampling stages are omitted.

2.2.1 Modulator

The modulation process implies the controlled change of some signal carrier properties in order to represent bits of information. As mentioned before, the most common method is to represent ones and zeros with changes in the carrier amplitude. Also, the same bits can be represented with π changes in the carrier phase (BPSK), or even encoding pairs of bits within additional phase changes of the carried; e.g. with for phase levels (QPSK). To achieve such modulations, an electro-optic phase modulator is used and combined.

When a nonlinear crystal material of length L is exposed to an electric field F , an electro-optic effect occurs that modifies the material refractive index n . As shown in Fig. 2.10, this electric field can be generated by applying a voltage U to a pair of electrodes located at the sides of the crystal and separated a distance d [65].

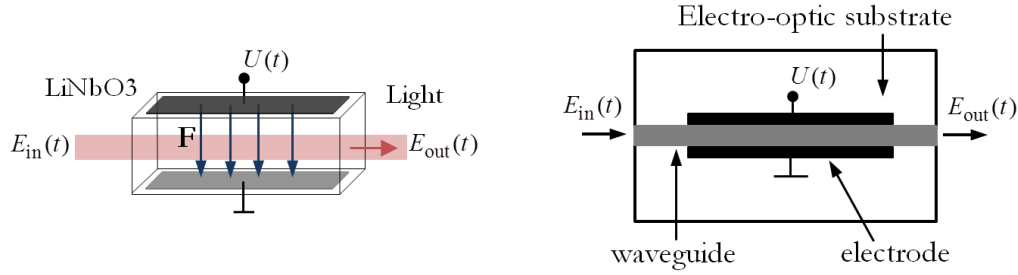


Fig. 2.10: schematic of a Pockels cell and representation of the π phase shift with U_π .

A beam of light passing through this material experiences a phase shift $\phi = 2\pi n(F)L/\lambda$, where λ is the free-space wavelength. Considering only the linear refractive index variation (Pockels effect), the change of ϕ is also linear with respect to the external voltage U as

$$\phi = \pi \frac{n^3 r_{\text{eff}} L F}{\lambda} = \pi \frac{n^3 r_{\text{eff}} L U}{d}, \quad (2.47)$$

where r_{eff} is an electro-optic coefficient [65]. In practice, this device consists of an optical waveguide built over a substrate, often a Lithium niobate (LiNbO3) crystal material, see Fig. 2.10. The required voltage to induce a phase change of π in the propagating wave is equal to $U_\pi = \lambda d / (Ln^3 r_{\text{eff}})$, typically 4 Vpp (Volts peak-to-peak) for LiNbO3, thus Eq. (2.47) can be written as

$$\phi(t) = \pi \frac{U(t)}{U_\pi}, \quad (2.48)$$

and the transfer function $T(t)$ can be expressed as

$$T(t) = \frac{E_{\text{out}}(t)}{E_{\text{in}}(t)} = \exp(j\phi(t)) = \exp\left(j\pi \frac{U(t)}{U_\pi}\right) \quad (2.49)$$

If a voltage $U(t) = U_\pi$ is applied in Eq. (2.49), the carrier $E_{\text{in}}(t)$ will experience a phase shift $\phi(t) = \pi$ and result in an output signal $E_{\text{out}}(t) = -E_{\text{in}}(t)$, leading to a BPSK modulation of the input signal.

To implement an amplitude and phase modulation of a carrier signal, two electro-optic phase modulators are combined in a Mach-Zehnder interferometer configuration, leading to the well-known Mach-Zehnder modulator (MZM). In this configuration, two 3 dB couplers/combiners are used to divide and combine the input/output signal sent to each modulator, see Fig. 2.11. In the upper arms, a phase bias ϕ_b can be adjusted with a bias voltage U_b to implement the different modulation formats. The half-split input optical electric field $E_{\text{in}}(t)$ on each arm is altered in phase with the applied voltages $U_{1,2}(t)$ and the resulting fields E_1 and E_2 are then recombined to obtain $E_{\text{out}}(t)$. The MZM modulator can be described in matrix notation as

$$E_{\text{out}} = \begin{bmatrix} \frac{1}{\sqrt{2}} & \frac{1}{\sqrt{2}} \\ \frac{1}{\sqrt{2}} & \frac{1}{\sqrt{2}} \end{bmatrix} \begin{bmatrix} \exp(j(\phi_1(t) + \phi_b)) & 0 \\ 0 & \exp(j\phi_2(t)) \end{bmatrix} \begin{bmatrix} \frac{1}{\sqrt{2}} \\ \frac{1}{\sqrt{2}} \end{bmatrix} E_{\text{in}}, \quad (2.50)$$

where the field transfer function T_{MZM} is equal to

$$T_{\text{MZM}} = \frac{E_{\text{out}}(t)}{E_{\text{in}}(t)} = \frac{1}{2} (\exp(j(\phi_1(t) + \phi_b)) + \exp(j\phi_2(t))) \quad (2.51)$$

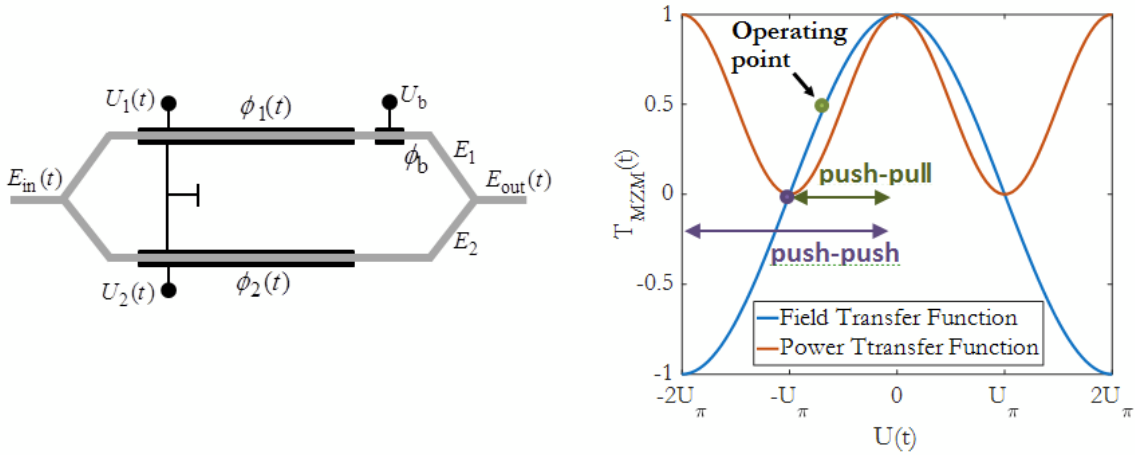


Fig. 2.11: Schematic of Mach-Zehnder modulator and Field/Power transfer functions. Biased operating points allow amplitude and phase modulations in push-pull and push-push modes, respectively.

with

$$\phi_{1,2}(t) = \pi \frac{U_{1,2}(t)}{U_\pi}. \quad (2.52)$$

Amplitude modulation on-off keying (OOK) is achieved by setting the MZM in *push-pull* mode, that is setting a $U_b = -U_\pi/2$ to the quadrature point and working with a peak-to-peak swing voltage $U(t) = U_\pi$ and $U_1 = -U_2 = U(t)/2$, see Fig. 2.11. In this mode, the phase term in Eq. (2.51) remains constant and only the amplitude is altered with the cosine term as

$$E_{\text{out}}(t) = E_{\text{in}}(t) \cos\left(\pi \frac{U(t)}{2U_\pi}\right). \quad (2.53)$$

Phase modulation BPSK is achieved in *push-push* mode by setting a $U_b = -U_\pi$ to the null operating point, with a peak-to-peak swing voltage $U(t) = 2U_\pi$ and $U_1 = U_2 = U(t)$. Note that the movement of the operating point through the null point invert the phase of the output signal.

To enable higher order modulations, like QAM or M-PSK, an IQ-modulator is used. This configuration combines two MZM modulators separated in two arms, each one set in push-pull mode and phase-shifted by $\pi/2$. The amplitude signals of each MZM are then combined to create the desired constellation. This modulation scheme is explained more in detail in Chapter 6 for the experimental validation of the AO system in a communication scenario.

Figure 2.12 shows the constellation diagram, bits/symbol, and modulator configuration of the OOK, BPSK, and QPSK modulation formats. At this point, the output signal of the modulator $E_{\text{out}}(t)$ can be written as

$$E_{\text{out}}(t) = a(t) \sqrt{P_s} \exp(j[w_s t + \phi_s(t) + \phi_{\text{ls}}(t)]) \quad (2.54)$$

where, depending on the adopted modulation format, the carrier is modified in amplitude $a(t)$ and in phase $\phi_s(t)$.

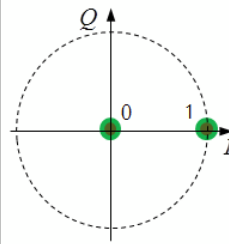
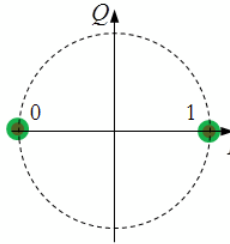
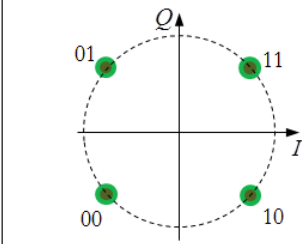
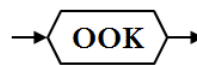
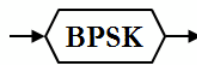
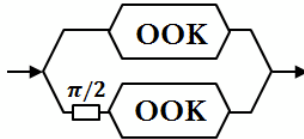
MODULATION FORMAT	OOK	BPSK	QPSK
Constellation map			
Bits/Symbol	1	1	2
Modulator configuration	 $\phi_b = -U\pi/2$ $U_1 = -U_2 = U(t)/2$ $U(t) = U\pi$	 $\phi_b = -U\pi$ $U_1 = U_2 = U(t)$ $U(t) = 2U\pi$	 $\phi_b = -U\pi$ $U_1 = -U_2 = U(t)$ $U(t) = 2U\pi$

Fig. 2.12: Constellation diagram, bits per symbol, and modulator configuration for the modulation formats OOK, BPSK, and QPSK.

2.2.2 Demodulator

When the transmitted signal has been modulated in amplitude, the demodulation of the received signal can be performed using a simple pin-photodiode followed by amplification, sampling, and signal processing stages where thresholding is used to decide between ones and zeros. This type of optical demodulation technique is known as direct detection, and benefits from its simplicity and immunity to signal phase variations. The cons are associated mainly when facing large dynamics in the signal fluctuations, mostly due to atmospheric scintillation effects. For higher order modulation formats, like BPSK or QPSK, the receiver requires more complexity. The received signal needs to be coherently combined with a reference one from a local oscillator. The demodulator mixes and delivers a set of signals that are further amplified, sampled, and processed with a DSP. In the DSP, the post-processing steps are more complex than in direct detection, correcting induced signal phase and frequency variations. Today's adoption of these type of demodulators is rising due to the increase improvement in computing power of DSP systems. The following subsections give an overview of the direct and coherent detection process.

2.2.2.1 Direct detection

Direct detection is the simplest and the most used detection scheme in FSOC. The receiver consists of a reverse-biased PIN diode that converts the optical input power into an electric current, see Fig. 2.13. A received signal

$$E_s(t) = \sqrt{P_s} \exp(j [w_s t + \phi_m(t)]) \tag{2.55}$$

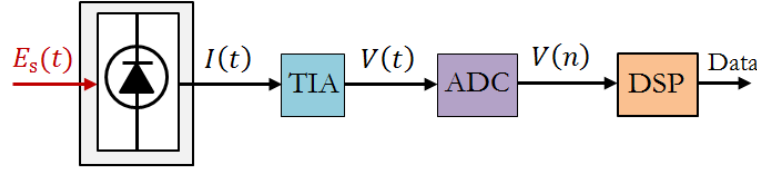


Fig. 2.13: Block diagram of the direct detection receiver.

with power P_s , angular frequency ω_s , and phase variations $\phi_m(t) = \phi_{ls}(t) + \phi_{pt}(t)$ due to laser phase shift $\phi_{ls}(t)$ and induced atmospheric phase piston $\phi_{pt}(t)$, will be converted into an electric current. In the photocurrent conversion process, the complex term is removed showing that direct detection is non-sensitive to phase disturbances of the signal, resulting in an average current

$$I_p = E_s(t)E_s(t)^* = RP_s \quad (2.56)$$

where R is the responsivity of the photodetector (in units of Ampere/Watts). The responsivity can be expressed in term of the quantum efficiency η_e as [2]

$$\eta_e = \frac{\text{electron generation rate}}{\text{photon incidence rate}} = \frac{I_p/q}{P_s/h\nu} = \frac{h\nu}{q} R, \quad (2.57)$$

$$R = \frac{\eta_e q}{h\nu} \quad (2.58)$$

where $h = 6.6 \times 10^{-34}$ [m²kg/s] is the Planck constant, ν is the laser frequency, $\lambda = c/\nu$ is the laser wavelength with $c = 3 \times 10^8$ [m/s] being the velocity of light, and $q = 1.6 \times 10^{-19}$ [C] is the electron charge.

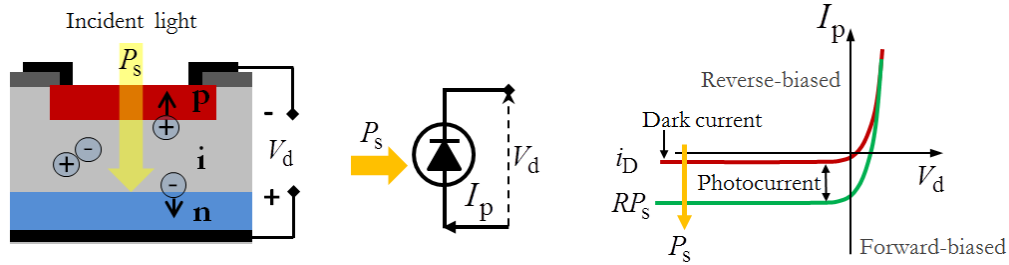


Fig. 2.14: Reversed-biased photodiode configuration for optical detection. Incident light power generates free charges which are drawn from the p-n junction producing an electric current. In absence of light, a small dark current is present.

In reverse biased, the photodiode reacts faster than in direct biased thus this configuration is used for optical detection. Without incident light, all the electrons and protons are drawn from the p-n junction creating a depleted region. In this state, a small current still flows and it is commonly known as dark current i_D . When light with sufficient power P_s hits the depleted region, electro-hole pairs appear. Due to the reverse bias potential, these new carriers drift away from the junction producing a flow of charges I_p (electric current). Figure 2.14 shows the proportional increment of i_d with the input power P_s . The total current I is then equal to

$$I = RP_s + i_D \quad (2.59)$$

The I is influenced by shot noise $n_{\text{sn}}(t) \sim \mathcal{N}(0, \sigma_{\text{sn}}^2)$ and thermal noise $n_{\text{T}}(t) \sim \mathcal{N}(0, \sigma_{\text{T}}^2)$ current, which are the two fundamental noise mechanisms that produce current fluctuations in an optical receiver [2]

$$I(t) = I_{\text{p}} + i_{\text{D}} + n_{\text{sn}}(t) + n_{\text{T}}(t). \quad (2.60)$$

Shot noise is originated by the randomness of the photon arrival and conversion into electrons. Thermal noise is produced by the random electron movement in a conductor or resistor due to a finite temperature. The $n_{\text{sn}}(t)$ is a stationary random process with Poisson statistics (low received power) often well approximated by Gaussian statistics (higher received power) [66–68]. Its autocorrelation is related to the spectral density $S_{\text{sn}}(f)$ by the Wiener-Khinchin theorem [66]

$$\langle n_{\text{sn}}(t)n_{\text{sn}}(t - \tau) \rangle = \int_{-\infty}^{\infty} S_{\text{sn}}(f)\exp(j2\pi f\tau)df, \quad (2.61)$$

where the brackets denote an ensemble average over the fluctuations, and the integral is the back-Fourier transform of $S_{\text{sn}}(f)$. Considering a one-side spectral density, with the lower limit of the integral set to zero, the $S_{\text{sn}}(f) = 2qI_{\text{p}}$, thus the shot noise variance is obtained with $\tau = 0$ as

$$\sigma_{\text{sn}}^2 = \langle n_{\text{sn}}^2(t) \rangle = 2qI\Delta f = 2q(RP_{\text{s}} + i_{\text{D}})\Delta f \quad (2.62)$$

Thermal noise or Johnson-Nyquist noise is associated to the thermal generation of carriers in the shunt resistance R_{sh} of the photodetector [69, 70]. It can be modeled as a stationary Gaussian random process with a spectral density $S_{\text{T}}(f) = 2k_{\text{B}}T/R_{\text{sh}}$, where T is the absolute temperature in degrees Kelvin ($273\text{K} = 0^\circ \text{C}$), $k_{\text{B}} = 1.38 \times 10^{-23}$ [J/K] is the Boltzmann's constant. Applying the same procedure of the calculation of the shot noise variance, the thermal noise variance is equal to

$$\sigma_{\text{T}}^2 = \frac{4k_{\text{B}}T\Delta f}{R_{\text{sh}}} \quad (2.63)$$

where Δf is the noise measurement bandwidth in Hertz. Note that the σ_{T}^2 is independent of I_{p} . Amplifiers unavoidably add additional thermal noise to the signal current. The extra noise produced by the different resistors in the amplification stages can be included through the amplifier noise figure F_{n} as

$$\sigma_{\text{T}}^2 = \frac{4k_{\text{B}}TF_{\text{n}}\Delta f}{R_{\text{sh}}} \quad (2.64)$$

These Gaussian-like noise sources are decorrelated and can be added

$$\sigma_{\text{N}}^2 = \sigma_{\text{T}}^2 + \sigma_{\text{sn}}^2, \quad (2.65)$$

thus the total noise current $n_{\text{N}}(t) \sim \mathcal{N}(0, \sigma_{\text{N}}^2)$ and

$$I(t) = I_{\text{p}} + i_{\text{D}} + n_{\text{N}}(t). \quad (2.66)$$

After the detection process, the signal $I(t)$ is amplified with a TIA and the resultant $V(t)$ is sampled with an ADC. The digitized signal is sent to the DSP which perform timing recovery to control the ADC sampling rate. Figure 2.15 shows a signal and the sampled points at different t_{s} . Then, the DSP compares the sampled points voltages against a threshold level V_{th} to discriminate between ones $V_1 > V_{\text{th}}$ and zeros $V_2 < V_{\text{th}}$.

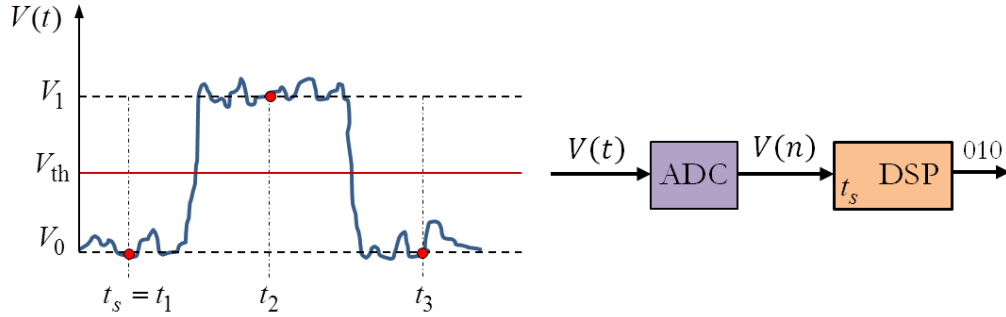


Fig. 2.15: Voltage signal after the TIA is sampled at intervals t_s , defined by the timing recovery performed within the DSP. The digitized signal is processed in the DSP and thresholding is applied to decide between received 1's and 0's.

2.2.2.2 Coherent detection

A coherent receiver is used to demodulate signals encoded with higher order modulation formats. This receiver requires the mixing of the incoming signal with the one of a local oscillator. At this point, it is only considered the modulated carrier signal components in Eq. (2.44) to represent the incoming signal $E_s(t)$

$$E_s(t) = \sqrt{P_s} \exp(j(2\pi\nu_s t + \phi_s(t))), \quad (2.67)$$

and the local oscillator (LO) signal $E_{lo}(t)$ is described as

$$E_{lo}(t) = \sqrt{P_{lo}} \exp(j(2\pi\nu_{lo} t + \phi_{lo}(t))) \quad (2.68)$$

where the input signal power P_s , frequency ν_s , and phase $\phi_s(t)$ are combined with their equivalents local oscillator signal power P_{lo} , frequency ν_{lo} , and LO phase $\phi_{lo}(t)$ to reconstruct the constellation of the modulated signal. This process is performed with the help of a so-called 90° -Hybrid and balanced detectors, which discriminate the in-phase $I_I(t)$ and quadrature $I_Q(t)$ signals from $E_s(t)$, see Fig. 2.16.

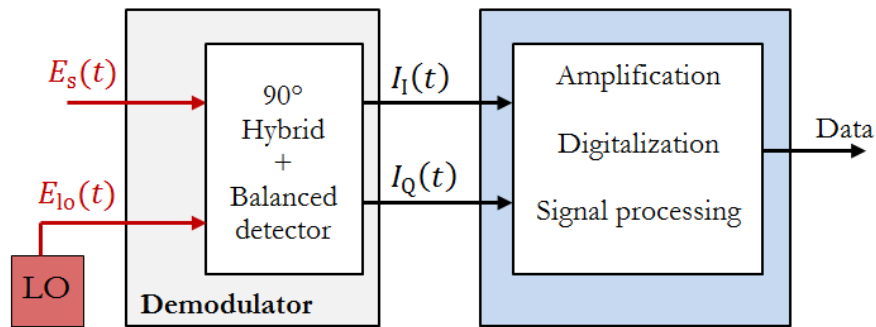


Fig. 2.16: Block diagram of the coherent receiver.

$$I_I(t) = R\sqrt{P_s P_{lo}} \cos(2\pi\nu_b t + \phi_s - \phi_{lo}) \quad (2.69)$$

$$I_Q(t) = R\sqrt{P_s P_{lo}} \sin(2\pi\nu_b t + \phi_s - \phi_{lo}) \quad (2.70)$$

These signals are then amplified, digitized, and processed with a digital signal processor (DSP), after which the original data is retrieved. This demodulation scheme is explained with more detail in Chapter 6 for the experimental validation of the AO system in a communication scenario.

2.2.3 Detection Signal-to-Noise ratio

PIN-Receiver: The electrical signal-to-noise ratio (SNR) of a PIN-based photoreceiver is equal to the ratio of the total input power and the total noise power (thermal and shot noise), and can be calculated with Eq. (2.56) and Eq. (2.65) as

$$\text{SNR} = \frac{R^2 P_s^2}{2q(RP_s + i_D)\Delta f + 4(k_B T F_n \Delta f / R_{sh})} \quad (2.71)$$

Direct detection is in general thermal noise limited, which means that thermal noise dominates $\sigma_T^2 \gg \sigma_{sn}^2$, thus Eq. (2.71) gets reduced to

$$\text{SNR}_{th} = \frac{R_{sh}(RP_s)^2}{4K_b T F_n \Delta_f} \quad (2.72)$$

Clearly, the SNR improves proportionally to the input power P_s and with the increment of R_{sh} . This is the reason for the use of a TIA which has high input impedance. Considering the shot noise limit $\sigma_{sn}^2 \gg \sigma_T^2$, which occurs when the input power is amplified before detection, or when coherent reception is used, the SNR can be written as

$$\text{SNR}_{sn} = \frac{RP_s}{2q\Delta_f} = \frac{\eta_e P_s}{2h\nu\Delta_f} \quad (2.73)$$

The SNR_{sn} can also be expressed in terms of the number of received photons per bit N_p , by considering the energy per bit [71]

$$E_b = \frac{P_s}{R_b} = N_p h\nu, \quad (2.74)$$

$$\text{SNR}_{sn} = \eta_e N_p \quad (2.75)$$

where R_b is the bit rate, and $\Delta f = R_b/2$ for an ideal receiver. Equations (2.74)-(2.75) are later used in Chapter 6 for the experimental analyses.

APD-Receiver: An important remark needs to be done when an avalanche photodiode (APD) is used in direct detection. Optical receivers that employ APD provide better performance for the same input power. This improvement is given by the use of an amplification circuit that increases the photocurrent by a multiplication factor M . Hence, the current I_p in Eq. (2.56) now becomes

$$I_p = MRP_s = R_{APD}P_s, \quad (2.76)$$

where R_{APD} is the responsivity of the APD, enhanced by the M factor. The thermal noise remains the same for APD receivers since it is given by the internal components like conductors and resistors. Instead, shot noise increases due to the generation of additional electron-hole pairs through the process of impact ionization [2]. The shot noise variance can be written as

$$\sigma_{sn}^2 = 2qM^2 F_A (RP_s + i_D)\Delta f \quad (2.77)$$

where F_A is the excess noise factor of the APD given by

$$F_A(M) = k_A M + (1 - k_A)(2 - 1/M). \quad (2.78)$$

In Eq. (2.78) the term $0 \leq k_A \leq 1$ is a ionization coefficient ratio that relates the excess noise factor with the gain multiplication factor M [2, 72]. Nevertheless, in practice thermal noise dominates over shot noise and the signal enhancement remains proportional to M^2 . The thermal noise and shot noise limited SNR for an APD are given by

$$\text{SNR}_{\text{APDth}} = \frac{R_{\text{sh}}(MRP_s)^2}{4K_b T F_n \Delta_f} \quad (2.79)$$

$$\text{SNR}_{\text{APDsn}} = \frac{RP_s}{2qF_A\Delta_f} = \frac{\eta_e P_s}{2h\nu F_A \Delta_f} \quad (2.80)$$

In the thermal noise limit regime, the SNR improves with the gain factor M . In the shot noise limit, the SNR deteriorates with an increased APD gain due to the fact that the excess noise factor F_A rises.

Coherent Receiver: The SNR in a coherent receiver SNR_{ch} benefits from the fact that P_{lo} can be made much larger than the received signal power P_s , thus the signal noise variance is dominated by shot noise leading to

$$\text{SNR}_{\text{ch}} \approx \frac{RP_{\text{lo}}}{2q\Delta_f}. \quad (2.81)$$

By applying Eq. (2.74), the coherent SNR shows a direct proportionality with the number of received photons N_p

$$\text{SNR}_{\text{ch}} \approx \eta_e N_p. \quad (2.82)$$

2.3 Communications performance

Laser downlinks from low-earth-orbit (LEO) satellites represent one of the most challenging scenarios. This kind of link has a duration time in the order of 10 minutes, with most of the active transmission time occurring below the 30 degrees of elevation. At such low elevation angles, the beam is affected by strong turbulence that induces strong scintillation and high order phase wave-front distortions which affect the coupling of the beam into a single mode fiber. As a rule of thumb, direct detection with PIN-based receiver front-ends can be used for data transmissions up to 10 Gbps due to the size of the photodiodes. These type of receivers are mainly affected by scintillation and background noise light. For very high data rates employing advanced modulation formats, amplifiers and coherent receivers need a stable and efficient single-mode fiber coupling. Consequently, it is necessary to quantify the impact of the turbulence and, if necessary, mitigate its effects.

A valid approach to minimize the phase distortions requires the use of a smaller receiver aperture, i.e. $D \approx 10$ cm. When D/r_0 approaches unity, the captured beam is mostly affected by the beam angle of incidence and has a quasi-uniform phase over the aperture; thus it can be easily tracked and corrected with a tip-tilt system to be coupled into the single-mode fiber. On the other hand, as shown in Fig. 2.8, the aperture averaging of scintillation is diminished and the received power substantially lowered, i.e. less power and less signal stability.

In a downlink scenario, satellites need to minimize the transmission power due to the limitations of the satellite platform, which leads to larger OGS apertures to collect sufficient signal power. Typical OGSs are designed

with an aperture size between 40 cm and 1 meter. Increasing the D unavoidably exposes the decoherence of the beam wave-front within the aperture area, producing a random focusing of the beam power (focal speckles). Without any type of wave-front compensation system, this phenomena becomes dominant and the consequences in the coupled signal are severe.

The impact of the atmosphere in a FSOC communication system can be quantified with several metrics. The relevant ones, to some extent interrelated, are the mean SNR, the mean BER, and the single-mode fiber coupling efficiency η . Particularly with coherent reception, a good $\langle \eta \rangle$ and variance σ_η^2 of the coupled signal directly impact in the system BER. The BER quantifies the link quality from the perspective of data communication. The mean and variance of the η define the quality of the channel. The Strehl ratio is an image quality metric widely used in astronomy and also employed in FSOC as an estimate of performance tendency. The following subsections extend on these concepts.

2.3.1 Strehl ratio

A coarse estimation of the signal loss produced by the wave-front decoherence α_{ph} can be performed in the focal plane with the Strehl ratio SR . This metric is defined as the ratio between the mean on-axis maximum irradiance of a beam affected by turbulence $I_S(0,0)$, and the maximum irradiance of the reference turbulence-free case I_{airy} (diffraction limited airy pattern). The Strehl ratio can be expressed in function of the D/r_0 as [73]

$$SR = \frac{\langle I_S(0,0) \rangle}{I_{\text{airy}}} = \frac{1}{\left[1 + \left(\frac{D}{r_0} \right)^{5/3} \right]^{6/5}}, \quad (2.83)$$

Assuming the ergodicity of the fields affected by atmospheric turbulence, the mean of $\alpha_{\text{ph}}(t)$ can be made proportional to the SR as

$$\langle \alpha_{\text{ph}}(t) \rangle \propto 10 \log_{10}(SR). \quad (2.84)$$

It is important to highlight that the SR does not accurately represent the signal fading, particularly under strong turbulence conditions. A better metric to quantify the signal attenuation is the single-mode fiber coupling efficiency, which will be later discussed in the evaluation of the system communication performance. Nevertheless, it is a useful metric to estimate the degree of wave-front degradation in different turbulent regimes. Figure 2.17 shows the Strehl ratio for different values of r_0 and three FSOC standard telescope aperture diameters D . Note that a $SR = 0.43$ or $\langle \alpha_{\text{ph}}(t) \rangle \approx -3.66$ dB is obtained when $r_0 \approx D$, thus the wave-front coherence diameter r_0 needs to increase beyond the aperture size to approach diffraction limit performance.

2.3.2 Signal to noise ratio in a turbulent channel

The signal-to-noise ratio quantifies the ratio of the signal power over the overall noise power. The higher the SNR, the better for the data detection process in a communication receiver. As previously introduced, there are several noise sources to be considered in an optical receiver, but the dominant ones are the shot noise and thermal noise, see Sec. 2.2.2.1. When working with direct detection, the thermal noise becomes dominant but, with the help of signal amplification, it is possible to operate in the shot noise regime. In coherent reception, the received signal results boosted with the power of the local oscillator signal and these type of receiver are

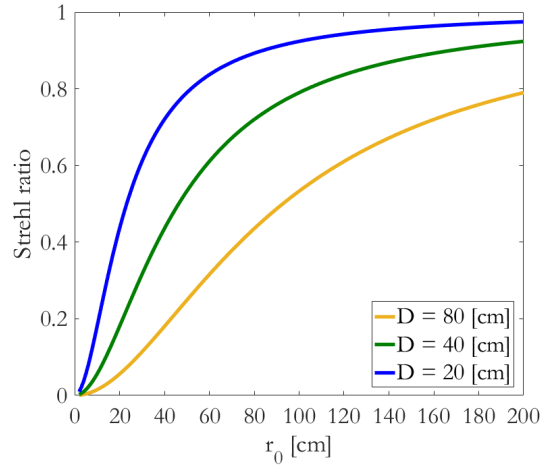


Fig. 2.17: Strehl ratio vs. Fried parameter for different telescope aperture diameter D

generally assumed to be shot noise limited. The advantage of working in this regime is that the instantaneous SNR can be directly estimated with the number of received photons as shown in Eq. (2.74)-(2.82). In this work, only shot-noise limited receivers are considered.

Lets now define the SNR in absence of turbulence as SNR_0 . Independently of the modulation format, in the presence of turbulence the SNR_0 becomes a fluctuating term and the mean SNR affected by turbulence $\langle \text{SNR} \rangle$ can be approximated as [59]

$$\langle \text{SNR} \rangle = \frac{\text{SNR}_0}{\sqrt{\frac{P_0}{\langle P_S \rangle} + \sigma_I^2(D)\text{SNR}_0^2}}. \quad (2.85)$$

where P_0 is the signal power in absence of turbulence, and P_S is the mean of the instantaneous input signal affected by turbulence. The $\sigma_I^2(D)$ is the previously introduced aperture-averaged scintillation index, Eq. (2.31). Note that the ratio $P_0/\langle P_S \rangle$ is nothing else than the inverse strehl ratio $1/(SR)$, see Eq. (2.83), and thus Eq. (2.85) becomes [20]

$$\langle \text{SNR} \rangle = \frac{\text{SNR}_0}{\sqrt{\left(\frac{1}{SR}\right) + \sigma_I^2(D)\text{SNR}_0^2}}. \quad (2.86)$$

Power scintillation has a stronger impact in the $\langle \text{SNR} \rangle$ and can be attenuated using a large aperture collecting lens or an array of small apertures [20, 74]. When the scintillation is minimized, the $\langle \text{SNR} \rangle$ is clearly dependent on the degree of aberration of the phase wave-front, quantified through the SR. If the aberration is compensated, the SR approaches to 1 and the $\langle \text{SNR} \rangle \approx \text{SNR}_0$. Considering that the impact of phase distortions is dominant over the beam scintillation effects, the need of phase wave-front compensation becomes evident.

2.3.3 Receiver sensitivity and atmospheric impact

One of the most adopted performance metrics for digital optical receivers is the instantaneous bit-error-ratio (BER). The BER represents the ratio of the number of erroneously received bits over the total transmitted bits in a predefined time interval, and can also be defined as the probability of incorrect identification of a bit. It is widely adopted a $\text{BER} = 1 \times 10^{-9}$ as the metric for error-free transmission and implies 1 error per 10^9 received

bits. In FSOC, a BER better than 10^{-3} is sufficient, as it is approximately the limit of error correction systems to take over and deliver error-free transmission. The receiver sensitivity is then selected to assure this performance.

Figure 2.18 shows the probability density distributions of sampled values at the position of one's and zero's. These distributions are defined by the Gaussian-like noise statistics of thermal and shot noise with variances σ_N^2 given by Eq. (2.65).

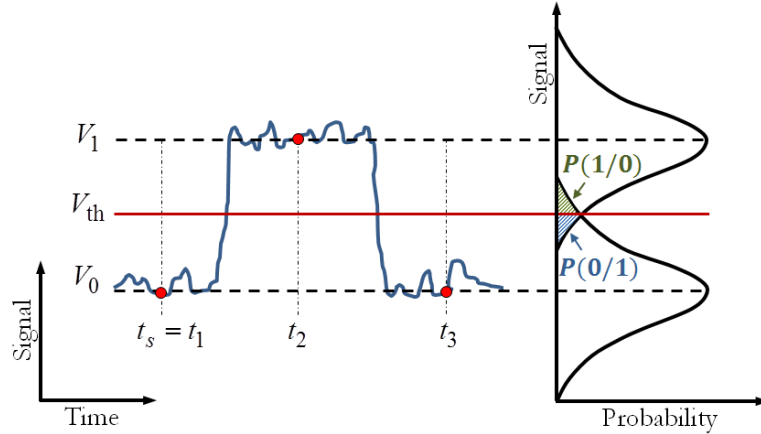


Fig. 2.18: Signal generated at the receiver, and probability densities associated to received ones' and zeros'. The dashed regions highlight the probability of incorrect detection. Graphic inspired from [2].

As previously mentioned, a decision circuit uses a threshold level V_{th} to discriminate between a one $V_1 > V_{th}$ and a zero $V_0 < V_{th}$. Here, a probability of receiving a 1 or a 0 is defined as $P(1)$ and $P(0)$, respectively. An error may occur identifying a 0 when a 1 is received $P(0/1)$, or deciding for a 1 when a 0 is received $P(1/0)$. The BER is then defined as

$$\text{BER} = P(1)P(0/1) + P(0)P(1/0) \quad (2.87)$$

where one's and zero's are equally likely to occur, thus $P(0) = P(1) = 1/2$ and

$$\text{BER} = \frac{1}{2}[P(0/1) + P(1/0)]. \quad (2.88)$$

These two conditional probabilities with Gaussian distribution and variances σ_0^2 and σ_1^2 , can be defined as

$$P(0/1) = \frac{1}{\sigma_1\sqrt{2\pi}} \int_{-\infty}^{V_{th}} \exp\left(-\frac{(V - V_1)^2}{2\sigma_1^2}\right) dV = \frac{1}{2} \text{erfc}\left(\frac{V_1 - V_{th}}{\sigma_1\sqrt{2}}\right) \quad (2.89)$$

$$P(1/0) = \frac{1}{\sigma_0\sqrt{2\pi}} \int_{V_{th}}^{\infty} \exp\left(-\frac{(V - V_0)^2}{2\sigma_0^2}\right) dV = \frac{1}{2} \text{erfc}\left(\frac{V_{th} - V_0}{\sigma_0\sqrt{2}}\right) \quad (2.90)$$

where the *erfc* stands for the complementary error function [75]

$$\text{erfc}(x) = \frac{2}{\sqrt{\pi}} \int_x^{\infty} \exp(-y^2) dy \quad (2.91)$$

Equation (2.88) can now be written as

$$\text{BER} = \frac{1}{4} \left[\text{erfc}\left(\frac{V_1 - V_{th}}{\sigma_1\sqrt{2}}\right) + \text{erfc}\left(\frac{V_{th} - V_0}{\sigma_0\sqrt{2}}\right) \right] \quad (2.92)$$

where the minimum BER is obtained by optimizing V_{th} , which is performed as

$$Q \equiv \frac{V_1 - V_{th}}{\sigma_1} = \frac{V_{th} - V_0}{\sigma_0} \quad (2.93)$$

$$V_{th} = \frac{\sigma_0 V_1 + \sigma_1 V_0}{\sigma_0 + \sigma_1} \quad (2.94)$$

Considering a PIN-receiver where thermal noise is dominant, $\sigma_0 = \sigma_1$, thus $V_{th} = (V_1 + V_0)/2$ or the average between the sample voltages. In Eq. (2.93), the Q-factor (Q) represents a quality metric that can be related to the electrical signal-to-noise ratio (SNR) as $Q \approx \sqrt{SNR}$ [76]. Now, by combining Eq. (2.93) and Eq. (2.94), the Q-factor is equal to

$$Q = \frac{V_1 - V_0}{\sigma_1 + \sigma_0}. \quad (2.95)$$

Hence, the BER can be written in function of the Q-factor as [2]

$$BER = \frac{1}{2} \operatorname{erfc} \left(\frac{Q}{\sqrt{2}} \right) \quad (2.96)$$

In thermal noise limit $\sigma_1 = \sigma_0$, assuming $V_0 = 0$, the $Q = V_1/(2\sigma_1)$ thus $SNR = V_1^2/\sigma_1^2 = 4Q^2$. For error-free data transmission $BER \approx 10^{-9}$ a $Q = 6$ is required, which implies a $SNR = 144$ or 21 dB. The BER for direct detection in thermal noise limit results

$$BER_{(OOK)th} = \frac{1}{2} \operatorname{erfc} \left(\frac{1}{2} \sqrt{\frac{SNR}{2}} \right) \quad (2.97)$$

Instead, in the shot noise limit, a zero has no photons and $\sigma_0 = 0$. Assuming zero dark current, $Q = V_1/\sigma_1 = \sqrt{SNR}$ and a SNR of 15.6 dB is needed for a BER of 10^{-9} . In addition, considering that the $SNR \approx \eta_e N_p$, with N_p being the number of received photons per bit and η_e the quantum efficiency of the diode, the BER can be expressed as

$$BER_{(OOK)sn} = \frac{1}{2} \operatorname{erfc} \left(\sqrt{\frac{SNR}{2}} \right) = \frac{1}{2} \operatorname{erfc} \left(\sqrt{\frac{\eta_e N_p}{2}} \right) \quad (2.98)$$

In this noise regime, with $\eta_e = 1$, error-free transmission is achieved with $N_p = 36$. In practice, this is not possible due to thermal noise, thus a more realistic number is $N_p \approx 1000$.

The performance of BPSK and QPSK in coherent reception can be derived in a similar manner, leading to the following expressions [77–79]

$$BER_{(BSPK)} = BER_{(QSPK)} = \frac{1}{2} \operatorname{erfc} \left(\sqrt{SNR} \right) = \frac{1}{2} \operatorname{erfc} \left(\sqrt{\eta_e N_p} \right). \quad (2.99)$$

Equation (2.99) will be used in chapter 6 for the experimental analysis of the communication scenario.

Atmospheric impact on receiver sensitivity

The received signal after a beam propagates through a turbulent channel is not only affected by the receiver noise, but it must also consider the induced fluctuations due to the atmospheric effects. As a rule of thumb, the BER deterioration must not drop below the limit 1×10^{-3} of Forward Error Correction (FEC) systems. If the

BER fluctuates below this limit, a FEC system can deliver error-free data communications. The instantaneous BER, described in Eq. (2.96)-(2.99), is considered a conditional BER in the presence of turbulence and thus it must be averaged with the PDF of the irradiance fluctuations $p_I(u)$. The resultant unconditional mean BER, for a normalized signal with unit mean, can be expressed as [20]

$$\langle \text{BER} \rangle = \frac{1}{2} \int_0^\infty p_I(u) \operatorname{erfc} \left(\frac{\langle \text{SNR} \rangle}{\sqrt{2}} u \right) du, \quad (2.100)$$

where $p_I(u)$ is taken to be the gamma-gamma distribution with unit mean, Eq. (2.35), and the $\langle \text{SNR} \rangle$ is given by Eq. (2.86). To evaluate the enhancement of the $\langle \text{SNR} \rangle$ and proportional improvement of $\langle \text{BER} \rangle$ after the correction of the phase wave-front aberration, let's consider Noll's wave-front representation in function of orthogonal polynomials (Zernike modes), and the defined the residual wave-front variance $\Delta_m = \langle \sigma_\varphi^2 \rangle$ after the compensation of m modes [64]

$$\Delta_m \approx 0.2944 m^{-\sqrt{3}/2} \left(\frac{D}{r_0} \right)^{5/3} \quad m > 21, \quad (2.101)$$

In Eq. (2.101), the wave-front variance is reduced with each corrected m mode (the values of the first 21 residual errors Δ_m are listed in [64]). By considering the definition of Strehl ratio given by Maréchal and [80], the SR can be estimated from the statistics of the wave-front phase $\varphi(\mathbf{r})$ deviation

$$SR \approx |\langle \exp [j(\varphi(\mathbf{r}) - \langle \varphi(\mathbf{r}) \rangle)] \rangle|^2 \quad (2.102)$$

Note that the Strehl ratio is a scalar, and the phases develop in a 2D space represented by the vector \mathbf{r} . After the expansion of the complex exponential and retaining only the first terms, Eq. (2.102) leads to the well-known expression

$$SR \approx \exp \left(\langle \sigma_\varphi^2 \rangle \right) \quad (2.103)$$

which allows, after combining Eq. (2.103) with Eq. (2.101), an approximation of the SR improvement with each corrected mode. By introducing Eq. (2.103) in Eq.(2.86), the mean BER enhancement can be evaluated against turbulence correction.

Figure 2.19 shows the mean BER for OOK and QPSK modulation formats as a function of the mean SNR and for two LEO-downlinks scenarios with elevation 10° and 90° . The simulation consider a telescope aperture $D = 40$ cm, corresponding to $D/r_0 = 6$ and $D/r_0 = 2$ calculated with Eq. (2.20). The red curves show the reference shot-noise limit in the absence of turbulence. The dashed curves represent the BER for the uncompensated turbulence effects. The dotted curves show the BER improvement after tilt correction ($m=3$ modes). The continuous curves show the BER improvement after the correction of a hundred modes ($m=100$), where the SR approaches 1 and the $\langle \text{SNR} \rangle$ increases, improving the $\langle \text{BER} \rangle$. These results evidence the data communication enhancement after the compensation of the distorted phase wave-front. Note that at lower elevations, the tilt correction is not yet sufficient to reach a $\text{BER} \geq 10^{-3}$. This task can be achieved, to a certain extent, with wave-front correction methods.

2.3.4 Fiber coupling

To achieve very high data rates and benefits from the high sensitive modulation formats; e.g. BPSK and QPSK, an efficient and stable single-mode fiber (SMF) coupling is required. A laser downlink working with a

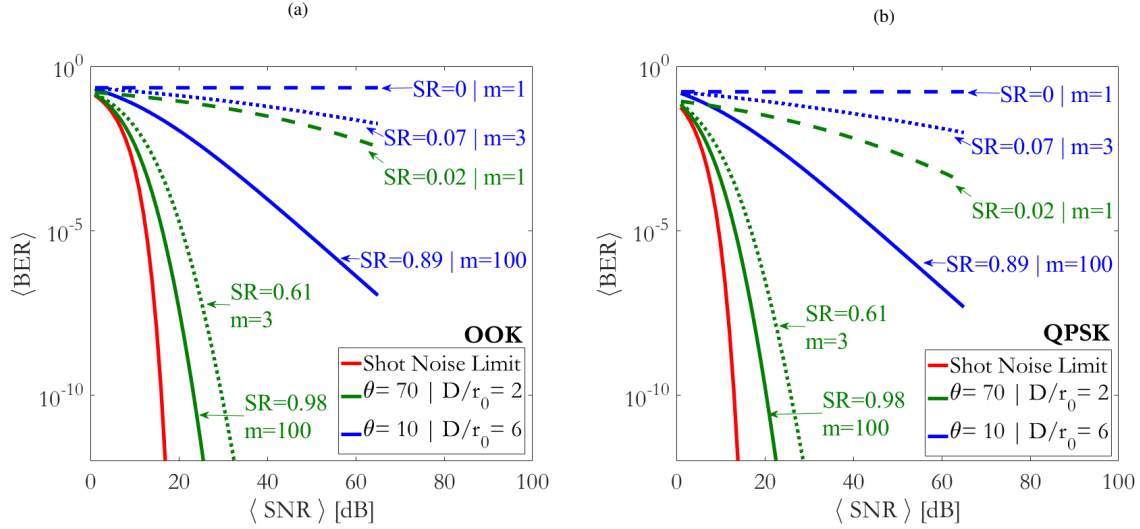


Fig. 2.19: Mean BER in function of the mean SNR affected by the turbulence at 70° and 10° laser downlink elevations and considering a telescope aperture of 40 cm. The BER is calculated for a receiver working with (a) OOK direct detection and (b) QPSK coherent reception. The curves show the BER improvement in the absence of correction $m=1$, after tilt correction $m=3$, and after higher order compensation $m=100$ of the phase wave-front.

wavelength of 1550 nm and synchronous detection needs amplifiers and demodulators specifically designed to work with this kind of fiber. Because of the previously described turbulence effects in the laser channel, and mainly due to the higher order phase wave-front distortions, the SMF coupling of the received signal results very difficult in scenarios of weak turbulence, and practically impossible under strong turbulence regimes. This problem can be addressed with different wave-front compensation systems. Synchronous receivers are highly dependent on the good matching between the spatial fields of the received signal and that of the local oscillator. The turbulence-induced aberration diminishes the downconverted power due to field mismatching. Since the LO field in a synchronous receiver results from the fundamental Gaussian mode of a single-mode fiber, the degradation of the mixing efficiency can be calculated as the loss of SMF coupling efficiency.

2.3.4.1 Single-mode fiber coupling efficiency

The SMF coupling efficiency η quantifies how efficiently the energy of a free-space laser beam can be coupled into the core of the fiber. The η is calculated in the pupil plane (lens position) as the ratio of the average optical power coupled into the fiber $\langle P_f \rangle$ to the average captured power in the system aperture (focusing lens) $\langle P_a \rangle$. This is performed with the overlap integral between the incident complex pupil field $\mathbf{P}_i(\mathbf{r})$, and the back propagated fundamental mode of the fiber $\mathbf{U}_0(\mathbf{r})$ [81]

$$\eta = \frac{\langle P_f \rangle}{\langle P_a \rangle} = \frac{\left| \int_A \mathbf{P}_i^*(\mathbf{r}) \mathbf{U}_0(\mathbf{r}) d\mathbf{r} \right|^2}{\int_A |\mathbf{P}_i(\mathbf{r})|^2 d\mathbf{r} \cdot \int_A |\mathbf{U}_0(\mathbf{r})|^2 d\mathbf{r}}. \quad (2.104)$$

where \mathbf{r} represents the spatial coordinate over the receiving aperture of area A , and the complex conjugate is indicated by $*$. The power-normalized, back propagated mode of a single-mode fiber with $1/e$ mode field radius w_0 , is calculated as

$$\mathbf{U}_0(\mathbf{r}) = \sqrt{\frac{2}{\pi w_a^2}} \exp\left(-\frac{\mathbf{r}^2}{w_a^2}\right) \quad (2.105)$$

where $w_a = \lambda f / (\pi w_0)$ is the back propagated mode field radius of the fiber, λ is the laser wavelength, and f is the focal length of the coupling lens. Assuming an ideal plane wave in the absence of turbulence, the maximum possible SMF coupling efficiency is $\eta = 0.814$. The loss of coupling efficiency is associated with the aperture truncation of the plane wave, leading to an Airy pattern of intensity at the fiber core. The difference between the Gaussian-shape fiber mode and the Airy intensity distribution results in the efficiency drop.

In Eq. (2.104) the incident field $\mathbf{P}_i(\mathbf{r})$ is considered with unitary amplitude and a constant phase over the aperture. The fiber field mode is also considered to have a constant phase, and thus these terms are not highlighted in the equation. In a real scenario, the amplitude and the phase of the incident field result distorted by the atmosphere. It is then useful to estimate the impact of different turbulent regimes in the fiber coupling efficiency. Let's assume only phase wave-front distortions, as their effect is generally dominant over amplitude fluctuations. As mentioned before, different turbulent regimes can be characterized by the D/r_0 for a predefined aperture diameter D . Since the Eq. (2.104) works with synthetically generated 2D complex fields and it is optimum for numerical simulations, let's generalize this equation in function of D/r_0 for plane wave and Kolmogorov spectrum. To do so, the authors [81–84] reformulate Eq. (2.104) as

$$\eta = \frac{1}{\langle P_a \rangle} \int \int_A \Gamma_i(\mathbf{r}_1, \mathbf{r}_2) \mathbf{U}_0^*(\mathbf{r}_1) \mathbf{U}_0(\mathbf{r}_2) d\mathbf{r}_1 d\mathbf{r}_2, \quad (2.106)$$

where the mutual coherence function of the incident field can be written as

$$\Gamma_i(\mathbf{r}_1, \mathbf{r}_2) = \langle \mathbf{P}_i(\mathbf{r}_1) \mathbf{P}_i^*(\mathbf{r}_2) \rangle \approx I_i \exp\left(-\frac{|\mathbf{r}_1 - \mathbf{r}_2|^2}{\rho_0^2}\right) \quad (2.107)$$

by considering weak fluctuation conditions and Gaussian spatial dependence for the mutual coherence function. In Eq. (2.107), the term I_i is the intensity of the incident plane wave, and ρ_0 is given by Eq. (2.19) considering $\zeta = 0$. Using Eq. (2.105) and Eq. (2.107) in Eq. (2.106), after some algebraic manipulation detailed in [82], the η can be expressed as

$$\eta = 8a^2 \int_0^1 \int_0^1 \exp\left[-\left(a^2 + \left(\frac{D}{r_0}\right)^2\right)(x^2 + y^2)\right] I_0\left(2\left(\frac{D}{r_0}\right)^2 xy\right) xy dx dy. \quad (2.108)$$

In Eq. (2.108) I_0 is the modified Bessel function of the first kind and zero order, which results from the back transformation of the fundamental fiber mode from the focal plane to the pupil plane. The parameter a is a design coefficient relating the radius of the pupil $D/2$ to the radius of the fiber core, set equal to 1.12 to achieve maximum coupling efficiency. The ratio $(D/r_0)^2$ represents the number of phase speckles in the aperture, which is generally assumed equal to the number of intensity speckles in the focal plane [20].

Considering the modal representation of the wave-front presented in Sec. 2.1.4, this work proposes an approximation for the calculus of the r_0 . Based on the Strehl ratio definition given in Eq. (2.83) and Eq. (2.103), the r_0 can be approximated after the reduction of the wave-front variance as

$$SR \approx \exp(-\Delta_m) \approx \frac{1}{\left(1 + \left(\frac{D}{r_c}\right)^{5/3}\right)^{6/5}}, \quad (2.109)$$

where r_c represents the changing in the wave-front coherence that maintains the equality, resulting in

$$r_c = \frac{D}{\left(\left(\frac{1}{\exp(-\Delta_m)} \right)^{5/6} - 1 \right)^{3/5}}. \quad (2.110)$$

In Eq. (2.110), Δ_m is the phase residual error defined by [64], which get reduced with the increment of m corrected modes. Using r_c in Eq. (2.108) allows estimating the improvement in the η after wave-front correction.

$$\Delta_m \approx 0.2944m^{-\sqrt{3}/2} \left(\frac{D}{r_0} \right)^{5/3} \quad m > 21 \quad (2.111)$$

The values of the first 21 residual errors Δ_m are listed in [64]. Figure 2.20 shows the SMF coupling efficiency

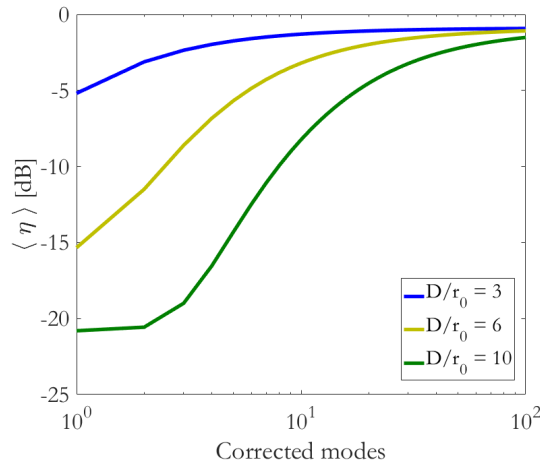


Fig. 2.20: Coupling efficiency vs. corrected modes for $D/r_0 = [3, 6, 10]$ and a telescope aperture $D = 40$ cm.

for turbulent regimes represented by $D/r_0 = [3, 6, 10]$, and considering a $D = 40$ cm. Substantial coupling losses are present in the absence of correction, particularly in scenarios of stronger turbulence. The correction of the wave-front tilt (modes 2 and 3) delivers the highest improvement, except for scenarios of stronger turbulence, characterized here with $D/r_0 = 10$. This is expected since strong wave-front aberration lead to high energy dispersion of the focused beam and thus centroid tilt correction does not assure energy at the fiber core. Proceeding with additional mode compensation from $m = 4$ to $m = 100$, further improves the coupling efficiency until a plateau is reached. Higher order modes have less energy and are associated with high-frequency components of the distorted phase, thus their contribution is minimal. Systems with more phase distortion require more corrected modes, i.e. the compensation of fields with $D/r_0 = 10$ involves 70 corrected modes. This example highlights the importance of wave-front compensation to enhance the quality of the received beam wave-front.

2.3.4.2 Mixing efficiency and fading statistics

The performance of synchronous receivers can be evaluated with the mixing efficiency η_h , which measures how similar are the received field $\mathbf{E}_s(\mathbf{r}, t)$ and the reference local oscillator field $\mathbf{E}_{10}(\mathbf{r}, t)$ in terms of their

transverse amplitude and phase coherence. The probability distribution of the signal fading becomes relevant in the calculation of the symbol-error-probability (SEP) in M -ary PSK systems. As initially mentioned, the calculation of the heterodyne/homodyne efficiency is equivalent to that of the SMF coupling efficiency because the reference LO signal also results from the back-propagated Gaussian mode of the fiber to the aperture [85]. Here it is important to distinguish between the time domain component of the signals and the spatially varying components associated with the transverse beam profile.

The mixing efficiency and the intensity fading statistics were derived by [86]. Following the same procedure, the Eq. (2.104) can be written as

$$\eta_h = \frac{\left| \int_A \mathbf{E}_s^*(\mathbf{r}, t) \mathbf{E}_{10}(\mathbf{r}, t) d\mathbf{r} \right|^2}{\int_A |\mathbf{E}_s(\mathbf{r}, t)|^2 d\mathbf{r} \cdot \int_A |\mathbf{E}_{10}(\mathbf{r}, t)|^2 d\mathbf{r}}. \quad (2.112)$$

where A represents the aperture area of the coupling lens where the fields are integrated. In order to evaluate the impact of the turbulence, both the log-amplitude $\chi(\mathbf{r})$ and the phase fluctuations $\varphi_s(\mathbf{r})$ are considered in the received field as

$$\mathbf{E}_s(\mathbf{r}, t) = A_s \exp[\chi(\mathbf{r})] \exp[j(w_s(t) + \varphi_s(\mathbf{r}) + \phi_s(t))] \quad (2.113)$$

where A_s is the amplitude in the absence of turbulence, $w_s(t)$ is the signal frequency, and $\phi_s(t)$ the signal phase. Note that these temporal terms are congruent with the terminology presented in Sec. 2.2. Likewise, the LO signal can be expressed as

$$\mathbf{E}_{10}(\mathbf{r}, t) = A_{10} \exp[j(w_{10}(t) + \varphi_{10}(\mathbf{r}) + \phi_{10}(t))] \quad (2.114)$$

where $\varphi_{10}(\mathbf{r})$ is the beam phase, A_{10} is the amplitude of the local oscillator, and where the signal frequency and phase are represented by $w_{10}(t)$ and $\phi_{10}(t)$, respectively. Assuming homodyne detection and perfect phase lock, the beat frequency ($w_s(t) - w_{10}(t) = 0$) and so ($\phi_s(t) - \phi_{10}(t) = 0$), thus after coupling and detection the intensity can be written as

$$I_s = \eta_e \left| \int_A A_s A_{10} \exp[\chi(\mathbf{r}) + j\varphi_s(\mathbf{r})] d\mathbf{r} \right| \quad (2.115)$$

where η_e is the quantum efficiency. After taking a time average, the average signal power can be written as

$$\overline{I_s^2} = \frac{1}{2} \left(\eta_e \frac{\pi}{4} D^2 A_s A_{10} \right)^2 \alpha_T^2. \quad (2.116)$$

In Eq. (2.116), the term $(\pi D^2/4)$ results from the aperture integration, and α_T represents the total fading intensity due to scintillation and phase aberrations, which can be expressed as

$$\alpha_T^2 = \left| \left(\frac{\pi D^2}{4} \right)^{-1} \int_A \exp[\chi(\mathbf{r}) + j\varphi_s(\mathbf{r})] d\mathbf{r} \right|^2, \quad (2.117)$$

Hence Eq. (2.116) can be equivalently written in function of the unperturbed mean signal power $\overline{I_z^2}$, given by the geometric Lens-to-fiber coupling, affected by the fading term as

$$\overline{I_s^2} = \overline{I_z^2} \alpha_T^2 \quad (2.118)$$

Equation (2.117) can also be decomposed in terms of its real and imaginary terms as $\alpha_T^2 = \alpha_r^2 + \alpha_i^2$, where

$$\alpha_r = \left(\frac{\pi D^2}{4}\right)^{-1} \int_A \exp[\chi(\mathbf{r})] \cos[\varphi_s(\mathbf{r})] d\mathbf{r} \quad (2.119)$$

$$\alpha_i = \left(\frac{\pi D^2}{4}\right)^{-1} \int_A \exp[\chi(\mathbf{r})] \sin[\varphi_s(\mathbf{r})] d\mathbf{r}. \quad (2.120)$$

The terms α_r and α_i are integrals of the optical field affected in amplitude and phase over the aperture. Considering that the field aperture can be represented as a sum of M statistically independent coherent patches of average size r_0 , and assuming a large number of cells $M \gg 1$ (expected in strong turbulence), the joint probability distribution of the real and imaginary part of the field can be modeled following circular Gaussian statistics as

$$P_{\alpha_T^2}(\alpha_T^2) = \frac{1}{2\pi\sigma_r\sigma_i} \exp\left[-\frac{(\alpha_r - \bar{\alpha}_r)^2}{2\sigma_r^2}\right] \left[-\frac{(\alpha_i - \bar{\alpha}_i)^2}{2\sigma_i^2}\right] \quad (2.121)$$

where $\sigma_{r,i}^2$ and $\bar{\alpha}_{r,i}$ are the variances and mean of the $\alpha_{r,i}$ that can be calculated as [4]

$$\bar{\alpha}_r = \exp\left(-\frac{1}{2}\sigma_\chi^2\right) \exp\left(-\frac{1}{2}\sigma_\varphi^2\right), \quad (2.122)$$

$$\bar{\alpha}_i = 0, \quad (2.123)$$

$$\sigma_r^2 = \frac{1}{2M} \left[1 + \exp(-2\sigma_\varphi^2) - 2\exp(-\sigma_\chi^2) \exp(-\sigma_\varphi^2)\right], \quad (2.124)$$

$$\sigma_i^2 = \frac{1}{2M} \left[1 - \exp(-2\sigma_\varphi^2)\right] \quad (2.125)$$

where σ_φ^2 is the wave-front phase variance that can be calculated with the phase piston-removed residual error Δ_1 , defined by [64] as

$$\sigma_\varphi^2 = \Delta_1 = 1.0333 \left(\frac{D}{r_0}\right)^{5/3} \quad (2.126)$$

In Eq. (2.126), the coherence width r_0 is calculated with Eq. (2.20). Following the same approach for the evaluation of the η_e after modal compensation, introduced in Sec. 2.3.4.1, the σ_φ^2 can be approximated for higher order wave-front compensation with Eq. (2.111). The calculation of the log-amplitude variance σ_χ^2 can be carried out as [87]

$$\sigma_\chi^2 = 0.5631k^{7/6} \int_0^L C_n^2(z)(L-z)^{5/6} \zeta^{5/6} dz \quad (2.127)$$

following the terminology presented in Sec. 2.1.2-2.1.3.1. The size ratio between the long-term field coherence and aperture can be used to determine the number of coherent speckles in the aperture as

$$M = \left[\frac{1}{S} \int_A C(\mathbf{r}) d\mathbf{r}\right]^{-1} \quad (2.128)$$

where $S = \int_A d\mathbf{r} = (\pi D^2/4)$, and $C(\mathbf{r})$ represents the degree of coherence over the aperture presented in Eq. (2.16). Assuming phase aberration as the dominant phenomena in the phase structure function $D(\rho, L) \rightarrow$

$D_S(\rho, L)$, Eq. (2.17), and following the assumption of large number of coherent cells within the aperture, the approximation in Eq. (2.23) can be used resulting in

$$C(\mathbf{r}) = \exp \left[-\frac{1}{2} 6.88 \left(\frac{\mathbf{r}}{r_0} \right)^{5/3} \right] \quad (2.129)$$

leading to the general expression

$$M = \left[1.09 \left(\frac{r_0}{D} \right)^2 \Gamma \left[\frac{6}{5}, 1.08 \left(\frac{D}{r_0} \right)^{5/3} \right] \right]^{-1} \quad (2.130)$$

where $\Gamma(s, x)$ is the lower incomplete gamma function. In agreement with [4], Equation (2.130) converges to $M \approx (D/r_0)^2$ independent cells of diameter r_0 . Finally, the author [86] concludes that Eq. (2.121) can be expressed in function of a constant coherent term α_r with amplitude $\bar{\alpha}_r$, and a random incoherent term α_i with zero mean and variance σ_i^2 , characterized as a Rice probability density function [4]

$$P_{\alpha_r^2}(\alpha_r^2) = \frac{1}{2\sigma^2} \exp \left[-\frac{\alpha_r^2 + a^2}{2\sigma^2} \right] I_0 \left(\frac{a\alpha_r}{\sigma^2} \right) \quad (2.131)$$

where $a^2 = \bar{\alpha}_r^2$ and $2\sigma^2 = \sigma_i^2$. With the Eq. (2.131) the probability distribution of the fading intensity can be calculated.

2.4 Conclusion of the chapter

Earth observations satellites collect massive amounts of information that require downloading in the limited time of the satellite pass. Only laser links can efficiently cope with the bandwidth demand, but atmospheric turbulence limits the possibility of high throughput data transmissions, especially in scenarios like low-elevations LEO downlinks where the strength of scintillation and phase distortion dramatically increases. Establishing a robust laser link under such conditions is important because most of the flying time of LEO satellite occurs below 30 degrees.

The communications systems and modulation formats employed in FSOC are the same as those used in terrestrial fibered networks. The difference is localized in the free-space channel which, affected by the turbulence, induces random amplitude and phase fluctuations in the received communication signal. Up to 10 Gbps direct detection is the preferred technology due to its simplicity, but highly scintillated fields strongly impact on its performance. To increase the spectral efficiency and allow even higher throughput, coherent modulation formats are being investigated, where BPSK and QPSK represent the new trend. Single-mode fiber coupling is a must to employ coherent receivers, amplifiers, and achieve multi-gigabit data transmissions, but to obtain a stable power coupling, the distorted beam wave-front must be compensated. The FSOC community has focused on adaptive optics solutions, since a long time employed in astronomy, to improve the quality of the received beam. The next chapter presents and discusses these systems in the framework of laser communications.

Chapter 3

ADAPTIVE OPTICS SYSTEMS

ONE of the main challenges in FSOC, is the compensation of the turbulence-induced wave-front distortions that deteriorate the quality of the received signal. Lasercoms targeting very high throughput and seeking to implement coherent communications systems need to couple the received beam into a single-mode fiber efficiently. Laser downlinks from LEO satellites experience strong wave-front distortions, particularly at low elevations, making extremely difficult and certainly inefficient the fiber coupling. Adaptive optics enhance the temporal and spatial coherence of the field by mitigating the consequences of atmospheric turbulence [43–45]. However, existing AO systems experience different limitations under strong turbulence.

This chapter presents different adaptive optics systems from the perspective of free-space optical communications, focusing on satellite-to-ground links. The most popular direct and indirect AO compensation methods are explained, highlighting their strengths and limitations within the FSOC framework. The chapter concludes with the arguments that motivate the proposal of a new AO method.

3.1 Adaptive optics

The previous sections have established the impact of the turbulence in a laser beam wave-front, and highlighted the associated performance deterioration of the data communication link. Adaptive optics (AO) is a technology employed to correct the high order phase wave-front aberrations, which is the dominant atmospheric effect impairing the communication link. Following the scheme presented in Fig. (2.9), here Fig. 3.1 shows the received beam $\mathbf{P}(\mathbf{r})$ affected in amplitude $A(\mathbf{r})$ and phase $\varphi(\mathbf{r})$, being received by the telescope and guided to the AO systems where, after wave-front correction and fiber coupling, results in a temporal varying optical signal $E_{RX}(t)$ sent to the demodulation stages. As the Taylor's frozen turbulence hypothesis considers a static field within its coherence time, see Sec. 2.1.3.2, the temporal variable of \mathbf{P} is generally omitted.

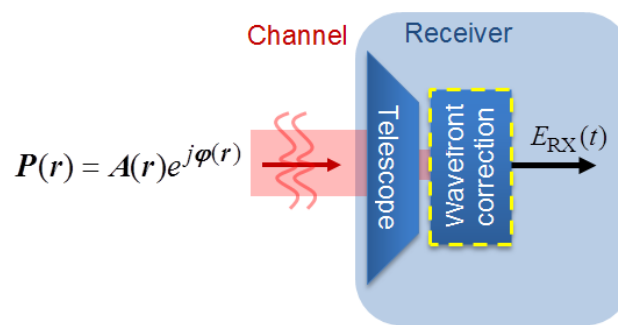


Fig. 3.1: The received beam is captured with the telescope and guided to the AO system, which corrects the high order phase distortions and couples the light into a SMF fiber. The resultant optical signal represents the modulated signal.

The main tasks of an AO system are to measure the phase distortions of the received wave-front and then cancel these out by applying compensating aberrations [88]. Phase wave-front aberrations cannot be measured directly; instead, they are estimated through intensity measurements acquired in the aperture or the focal plane. Adopted AO systems in FSOC are a heritage of astronomy, and thus they follow the same designs and concepts [73].

The general design is shown in Fig. 3.2. A distorted beam $\mathbf{P}(\mathbf{r})$ is partially captured by the telescope aperture and guided first to a tip-tilt system (not present in the setup), where a tip-tilt mirror (TTM) corrects the beam angle of incidence. Then, the beam is reflected in a deformable mirror (DM) that corrects the higher order phase distortions $\varphi(\mathbf{r})$ by shaping a thin reflective membrane, mirroring the phase wave-front. To discover the membrane shape, the reflected beam is split and guided to a wave-front sensor (WFS) and an optical fiber and detector. The wave-front sensor performs intensity measurements, which are processed to approximate the beam phase. Amplitude distortions of the beam cannot be corrected with this system, which must run a dedicated algorithm in closed-loop trying to maintain the phase-only correction dynamically.

The essential components of an AO system are the tip-tilt mirror, the deformable mirror, and the wave-front sensor. The wave-front sensors can be broadly classified within two families, i.e direct and indirect WFS. The following sections offer an inside to the relevant AO hardware, sensors, and methods.

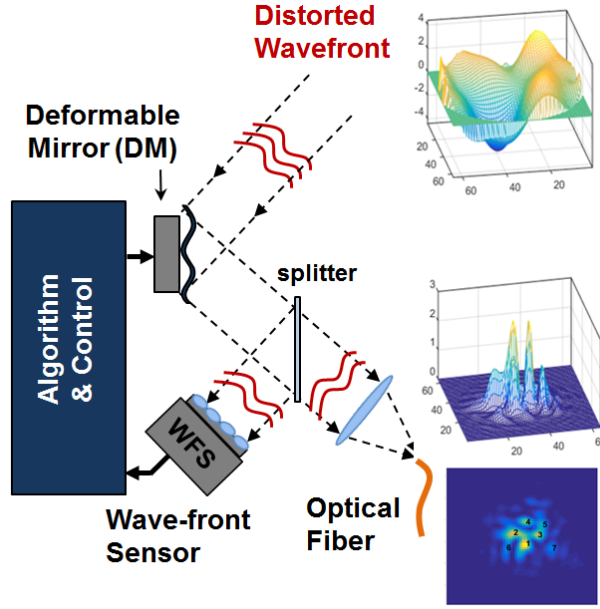


Fig. 3.2: Typical adaptive optic setup with the principal hardware components. The tilt stage is not shown.

3.1.1 Tip-tilt mirror

A fast steering mirror is used in the AO system to compensate for the phase tilt due to the beam angle of incidence. This TTM is essential to maintain the focused beam within the detector area, particularly critical in fiber-based receivers. In an FSOC system, this type of mirror is operated in a closed loop to improve the fiber coupling efficiency and compensate for residual tilts and/or vibrations of the system.

Regarding the overall phase compensation due to turbulence, the TTM delivers the initial and higher improvement in signal power as the tilt deviation represents up to 80% of the power loss. In the modal representation of the wave-front, described in Sec. 2.1.4 and Eq. (4.47), the tilt correction implies the compensation of the Zernike modes 2 and 3. The coupling gain due to tilt correction is evident in Fig. 2.20 due to centroid compensation. Naturally, the stronger the turbulence, the minor the improvement as the focal energy disperses more (larger speckle pattern) and less power is contained on each intensity spot. The TTM is selected based on its resonance frequency, which limits the closed-loop bandwidth, and on its maximum angular deflection φ_{tm} [rad]. The maximum atmospheric tilt that the mirror should be able to remove is

$$\varphi_{tm} = \pm 2.525\sigma_{tl}, \quad (3.1)$$

where σ_{tl} [rad] is the standard deviation of the atmospheric tilt, calculated as [73]

$$\sigma_{tl} = \sqrt{0.184 \left(\frac{D}{r_0}\right)^{5/3} \left(\frac{\lambda}{r_0}\right)^2} \quad (3.2)$$

In Eq. (3.2), the normalized aperture D/r_0 is defined by the telescope aperture diameter D and the Fried parameter r_0 , Eq. (2.20), and λ is the wavelength of the laser. Considering that the motion of the mirror implies twice the angular tilt of the reflected beam, the minimum stroke required for the TTM is $\varphi_{tm}/2$.

3.1.2 Deformable mirror

A deformable mirror is a micromechanical device that introduces a spatial phase-only modulation on the beam wave-front. It is used in laser downlinks to compensate the residual phase distortion after beam tilt correction, or to perform beam pre-distortion in laser uplinks. As shown in Fig. 3.3, when a distorted phase wave-front $\varphi(\mathbf{r})$ is reflected in the DM, which is shaped with $\hat{\varphi}(\mathbf{r})$, the residual phase variance σ_{res}^2 of the compensated phase $\varphi_c(\mathbf{r})$ can be expressed as

$$\sigma_{\text{res}}^2 = \frac{1}{\pi} \int (\varphi(\mathbf{r}) - \hat{\varphi}(\mathbf{r}))^2 d\mathbf{r} = \frac{1}{\pi} \int (\varphi_c(\mathbf{r}))^2 d\mathbf{r} \quad (3.3)$$

The modal representation of the wave-front, presented in Sec. 2.1.4 and Eq. (4.35), can be used to describe $\hat{\varphi}(\mathbf{r})$ as the summation of M Zernike polynomials

$$\hat{\varphi}(\mathbf{r}) = \sum_{l=0}^M (c_l \mathbf{Z}_l(r, \psi)). \quad (3.4)$$

Indeed, the modal correction technique implies finding the right Zernike coefficients that approximate $\varphi(\mathbf{r})$ by shaping the DM at a whole with different modes. Assuming an ideal DM, meaning that the DM can represent the combined set of modes shapes and excursions with high accuracy, then the residual phase variance can be calculated as in Eq. (2.111)

$$\sigma_{\text{res}}^2 \approx 0.2944m^{-\sqrt{3}/2} \left(\frac{D}{r_0}\right)^{5/3} \quad m > 21 \quad (3.5)$$

where the values of the first 21 residual errors Δ_m are listed in [64].

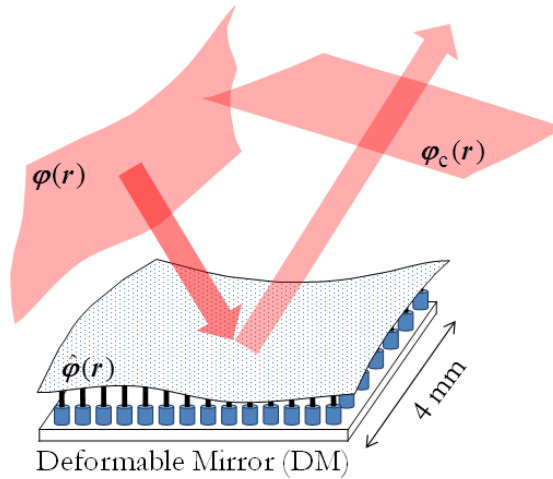


Fig. 3.3: Representation of a DM compensating a distorted phase wave-front.

In practice, a DM has physical limitations to represent the desired shape. There are many designs for different purposes, mostly oriented to astronomical applications [89]. The most widely adopted technology for FSO is the membrane-based microelectromechanical systems (MEMS). These mirrors have a high actuator count and high bandwidth. Higher actuator counts allow a better representation of the intended phase shape. A MEMS-based DM typically deflect the membrane in a range between $1.5 \mu\text{m}$ and $5 \mu\text{m}$ and, depending on the membrane

deflection technology, some DM's have several Kilohertz bandwidths. Deformable mirrors having at least 2 KHz bandwidth are of interest in FSOC applications as they may be able to deal with the time constraints due to the small τ_0 of the fields.

Within the family of MEMS-DMs, the ones based on electrostatic membrane deflection allows very high bandwidths. The working principle of this kind of DM is based on the electrostatic attraction of a grounded double cantilever flexure. As shown in Fig. 3.4, the actuators are distributed in a square grid structure with underneath localized electrodes. The reflective membrane is attached to the center of each actuator by posts, which translate the motion to the mirror [90,91]. An example of a DM using this technology is the BMC-144 of Boston Micromachines. Alternatively, a segmented DM replaces the membrane by individual mirrors on each actuator. High order diffraction is expected due to the individual segments along with the inter-segment spacing, which acts as a finite extent diffraction grating [92]. This effect is particularly unwanted with high power lasers. The principal benefit of segmented mirrors is the very high actuator number and their very high bandwidth ($\approx 120\text{KHz}$); a required property for iterative AO solutions [38,93].

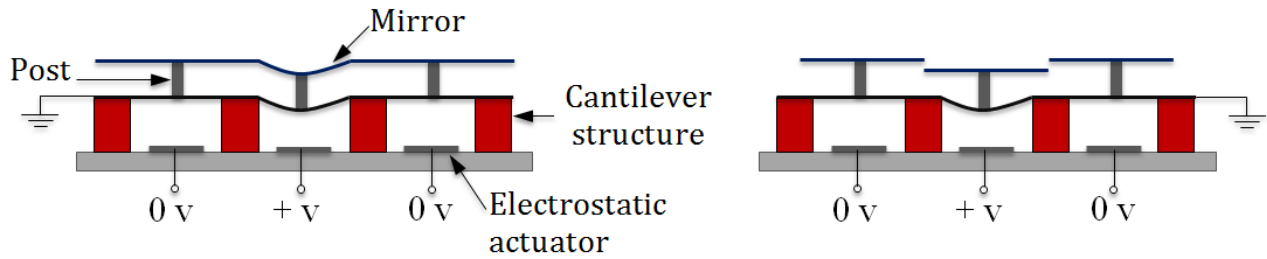


Fig. 3.4: Working principle of the Boston Micromachines membrane-based and segmented DM. Square plates are connected to a negative potential and experience electrostatic attraction to the bottom positive electrodes. The displacement deflects the attached reflective membrane or the individual reflective segments.

The DM is first selected based on the maximum surface stroke δ_{DM} , which can be calculated in function of the normalized aperture D/r_0 as [94],

$$\delta_{\text{DM}} = \pm 2.5 \frac{\lambda}{2\pi} \sqrt{l} \left(\frac{D}{r_0} \right)^{5/6}, \quad (3.6)$$

where $l = 1.03$ if the DM needs to correct the full aberration and tilt, or $l = 0.134$ if the tilt is already compensated. Note that the required peak-to-valley DM stroke at the center of the pupil is equal to $2\delta_{\text{DM}}$ [94]. As previously mentioned, the DM bandwidth can be ruffly rounded as $B_{\text{DM}} = 1/\tau_0$ with τ_0 defined in Eq. (2.26).

The overall expected compensation error is represented by the residual phase variance σ_{res}^2 approximated by the fitting error σ_{fit}^2 , due to the limited number of actuators N_d , plus the temporal error σ_{t}^2 due to limited bandwidth

$$\sigma_{\text{res}}^2 = \sigma_{\text{fit}}^2 + \sigma_{\text{t}}^2 = k_d \left(\frac{D}{r_0} \right)^{5/3} N_d^{-5/6} + \left(\frac{\tau}{\tau_0} \right)^{5/3}. \quad (3.7)$$

In Eq. (3.7), τ represents the time lag of the AO loop, and k_d is a factor depending on the type of DM, which takes the value 0.23 for segmented mirrors and 0.35 for continuous membrane DMs.

It is important also to mention the problem of phase singularities or branch points (BP), which are dislocations of the phase wave-front that occur when the amplitude of the field drops to zero. At this point, the real and

imaginary part of the field are non-defined, thus the phase is also undefined. The origin of phase singularities was studied by Fried and Vaughn [95]. The density of turbulence-induced phase dislocations, associated with different turbulent regimes, was studied by [96] defining four regions with different growth rate and distributions. The impact of BP on adaptive optics systems was studied by [97, 98].

Branch points appear in pairs of opposite sign, connected by branch cuts (wave dislocations) along with the phase undergoes a 2π jump. Figure 3.5 shows a section of a phase wave-front with 2 BP, highlighting the branch cut and abrupt phase jump. These phenomenon is typical in scenarios of strong turbulence, which is expected in laser downlink at low elevation angles.

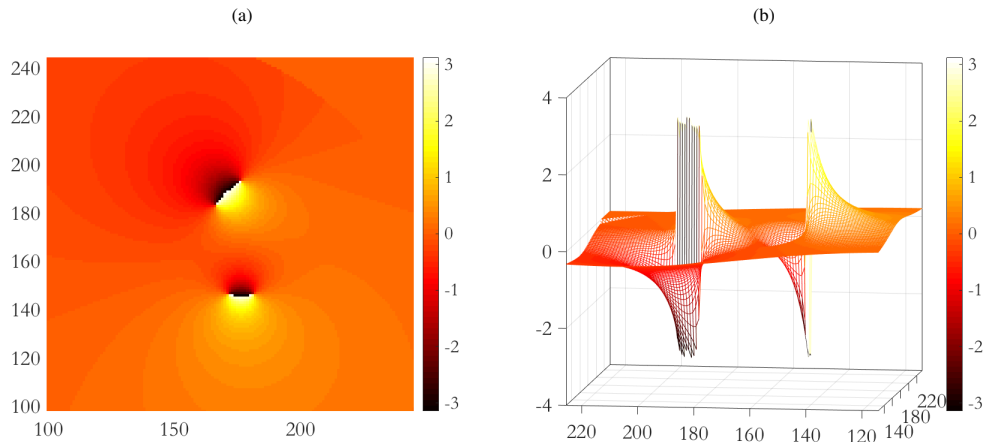


Fig. 3.5: (a) Branch points in the phase wave-front. (b) 3D view of the branch cut phase jump between branch points.

The impact on deformable mirrors was investigated by Baranova [99] and concluded that these BP cannot be corrected with membrane-based DMs, as the membrane has limited deflection properties and cannot mimic the abrupt phase jump. Instead, segmented DMs can represent the phase dislocation and address this issue, provided the detection of the BP position. The problem of BP is also a limiting factor for some wave-front sensors.

3.1.3 Wave-front sensing methods

Wave-front sensing methods can be broadly classified as direct (deterministic) and indirect (iterative), following the AO scheme presented Fig. 3.2. In this scheme the phase wave-front can be estimated through intensity measurements performed either in the pupil plane or focal plane of the optical system, requiring one or many iterations with the consequent post-processing and DM shaping to compensate the distorted field. Free-space optical communication imposes some unique conditions to the standard AO techniques. Wave-front sensors need to deal with:

- Very strong phase distortions due to the long optical path at lower link elevations
- Strong intensity fluctuations at lower elevations due to accumulative atmospheric effects
- Phase singularities that seriously affect some types of WFSs and may limit the use of membrane-based DMs

Detailing the vast variety of techniques is out of the scope of this thesis. Table 3.1 list some relevant AO sensing techniques and only a brief conceptual overview will be given. A detailed analysis of the different WFS for FSOC applications can be found in [33]. Here, more emphasis is given to the Shack-Hartmann WFS and the stochastic sensor-less technique as these two methods have attracted the most interest within the FSOC scientific and commercial community.

Indirect Method		Direct Methods	
Iterative techniques	Speckle Imaging Techniques	Geometric Optics	Interferometric Methods
Wave-front sensor- less	Speckle interferometry	Shack-Hartmann	Point-Diffraction
Image sharpening	Fourier phase techniques	Curvature sensor	Interferometer
Phase retrieval	(Knox-Thompson & Bispectrum)	Pyramid Sensor	Common Path
Phase diversity			Interferometer

Table 3.1: Classification of wave-front sensor types.

3.2 Direct methods

Direct methods are based on the wave-front conjugation principle, which merely means the equalization of the residual phase after DM compensation. These methods rely on wave-front sensors that profile the phase wave-front in one loop iteration. Here, the intensity information is acquired in a single step and then it is delivered to the feedback algorithm to approximate the phase shape, generating the control signal to drive the DM, thus, closing the loop. The process must be performed within the coherence time of the field τ_0 and then repeated in order to follow the evolution of the field. Consequently, these methods require loop bandwidths in the order of a couple of kilohertz to maintain the correction dynamically. Note that the AO loop bandwidth involves all times lag of the system, namely signal acquisition, signal processing, and hardware control.

The control of the deformable mirror follows a simple concept [73]. Every DM has a set of control commands (voltages) X_d to deflect the membrane. From the wave-front sensor and algorithm, an approximated phase φ_d is obtained. Both are linked with an interaction matrix M_d as

$$\varphi_d = M_d X_d. \quad (3.8)$$

The M_d is obtained through a calibration process. The control commands to drive the DM are calculated from the predetermined phase as

$$X_d = M_d^{-1} \varphi_d \quad (3.9)$$

where the M_d^{-1} is the pseudo-inverse calculated by performing the single value decomposition of M_d as

$$M_d^{-1} = VS^{-1}U^T \quad (3.10)$$

Direct methods heavily rely on the type of wave-front sensor (WFS). There is a multitude of designs [33, 73], like Shack-Hartmann (SH), curvature sensor (CS), interferometer sensors (SI), pyramid sensor (PS), etc. In

the field of FSOC, the most popular is the Shack-Hartmann wave-front sensor (SHWFS). This sensor has been used for many years in AO systems for astronomy, leading to a very mature technology. Let's first focus on the SHWFS and then briefly overview the other direct methods listed in table. 3.1.

3.2.1 Shack-Hartmann sensor

The working principle of SHWFS involves the spatial sampling of the distorted wavefront with a grid of small lenslets or sub-apertures. Each sub-aperture captures only a small portion of the whole wave-front and produces a focal spot in a CCD sensor located in the image plane. A square grid larger than 4x4 CCD pixels (even 2x2 in Quad cell for low readout noise) is assigned to each sub-aperture; thus the spot displacement can be measured. A non-tilted flat phase produces a focal spot in the center of each grid. Instead, with a distorted phase, some sub-apertures capture a tilted portion of the phase-front and thus the focal spot shows a displacement $\Delta_{x,y}$. The result is a grid of randomly located focal spots over the CCD sensor. Figure 3.6 depicts the process.

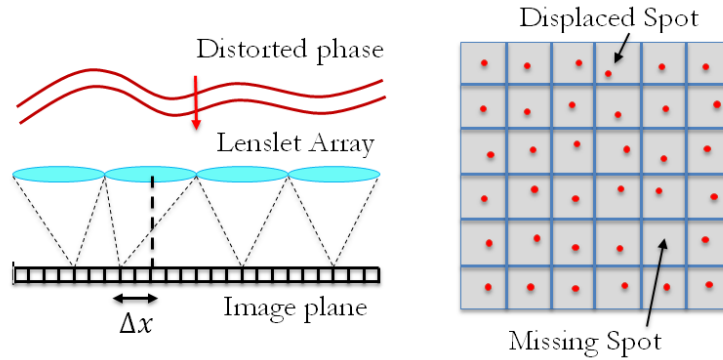


Fig. 3.6: Working principle of the Shack-Hartmann wave-front sensor. An array of small lenses capture a portion of the distorted wave-front, which get focused at different positions in the image plane. Each focal displacement in X-Y can be translated into a phase slope at the lenslet position. All the phase slopes are used to approximate the overall wave-front phase.

The displacement of each focal spot is proportional to the averaged gradient of the phase $\varphi(x, y)$ in the associated sub-aperture. In Fig. 3.6, the displacement Δ_x is calculated as

$$\Delta_x = \frac{\lambda}{2\pi A_s} \int_{A_s} \frac{\partial \varphi(x, y)}{\partial x} dx, \quad (3.11)$$

where A_s is the sub-aperture area. A general description can be written as [100],

$$s = \frac{\int d\vec{r} W(\vec{r}) I(\vec{r}) \nabla \varphi(\vec{r})}{\int d\vec{r} W(\vec{r}) I(\vec{r})}, \quad (3.12)$$

where s is the gradient measurement proportional to the centroid in the detector, $W(\vec{r})$ describes the extent of the sub-aperture, $I(\vec{r})$ is the intensity over the sub-aperture that acts as weighting factor and has more impact in scenarios of strong turbulence, $\nabla \varphi(\vec{r})$ is the gradient of the phase, and $\vec{r} = (x, y)$. The gradient measurements are related to the phase values of the wavefront φ as [31]

$$s = A\varphi, \quad (3.13)$$

where A is a geometry matrix that relates φ with the slopes. Coordinates are avoided for mathematical simplification. Then, the least square reconstruction is carried out as

$$\varphi_{\text{lse}} = \left((A^T A)^{-1} A^T \right) s, \quad (3.14)$$

where φ_{lse} is the reconstructed phase, and A^T is the transpose of A . The truth of the matter is that the least square reconstructor only accounts for the continuous phase. Under strong turbulence conditions there is also a hidden phase φ_{hid} associated with phase discontinuities [30], hence

$$\nabla \varphi = \nabla \varphi_{\text{lse}} + \nabla \varphi_{\text{hid}}. \quad (3.15)$$

In Eq. (3.15), the hidden phase gradient is equal to the curl of the vector potential $H(\vec{r})$ as,

$$\nabla \varphi_{\text{hid}} = \nabla \times H(\vec{r}). \quad (3.16)$$

Under weak turbulence, the SHWFS experiences minimum phase discontinuities showing high efficiency in the wave-front compensation with minimum impact of the φ_{hid} . With strong turbulence φ_{hid} becomes relevant. Since the SHWFS working principle is based on the gradient of the phase, and because the gradient of a rotational field is zero, the hidden phase cannot be directly measured. Consequently, with strong turbulence, the $\nabla \varphi$ is wrongly approximated and the SHWFS performance degrades.

Limitations of Sack-Hartmann sensor

A wave-front conjugation method is based on the reciprocity principle [101], which requires the compensation of the complex amplitude of the field by its weighted conjugated. The phase-only compensation performed with a DM, ignores the amplitude correction. If the amplitude modulation is small, which is frequent in Astronomy, the impact is not severe [38]. This is not the case of free-space optical communications because at lower elevations (from 7° to 30°) long optical paths induce strong intensity modulation (scintillation) and phase dislocations (branch points). Both phenomena seriously degrade the performance of this type of WFS.

Scintillation affects SHWFS because of non-uniform or poor illumination of the sub-apertures. This leads to the reduction of the sensor SNR and wrong slope calculation in the poorly illuminated subapertures, and the impossibility of retrieving information from those non-illuminated ones. This affects the phase reconstruction. Note in Eq. (3.12) that weak scintillation, thus, uniform illumination $I(\vec{r})$ in the sub-aperture, results in the gradient tilt (G-tilt). Under strong turbulence and more scintillation, the SH measurement is the average of the intensity-weighted gradient across a sub-aperture. This is proportional to the displacement of the image centroid, so-called centroid tilt (C-tilt). The difference between both tilts strongly affects the wavefront reconstruction [100].

The intensity sensitivity is determined by the camera noise. There is a drastic error increment in the phase slope estimation when the spot intensity nears the level of the sensor noise. This problem can be addressed with thresholding that eliminates spots in poorly illuminated lenslets. The threshold can be established when the wavefront error is greater than $\lambda/10$ [102].

Subaperture overfill is associated with pixel saturation, which leads to errors in the wave-front estimation. As the intensity increases, more pixels result illuminated and saturate. The spot increases in area and eventually invades neighboring subapertures. This overlap leads to invalid wave-front estimations [102]. This problem worsens when spots are represented with fewer pixels, as they saturate rapidly. The use of more pixels per lenslet naturally increases the post-processing requirements but reduces the saturation problem.

Overcoming these considerations require costly technical effort when it comes to scenarios like LEO down-links, which exposes the WFS to different levels of scintillation or irradiance dynamics.

3.2.2 Curvature Sensor

The curvature sensor was proposed by Roddier [35] and, while SHWFS is based on the first derivative of the phase (slope of the phase), the curvature sensor uses the second derivative (curvature of the phase). To do so, as shown in Fig. 3.7, this sensor measures the intra-focal intensity distribution $I_1(\mathbf{r})$ before the focal plane at the position P1, and the extra-focal intensity distribution $I_2(\mathbf{r})$ after the focal plane at the position P2. Then, it calculates the normalized difference between both intensities.

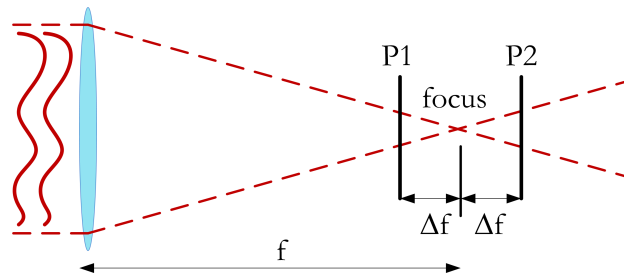


Fig. 3.7: Curvature wave-front sensor working principle.

$$\frac{I_2(\mathbf{r}) - I_1(\mathbf{r})}{I_2(\mathbf{r}) + I_1(\mathbf{r})} = \frac{f(f - \Delta f)}{2\Delta f} \left[\frac{\partial}{\partial(\mathbf{n})} \varphi \left(\frac{f}{\Delta f} \mathbf{r} \right) \delta_c + \nabla^2 \varphi \left(\frac{f}{\Delta f} \mathbf{r} \right) \right] \quad (3.17)$$

where δ_c is a linear impulse distribution around the pupil edge weighted by the wave-front radial tilt $\frac{\partial}{\partial(\mathbf{n})}$ and $\nabla^2 \varphi$ is the wave-front curvature. Through this equation, the sensor provides all the information required for the wave-front reconstruction.

The performance of this sensor is limited by the separation between measurement planes that needs to be sufficiently large to resolve the intensity pattern, leading to high resolution requirements. Meaning that this sensor may face problems for sensing high-order aberrations. Also, like Shack-Hartmann, this sensor cannot detect phase singularities leading to wrong phase estimation in scenarios of strong turbulence [33, 88, 103]. In addition, the curvature sensor does not perform well in strong scintillation, and requires linear or nonlinear algorithms to reconstruct the wave-front from the defocused images.

3.2.3 Pyramid Sensor

The Pyramid wave-front sensor is a pupil plane sensor that uses a pyramidal prism in the image plane and a relay lens after the prism, to create four sub-beams and form four images of the pupil on a detector array. The

intensity of each sub-beam ($I_{0,0}(\mathbf{r}) > I_{0,1}(\mathbf{r}) > I_{1,0}(\mathbf{r}) > I_{1,1}(\mathbf{r})$), at the position \mathbf{r} in the detector plane, varies with the local tilt and it is used to find the correspondent (x, y) wave-front slope.

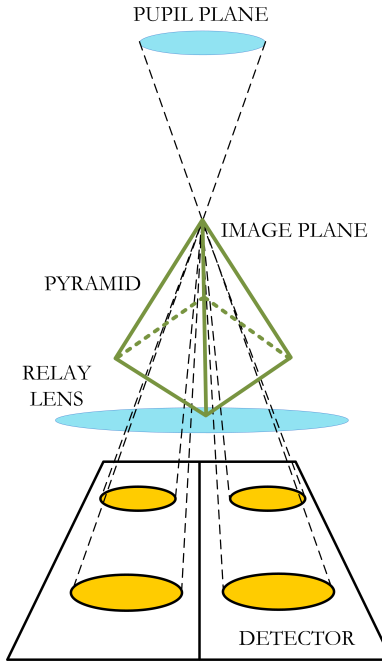


Fig. 3.8: Pyramid wave-front sensor working principle.

$$S_x(\mathbf{r}) = \frac{I_{0,0}(\mathbf{r}) - I_{1,0}(\mathbf{r}) + I_{0,1}(\mathbf{r}) - I_{1,1}(\mathbf{r})}{I_t} \quad (3.18)$$

$$S_y(\mathbf{r}) = \frac{I_{0,0}(\mathbf{r}) + I_{1,0}(\mathbf{r}) - I_{0,1}(\mathbf{r}) - I_{1,1}(\mathbf{r})}{I_t} \quad (3.19)$$

where I_t is the mean intensity over the detector. The spatial resolution of this sensor is given by the size of the detector pixel, while SHWFS relies on the lenslet size. Hence, it offers better performance and sensitivity.

On the other hand, the pyramid sensor works only for low order aberrations, and the sub-micron accuracy of the prism makes manufacturing difficult and costly [104].

3.2.4 Interferometric sensor

The interferometric wave-front sensor follows a similar principle to the coherent communication receiver, where a received distorted beam U_S is mix with a reference beam U_L to extract the phase information. As in coherent receivers, the reference beam can be locally generated and locked in phase with the incoming one; this allows high sensitivity in detection but it requires high complexity to deal with highly scintillated fields. A more robust approach split and filter the received beam to create a reference "clean" wave-front to be mix with, and it is known as self-referencing interferometer. There are many different design, namely, Point-diffraction interferometer [33, 105], Common-path interferometer [106], Shearing Interferometer [107]. Figure 3.9 shows the point-diffraction interferometer, which results very intuitive to describe.

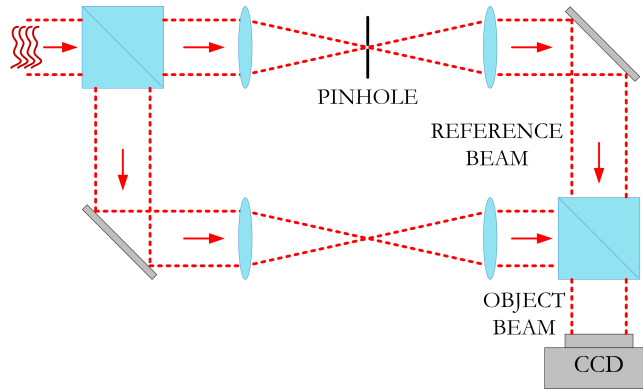


Fig. 3.9: Interferometer wave-front sensor working principle.

As previously said, the beam U_S is split into the object beam (distorted wave) and the reference beam (plane wave). The reference beam is obtained by performing a Fourier spatial filtering with a pinhole, thus blocking all higher order frequency components in the Fourier domain, and allowing the zero-order component to continue as a cleaner matched in frequency signal that resembles a plane wave. With this, frequency lock is not required and both beams interfere producing an interference pattern as $I = |U_S + U_L|^2$, leading to

$$I = I_L + I_S + 2\sqrt{I_L I_S} \cos[(w_S - w_L)t + \varphi_S + \varphi_L] \quad (3.20)$$

where the beat frequency $(w_S - w_L) = 0$, and the terms $I_{S,L}$ form the intensity fringe pattern (provided bias subtraction) from where the distorted phase φ_S can be extracted.

This type of sensors has a field estimation performance that is tolerant of scintillated fields, and invariant against branch points. However, the pin-hole filters most of the power of the reference beam, reducing the system efficiency. Furthermore, in moderate to strong turbulence, the speckled focus reduces the on-axis intensity at the pin-hole position, which lowers the fringe contrast and the SNR and may lead to wrong phase estimations.

3.3 Indirect methods

Indirect methods are technically more simple and do not rely on the use of complex WFS. Instead, they are based on the direct optimization of a system performance metric, like power in the bucket, coupled power, image sharpening, among others.

Sensor-less systems perform the wave-front optimization with several iterations that require continuous sensing of the metric as feedback. Sensor-less systems can be classified into stochastic, and sequential image-based methods [3]. The stochastic approach is generally based on blind algorithms that start the optimization with a random set of variables, applying an iterative approximation of the best solution. The DM shaping can work in a zonal or modal basis. The zonal approach randomly changes the states of single DM actuators in searching for an optimal metric; the modal approach shapes all actuators at once, following an orthogonal modal basis (e.g., Zernike polynomials) [37]. The later converges faster, reducing the number of iterations. Popular algorithms for such task are the Stochastic Parallel Gradient Descent (SPGD) [38, 108], Simulated Annealing [109], Algorithm of Pattern Extraction [110], and Genetic Algorithm [111].

Image-based systems seek to sharpen the image following an iterative DM shaping and image quality control until a quality metric is reached. Acquisition of multiple images is commonly required to perform the optimization and wave-front correction. Some examples are sensor-less systems based on PSF optimization [112], or modal correction which uses a special type of mirror called modal DM (MDM).

Speckle interferometry and Fourier phase spectrum methods are speckle-based techniques that acquire hundred or even thousands of focal images that are contrasted with a reference pattern. With this, the modulus and phase of the Fourier spectrum is estimated and back-transformed to obtain the complex image field.

A particularly interesting method is the optimization of low spatial frequencies [113], based on the acquisition and sharpening of several focal images created with Lukosz modes as predefined DM aberrations. Lukosz modes have the advantage, over Zernike modes, that the effect of the coefficients on the image sharpness is quadratic. Hence, the optimization of each mode can be done with three acquired images by interpolating the result of a quadratic function, which is the rms spot radius [3]. The following sections offer an overview of these techniques.

3.3.1 Sensor-less stochastic technique

The objective of a sensor-less iterative compensation system in FSOC, is to enhance the BER by increasing the mean coupled signal and reducing its variance. A sensor-less AO system has most of the required characteristics for FSOC. Regarding turbulence compensation, it shows robustness facing phase singularities [33, 40], high power efficiency, and good tolerance to scintillation [33]. Also, it compensates for the receiver aberration and shows dynamic adaptation, without any intervention, to a loss of calibration or unexpected events. Regarding technical aspects, these systems have a straight forward implementation and they are very simple to calibrate, making accessible the integration on existing systems. Its mechanical simplicity also implies robustness when it comes to portable optical ground stations. A significant plus comes with the cost reduction in the AO system, due to the absence of WFS.

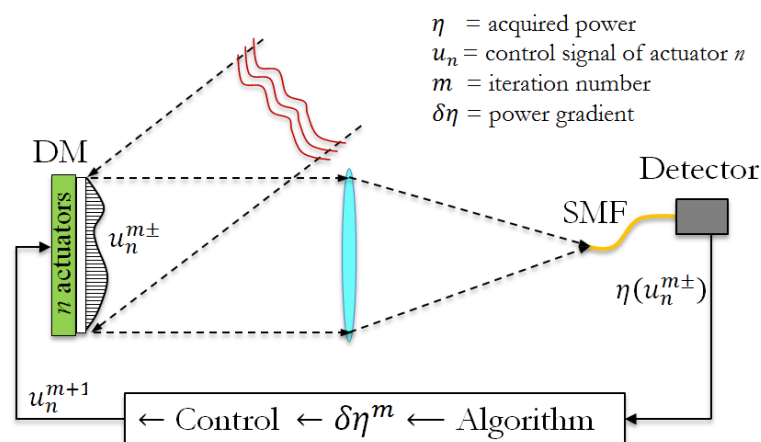


Fig. 3.10: Setup for sensor-less iterative AO system with SPGD blind phase optimization algorithm.

One of the most tested blind algorithms with potential uses in FSOC, is the SPGD [37, 38, 114], see Fig. 3.10. A standard zonal SPGD applies, with each m iteration and through DM control signals v_n , random positive and

negative perturbations $\pm\gamma_n^m \delta v$ to each DM actuator as,

$$\begin{aligned} v_n^{m+} &= v_n^m + \gamma_n^m \cdot \delta v \\ v_n^{m-} &= v_n^m - \gamma_n^m \cdot \delta v \end{aligned} \quad (3.21)$$

where $\gamma = \pm 1$ is a random sign vector, δv is a perturbation parameter chosen empirically, and n is the actuator number. Note that the optimization problem has n dimensions. With each perturbation, a value of the performance metric η (SMF coupling power) is acquired and the gradient is calculated

$$\delta\eta^m = \eta(v_n^{m+}) - \eta(v_n^{m-}). \quad (3.22)$$

With the gradient $\delta\eta^m$, the actuators are updated based on a gain parameter G and the previous state v_n^m as,

$$v_n^{m+1} = v_n^m + G \cdot \delta\eta^m \cdot \gamma_n^m \cdot \delta v \quad (3.23)$$

The parameters G and δv define the rate of convergence and precision in the phase compensation. Large values of gain and perturbation increase the rate of convergence but also induces more signal variance and less precision. Smaller values of these parameters lead to slower convergence but better precision (reach the maximum possible of optimization). For FSOC, precision is not crucial, rather a stable signal enhancement. Nevertheless, the signal variance must be constrained to small η to reduce its impact in the BER. Therefore, a trade-off is necessary.

Modal SPGD iterates over the coefficients of the selected orthogonal basis (i.e. Zernikes), which must be projected into the displacement of the whole set of actuators. The modal approach implies additional computation but accelerates the convergence of the algorithm [37]. A reduction in the total number of iterations per field is essential to cope with the constrained τ_0 . Both approaches need over 100 iterations to reach sufficient signal optimization.

Limitations of SPGD technique

The limiting factor of any iterative approach for FSOC is the correction time, which depends on the total number of required iterations. As shown in Fig. 2.6, typical values for the coherence time of the field ranges between 0.5 and 1.5 milliseconds. Considering that existing solutions need more than 100 iterations to converge to an optimum [37], unpractical loop bandwidths above of 100 kHz are required.

Today's MEMS deformable mirrors run smoothly at 2 kHz and, depending on the working principle and maximum necessary strokes [89,93], some DMs can reach up to 120 kHz [115]. Naturally, such high frame rates can be achieved with tiny actuator excursions, smaller than 0.6 micrometers. Because a stochastic optimization starts with a blind set of actuator states, initial strokes are generally high until reaching optimum positions. A modal stochastic approach accelerates the process, but it still needs large initial strokes and above 100 iterations.

Some researchers have proposed hybrid systems that combine direct and indirect methods, generally using a SH sensor to provide a hot start to the sensor-less system. This reduces the number of iterations by half but increases the system complexity. Also, it may be considered inherited limitations of the WFS under strong scintillation.

3.3.2 Speckle imaging technique

Speckle imaging techniques recover the complex information in the focal plane, through the acquisition of a large number of short-exposure intensity images (speckle pattern) of the object and of a reference star. These images are processed to extract the Fourier spectrum modulus and phase via the use of speckle interferometry and the bispectrum/cross-spectrum methods, respectively. Then, the Fourier modulus and phase are combined and back-transformed to recover the complex focal image. Figure 3.12 shows the processing stages.

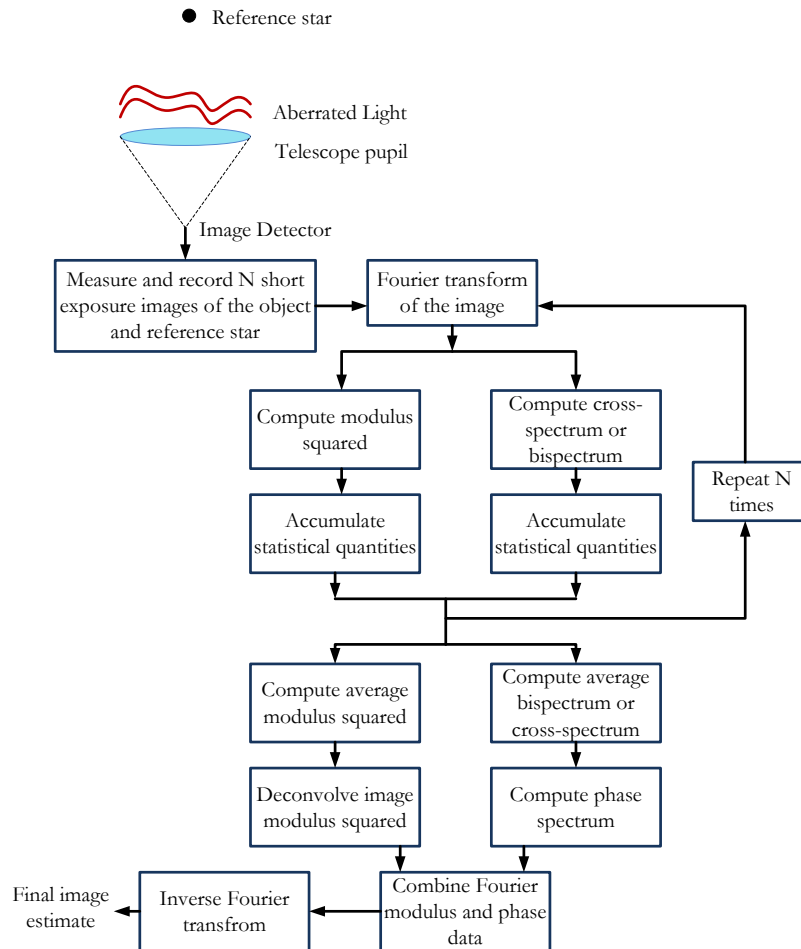


Fig. 3.11: Speckle imaging technique block diagram of principal processing stages.

The working principle is well detailed in the work of [116]. Consider that short-exposure focal images, acquired within the coherence time τ_0 of the field, see Sec. 2.1.3.2, retain high-resolution information of the object. In astronomy, the coherence time rounds 60 milliseconds. The recorded image $I(x)$ (detector plane) of an object $O(x)$ of interest (pupil plane) is the convolution of the object with the point spread function of the atmosphere $P(x)$. Labeyrie first proposed to calculate the Fourier transform of each image $I(x)$, which is just the product of the individual Fourier transforms [117]

$$I_{\text{obj}}(u) = O(u)P(u), \quad (3.24)$$

and do the same with a reference star that, assumed as a point source, can be considered a delta leading to

$$I_{\text{ref}}(u) = P(u). \quad (3.25)$$

Then, Labeyrie suggested to use their respective power spectrums, $|I_{\text{obj}}(u)|^2$ and $|I_{\text{ref}}(u)|^2$, to recover the modulus of the object by calculating the ratio of the ensemble over N images as

$$|O_{\text{obj}}(u)|^2 = \frac{\langle |I_{\text{obj}}(u)|^2 \rangle}{\langle |I_{\text{ref}}(u)|^2 \rangle}. \quad (3.26)$$

To recover the phase, Knox and Thompson proposed the so-called cross-spectrum of the image,

$$\langle I_{\text{obj}}(u)I_{\text{obj}}^*(v) \rangle = |I_{\text{obj}}(u)||I_{\text{obj}}(v)|\exp [j(\theta_{\text{obj}}(u) - \theta_{\text{obj}}(v) + \theta_{\text{PSF}}(u) - \theta_{\text{obj}}(v))] \quad (3.27)$$

where $*$ indicates complex conjugate, θ_{obj} is the phase of the object, and θ_{PSF} are the aberrations introduced by the atmosphere. By using the reference star, the phase difference of the distortions is found

$$\theta_{\text{PSF}}(u) - \theta_{\text{PSF}}(v) = \angle (\langle I_{\text{ref}}(u)I_{\text{ref}}^*(v) \rangle) \quad (3.28)$$

from which the phase difference of the object can be estimated as

$$\theta_{\text{obj}}(u) - \theta_{\text{obj}}(v) = \angle (\langle I_{\text{obj}}(u)I_{\text{obj}}^*(v) \rangle) - \angle (\langle I_{\text{ref}}(u)I_{\text{ref}}^*(v) \rangle) \quad (3.29)$$

The phase at all frequencies can be discovered by repeating iteratively the same process with small changes in the frequency difference $|u - v|$. The bispectrum method follows a similar concept and can be found in [116, 118].

Even though this method can deliver very high resolution imaging, the limitation in FSOC is obvious. Several hundred of images need to be acquired and heavy post processing must be performed to obtain the modulus and phase of the complex image. Infrared cameras cannot acquire that quantity of images within the 2 milliseconds available in satellite downlink applications.

3.3.3 Image sharpening

Image sharpening techniques seek to iteratively sharp the focal image by applying a set of modal changes in the DM. In the particular case of FSOC, a speckled focal intensity pattern deviates from the diffraction limited airy pattern, which occurs in the absence of turbulence. Like in speckle interferometry, several short exposure intensity images need to be acquired within an iterative process until the quality criteria is reached [119]. The acquisition and control of the DM can be performed with different algorithms, e.g. simplex optimization, conjugate gradient search, or multidithering [120–123]

A particularly interesting method is the optimization of low spatial frequencies [113], based on the acquisition and sharpening of several focal images created with Lukosz-Braat (LB) polynomials as predefined DM aberrations [124]. The LB polynomials have the advantage, over Zernike polynomials, that the effect of the coefficients on the image sharpness is quadratic and thus the optimum can be discovered with 3 trials and parabolic optimization. The image sharpness can be quantified with

$$M = \int \int I(x, y)^2 dx dy \quad (3.30)$$

where $I(x, y)$ is the focal image. If the aberrated phase wave-front $\varphi(\mathbf{r})$ is decomposed in terms of weighted Lukosz modes $L_l(\mathbf{r})$ as

$$\varphi(\mathbf{r}) = \sum_{l=1}^N (b_l L_l(\mathbf{r})) \quad (3.31)$$

the coefficients b_l can be found by the sequential modal shape of the DM, where each mode is altered by a positive/negative amount with a predefined step size c . The optimization of each mode can be done with three acquired images by calculating the metric for the unchanged mode M_0 and the altered modes M_+ and M_- , interpolating the result and finding the maximum of the quadratic function [3].

$$b = \frac{c(M_+ - M_-)}{2M_+ - 4M_0 + 2M_-} \quad (3.32)$$

Assuming a distorted wave-front composed of N modes, the sequential optimization would require $2N + 1$ captured images.

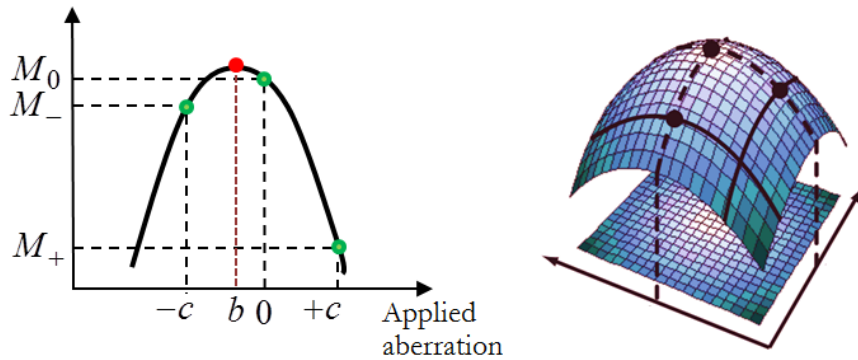


Fig. 3.12: Image sharpening parabolic optimization process [3].

This method reduces the number of DM changes in the iterative process since only 3 trials are needed to optimize each polynomial. However, the process needs several images to correct one aberrated wave-front, which may be not possible in the contained time of FSOC scenarios. Additionally, highly aberrated fields need to consider a larger number of modes, increasing also the number of camera acquisitions. Image-based systems are slow due to limitations in the camera frame rate. Such approaches need to capture several images during the optimization process, and infrared cameras cannot run efficiently above 8 kHz. Hence, the camera becomes the bottleneck regarding the closed loop bandwidth.

3.4 Comparison of AO techniques

To conclude with the discussion of some of the traditional AO techniques that may be used in FSOC, a summary of the relevant characteristics for laser downlinks is shown in Table. 3.2. Details of the analysis can be found in [33]. Some additions, like Speckle imaging and image sharpening have been included. The listed WFS are compared regarding resolution, complexity of wave-front reconstruction and speed, robustness against phase singularities and scintillation, and hardware complexity. The comparison is made with a "+" a "-" and a "o" to indicate a positive, negative, or neutral characteristic in an FSOC downlink.

Wavefront Sensor	Resolution	Complexity of reconstruction / Speed	Robustness to singularities	Sensitivity to scintillation	Hardware Complexity
Shack Hartmann	-	○	-	-	○
Curvature Sensor	○	○	-	-	○
Pyramid Sensor	+	+	○	-	-
Point-diffraction interferometer	+	○	+	○	-
Speckle imaging	+	-	+	○	+
Wave-front sensor-less	-	-	+	○	++
Image sharpening	○	-	+	○	○

Table 3.2: Summary comparison of wave-front sensors characteristics.

Resolution: The resolution is very important in imaging AO, where a clear image of the object is targeted, thus higher spatial resolution of the WFS allows more accuracy in the phase reconstruction. Lasecoms does not require that high quality and AO only needs to sufficiently correct the dominant wave-front aberrations to allow a stable and efficient focusing of the beam energy in the fiber. Here, the SH-WFS can increase the resolution with a densely packed lenslet but at the expense of rising the post-processing requirements. Interferometric methods, the Pyramid sensor, and Speckle imaging perform better but the hardware complexity increases in the first two cases, and several images are needed in the speckle-based technique, unwanted conditions for an AO-FSOC solution.

Reconstruction complexity and speed: This is a key point for FSOC due to the constrained time for correction (1 to 2 milliseconds). Clearly, non-iterative AO solutions vastly overcome their iterative counterparts, which to the date still require too many iterations to converge (> 100), limiting their use in FSOC. To correct a wave-front within 1 millisecond, a closed loop running at 100 KHz would be needed for 100 iterations, which is unpractical.

Robustness to singularities and scintillation: Here the trends are inverted, and the pupil-based AO solutions perform worse than the iterative solutions. Considering that scintillation can be, to some extent, attenuated with aperture averaging, iterative systems outperform other systems. Low illumination over the lens area, also originated due to intensity scintillation, additionally affect pupil-based techniques. Likewise is the impact of phase singularities. Particularly for the SH-WFS, a BP in one or many of the lenslets (expected in low elevation links) would imply a spot focused outside the sensor area and a wrong phase estimation.

Hardware complexity: Here the clear winner is the family of sensor-less AO solutions, as they require no complex WFS. Lasercom also targets a simple system, easy to adjust and calibrate, as many of the OGS are intended to be mobile and ready for on-demand deployment. Complex AO systems are costly and may be a limiting factor from the commercial point of view.

3.5 Conclusion of the chapter

The implementation of spectrally efficient coherent modulation formats in scenarios of LEO downlinks represents a very difficult challenge. This task must consider an efficient single-mode fiber coupling, which can only be achieved after the distorted beam wave-front is compensated. Even though the impact of the scintillation is attenuated with aperture averaging, phase distortions are dominant. The use of standard AO techniques adopting the mature Shack-Hartmann sensing technology is efficient up to a certain degree of turbulence. Its original design is well suited to weak turbulence regimes and, in such scenarios, a Hartmann-based AO system delivers sufficient signal stabilization. Naturally, the incursion into strong turbulence regimes highlights predicted limitations. Other pupil-based techniques may offer better performance in the speed of the wave-front reconstruction, or robustness against phase singularities, at expenses of more hardware complexity, and still being limited by large irradiance dynamics.

In the search for alternatives, and considering that high resolution is not that crucial in FSOC, sensor-less techniques show most of the wanted characteristics of an AO system in FSOC, but suffer from time constraints; the iterative nature of this approach exceeds the expected coherence time of the field (≈ 1 ms). The SPGD is the most promising iterative technique, but still requires a loop bandwidth above 100 kHz, which is technically unpractical.

One can conclude that the set of positive characteristics of sensor-less techniques encourage further research of similar methods capable of reducing the required number of iterations. By doing so, this technology may provide a solution to FSOC under strong turbulence breaching today's gap in high bandwidth laser downlinks. The following sections address the convergence time problem by proposing a new iterative AO approach.

SPECKLE-BASED ADAPTATION

THE adoption of standard adaptive optics systems has been the first logical approach to solve the turbulence problem in satellite-to-earth lasercoms. Naturally, many of these techniques have experienced substantial refinement since their first appearance, being optimized for their original field of application. Most of them were created or proposed to help to visualize celestial objects with higher definition, where the typical scenario involves a telescope located at the top of a mountain, pointing to the clear sky at higher elevations. Consequently, these AO systems deal with more benign turbulence regimes than the ones presents in FSOC.

Recent years have shown many attempts of the FSOC community to use these AO systems to overcome the turbulence constraints. The preferred one has been, without question, the Hartmann-based AO system. Its technological maturity and reasonable hardware complexity has inclined the scientific community, and recently some commercial endeavors, to use this solution towards their goal of providing a stable solution in all turbulent regimes. Under low to moderate turbulence, the adoption of SHWFS for laser communications has proven to successfully correct phase distortions, allowing efficient single-mode fiber coupling and gigabit data rates [43–47]. However, the predicted limitations of this type of solutions become evident entering into strong turbulent regimes, thus most of the successful campaigns have been done at elevations above 30 degrees.

To deal with low elevation laser links, scientist have considered the robustness of sensor-less adaptive optics and focused on its use in lasercoms. This approach has properties very much wanted in FSOC systems, like simplicity, robustness, easy calibration, and metric-oriented optimization. This means that by constant blind optimization of the power coupled in the fiber, the system can dynamically adapt itself to sudden atmospherically-induced changes in the signal. The critical impediment has been, and even though significant progress still is, the high number of iterations (above 100) needed to correct the wave-front. This limitation is linked to the mechanical capabilities of the DM, which would need to reshape at 100 KHz within 1 millisecond.

Consequently, it is of high interest to reduce the number of iterations in iterative solutions while keeping their robustness and simplicity. The previous chapter introduced other indirect techniques like speckle imaging, highlighting that short-exposure speckles posses useful information Fourier-related to the distorted pupil phase. The limitations of such approach is the large number of images that need to be acquired and the heavy processing workload. This limitation is shared by the image sharpening technique, that seeks to sharp the focal PSF optimizing a set of Lukosz modes in a quadratic manner. In the later, the intensity distribution itself is not directly related to the applied polynomials, thus the optimization goes through a large set of modes sequentially. Note that each one of these indirect methods has key strengths but they do not solve the convergence speed problem on their own.

This chapter presents a new modal iterative method that combines some of the properties of the described indirect methods, allowing a substantial reduction in the loop bandwidth utilization during the iterative process. This method uses the individual speckles of a single short-exposure intensity image, assuming that each speckle

can be Fourier related with a plane wave mode in the pupil plane. Each mode can be optimized in a quadratic manner and sequentially combined, improving the focal intensity distribution after each optimization. The optimization process works with the power of the coupled light in the fiber, and reaches convergence with a number of iterations proportional to the number of selected speckles. The proposed technique only needs a single captured image per field, and it allows the in-advance knowledge of the set of modes as well as the number of iterations required, thus it performs a non-blind sequential optimization process. Consequently, the loop bandwidth utilization is reduced, while giving more control over the correction process.

The following sections present an overview of some relevant properties of a short-exposure focal image, regarding the intensity distribution among speckles and the intrinsic limitation for the direct phase recovery. Then, the general mathematical framework is presented and the method is detailed. This chapter concludes with an estimation of the method performance, analyzed numerically under turbulent conditions of a satellite downlink scenario.

4.1 The focal speckle pattern

A speckled image is a random pattern of intensity that originates from the interference of a multitude of wave-fronts of the same frequency, but different amplitudes and phases. A coherent light beam propagating through a turbulent channel must cross through different inhomogeneities of varying size, that results in both amplitude and phase fluctuations of the wave-front entering the lens of the optical receiver. Assuming a photodetector array in the focal plane of the lens, each point in the detector will result from the field contribution of each point in the aperture. Since different parts of the aperture have suffered non-equal amounts of atmospherically induced phase delay, interfering waves with phase differences larger than one wavelength result in random pattern of intensity. Goodman modeled this phenomenon representing the waves as vectors, and presented an intuitive explanation for the speckle formation based on the concept of "random walk" [4]. In Goodman's model a focal speckle arises from the interference of a multitude of independently phase additive complex components in a signal. Each component may have a random length (amplitude) and direction (phase) in the complex plane that, when added together, they constitute a random walk. Depending on their phases, the sum may result in destructive or constructive interference, with the squared length of the resultant being the intensity of the observed wave. Figure 2.2 depicts a random walk of a light ray propagating from the laser source to the detector.

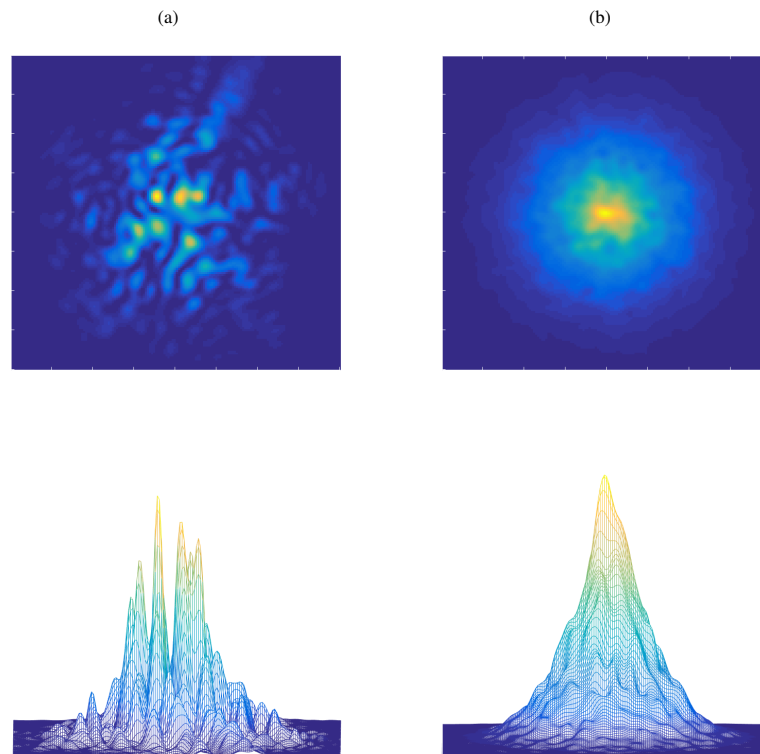


Fig. 4.1: (a) Short exposure PSF and (b) long exposure PSF. Turbulent scenario $D/r_0 = 6$, with $D = 40$ [cm]

A distinction between the short and long exposure speckle pattern needs to be made. Figure 4.1 (a) shows a typical short-exposure focal intensity image, while Fig. 4.1 (b) depicts the long-exposure one. Whether both patterns differ between each other, depends on the integration time of the focal sensor with respect to the coherent

time of the fields τ_0 . The short-exposure image shows a speckled intensity pattern and statistically independent intensity spots. Assuming a camera capable of acquiring many images within τ_0 , then the resultant focal speckle would still resemble the one in Fig. 4.1 (a). Instead, longer acquisition times $t > \tau_0$ result in an averaging process with a broader spread function. These long exposure images do not contain useful information.

Turbulence compensation in FSO systems must be performed within τ_0 to avoid signal fades. Speckle-based imaging techniques rely on short-exposure images which contain spectral information and where, even though not directly retrievable, the phase information is preserved [117].

An important property of the focal intensity patterns is that a linear phase tilt in the pupil distribution only shift the speckle pattern but does not introduce any blur or broadening. Therefore, the tilt can be pre-compensated to center the pattern without altering the information related to higher order phase distortions.

In the concerning scenario of laser propagation over turbulent channels, the speckle phenomena can also be modeled considering that discrete regions of the pupil wave-front suffer different amounts of atmospherically induced phase delays [4]. This loss of coherence of the wave-front can be represented by circular symmetric correlation cells with a diameter defined by the Fried parameter r_0 , calculated with Eq. (2.20), and depicted in Fig. 4.2. Each cell is assumed to have a uniform phase, which is random with Gaussian statistics respect to the others [4]. The ratio of correlation cells embraced by the aperture of diameter D , known as the normalized aperture D/r_0 , defines the impact of the phase distortions in the optical system. The number of uncorrelated cells in the pupil plane can be approximated as $N_0 = (D/r_0)^2$.

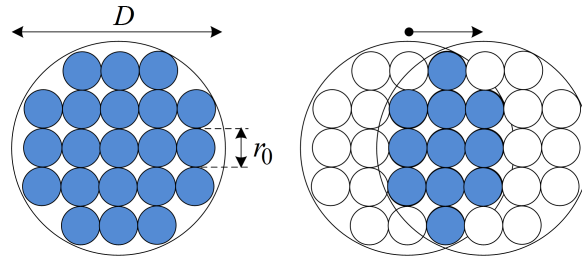


Fig. 4.2: Representation of the pupil field loss of coherence and autocorrelation process [4].

The extent of the performance deterioration in the optical receiver is estimated through the autocorrelation of a complex pupil field. In Fig. 4.2, the autocorrelation is represented by the shifted overlap of the field with its identical conjugated version. The shaded areas represent the full overlap of the cells. By shifting the field a distance r_0 , the overlap between uncorrelated cell results in a random phase and amplitude leading to a reduction in the system performance. As a result, the cell size limits the system resolution to that of a system with aperture diameter equal to r_0 . Because the speckle pattern results from the Fourier transform of the complex pupil field, the dimension of each focal speckle (single intensity spot) is proportional to λ/D , and the extension of the whole speckle pattern is given by λ/r_0 .

Generally, the number of intensity spots in a short-exposure speckle pattern is also approximated as $(D/r_0)^2$. In reality, the speckles do not have the same intensity, and those with higher intensity contain more information of the aberrated wave-front.

4.1.1 Speckle intensity distribution

As previously said, the power distribution among the speckles in the focal plane changes with the turbulence strength. When the turbulence is weak, most of the wave-front energy gets focused in a few bright speckles. Instead, under strong turbulence, a large number of intensity spots appear, typically spread around the central position in the focal plane. The on-axis focal intensity can be estimated numerically by generating a set of synthetic speckle patterns and registering the Strehl factor [125]. This factor is equal to the intensity at the central point $I(0)$, normalized to the peak intensity I_{\max} of the diffraction-limited pattern (Airy pattern). For this analysis, a large set of $N = 400$ focal images is generated by Fourier transforming an equal number of complex pupil fields. Each set of pupil fields is created with unitary amplitude, and a phase generated with the single-screen phase method, presented in Sec. 2.1.4. The simulated scenarios consider normalized apertures equal to $D/r_0 \approx [1, 3, 6, 10]$ with $D = 40$ cm.

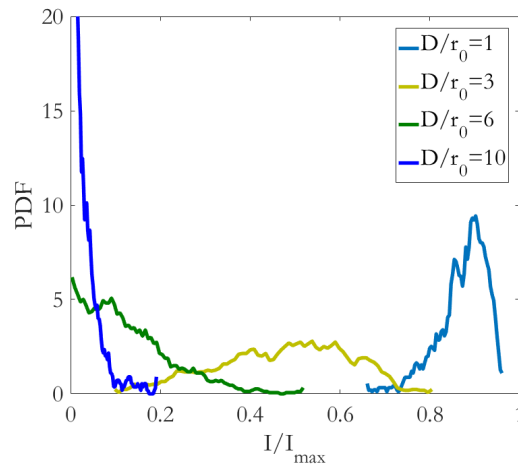


Fig. 4.3: Probability distribution of the on-axis intensity of a large set of speckle pattern.

Figure 4.3 shows the PDF of the normalized on-axis intensity. The probability of having high-intensity values at the central position of the focal plane (expected position of a single-mode fiber) reduces because most of the bright speckles typically evolve around the central position. Such phenomenon is related to high order phase distortions in the pupil field.

Assuming the possibility of target-and-correction of each speckle, it results useful the estimation of the number of speckles that should be considered to optimize the correction. This would imply having the capacity of selecting the more intense speckles, and being able to “*move them*” towards the central position to increase the composite signal. The trend of the mean intensity distribution per speckle can be analyzed numerically, and requires the detection and classification of the speckles on each short-exposure intensity pattern.

The process starts by normalizing each focal image to the sum of its intensity components, see Figure 4.4 (b). Then, the normalized image I_n is segmented and the detected speckles are classified in descending order based on their intensity strength. Once sorted, the total intensity within each speckle area I_s is calculated. For example, if the normalized image has four intense speckles, then $I_n \approx \sum_{m=1}^4 I_s(m)$. The procedure is repeated for a large set of images within different D/r_0 .

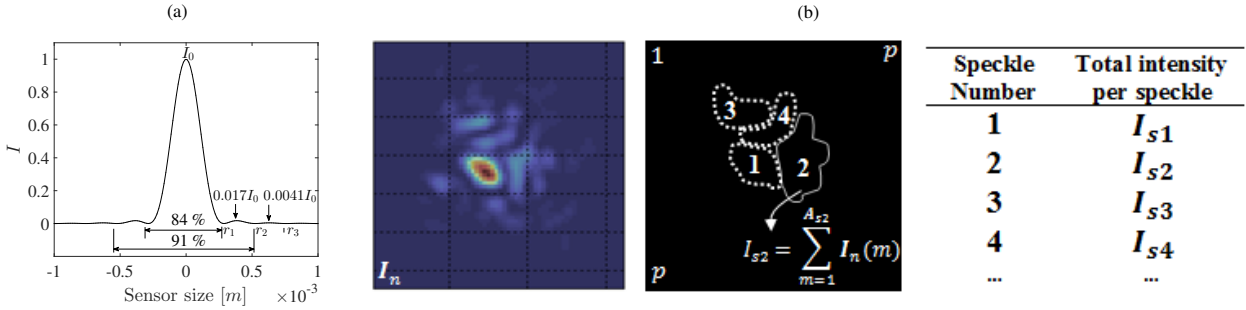


Fig. 4.4: (a) Airy pattern. (b) Representation of the image processing steps applied to each focal image. The table classifies the speckles based on their peak intensities and shows the total intensity contained on their respective speckle areas.

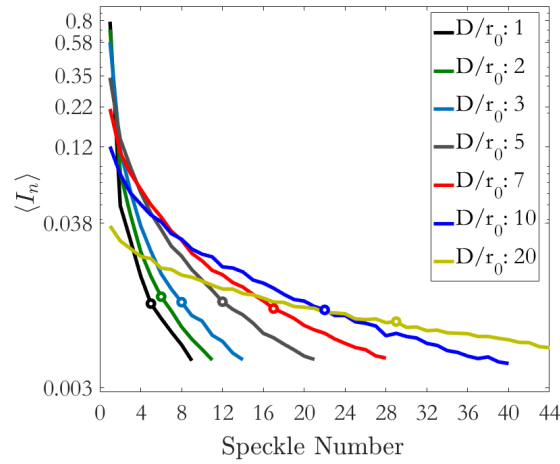


Fig. 4.5: Mean intensity distribution per speckle for different turbulent scenarios. The markers indicate the optimum number of processed speckles equivalent to 81% of the total focal intensity.

The results are shown in Fig. 4.5. Each curve shows the trend of the mean normalized intensity per speckle, for a particular D/r_0 . Consider that a plane wave received by a circular aperture, and focused by a single lens, results in an Airy pattern of intensity, see Fig. 4.4 (a). Note that in an airy pattern, the encircled energy in the first ring is equal to 84% of the total, and the intensity ratio between the first and principal lobe of an Airy pattern is 1.7%. Consequently, as the maximum SMF coupling efficiency is no more than 81% of the total focal power, the optimum number of speckles considered for processing in Fig. 4.5 are those with an intensity strength above 1.7% of the total. This optimum number of speckles, equivalent to 81% of the total focal intensity, is highlighted with a marker on each curve.

As expected, the distribution of the focal intensity varies with D/r_0 . The stronger the turbulence, the more is the intensity distribution among the focal speckles. For nearly ideal conditions $D/r_0 = 1$, most of the power accumulates in less than 3 speckles. For higher D/r_0 , more speckles need to be considered to reach 81% of the maximum. The curves confirm that most of the focal power concentrates in a small number of speckles, hence the $(D/r_0)^2$ assumption, made in Sec. 4.1, overestimates the required number of speckles for correction.

To provide an estimation of the required speckles for correction under different turbulent regimes, the curves

in Fig. 4.5 can be approximated with the function

$$\log_{10}(\langle I_n \rangle) = A_0 \exp(B_0 M) + C_0 \exp(D_0 M), \quad (4.1)$$

where M is the number of speckles to be processed, and the coefficients $\{A_0, B_0, C_0, D_0\}$ can be calculated in function of the D/r_0 as shown in Table 4.1. The Eq. (4.1) results of a numerical fitting of the curves and coefficients. This equation is well suited for all D/r_0 scenarios within the stipulated range. Note that the optimum number of speckles M can be recursively calculated for a predefined D/r_0 .

	D/r_0	Function	Coefficients
A_0	$1 \leq D/r_0 \leq 20$	$p_1 \left(\frac{D}{r_0}\right)^{p_2} + p_3$	$p_1 = -0.01546$ $p_2 = 0.9688$ $p_3 = -1.476$
B_0	$1 \leq D/r_0 \leq 20$	$p_1 \exp\left[p_2 \left(\frac{D}{r_0}\right)\right] + p_3 \exp\left[p_4 \left(\frac{D}{r_0}\right)\right]$	$p_1 = 0.05685$ $p_2 = -0.2836$ $p_3 = 0.006063$ $p_4 = -0.006485$
C_0	$1 \leq D/r_0 \leq 20$	$p_1 \exp\left[p_2 \left(\frac{D}{r_0}\right)\right] + p_3 \exp\left[p_4 \left(\frac{D}{r_0}\right)\right]$	$p_1 = 8.108$ $p_2 = -0.9132$ $p_3 = 2.136$ $p_4 = -0.09269$
D_0	$1 \leq D/r_0 \leq 20$	$p_1 \exp\left[p_2 \left(\frac{D}{r_0}\right)\right] + p_3 \exp\left[p_4 \left(\frac{D}{r_0}\right)\right]$	$p_1 = -1.933$ $p_2 = -0.55$ $p_3 = -0.1496$ $p_4 = 0.01146$

Table 4.1: Range of D/r_0 and formulae for the main coefficients of Eq. (4.1).

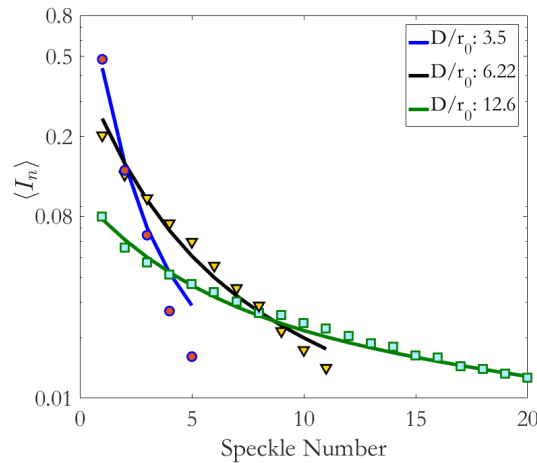


Fig. 4.6: Comparison between the distribution of the mean normalized intensity per speckle between measured focal images (markers) of a GEO downlink and the analytic fitting based on simulations (continuous curve) of table 4.1.

The validation of Eq. (4.1) is performed against a set of focal images obtained during a TESAT-DLR measurement campaign (2016-2018) [43], see Fig. 4.6. The focal images correspond to a laser downlink (1064

nm) between the GEO satellite Alphasat (35700 km) and the ESA-OGS located in Tenerife (Spain). The r_0 is estimated using the method described in [126] on different days and daytime. The selected scenarios have an approximated normalized aperture $D/r_0 = [3.5, 6.22, 12.6]$ with $D = 1\text{m}$.

In Fig. 4.6, the continuous curves are the numerical approximation, based on simulations, and calculated with Eq. (4.1). These curves are compared against the ones resulted from the processing of the measured focal images, represented with markers. There is a good matching in the slopes, particularly for strong turbulence. A deviation occurs approaching weak turbulence, $D/r_0 = 3.5$, which may be originated by the fact that the synthetic fields are created with unitary amplitude, while the real focal images also consider scintillation effects and slant-path.

4.1.2 Focal speckle phase

The main challenge for the phase retrieval from a focal intensity image is an intrinsic phase ambiguity. If the phase of the complex focal field is missing, there is always ambiguous solutions for the recovered complex pupil field. In other words, there exist several focal phase map alternatives leading to the same measurable focal intensity pattern. This claim is also valid for the pupil function, where several pupil phases result in an identical focal pattern of intensity. A mathematical analysis of the problem was performed by J.C. Dainty in 1979, where he established that “*on the basis of measurements of intensity alone, there is no possible way to distinguish between these alternatives without additional information*” [127]. Several approaches have been proposed to deal with the problem, concluding on the impossibility of a direct phase retrieval from power intensity measurements [127–131].

As explained in Sec. 3.3.2, when working with focal intensity patterns as an input of the phase compensation system, amplitude and phase are addressed independently. The amplitude spectrum of the field is estimated with speckle interferometry [117]. The phase spectrum of an object can be recovered with post detection image processing techniques like the cross-spectrum and bispectrum methods [16]. Both processes require a large set (>100) of focal images that need to be Fourier transformed; thus the task involves fast camera acquisition rates and substantial software post-processing workload. Since FSOC turbulence compensation must be constrained to approximately 2 milliseconds, these methods do not qualify for the task, mainly due to camera acquisition rates constraints.

4.2 Speckle-based sequential technique

This thesis proposes a new iterative adaptive optics method that uses the intensity information of a single focal image to reduce the number of iterations required. The adaptation method operates on each main intensity speckle sequentially, updating and optimizing their phases iteratively. The method has the attractive property that each phase estimation can be obtained in a closed form via the quadratic optimization of a cost function based on power measurements. Because quadratic optimization problems are always convex, a standard multivariate quadratic algorithm would always find a global optimum. This means that the algorithm does not need to react based on the trend of the coupled signal, like stochastic blind algorithms, and instead perform the pre-established measurements and optimization steps sequentially.

To facilitate the understanding of the next sections, a summary of the main processing stages is given as follows:

- The method uses a single short-exposure focal image and identifies the peak amplitude and coordinate position of the most intense speckles
- In the framework of Fourier optics, the method associates the speckle pattern with a summation of pondered pupil plane waves, each one propagating towards its own associated focal speckle
- Optimizing the phase of the speckles is equivalent to phase-shift the associated plane waves until the best coherent combination compensates the distorted field. This is done sequentially, shaping the DM and concurrently sensing the fiber-coupled power
- Because the power optimization process fulfills conditions of a convex problem, it requires only three power measurements for each optimization
- As a result, the total number of iterations needed is proportional to three times the number of selected speckles, substantially reducing the total number of iterations required per field compensation

4.2.1 The turbulence compensation system

Before detailing the adaptation method, let's describe the turbulence compensation system and define the signal terms. Figure. 4.7 shows the main hardware components of the receiver. Like the sensor-less system shown in Fig. 3.10, a deformable mirror and a fiber coupling section are required for the working algorithm. Additionally, a focal camera and a tilt correction stage are shown. Tilt correction systems are always present to compensate for the beam angle of incidence, allowing the DM to correct only the higher order aberrations. Because the satellite needs to be tracked, optical ground stations always have a focal camera. The optical system for the tracking camera normally uses a rather large focal length (≈ 4 meters in DLR-OGS) and high-resolution IR cameras. Hence, the focal image (speckle pattern) can be well-resolved, and the adaptation method does not need to add an extra piece of hardware.

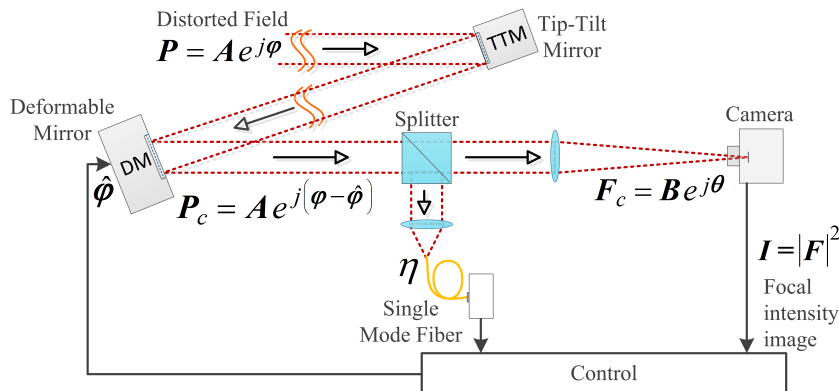


Fig. 4.7: Simplified scheme of the optical receiver. The incoming beam is corrected in tilt, reflected in the deformable mirror, and focused on an infrared camera and single mode fiber. The speckle image and the coupled signal are used to sequentially compensate the distorted phase-front via the iterative control of the deformable mirror.

When a laser beam passes through the turbulent atmosphere, the wavefront $P = A \exp(j\varphi)$ is affected by

distortions in amplitude A and phase φ . In the receiver, the distorted beam is captured by a single monolithic aperture, guided to the tip-tilt mirror (TTM) for angle-of-incidence correction, and reflected in the deformable mirror (DM). The DM modifies its shape according to an estimated phase $\hat{\varphi}$, inducing phase-only variations on the wavefront P , and resulting in a phase-compensated reflected beam

$$P_c = A \exp(j(\varphi - \hat{\varphi})). \quad (4.2)$$

Here, $\hat{\varphi}$ is defined by an iterative algorithm requiring two inputs. The first input is a focal intensity image $I = |F|^2$ captured by a camera sensor. The complex field $F = B \exp(j\theta)$, with amplitude B and phase θ , results from the optical Fourier transform of P_c . The second input is a real-time acquisition of the signal power coupled into a single mode fiber. The power of the coupled signal is defined by the SMF coupling efficiency η , which is calculated in the pupil plane applying Eq. (4.2) into Eq. (2.104).

4.2.2 Mathematical framework

The proposed technique considers Fourier optics and the angular wave spectrum (AWS) method. Fourier optics explains the fundamental principles and processes of the technique, while the AWS method helps to understand the assumption leading to the problem simplification.

4.2.2.1 Fourier Optics representation

In Fourier optics, a wave-front can be described by the sum of an infinite number of plane waves oriented in different directions in space, each one carrying a part of the total energy of the field. After the wave-front passes through a lens, the energy of each plane wave converges in a unique non-equal point in the focal plane. This focal plane is known as the Fourier transform plane, where the wave-front is transformed into spatial frequency spectra [132]. When a distorted wave-front is considered, measurements of intensity in the focal plane show fine-scale fluctuations in space, i.e., speckles. In this framework, these speckles appear because the wave-front is composed of a multitude of independent complex plane waves having both random amplitude and random phase. Let's consider a plane wave defined as

$$u(x, y, z) = A \exp [j(k_x x + k_y y + k_z z)] \quad (4.3)$$

propagating in a particular direction in space, indicated by the wave vector $\mathbf{k} = (k_x, k_y, k_z)$, having a wavelength λ , wave number $k = \sqrt{k_x^2 + k_y^2 + k_z^2} = 2\pi/\lambda$, and complex envelope A . The wave vector \mathbf{k} makes angles $\beta_x = \sin^{-1}(k_x/k)$ and $\beta_y = \sin^{-1}(k_y/k)$ with the $y-z$ and $x-z$ planes, respectively. In Fig. 4.8 the angle $\beta_x = 0$. At the position $z = 0$, the complex amplitude $u(x, y, z = 0)$ is a spatial harmonic function of the type

$$f(x, y) = A \exp [j2\pi(v_x x + v_y y)] \quad (4.4)$$

with spatial frequencies $v_{x,y} = k_{x,y}/2\pi$ (cycles/mm) and harmonic periods $\Lambda_{x,y} = 1/v_{x,y}$ in the x and y directions, respectively. The propagation direction of the plane wave is clearly defined by the frequencies of the harmonic as

$$\beta_x = \sin^{-1}(k_x/k) = \sin^{-1}(\lambda v_x) \quad (4.5)$$

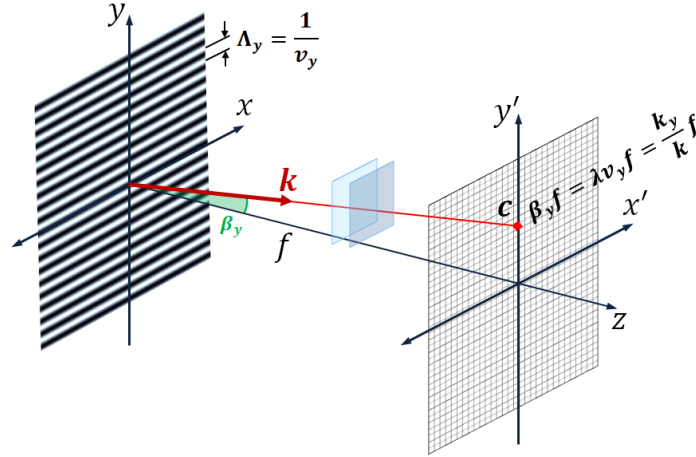


Fig. 4.8: Representation of a pupil harmonic (plane wave) propagating in the direction of the wave vector \mathbf{k} to the focal point of coordinates \mathbf{c} , with and angle β_y proportional to the harmonic frequency ν_y .

$$\beta_y = \sin^{-1}(k_y/k) = \sin^{-1}(\lambda\nu_y). \quad (4.6)$$

In the paraxial approximation $k_{x,y} \ll k$, and the propagation angles in Eq. (4.5)-(4.6) are small enough to be approximated as

$$\beta_{x,y} \approx \lambda\nu_{x,y}. \quad (4.7)$$

As initially mentioned, a complex wave-front is composed by a multitude of plane waves. A lens separates and focus each plane wave propagating in the direction (β_x, β_y) onto a unique point $(x' = \beta_x f, y' = \beta_y f)$ in the focal plane, where

$$x' = \beta_x f = \lambda\nu_x f \quad (4.8)$$

$$y' = \beta_y f = \lambda\nu_y f \quad (4.9)$$

Clearly, from Eq. (4.8)-(4.9), the complex amplitude at the point (x', y') is proportional to the Fourier transform of the function $f(x, y)$, Eq. (4.4), evaluated at the frequencies $\nu_x = x'/\lambda f$ and $\nu_y = y'/\lambda f$. The Fourier transform of the aperture function $f(x, y)$ with Fourier components $F(\nu_x, \nu_y)$ can be written in the K-space as

$$F(\mathbf{k}) = \iint_{-\infty}^{\infty} f(\mathbf{r}) \exp(-j\mathbf{k} \cdot \mathbf{r}) \quad (4.10)$$

with an inverse

$$f(\mathbf{r}) = \iint_{-\infty}^{\infty} F(\mathbf{k}) \exp(j\mathbf{k} \cdot \mathbf{r}) \quad (4.11)$$

where $\mathbf{k} \cdot \mathbf{r} = (k_x x + k_y y)$. Considering the aperture function that equals unity for $|\mathbf{r}| \leq D/2$ and zero for $|\mathbf{r}| > D/2$, with D being the lens aperture diameter, the Fourier transform of a truncated plane wave can be expressed as

$$F(\mathbf{k}) = \iint_{-\infty}^{\infty} W(\mathbf{r}) f(\mathbf{r}) \exp(-j\mathbf{k} \cdot \mathbf{r}) = \frac{2\pi J_1\left(\frac{D}{2} \sqrt{k_x^2 + k_y^2}\right)}{\sqrt{k_x^2 + k_y^2}} \quad (4.12)$$

where $J_1(\cdot)$ is the Bessel function of the first kind of order one. The focal intensity pattern $I(\mathbf{k})$ results in the well-known Airy pattern

$$I_a(\mathbf{k}) = \left[\frac{2\pi J_1\left(\frac{D}{2}\sqrt{k_x^2 + k_y^2}\right)}{\sqrt{k_x^2 + k_y^2}} \right]^2 \quad (4.13)$$

4.2.2.2 Angular wave spectrum representation

The angular wave spectrum (AWS), also known as angular-spectrum of plane waves, is a mathematical tool used to describe and analyze optical wave fields. The AWS represents a field as the superposition of homogeneous and in-homogeneous (evanescent) plane waves, propagating in different directions in space. The full derivation of the AWS is not given to avoid confusion with the previous derivation, and can be found in [132, 133]. Instead, the most relevant concept is explained.

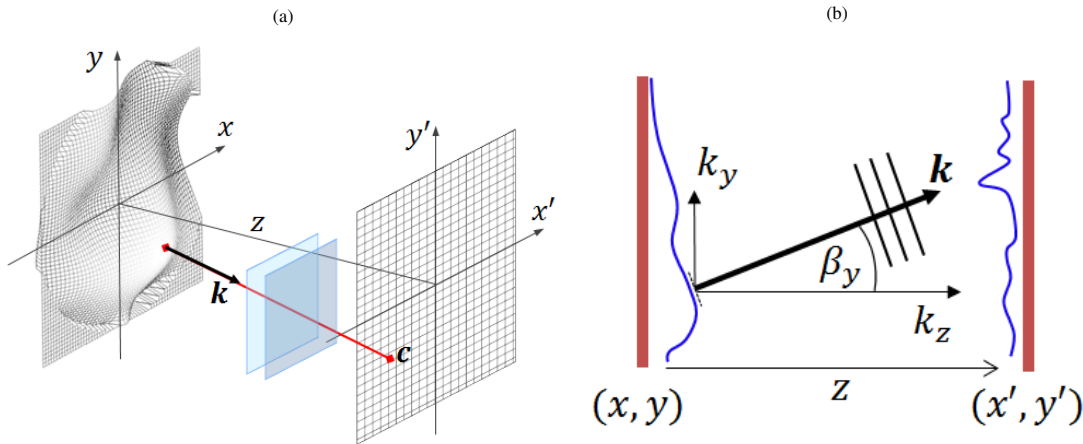


Fig. 4.9: (a) Object plane and image plane representation. A plane wave originates from a point source in the object plane and propagates in the direction of the \mathbf{k} vector to a unique point \mathbf{c} in the image plane. (b) A plane wave propagates in the direction of the \mathbf{k} vector which has (k_x, k_y, k_z) components. In the far field and paraxial limit, the angle β_y is small, thus, the condition of propagating plane wave ($k_x^2 + k_y^2 < k^2$) is fulfilled.

The AWS establishes that each point in the object plane (x, y) of Fig. 4.9 (a), acts as a source of plane waves of the type

$$\mathbf{u}(x, y, z) = A \exp [j(k_x x + k_y y)] \exp [j(k_z z)] \quad (4.14)$$

propagating to the point \mathbf{c} based on a propagation factor $\exp(\pm j k_z z)$. Equation (4.14) can be written in the K-space as

$$\mathbf{u}(x, y, z) = A \exp(j\mathbf{k} \cdot \mathbf{r}) \quad (4.15)$$

where $\mathbf{k} = (k_x \hat{x} + k_y \hat{y} + k_z \hat{z})$ and $\mathbf{r} = (x \hat{x} + y \hat{y} + z \hat{z})$ define the propagation direction of the wave, and $\hat{\cdot}$ indicates a unit vector. Considering again the relation $k_x^2 + k_y^2 + k_z^2 = k^2$, the conditions for propagation and evanescence of plane waves is given by

$$k_z = \sqrt{k^2 - k_x^2 - k_y^2}, \quad (4.16)$$

where the propagator factor $\exp(\pm jk_z z)$ oscillate or exponentially decay based on

$$k_x^2 + k_y^2 \leq k^2 \quad \text{Plane waves} \quad (4.17)$$

$$k_x^2 + k_y^2 > k^2 \quad \text{Evanescent waves} \quad (4.18)$$

As a result, the larger the angle β_y between \mathbf{k} and the z axis, Fig. 4.9 (b), the more are the oscillation in the transverse plane and the faster the waves attenuates. Note that when $k_x^2 + k_y^2 > k^2$ then k_z becomes imaginary and the propagation factor turns into a negative exponential, attenuating the field.

G.C. Sherman [133] proved that, *in the framework of the AWS and paraxial limit, each point of the field $\mathbf{u}(x, y, 0)$ acts as a source of a plane wave that carries part of the total energy of the field to the observation point in the image plane. The amplitude of such point is equal to the amplitude of the plane wave. The rest of plane waves originated in different points of the object plane destructively interfere [132, 133]. Consequently, only a single plane wave contributes to each point of the image plane. If an optical system is considered, the far field is focused at the focal plane of the lens, hence, the energy of each plane wave converges in a unique non-equal point in the focal plane.*

4.2.3 The method

Consider now that a wave-front affected by turbulence experiences different amounts of phase delays [4]. Similar phase delays in the pupil define coherent regions in the phase-front. In Fig. 4.10(a), areas of the same color represent the regions where the phase remains coherent. From the theory of angular wave spectrum, Sec. 4.2.2.2, it is reasonably assumed that each coherent region in the pupil plane becomes a source of plane waves with similar propagation directions, focusing in a well-defined area in the focal plane, see Fig. 4.11. The contribution of this set of plane waves, with slight differences in the propagation direction, results in a speckle with a well-defined maximum of intensity. Additional speckles are produced by a different set of plane waves associated with other coherent regions in the pupil, see Fig. 4.10(b). Hence, it is possible to represent the net effect of each coherent region with a single plane wave, having properties defined by the associated focal speckle.

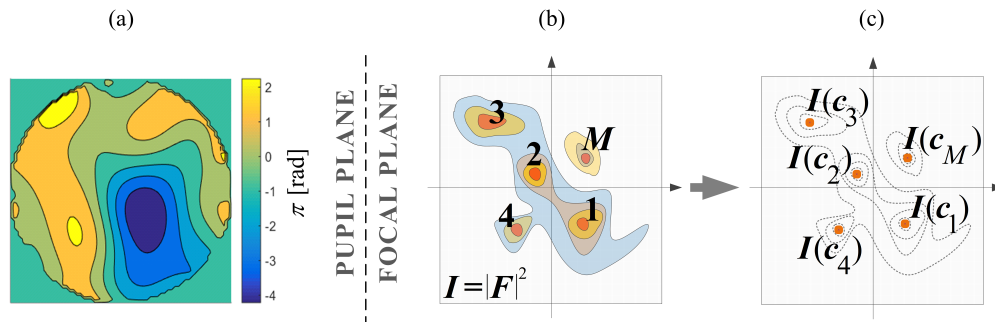


Fig. 4.10: (a) Representation of the coherent regions of phase in the pupil plane. (b) Representation of the focal intensity image with M main speckles. (c) Simplification with the M peak intensities.

These assumptions can be modeled by representing each main speckle of the focal intensity pattern in Fig. 4.10(b) as a spatially shifted airy pattern, weighted by the scalar speckle peak amplitude b_l , and matching the speckle peak coordinates $\mathbf{c} = (x', y')$ shown in Fig. 4.10(c). By performing the back Fourier transform of the

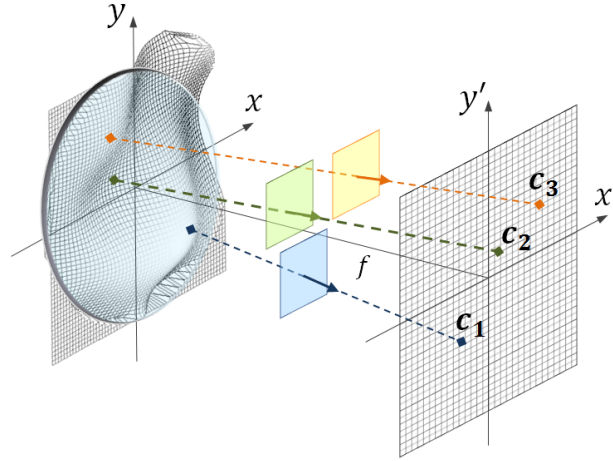


Fig. 4.11: Representation of a distorted phase wave-front reaching the focusing lens. Each coherent region in the wave-front can be considered a source of plane waves propagating to a particular point \mathbf{c} of the focal plane. The ensemble contribution of each focused set of plane waves results in the formation of a speckle.

summation of airy patterns, and considering that these main speckles are indeed sufficiently decorrelated [134], the pupil field $\mathbf{P}(\mathbf{r})$ can be written as

$$\mathbf{P}(\mathbf{r}) \approx \sum_{l=1}^M \left[b_l \iint_{-\infty}^{\infty} \delta(\mathbf{k} - \mathbf{k}_l) \sqrt{I_a(\mathbf{k})} \exp(j\mathbf{k} \cdot \mathbf{r}) d\mathbf{k} \right] \quad (4.19)$$

where \mathbf{k}_l can be defined as

$$\mathbf{k}_l = \left(\frac{2\pi x'_l}{\lambda f}, \frac{2\pi y'_l}{\lambda f} \right). \quad (4.20)$$

In Eq. (4.20) the reader may consider Eq. (4.8)-(4.9) and recall $\beta_{x,y} = k_{x,y}/k$ from Sec. 4.2.2.1. Naturally, the speckle phase information is still missing and its inherent ambiguity is generally addressed with the method introduced in Sec. 3.3.2, which is not suitable for FSO applications. However, from the work of Freund [134], it is known that each speckle shows a local spatial correlation between its intensity distribution and phase gradient, with a high correlation between the minimum phase gradients and the maximum slopes of intensity. In simple words, on each well-defined speckle of intensity, there is a small gradient of phase that allows the assignment of a constant phase value to its entire area. With this approximation, the speckle phase can be modeled as a constant scalar value and

$$\mathbf{P}(\mathbf{r}) \approx \sum_{l=1}^M \left[b_l \exp(j\theta_l) \iint_{-\infty}^{\infty} \delta(\mathbf{k} - \mathbf{k}_l) \sqrt{I_a(\mathbf{k})} \exp(j\mathbf{k} \cdot \mathbf{r}) d\mathbf{k} \right]. \quad (4.21)$$

Therefore, this model approximates the distorted wave-front $\mathbf{P}(\mathbf{r})$ by a finite set of M dominant plane waves, each one related to one of the M main focal speckles which define the scalar amplitude $b_l \in \mathbb{R}$, and the propagation direction given by the wave vector \mathbf{k}_l . Based on that, the wave-front is written as

$$\mathbf{P}(\mathbf{r}) \approx W(\mathbf{r}) \sum_{l=1}^M b_l \exp(j\theta_l) \exp(j\mathbf{k}_l \cdot \mathbf{r}). \quad (4.22)$$

Note that the still unknown scalar phase $\theta_l \in \mathbb{R}$ represents the phase shift of the l harmonic (plane wave) respect to the others. Figure 4.12 depicts the real term of a single pupil harmonic of amplitude b and frequency ν_x , highlighting the possible phase shift direction.

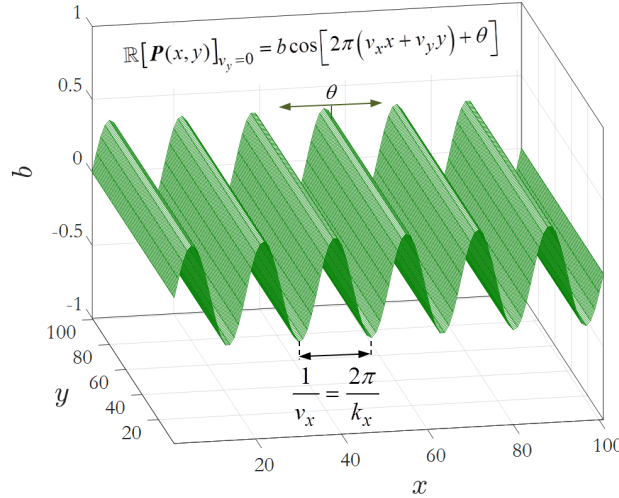


Fig. 4.12: Representation of harmonic term with spatial frequency ν_x , amplitude b , and phase shift θ .

In consequence, the problem gets reduced to the iterative search for a set of θ_l that deliver the right combination of harmonics in the pupil plane. Considering the orthogonality between harmonics/speckles, this task can be performed with the coordinate-wise ascent algorithm [135]. This algorithm treats the multivariate problem as a set of simpler sub-problems of a single dimension, maximizing an objective function by optimizing the scalar variables θ_l in sequence. In other words, the algorithm finds each optimum phase shift sequentially, optimizing each variable at a time and independently.

$$\hat{\varphi}(\mathbf{r}) = \arg \left\{ b_1 \exp(j\mathbf{k}_1 \cdot \mathbf{r}) + \sum_{l=2}^M \left(b_l \exp(j(\mathbf{k}_l \cdot \mathbf{r} + \theta_l)) + \left[\sum_{q \neq l} b_q \exp(j(\mathbf{k}_q \cdot \mathbf{r} + \theta_q)) \right] \right) \right\}. \quad (4.23)$$

In Eq. (4.23), the M plane waves are sequentially added and the estimated phase $\hat{\varphi}(\mathbf{r})$ is calculated as the argument of the summation. The objective function is the fiber coupling efficiency η , calculated with Eq. (2.104) using the field $\mathbf{P}_c(\mathbf{r})$ compensated in phase with the estimated $\hat{\varphi}(\mathbf{r})$, see Eq. (4.2) and Fig. 4.7. The first term in Eq. (4.23) represents the first plane wave taken as a reference and from which the estimated field will evolve, thus, no phase shift is required. Starting with the second plane wave $l = 2$, the phase shift θ_l is found following a parabolic optimization process. In this process, depicted in Fig. 4.13, three scalar phase variations $[\theta_1, \theta_2, \theta_3]$ are applied to the plane wave, resulting in three pupil phase estimations $[\hat{\varphi}_1, \hat{\varphi}_2, \hat{\varphi}_3]$ which leads to $[\mathbf{P}_{c1}, \mathbf{P}_{c2}, \mathbf{P}_{c3}]$. Consequently, three values of coupling efficiency $[\eta_1, \eta_2, \eta_3]$ are sequentially obtained. A parabolic fitting is applied to the function $\eta = f(\theta_l)$ and the optimum phase shift θ_{optl} is found at the position of the maximum coupling η_{max} .

Note that each phase shift θ represents a perturbation of the compensator element (i.e. DM), which is translated into a change in $\hat{\varphi}(\theta)$ and concurrently to the control signals as

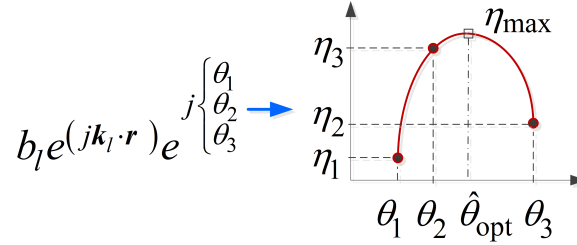


Fig. 4.13: Description of the optimization of the phase shift of a plane wave.

$$\mathbf{v}^m = M_d \hat{\boldsymbol{\phi}}_m, \quad (4.24)$$

where \mathbf{v} represents the control signals, M_d is transfer function of the compensator element, and m represents the iteration number. The difference with the SPGD method, presented in Sec. 3.3.1, is that the perturbations θ are non-stochastic but instead well-defined, and the number of iterations m is known in advance.

This procedure is repeated for each subsequent plane wave, keeping each $q \neq l$ previously optimized variable θ_q fixed. Consequently, the compensation of a distorted phase-front is done with a total number of iterations calculated as

$$N_{\text{iter}} = 3(M - 1) + 1, \quad (4.25)$$

which is directly proportional to the number of main intensity speckles. In Eq. (4.25) the number 3 indicates the three iterations, M is the total number of processed speckles, the factor “-1” represents the first plane wave which does not require the optimization, and the final “+1” represents the final iteration that imprints the final shape to the DM. Note the similarity with the image sharpening technique presented in Sec. 3.3.3, here performing the optimization with the power coupling instead of image comparisons, thus avoiding the bottleneck limit given by the camera acquisition frame rate.

4.2.4 Parabolic optimization

A parabolic optimization of each plane wave is possible because the coupled power in the fiber η varies periodically with θ_l . Before the mathematical formulation of the function $\eta = f(\theta_l)$, let's expand Fig. 4.12 with more plane wave harmonics. Figure. 4.14 (a) shows the field $\mathbf{P}(\mathbf{r})$ composed of 4 plane waves, each one represented with its real term components as, getting focused and producing 4 speckles spatially distributed in the focal plane, see 4.14 (b).

$$\Re[\mathbf{P}(\mathbf{r})] = \sum_{l=1}^{M=4} [b_l \cos(\mathbf{k}_l \cdot \mathbf{r} + \theta_l)]. \quad (4.26)$$

The speckle “A” is the resultant of a harmonic of lower frequency and higher amplitude, clearly visible in the image. Instead, the speckles “B”, “C”, and “D” result from the propagation of plane waves of lower amplitude and higher spatial frequency, thus, they are positioned further apart from the center of the image and have lower peak intensity. The summation of the waves is shown in Fig. 4.14 (c). A continuous variation of θ_1 (plane wave A) shift the position of the speckle “A” back and forward periodically, inducing the same change in the coupled

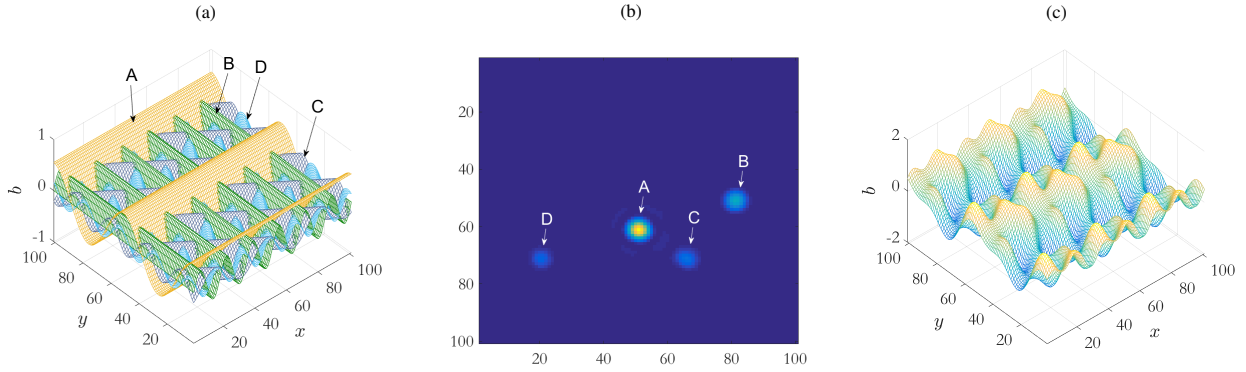


Fig. 4.14: (a) Real components of a combined set of four plane waves of different amplitudes, propagation directions, and spatial frequencies. (b) Focal image resulted of the Fourier transform of the combined plane wave set. (c) Resultant phase map of the combined set of plane waves.

power. From this representation, it is easy to visualize that the compensation of the distorted field involves finding the conjugated plane waves and the optimum phase matching between them.

A mathematical formulation of the periodicity of the function $\eta = f(\theta_l)$, can be found by combining the Eq. (4.2) with Eq. (4.22) as,

$$\mathbf{P}_c(\mathbf{r}) = \sum_{l=1}^M b_l \exp(j(\mathbf{k}_l \cdot \mathbf{r} + \theta_l)) \exp(-j(\mathbf{k}_l \cdot \mathbf{r} + \hat{\theta}_l)). \quad (4.27)$$

In this equation, $\hat{\theta}_l$ is the estimated phase shift of the l plane wave of $\mathbf{P}(\mathbf{r})$. As the l plane wave has an unknown θ_l , the optimization requires to optimize $\Delta\theta_l = \theta_l - \hat{\theta}_l$. Because the amplitude b_l and spatial frequency \mathbf{k}_l of the plane wave are known parameters, the equation can be reduced to a scalar problem in function of the variable $\Delta\theta_l$. Assuming ideal coupling $\eta = 1$ in Eq. (2.104), the coupling efficiency can be written as

$$\eta \propto \left| \sum_{l=1}^M \left(b_l \exp(j\Delta\theta_l) + \left[\sum_{t \neq l} b_t \exp(j\Delta\theta_t) \right] \right) \right|^2, \quad (4.28)$$

Considering the Euler expansion of the complex exponential, every l sub-problem can be expressed as,

$$\eta_l = A_0 + A_1 \cos(\Delta\theta_l) + A_2 \sin(\Delta\theta_l) \quad (4.29)$$

with coefficient,

$$A_0 = b_l^2 + \left[\sum_{t \neq l} b_t \cos(\Delta\theta_t) \right]^2 + \left[\sum_{t \neq l} b_t \sin(\Delta\theta_t) \right]^2 \quad (4.30)$$

$$A_1 = 2b_l \sum_{t \neq l} b_t \cos(\Delta\theta_t) \quad (4.31)$$

$$A_2 = 2b_l \sum_{t \neq l} b_t \sin(\Delta\theta_t) \quad (4.32)$$

In Eq. (4.29) the components $[A_0, A_1, A_2]$ represents the intensity contribution of the $t \neq l$ optimized plane waves, combined with the intensity b_l^2 of the current wave. Applying the trigonometric identity $a \cos(x) + b \sin(x) = R \cos(x - \alpha)$, the coupling efficiency shows its periodicity with each $\Delta\theta_l$ variation

$$\eta_l = A_0 + R \cos(\Delta\theta_l - \alpha), \quad (4.33)$$

where $R = \sqrt{A_1^2 + A_2^2}$ and $\alpha = \tan^{-1}(A_2/A_1)$. In Eq. (4.33), the coupling of each l sub-problem η_l is seen as a biased circular function of periodicity 2π , with a phase shift α that updates its value after every plane wave adjustment.

In order to perform a parabolic optimization, the value of $\Delta\theta_l$ must be constrained to a range of π . If the values are linearly assigned and equally spaced, the phase shift always spans in one, and no more than two, contiguous quadrants of a cosine period. Hence, whenever $\hat{\theta}_{\text{opt}}$ is found in a minimum, the maximum can be located at $\hat{\theta}_{\text{opt}} + \pi$.

Figure 4.15 (a) shows an example of the coupled signal variation and parabolic optimization. By applying a continuous variation of each θ_l between the plane waves, the output η follows the expected periodic behavior described in Eq. (4.33). Here, each θ_l varies between 0 and 3π . As mentioned before, the first speckle acts as a reference and only the plane waves associated with the speckles 2 to 4 are optimized. To verify the parabolic optimization, each θ_l is only changed with three discrete values $\theta = \{0, \pi/3, \pi/6\}$. The correspondents three values of η are shown with green markers on the curves together with the parabolic fitting (dashed lines). The $\eta_{\text{max}3}$ corresponds to a maximum, hence the optimum phase shift of the third plane wave is $\hat{\theta}_{\text{opt}3}$. The parabolic fitting for the waves 2 and 3 leads to minimums, thus the $\eta_{\text{max}2,4}$ and $\hat{\theta}_{\text{opt}2,4}$ are found at π distance. When each optimum phase shift is applied to the plane waves in Eq. (4.27), the estimation of the pupil phase is made and the distortion can be compensated.

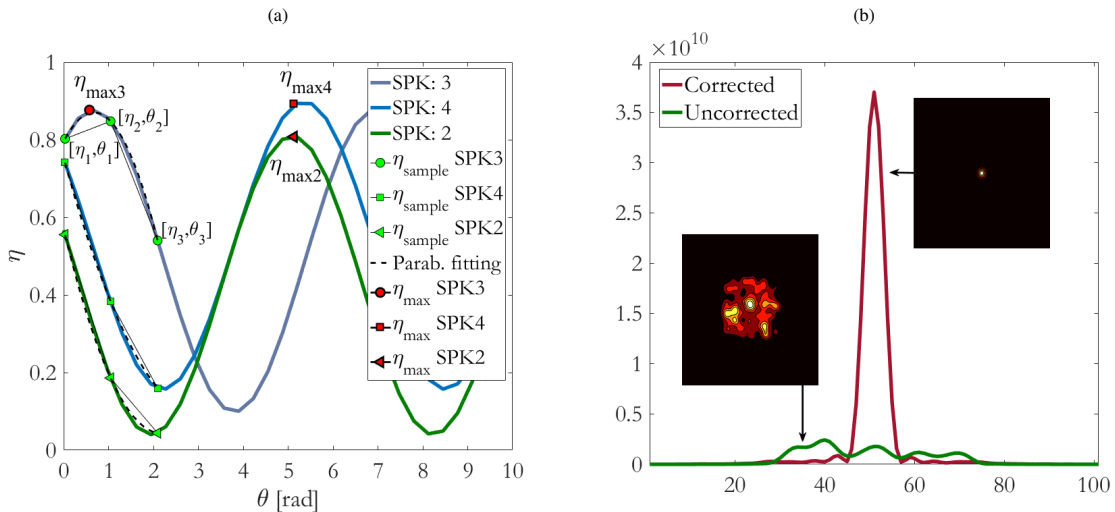


Fig. 4.15: (a) Representation of the coupled power behavior after the 3π phase shift variations of each plane wave in Fig. 4.14 (a). Markers indicate the three registered power values after three applied phase shifts, required for parabolic fitting. Black markers show the final calculated points of maximum coupling and optimum phase shift for each plane wave. (b) Ensemble average of intensity patterns before and after correction of alike randomly generated pupil fields.

Figure 4.15 (b) shows the intensity ensemble of 50 uncorrected and corrected fields. Each field is created as described in Fig. 4.14 (a) with 6 plane waves per field. On each case, the spatial frequencies, amplitudes, and phase shifts of the plane waves are randomly distributed following a normal distribution. The estimation of the phase shift of the planes waves is done with the Eq. (4.33). The insets show the contour plot of the ensemble pattern before and after correction, highlighting the improvement after the optimization.

4.2.5 Optimization process

The description of the optimization process is intended to guide the reader towards the practical implementation of the method. The details of the adaptation process are summarized in Fig. 4.16 and involve three main steps: laser speckle imaging and selection of the M most intense speckle spots in the focal plane; identification of the corresponding M plane waves in the pupil plane; and optimization of the M independent random phases. Fields coordinates are omitted for mathematical simplicity.

4.2.5.1 First step

In the first step of the method, an image of the focal intensity pattern I is captured with the camera, normalized, and square rooted to obtain amplitude coefficients $b_l = \sqrt{I(\mathbf{c}_l)}$. The M main speckles with coordinates \mathbf{r} are detected using image processing and classified in descending order based on their maximum amplitudes b_l at coordinates \mathbf{c}_l . The result is an array of coefficients $b = [b_1, b_2, b_3, \dots, b_M]$ that are associated with sensor coordinates $\mathbf{c} = [\mathbf{c}_1, \mathbf{c}_2, \mathbf{c}_3, \dots, \mathbf{c}_M]$, respectively. In Fig. 4.16, this is represented as a set of images, each one with a single component of amplitude b_l at the coordinate \mathbf{c}_l of maximum speckle intensity.

4.2.5.2 Second step

The second step involves identifying the M plane waves in the pupil plane corresponding to the M selected speckle spots in the focal plane. Each l plane wave has a propagation direction that is identified by a propagation vector \mathbf{k}_l and the speckle coordinate \mathbf{c}_l , see Eq. (4.22). In Fourier optics, a deviation in the direction a wave of light propagates is a tilt, and tilt angles can be used to quantify the slope of a phase profile across the pupil of an optical system. Consequently, the identification of the propagation directions of the M waves is performed by linking a specific tilt angle in the pupil with the corresponding speckle spot position in the focal plane. In this way, each $l \in \{1, 2, 3, \dots, M\}$ detected speckle, with coordinate \mathbf{c}_l and amplitude coefficient b_l , as measured by the CCD camera in the focal plane, will be associated to a well-defined tilted phase profile of a plane wave in the pupil plane. Note that no Fourier transform of the intensity speckle distribution is required. Instead, as part of the calibration process of the system, a lookup table is created containing information of DM's membrane tilts related to camera pixel coordinates, see Fig. 4.17. A scanning process is used, where tilts are applied to the DM producing a displacement of the speckle in the camera sensor and registering the peak coordinate of the displaced speckle.

4.2.5.3 Third step

In the third step, the method estimates and compensates the distorted pupil phase-front φ . This process requires adding up the identified M plane waves, calculating the argument of the summation $\hat{\varphi}$, and using this resultant phase to shape the DM, see Fig. 4.16. In this step, the optimum phase shift $\hat{\theta}_{\text{opt}}$ of each plane waves is iteratively estimated, using a quadratic cost function based on the measured coupling efficiency. Hence, three power measurements are enough to discover the optimum phase shift of each plane wave.

As depicted in step 3 of Fig. 4.16, the method always considers the first plane wave as an initial reference

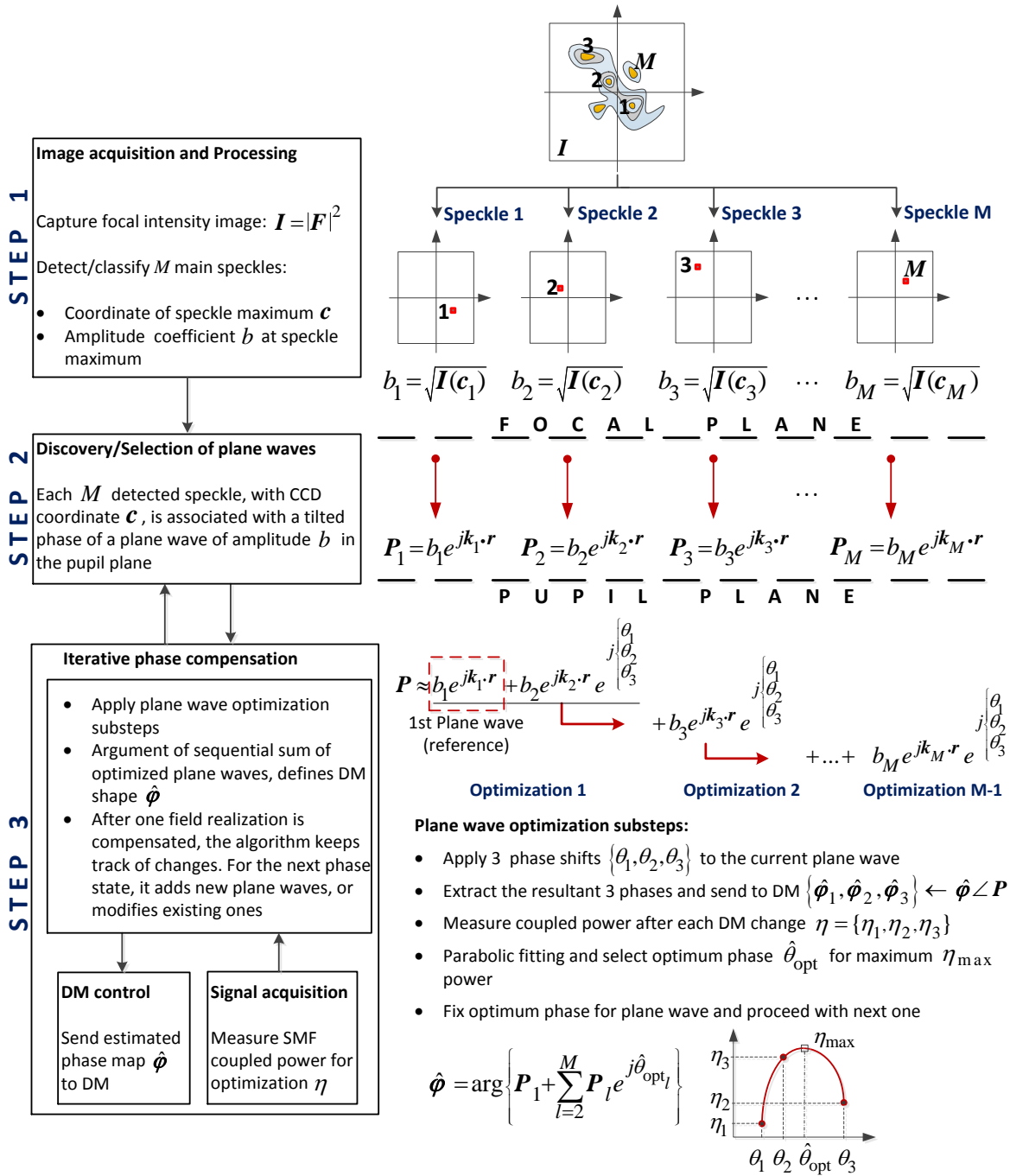


Fig. 4.16: Adaptation algorithm. The captured intensity image is used to create a set of pupil plane waves, each one associated with a main focal speckle. The plane waves are sequentially combined after the optimization of their respective phase shifts, which is done using the feedback power coupling. The argument of the optimized plane wave summation is applied to the DM and represents the estimated distorted phase-front.

from which the field will further evolve, thus, no phase shift is required here. With the coordinate position of the second speckle, the algorithm selects the correspondent phase map in the lookup table and creates the second plane wave. In order to find the optimum phase shift of the second plane wave $\hat{\theta}_{opt2}$, the method shifts

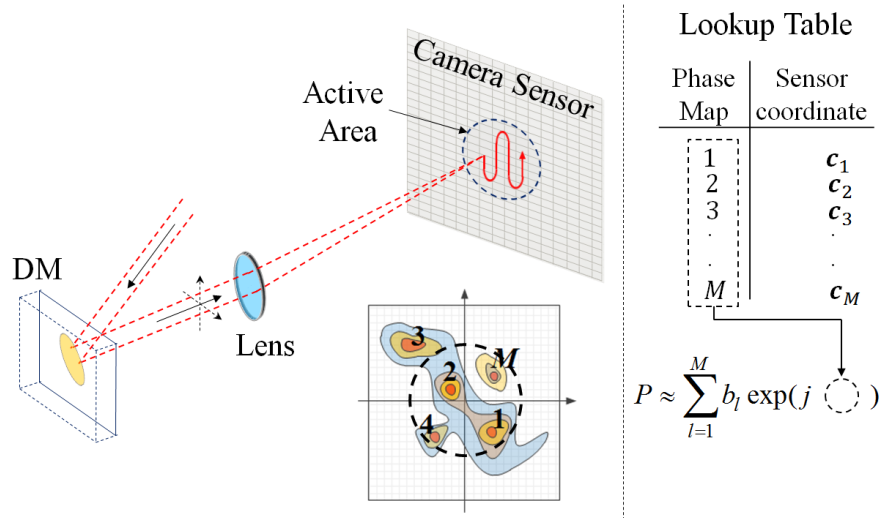


Fig. 4.17: A process to create the lookup table. The DM scans the camera sensor applying phase tilts to the reflected beam. The position of the speckle peak in the sensor is registered. During the correction of the distorted field, every speckle inside the active area can be assigned to a plane wave. Speckles outside the area are neglected

the phase of such a plane wave with three scalar phase settings $\theta = \{\theta_1, \theta_2, \theta_3\}$ and calculates the argument of the summation, so as three estimated pupil phases $\hat{\varphi} = \{\hat{\varphi}_1, \hat{\varphi}_2, \hat{\varphi}_3\}$ are obtained. These estimations are converted into control signal ν as shown in Eq. (4.24). Shaping the DM with these phases affects the power coupled into the single mode fiber. Thus, three optical powers $\eta = \{\eta_1, \eta_2, \eta_3\}$ are measured concurrently with each DM change, one for each pupil phase. Then, a parabolic fitting of these measured values is required, finding the optimum phase shift $\hat{\theta}_{\text{opt}2}$ at the position of the maximum coupling η_{max} . Repeating this procedure on the subsequent plane waves results in an optimal adaptation array $\hat{\theta}_{\text{opt}} = \{\hat{\theta}_{\text{opt}2}, \hat{\theta}_{\text{opt}3}, \dots, \hat{\theta}_{\text{opt}M}\}$, where each component is an optimum phase shift of its associated plane wave.

As an important remark, detailed in Sec. 4.2.4, a continuous variation of the scalar phase shift θ in Eq. (4.22) results in an oscillation of the coupled power η , which varies following a phase-shifted cosine function, see Fig. 4.15 (a). Consequently, to obtain the quadratic cost function for the optimization process, the values of θ need to be constrained to a range of π . Here, power variations will depend on the θ spacing. Especially when dealing with correlated phase distortions, the first set of plane wave optimization will show higher power excursions, while the subsequent optimization will be performed around the anterior optimums, reducing the variation of the coupling power. This control of the phase shift range is essential for real-time operation and considers gradual speckle evolution in a temporal scale of the coherence time of the field.

4.3 Numerical analysis of the adaptation method

Numerical analyses are carried out to illustrate the performance profiles offered by the proposed adaptation approach. The optical receiver of Fig. 4.7 is considered for the analyses and the tests are performed on synthetically built optical signals.

In order to synthesize the optical signals, Kolmogorov turbulence [16] is assumed. The atmospheric turbulence strength is quantified by the normalized aperture diameter D/r_0 , where D is the aperture diameter of the

single receiver system, and the wave-front coherence diameter r_0 describes the statistical spatial coherence of the field in the pupil plane. For a fixed aperture diameter, as the coherent diameter decreases, SMF coupling efficiency decreases. This phenomenon is typical in FSO from LEO satellites, where the elevation changes during the satellite pass.

A sufficiently large number of statistically uncorrelated phase wave-fronts is synthesized to simulate the effects of the turbulent propagation scenario. The phase fluctuations of the field are considered the dominant factor affecting the fiber coupling efficiency [37]. Hence, in most of the analyses, the single-screen phase method is adopted to impress the phase distortion into the optical signal. When required, the multiple-screen phase method is also used to see the impact of the scintillation and branch points in the overall performance of the algorithm.

4.3.1 Numerical wave-front generation

The single-screen phase method, introduced in Sec. 2.1.4, is well-suited for horizontal beam propagation. Nevertheless, it is also widely used in slant-path scenarios to approximate the effects of the turbulence in the wave-front. It is generally adopted because it gives more control over the type and magnitude of the aberrations involved, as it is entirely based on Zernike polynomials. Also, it is simple to implement and allows fast generation of a large number of fields. Regarding the dynamic range of the irradiance fluctuations of a focused beam in a Laser downlink scenario, the phase wave-front variance is considered to be the dominant factor over wave-front scintillation [58]. The reason is that laser downlinks require larger telescope apertures that produce an averaging of the intensity scintillation, but exposes the optical system to a larger amount of field phase decoherence. Consequently, as initially mentioned, the emulation of the turbulent channel effects can be done assuming a complex field with unitary amplitude $A(\mathbf{r}) = 1$ and an aberrated phase $\varphi(\mathbf{r})$ as

$$\mathbf{P}(\mathbf{r}) = A(\mathbf{r})\exp(j\varphi(\mathbf{r})), \quad (4.34)$$

where \mathbf{r} indicates a spatial coordinate. A phase wave-front $\varphi(\mathbf{r})$ in the pupil plane can be modeled as a sum of n_z Zernike polynomials \mathbf{Z}_l , each one weighted with a Zernike coefficient c_l as

$$\varphi(r, \psi) = \sum_{l=0}^{n_z} (c_l \mathbf{Z}_l(r, \psi)) \quad (4.35)$$

where r is the radial distance $0 < r < 1$, and ψ is the azimuthal angle. The Zernike polynomials are defined in a unit circle, based on the azimuthal and radial symmetry [64] as

$$\mathbf{Z}_l(r, \psi) = \mathbf{Z}_n^{|m|}(r, \psi) = \sqrt{n+1} \mathbf{R}_n^{|m|}(r) \begin{cases} \sqrt{2} \cos(|m|\psi) & m \neq 0 \text{ even} \\ \sqrt{2} \sin(|m|\psi) & m \neq 0 \text{ odd} \\ 1 & m = 0 \end{cases} \quad (4.36)$$

where $\mathbf{R}_n^{|m|}(r)$ is a radial polynomial with m and n being the azimuthal and radial frequencies, respectively [64]. The values of m and n are calculated using the mode number l as

$$n = \left(1 + \sqrt{8l - 7}\right) / 2 - 1 \quad (4.37)$$

$$m = l - (n + 1)(n/2) - 1, \quad (4.38)$$

and the radial polynomial $\mathbf{R}_n^m(r)$ is calculated as,

$$\mathbf{R}_n^m(r) = \sum_{s=0}^{(n-m)/2} \frac{(-1)^s (n-s)!}{s! \left[\frac{(n+m)}{2} - s \right]! \left[\frac{(n-m)}{2} - s \right]!} r^{(n-2s)}. \quad (4.39)$$

The Zernike coefficients c_l are obtained using a single value decomposition (SVD) of the covariance matrix \mathbf{E} of the Zernike modes. First, the covariance matrix is calculated as

$$\mathbf{E}(c_l, c_{l'}) = \frac{K_{zz'} \delta_z \Gamma[(n+n'-5/3)/2]}{\Gamma((n-n'+17/3)/2) \Gamma((n'-n+17/3)/2) \Gamma((n+n'+23/3)/2)} \quad (4.40)$$

$$\delta_z = 1 \quad m = m' \quad (4.41)$$

$$\delta_z = 0 \quad m \neq m' \quad (4.42)$$

$$K_{zz'} = 2.2698 (-1)^{(n+n'-2m)/2} \sqrt{(n+1)(n'+1)}, \quad (4.43)$$

where n, m and n', m' given by Eq. 4.37 and Eq. 4.38 and considering,

$$\mathbf{E}(c_l, c_{l'}) = 0 \quad l - l' = \text{odd}. \quad (4.44)$$

Second, with the covariance matrix $\mathbf{E}(c_l, c_{l'})$, the SVD is performed,

$$[\mathbf{U}, \mathbf{S}, \mathbf{V}] = \text{SVD}(\mathbf{E}) \quad (4.45)$$

Then, Zernike coefficients c_l are calculated using the Karhunen-Loève method to achieve random and uncorrelated coefficients [136]. In the Karhunen-Loève method, the natural random array b_n of length nz is generated with a variance given by $\sqrt{\mathbf{S}}$. Finally, the array of coefficients c_l is calculated

$$c_l = \mathbf{U} b_n, \quad (4.46)$$

and the single screen phase wave-front $\varphi(r, \psi)$ is generated for a predefined D/r_0 as

$$\varphi(r, \psi) = \left(\frac{D}{r_0} \right)^{5/6} \sum_{l=0}^{nz} (c_l \mathbf{Z}_l(r, \psi)) \quad (4.47)$$

To validate a generated set of uncorrelated fields, the Fried parameter r_0 can be calculated from a set of N complex fields $\mathbf{P}(\mathbf{r})$ in the pupil plane by using the second-order field moment Γ_2 or Mutual Coherence Function (MCF) [20], see Eq. (2.14)-(2.16). The MCF is calculated in the pupil plane as,

$$\Gamma_2(\mathbf{r}_1, \mathbf{r}_2) = \langle \mathbf{P}^*(\mathbf{r}_1) \mathbf{P}(\mathbf{r}_2) \rangle, \quad (4.48)$$

where $\langle \rangle$ denotes ensemble average, \mathbf{r}_1 and \mathbf{r}_2 represents points in the transverse plane, and $\mathbf{P}^*(\mathbf{r})$ indicates the complex conjugate of the field. From the MCF, and considering fields of unitary amplitude, the modulus of the complex degree of coherence (DOC) is equal to,

$$\text{DOC} = |\langle \mathbf{P}^*(\mathbf{r}_1) \mathbf{P}(\mathbf{r}_2) \rangle|. \quad (4.49)$$

Here, the DOC describes the loss of spatial coherence of the phase wave-front. The coherent radius ρ_0 can be approximated by the $1/e$ points of the DOC. Numerically, this can be performed through the ensemble average of the N pupil fields $\mathbf{P}(\mathbf{r})$ as,

$$\text{DOC} = \left| \frac{1}{N} \sum_{t=1}^N [\mathbf{P}_t^*(\mathbf{r}) \mathbf{P}_t(\mathbf{r}_{(0,0)})] \right|, \quad (4.50)$$

where \mathbf{r} represents all the points of the wave-front respect to the central coordinate $\mathbf{r}_{(0,0)}$ of the field. Then, the $r_0 \approx 2.1\rho_0$ is calculated with the coherent area A_{DOC} of the DOC, defined by the distance between the points where the DOC falls to $1/e$ of its maximum.

$$r_0 = \sqrt{(4/\pi) A_{\text{DOC}}} \quad (4.51)$$

To verify the method, a comparison between the reference Fried parameter $r_{0 \text{ ref}}$ used to create sets of 1000

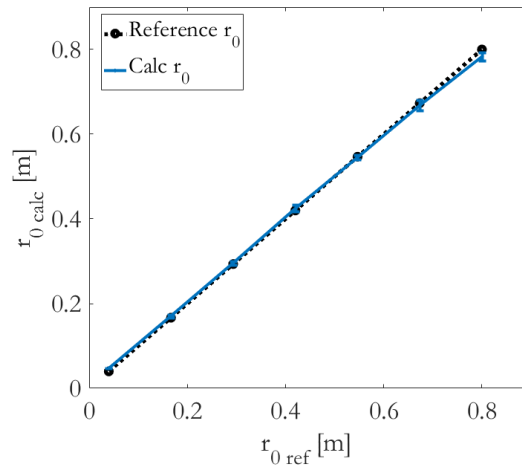


Fig. 4.18: Comparison between the reference Fried parameter $r_{0 \text{ ref}}$ used to create sets of 1000 fields for different turbulent conditions, and the estimated Fried $r_{0 \text{ calc}}$ calculated from these fields. Each field is created with 256×256 pixels and 600 Zernike polynomials.

fields for different turbulence conditions (dotted plot), and the estimated Fried $r_{0 \text{ calc}}$ calculated from these fields using the above-described method, is shown in Fig. 4.18. Each field is created with 256×256 pixels and 600 Zernike polynomials. The good match between the reference and calculated curves show that the simulation of turbulent fields is accurate.

The multiple-screen phase method is optimum for slant-path propagation but more complex to implement. In this work, the phase-screens are generated with an in-house software tool developed by the German Aerospace Center (DLR) called Pilab [62, 137–139]. This tool propagates the optical field through several phase screen layers, created based upon a given path length, turbulence profile, and elevation angle. This tool can also generate correlated fields, which are used Sec. 4.3.4 and Sec. 5.4.4 to evaluate the concept for the dynamic correction of the fields.

In the analyses, the Zernike-based generated phase wave-fronts are generated with no less than 600 polynomials. In both cases, each wave-front is created with a size of 256×256 pixels and a sampling spacing of 1.56 millimeters. This considers a received laser wave-front captured by the 40 cm diameter telescope aperture. To obtain the focal image with sufficient speckle resolution, each wave-front is zero padded and then Fourier

transformed. The size of the focal image, which represents the size of the CCD, is 256×256 pixels. The simulation considers a minimum of 7×7 pixels for resolving the minimum speckle size, which corresponds to the Airy pattern diameter when its intensity falls to $1/e^2$. At this stage, the compensation of the distorted phase is performed ideally without special consideration of a specific DM.

4.3.2 Algorithm performance under the effect of signal noise

The first analysis evaluates the capacity of the algorithm to improve the quality of the coupled signal by the correction of the wave-front distortions with an incremental number of speckles. An scenario of $D/r_0 = 10$ with $D = 40$ cm is considered for the analysis. This represents a realistic condition of a LEO downlink at 5° elevation from the horizon [140, 141]. Because noise affects the optimization process, introducing unwanted variations of the signal, its impact is also quantified. The overall analysis is performed using the single-screen phase method. A comparison with the case of slant-path propagation under the effect of scintillation and phase singularities is also performed.

Figure 4.19 shows (a) the mean SMF coupling efficiency, and (b) the normalized variance of the received signal, as a function of the number of compensated speckle spots and the SNR of the optimization signal. The normalized histogram of the coupled signal at the maximum of each curve is shown in plot (c). The optimum number of corrected speckles for different values of SNR is depicted in plot (d).

In Fig. 4.19 (a), the tilt correction of the first speckle greatly increases the coupling efficiency. Because the first speckle has a higher peak intensity level, the impact of the noise is minimum. For the case of $\text{SNR} = 50$ dB, the correction of additional speckles $M \geq 2$ improves the fiber coupling efficiency until saturation is reached (curve A). At this point, the correction of further speckles with lower intensity does not significantly contribute to the overall coupling. The same behavior is seen in Fig. 4.19 (b), where the normalized variance rapidly falls to a plateau for $M \geq 36$. Instead, with lower $\text{SNR} = [30, 10]$ dB, noise-induced deviations of the coupling efficiency affect the phase shift optimization process, penalizing the coupling gain and limiting the reduction of the variance (curves B and C). Note that keeping this variance minimal is a key factor for fading-free data links in the FSO scenarios. Furthermore, the performance with low SNR is dependent on the number of corrected speckles. The curves of $\text{SNR} = 30$ dB and 10 dB, in Fig. 4.19 (a), show maximums at $M \approx 16$ and $M \approx 6$, respectively, and negative slopes with an increasing number of corrected speckles. After these maximums, the noise has a greater effect in the optimization of plane waves associated with speckles of lower intensity. This leads to sub-optimal phase shifts and propagates errors, which affects the subsequent optimizations and reduces the overall performance.

The performance of the algorithm in a slant-path scenario (curve E), under the effects of scintillation and phase singularities, shows a penalty of 2 dB compared with the case of single-screen method. However, both curves of $\text{SNR} = 50$ dB also show identical slopes, reaching the plateau with a similar number of corrected speckles. The final normalized variance is slightly increased by 1 dB, but the slope does not significantly change in comparison with the single-screen method, still showing a reduction in the signal variance higher than 6 dB with less than 20 corrected speckles.

Figure 4.19 (c) depicts the normalized histogram of the coupling efficiency at the maximum of each curve, where the fields are corrected with the above-mentioned $M = [6, 16, 36]$. An improvement in gain and variance

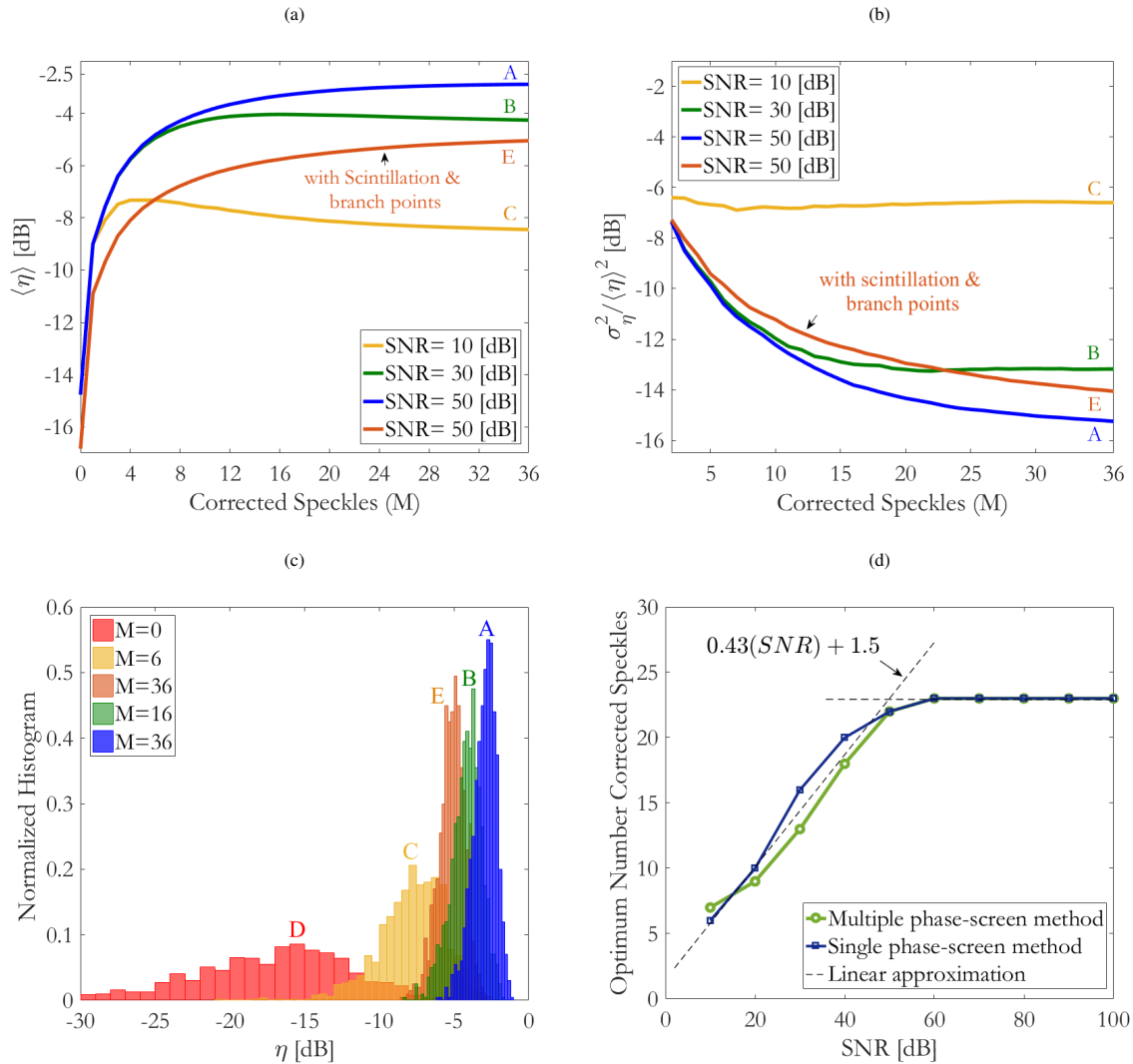


Fig. 4.19: (a) Mean SMF coupling efficiency and (b) normalized variance of the received signal as a function of the number of corrected speckle spots and the signal to noise ratio of the optimization signal (SNR). (c) Normalized histogram at the maximum of each curve. (d) Optimum number of corrected speckles for different SNR values of the optimization signal. All the analyses correspond to an scenario $D/r_0 = 10$ with a $D = 40$ cm.

compared to the absence of AO compensation (histogram D) can be appreciated. The algorithm seems to be robust facing scintillation (histogram E); despite the impact of the scintillation in the general gain, the variance remains comparatively similar to the case shown in histogram “A”.

Figure. 4.19 (d) extends the SNR analysis and establishes the optimum number of corrected speckles in the presence of different levels of noise. The result establishes a threshold around 50 dB, after which the noise has minimum impact. The optimum number of speckles to be corrected for varying SNR can be approximated as $M_{\text{opt}} = 0.43\text{SNR} + 1.5$ for $10 \leq \text{SNR} \leq 50\text{dB}$.

As explained in Sec. 4.1.1, the use of $(D/r_0)^2$ overestimates the effective number of speckles that need to be corrected. From the curves “A” and “E” in Fig. 4.19 (a,d), saturation is reached with M between 20 and 25 corrected speckles, which represents 1/4 of the 100 speckles, expected for $D/r_0 = 10$. Thus, the metric for selecting the M_{opt} can be chosen at the point where the curve of coupling efficiency reaches saturation and additional improvements are smaller than $\Delta\eta \leq 0.05$ dB. This $\Delta\eta$ corresponds to an increment smaller than 1%

of the total focal intensity.

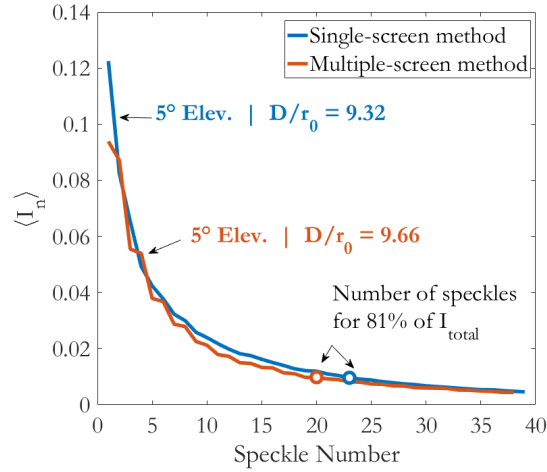


Fig. 4.20: Percentage of total focal intensity per speckle. Comparison between single-screen and multiple-screen method. Markers indicate the required speckles to reach 81% of the total focal intensity

Figure 4.20 shows the distribution of the mean normalized intensity per speckle from an ensemble of 500 analyzed focal fields of a similar scenario. The procedure for the image processing follows the description in Sec. 4.1.1. The analysis considers the single and multiple screen methods and the markers indicate the number of speckles to achieve 81% of the total focal intensity. For the scenario $D/r_0 \approx 9.3$, around 23 speckles contain 81% of the total focal intensity. For slant-path propagation, the number rounds to 20 speckles. Comparing this result with the Fig. 4.19 (a), the equivalent case (curve A) also reaches saturation with a similar number of processed speckles.

4.3.3 Overall performance and bandwidth utilization

The previous analysis can be extended to a broader range of turbulence conditions and a formula for the optimum number of corrected speckles M_{opt} can be obtained.

The main analysis for the discovery of the M_{opt} is performed over a range $D/r_0 = 1$ to $D/r_0 = 21$. The telescope aperture size is $D = 40$ cm and each scenario is emulated with 500 fields of unitary amplitude and phase generated with the single-screen phase method. On each scenario, every field is corrected with $M = 100$ speckles and the saturation point is identified to define the M_{opt} , as defined in the previous section. Then, the mean is calculated to define the optimum number of corrected speckles for that particular turbulent channel. The curve M_1 in Fig. 4.21 (a) shows these optimums for each scenario. In order to further reduce the required loop bandwidth, a trade-off between M and the maximum possible coupling efficiency can be established. Hence, the curve M_2 considers a coupling penalty up to 2 dB from the saturation level, allowing an important reduction in the required bandwidth. Both curves can be fitted with the following equations,

$$M_1 = \left[-0.057 \left(\frac{D}{r_0} \right)^2 + 2.9 \left(\frac{D}{r_0} \right) + -0.3 \right] \quad (4.52)$$

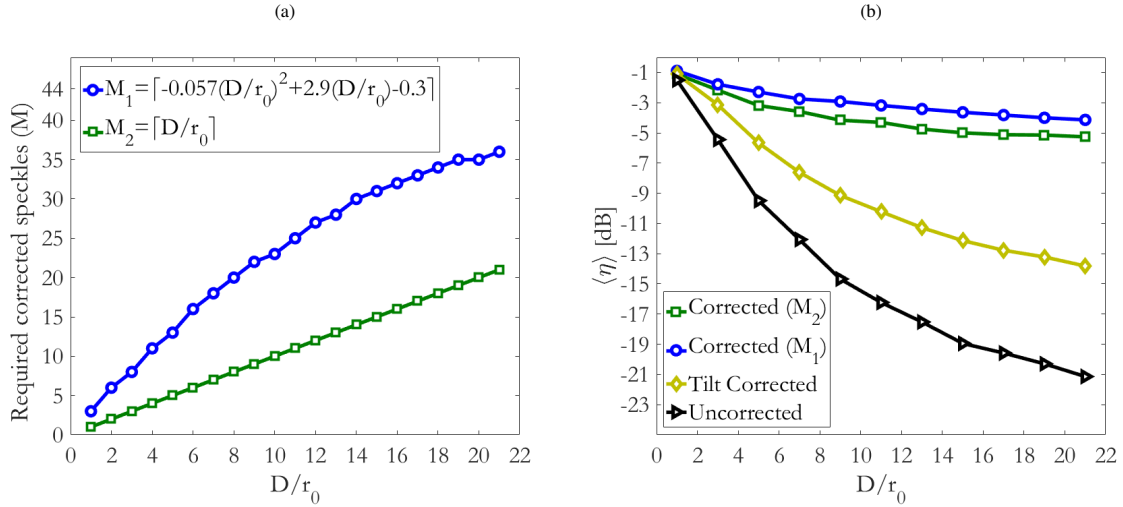


Fig. 4.21: (a) Required number of corrected speckles for different turbulent scenarios considering maximum performance M_1 and a penalty of 1 dB from the maximum M_2 . (b) Mean SMF coupling efficiency for different turbulent scenarios with M_1 and M_2 corrected speckles

$$M_2 = \left\lceil \frac{D}{r_0} \right\rceil \quad (4.53)$$

A comparative plot of the algorithm performance is shown in Fig. 4.21 (b). The mean SMF coupling efficiency for each turbulent scenario is plotted considering a number of corrected speckles given by the curves M_1 and M_2 . The signal improvement is contrasted with the cases where the fields are uncorrected and only compensated in tilt. The method offers a significant gain especially in cases of very high turbulence. For example, in the scenario of strong turbulence $D/r_0 = 10$ the number of required iterations falls from $N_{\text{iter}} = 82$ ($M = 28$ speckles) to $N_{\text{iter}} = 28$ ($M = 10$ speckles), which represents a drastic reduction in the loop bandwidth utilization. When compared with the Modal Stochastic Parallel Gradient Descent (MSPGD) algorithm, which typically requires around 100 iterations to converge, a reduction of 70% in the required loop bandwidth is appreciated.

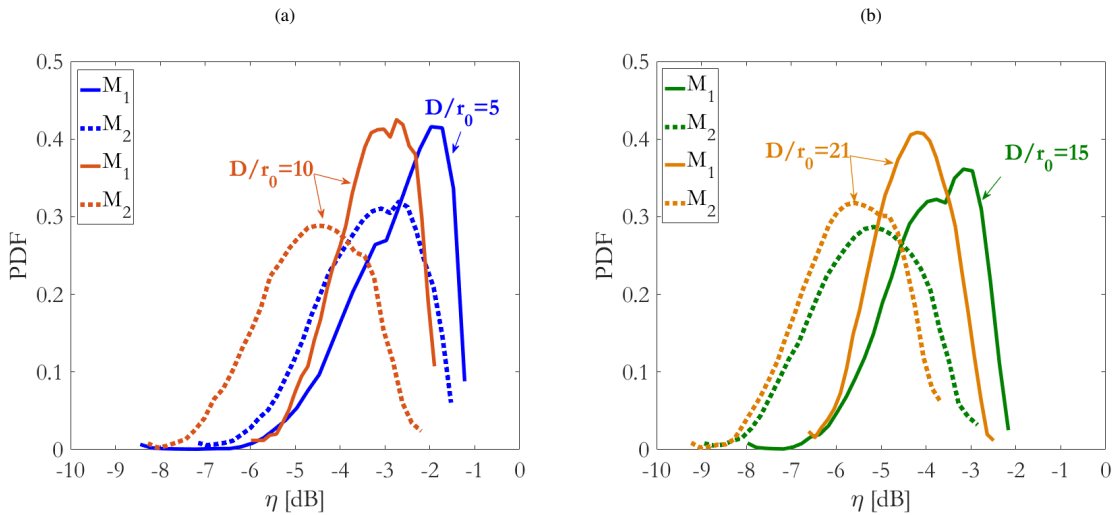


Fig. 4.22: Coupling efficiency distribution for (a) $D/r_0 = [5, 10]$ and (b) $D/r_0 = [15, 21]$, after the correction of the fields with M_1 (continuous plot) and M_2 (dashed plots) speckles.

The PDF for the scenarios of strong turbulence, corrected with M_1 (continuous plot) and M_2 (dashed plot)

speckles, are visualized in Fig. 4.22. The reduction in the number of corrected speckles, from $M1$ to $M2$, introduces the expected penalty in the coupling gain but does not greatly increase the variance of η . Particularly with higher D/r_0 , the number of corrected speckles can be dynamically selected in between the above-mentioned range to further reduce the signal variance and increase the signal gain. This flexibility in the correction process represents one of the principal strengths of the method.

4.3.4 Considerations for a closed-loop operation

In a real scenario, the turbulence induces a gradual change of the phase wave-front in the time scale of the field coherence time τ_0 , see Sec. 2.1.3.2. During this time, typically around 1 millisecond [28], the AO system needs to correct the first distorted field and lock the system in order to follow the changes dynamically. If the system fails to do that or requires correction times longer than τ_0 , the estimated DM shape mismatches the distorted phase and the coupled signal deteriorates. The control of this dynamic correction is a challenging task that involves AO loop bandwidths in the order of kilohertz in real-time-based solutions.

This process is even more challenging on iterative systems, since the correction requires several iterations and, unavoidably, the field will evolve in between the initial and final stage of the process. Assuming that the new state of the phase is approximated correctly within a time $t < \tau_0$, phase mismatches are expected to produce a certain degree of signal fade.

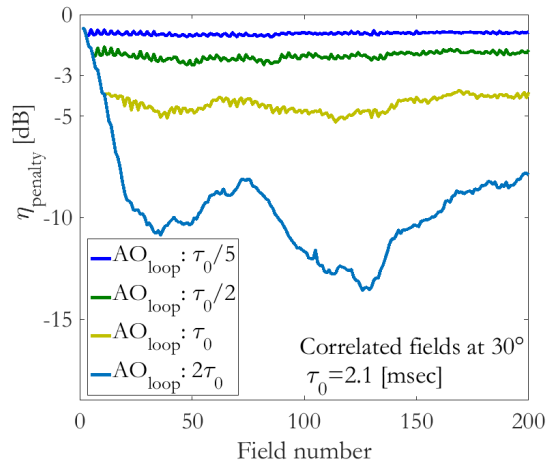


Fig. 4.23: Coupling penalty of correlated fields being corrected with their previous field states, considering a dynamic time gap of a fraction of t_0 between fields.

Figure 4.23 shows the SMF coupling penalty due to the delay in the correction. The set of fields are created with an in-house DLR tool called Pilab, for a scenario of a LEO-downlink at 30° elevation and $D/r_0 = 6$, considering an aperture $D = 40$ cm, a $\tau_0 = 2.1$ msec, and a transversal wind velocity $V_t = 10$ m/sec. When the AO loop time is short, $\tau_0/5$ and $\tau_0/2$, the coupling penalty remains below -3 dB. If the iterative process needs an AO loop time $t \geq \tau_0$, the penalty drastically increases since the fields become uncorrelated. From this plot, it is evident the importance of having an iterative system capable of performing the task with a minimum number of iterations. An achievable goal is not the total suppression of these fades. Instead, by maintaining the

mean and variance of the coupled signal within tolerable margins, sufficient signal stability may allow a stable communication link.

This work does not go into complex concepts of control theory. Instead, it proposes a preliminary approach for the dynamic processing of the images and correction of the field, adapted to the proposed AO method. In line with this, a small modification of the optical setup of Fig. 4.7 needs to be done. As shown in Fig. 4.24, the

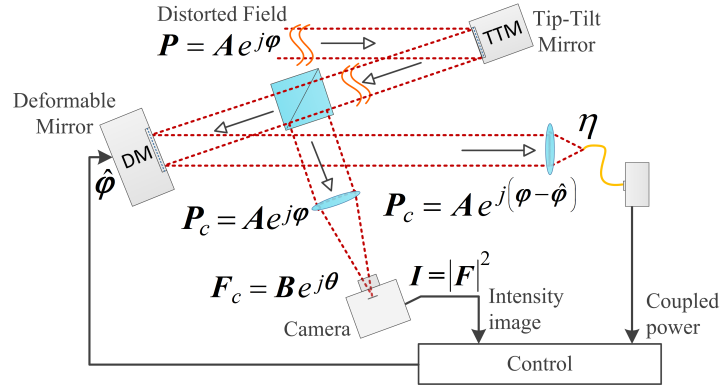


Fig. 4.24: Optical receiver adapted for a dynamic implementation of the method. The camera is positioned before the DM. No change in the algorithm, neither implementation of the method is required. The nomenclature follows the description of Fig. 4.7.

focal camera is now positioned before the DM to capture each focal speckle pattern without being altered by the shaping of the mirror. This change does not modify in any sense the concept or the AO method and allows the continuous tracking of the speckle evolution.

Figure 4.25 illustrates the idea for the dynamic correction. The first field realization I^{h-1} is acquired, processed with the method described in Sec. 4.2.5, and used to optimize the distorted field. Here, h represents a field realization. Another image I^h is acquired after a time $t < \tau_0$. In the second image the focal speckle pattern has evolved. Those speckles with minimum change in their position are adjusted with small variations $\Delta\theta$ around the anterior optimum phase shift $\hat{\theta}_{opt}$. This minimizes power fluctuations in the fiber. The speckles with significant changes in their positions are treated like new ones and optimized accordingly.

The decision-making process for the plane waves update and phase shift assignment is shown in the algorithm 1. Two inputs are required; the current focal image I^{h-1} which is being optimized, and the subsequent focal image I^h captured after a time $t < \tau_0$. The output of the algorithm is an array of new phase shift ranges θ^h to be used in the optimization of the plane waves of the field h . The coordinates components $[c_l^{h-1}]$ of the l speckle and $h-1$ field under correction are known. The coordinates components $[c_l^h]$ of the l speckle and h field need to be extracted and compared with the ones of the $h-1$ field realization. For each l speckle, the Euclidean distance $\|c_l^h - c_l^{h-1}\|$ is calculated and compared with a threshold Δr . If the speckle l in both realizations is separated more than the threshold, then the speckle in the field h is assumed to be new and a larger phase shift range for optimization $\{\pi/100, \pi/3, 2\pi/3\}$ is assigned. Otherwise, the speckle l in the realization h is considered to be the same as the one in the previous realization $h-1$ and the phase shift range is assigned around the known optimum θ_l^{h-1} , spaced by $\Delta\theta_2 = \theta_l^{h-1}/3$. Once all the M speckles have been processed, the new range of phase shifts θ^h for the correction of the field h is ready. Hence, the new field estimation P^h will evolve from the previous P^{h-1} .

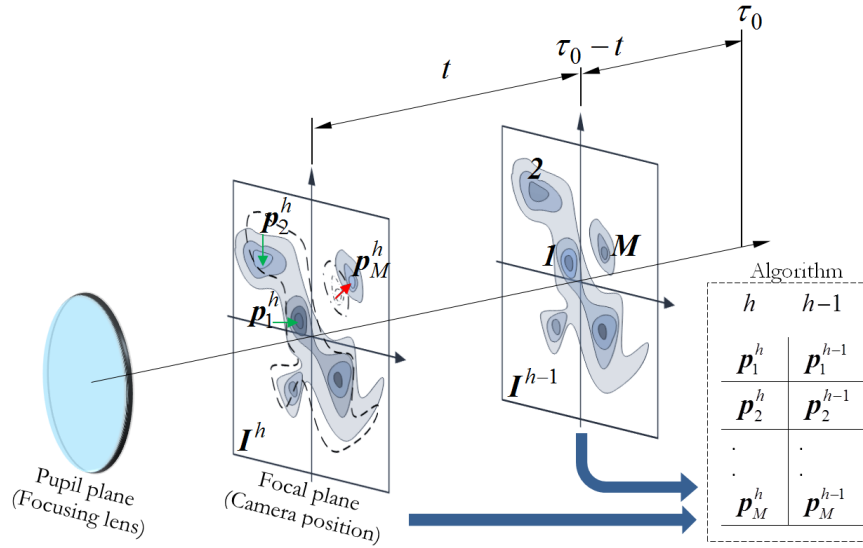


Fig. 4.25: Graphical representation of the dynamic processing of the speckle pattern. The image realization I^h is captured after a time t from the previously captured image I^{h-1} . The process is performed within the coherence time of the field τ_0 . The coordinates r_l of the speckles are compared as described in the algorithm 1.

Algorithm 1: Dynamic definition of phase shifts

INPUT: I^{h-1}, I^h
OUTPUT: θ^h

- 1: $I^{h-1} \rightarrow [c_l^{h-1}] \quad l = \{1, 2, \dots, M\}$
- 2: $I^h \rightarrow [c_l^h] \quad l = \{1, 2, \dots, M\}$
- 3: **while** $l < M$ **do**
- 4: **if** $\|c_l^h - c_l^{h-1}\| > \Delta r$ **then**
- 5: $\theta_l^h \leftarrow \{\pi/100, \pi/3, 2\pi/3\}$
- 6: **else**
- 7: $\theta_l^h \leftarrow \{\theta_l^{h-1} - \Delta\theta_2, \theta_l^{h-1}, \theta_l^{h-1} + \Delta\theta_2\} \quad \Delta\theta_2 = \theta_l^{h-1}/3$
- 8: **return** $\theta^h = [\theta_l^h] \quad l = \{1, 2, \dots, M\}$

- Intensity images
- Updated array of phase shifts
- Speckle coordinates field $h-1$
- Speckle coordinates field h
- Evaluate M speckles
- Euclidean distance
- Extended phase shift range
- Reduced phase shift range
- phase shifts for field h

$$P^h \approx \sum_{l=1}^M \left\{ \sqrt{I_l^h} \exp(j\theta_l^h) \exp[j(\mathbf{k}_l^h \cdot \mathbf{r})] \right\} \quad (4.54)$$

Figure. 4.26(a) shows a numerical simulation of the proposed algorithm for the dynamic correction of correlated field. The fields were corrected considering a decorrelation of $\tau_0/3$. When the algorithm is not used and each field is corrected independently, deep fades occur reaching up to -9 dB of coupling efficiency loss. When the algorithm is employed and tracking of the previous corrections is used, the signal fading between fields gets reduced, improving the coupling distribution shown in the PDF of Fig. 4.26(b). The smaller tail of the PDF after using the algorithm represents less signal fading and a reduction of the probability of error in transmission. Further analyses will be shown in the experimental test of the algorithm in chapter. 5.

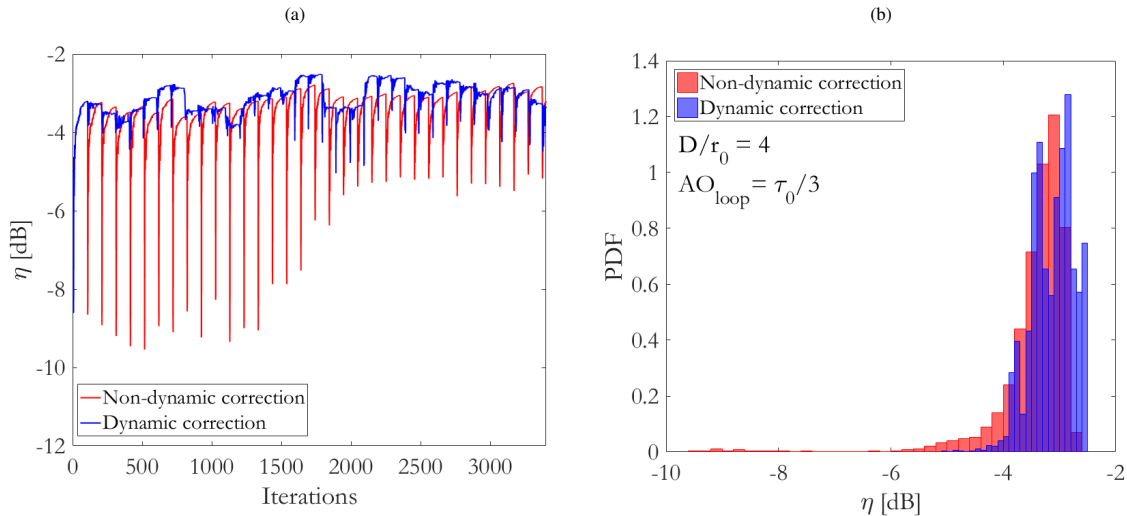


Fig. 4.26: (a) Numerical simulation of the proposed algorithm for the dynamic correction of correlated field. (b) PDF of the two different types of correction. The scenario corresponds to a 30° elevation link with $D/r_0 \approx 4$.

4.4 Conclusion of the chapter

This chapter has presented a novel phase-retrieval technique that indirectly determines the unknown phase wavefront from focal-plane intensity measurements. The adaptation approach is based on sequential optimization of the speckle pattern and works by the iterative update of the phases of individual speckles to maximize the received power. This approach offers a useful set of properties:

- The pupil modes (phases of the plane waves) to be optimized and combined can be known in advance and optimized with only three power measurement. This allows to estimate and manage the total number of required iterations for different turbulent regimes
- The technique only needs one image per field realization to perform the task. On each image, only the peak coordinates and magnitude of the focal speckles are required for the selection of plane waves. The camera can be replaced by any other sensor capable of providing such information, thus avoiding the possible bottleneck associated with the camera maximum frame rate
- It has a straightforward implementation and does not need complex mathematical processes; thus computation costs can be minimized
- The bandwidth utilization can be managed in real time depending on the turbulence conditions. Hence, when facing scenarios of low turbulence fewer bright speckles are considered, resulting in a significant reduction in the loop bandwidth utilization of the system. This property implies a truly flexible method able to adapt to the turbulence conditions
- The technique has the capacity of recovering the phase lock fast because it directly addresses the focal energy and searches for its coherent maximization, all carried out in a time scale of the field coherence time

The numerical results show that the proposed technique can deliver substantial signal gain and variance reduction by the sequential processing of the focal speckles and the parabolic optimization of their phases. There is a good overall performance in all range of turbulence conditions, and the technique is robust facing highly scintillated fields. It also shows robustness against signal noise, experiencing only a 2 dB gain penalty and 1 dB of variance increment facing a 20 dB SNR deterioration. The analyses have been extended beyond the expected turbulence conditions in FSOC LEO-downlinks. Here, typical dimensions of a telescope aperture range between $40 \leq D \leq 80$ cm, thus, based on measured r_0 at several LEO elevations [141], expected scenarios are not likely to be higher than $D/r_0 = 11$, and generally $D/r_0 \leq 6$. In principle, assuming less than 60 iterations ($M \approx 20$) allows a gain of $G_\eta \approx 6$ dB with respect to only tilt compensation, and also approximately 6 dB of reduction in the variance.

A first approach for the dynamic correction of the field has been presented. This approach tracks the position of the speckles of subsequent field realizations and optimize the associated plane waves if a change is significant. Naturally, the image acquisition of a new field state must be performed during the optimization process of the anterior one. This requirement moves the camera in front of the DM, which does not represent a change to the method but it allows continuous tracking of the field evolution without the influence of the DM shaping. The first numerical trials show that the idea effectively reduces the signal fading of the iterative correction between fields, but the performance is not ideal and this approach certainly needs more refinement, especially for cases of stronger turbulence. Experimental results are shown in chapter 5.

Overall, the numerical analyses show that this technique can compensate the distorted phase wave-front and increase the signal coupled with a significant reduction in the required number of iterations, resulting in a loop bandwidth utilization within reach of commercially available deformable mirrors [115].

Chapter 5

EXPERIMENTAL VALIDATION

THIS chapter details the experimental tests carried out for the proof of concept of the proposed AO solution. At this point, the goal of the thesis is to validate the working principle of the newly proposed method, to be refined in a future working prototype. The validation is performed under laboratory conditions in a non-real time regime. It seeks to support the made assumptions related to the plane wave decomposition of the speckle pattern and parabolic optimization. It is intended to demonstrate that these assumptions are not purely theoretical; instead, they have a practical application leading to the claimed benefits in the improvement of the signal quality and reduction of the bandwidth utilization.

A laboratory test requires the consideration of hardware constraints. The main impediment for a real-time evaluation of this concept is associated with limitations in the DM bandwidth, camera frame rate, and mostly due to the need of a proper control solution, which is still an open task. Assuming a suitable DM and control solution, still the camera frame rate would represent a constraint for a real-time evaluation of the concept. This factor does not constitute a hard constraint for future implementations because the technique only needs to know the spatial coordinates and magnitude of each speckle peak, allowing the camera to be replaced by a more suitable and faster sensor. The experimental tests do consider vibrations of the optical setup, signal noise, and hardware limitations of the turbulence emulation to quantify the method performance within realistic conditions. To emulate the turbulent channel, the tests are carried out first with decorrelated phase screens created with the single screen phase method, and second with an in-house DLR software that generate correlated screens of phase to test the concept of dynamic speckle correction.

5.1 Experimental setup

The objective of this section is to validate in the laboratory the theoretical concept and numerical analyses. It is aimed to demonstrate that this technique increases the mean coupled power and reduces its variance, minimizing the overall bandwidth utilization. For such purpose, a testbed is built in the laboratory. The block diagram of the design is shown in Fig. 5.1 (a). This diagram highlights the transmitter, turbulent channel, and receiver sections with the principal hardware components. The schematic of the optical design and the image of the built setup are shown in Fig. 5.1 (b) and Fig. 5.2, respectively. The trajectory of the laser beam is represented with the arrows. The relevant hardware components are listed in table 5.1. Note that this design follows the initial concept presented in Sec. 4.2.1, Fig. 4.7 and Fig. 4.24.

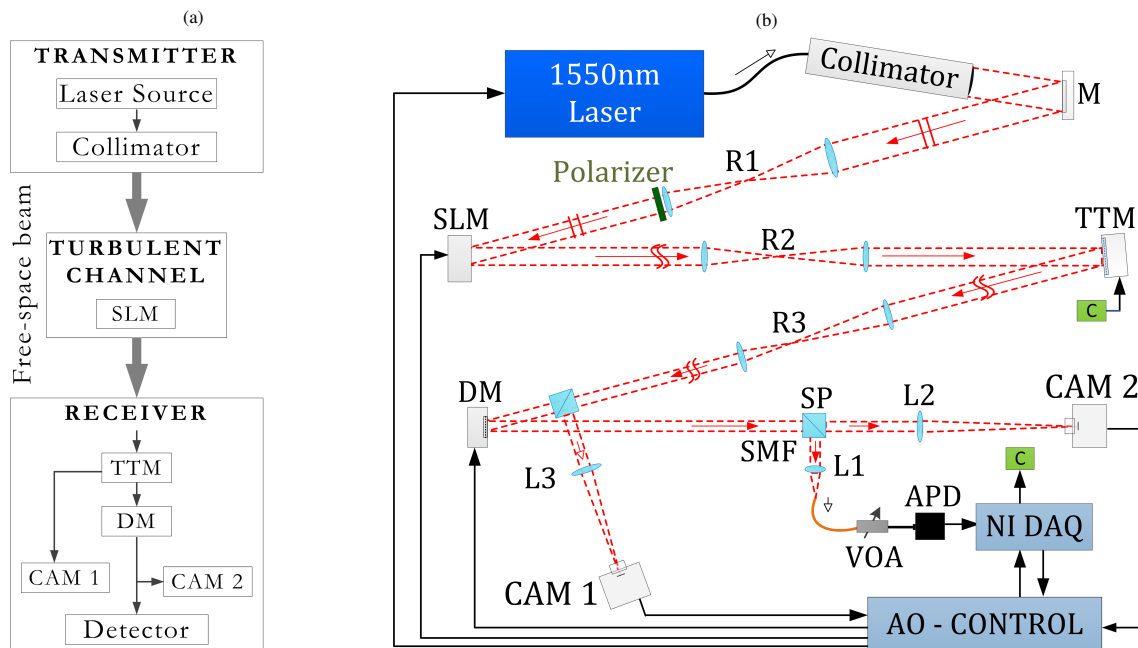


Fig. 5.1: (a) Block diagram of the laser downlink emulator, highlighting the transmitter, turbulent channel, and receiver sections, as well as the involved hardware. (b) Optical setup design to emulate the free-space link affected by the turbulence and corrected with the proposed iterative AO method.

The description of the setup is as follows:

- To emulate a laser downlink from a LEO satellite one must consider that, in this scenario, the laser is exposed to the turbulence in the last 20 km of the atmosphere, and the beam wave-front can be modeled as a plane wave, see Sec. 1.2. Here, a laser source is collimated to generate a free-space laser beam propagating towards the detector. The collimator is built with a large focal length and ring stops to produce the intended profile. This approach also induces some ring-like diffraction effect in the intensity pattern, which may reduce the maximum possible coupling efficiency but do not alter the functionality of the method.
- The beam size is modified throughout the system using a set of three optical relay systems (R1-3). After the first relay (R1) the beam passes through an H-polarizer previous being reflected in a spatial light modulator (SLM), which is used to impress the phase-only distortions in the wave-front. The SLM offers

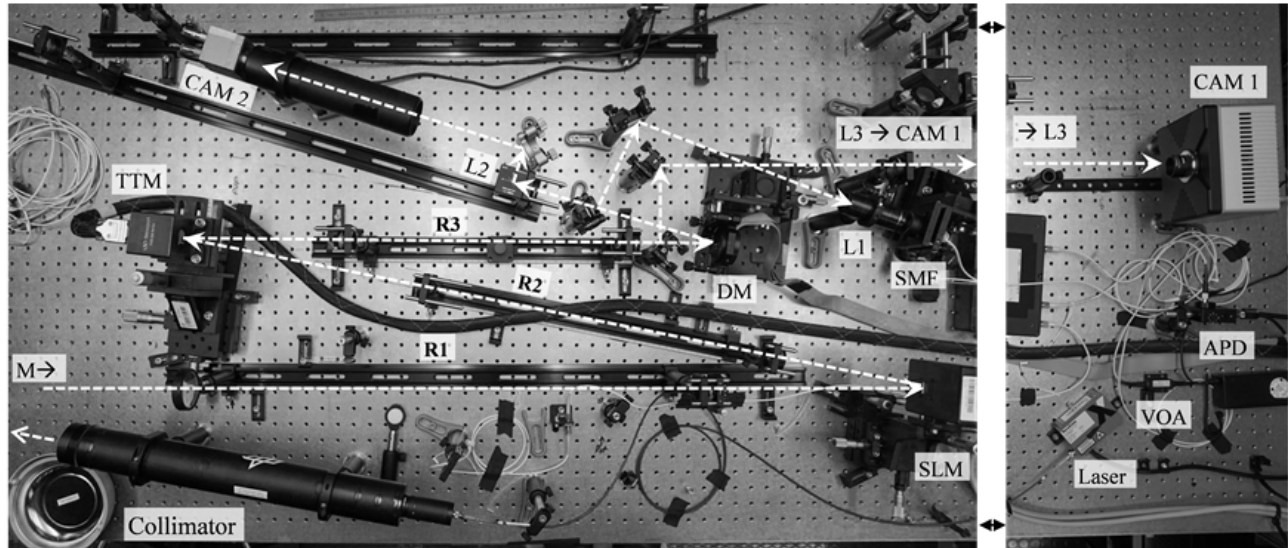


Fig. 5.2: Optical setup of the free-space laser downlink emulator.

<i>Hardware</i>	<i>Type</i>	<i>Details</i>
LASER	TeraXion PS-LM	1550 nm Lwidth < 1MHz Pmax= 100 mW
SLM	Hamamatsu X10468-LCOS	Windows=15.8x12 mm 800x600 pixels 20 μm pixel pitch Resolution= 25 lp/mm
TTM	Newport FSM-300	Angular Range= $\pm 26.2\text{mrad}$ Closed-loop= 600 Hz Resolution= $\approx 3\mu\text{rad}$
CAM 1	Xenics Cheetah 640-CL	InGaAs sensor 640x512 pixels Pixel Size 20 μm Frame rate= 400 Hz (Full)
CAM 2	Xenics Xeva XS-1.7-320	InGaAs sensor 320x256 pixels Pixel Size 30 μm Frame rate= 100 Hz (Full)
DM	BMC Multi-X-CL140-DM	Membrane 12x12 actuators Max. Stroke= 3.7 μm Mirror BW= 3.5 KHz
APD	Thorlabs PDA20CS-EC	InGaAs Gain: 0 - 70 dB
DAQ	NI BNC-2110 PCI-6221	12 bits
VOA	Thorlabs VOA50	50 dB

Table 5.1: List of hardware components of the optical setup.

flexibility to imprint the desired set of phase-screens for different turbulent conditions. It also gives the possibility to repeat experiments and verify the performance with identical field states. Additionally, it facilitates the synchronization of the experiment when a large set of screens is needed for testing. The drawback here is mostly linked with a phase wrapping effect in scenarios of strong turbulence, explained in Sec. 5.2.1.

- After the SLM, the distorted beam is guided to a tip-tilt mirror (TTM) to correct the phase-front tilt. In

this experiment, the TTM is used to maintain the illumination of the active area of the DM, coaligned with the fiber and camera axis.

- After the TTM, the beam is newly compressed with the relay (R3) to a diameter of 3.7 mm and split. One beam is focused in an infrared camera (CAM 1) with a 500 mm lens (L3) to obtain approximately 28×28 pixels per speckle. This camera is used for the optimization process. The second beam is reflected in a membrane-based DM. Note that the CAM 1 is located before the DM following the design of Fig. 4.24 and required for the test of the correction of correlated fields.
- The beam reflected in the DM is split and focused in a single mode fiber (SMF) and a second infrared camera (CAM 2). This camera is used to verify the evolution of the focal speckle pattern during the correction process, where a lens (L2) of 500 mm is selected to assure sufficient speckle resolution ($\approx 18 \times 18$ pixels). For the SMF, a lens (L1) of 19 mm allows a maximum coupling efficiency of $\approx 60\%$ when the wave-front is assumed with minimum aberration.
- The signal for the optimization process is measured with an avalanche photodetector (APD). The coupled power can be attenuated with a single mode variable optical attenuator (VOA). The output electrical signal from the photodetector is acquired with a data acquisition system (DAQ).

5.2 Hardware limitations

As mentioned before, the experiments are performed in a non-real-time regime. The algorithm, as well as the signal acquisition and control of the hardware, are implemented in Matlab. The following sections detail the characteristics and limitations of the relevant hardware of the AO system.

5.2.1 Spatial Light Modulator

The SLM is a device capable of modulating the amplitude and phase of a wavefront. In this case, the LCOS-SLM is a reflective phase-only modulator [5]. The working principle of this type of SLM is represented in Fig. 5.3 (a). A silicon substrate supports an array of pixels made by aluminum electrodes, and controlled by an addressing circuit. Each pixel can be controlled independently. In front of the array, a second transparent electrode and a glass substrate are placed. The gap between the electrode array and the transparent electrode is filled with a liquid crystal material. An alignment control system aligns all the crystal molecules in parallel. By controlling the electric field on each pixel, the molecules can be tilted, changing the refractive index locally with different tilt angles. The change in the refractive index modifies the optical path length in the liquid crystal layer and induces a phase difference in a particular region of an input beam. Consequently, the output reflected beam is modulated in phase by the active control of the pixel electrodes.

To imprint a phase distortion in the beam wave-front, a phase map is created and then converted to a 256 level grayscale in order to drive the pixels of the SLM. The SLM has a linear response between 0 and 2π in 256 levels, as shown in Fig. 5.3 (b). The conversion from the phase values φ to pixel input signal levels can be performed as $I_{\text{SLM}} = 95.9\varphi + 0.975$, which corresponds to the SLM transfer function.

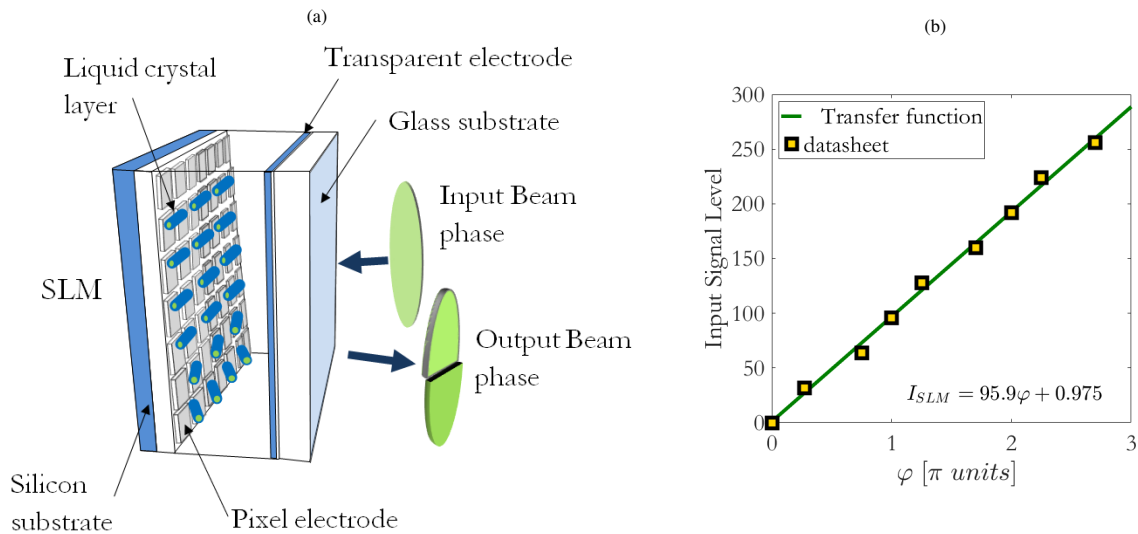


Fig. 5.3: (a) Structure of the LCOS SLM chip. Design based on the model Hamamatsu X10468-LCOS [5]. (b) Transfer function of the SLM.

The limitations of the SLM can be associated with an effect known as phase wrapping. The maximum excursion of the SLM is 2π , thus, larger phase variations experience jumps of 2π every time this limit is exceeded. Figure 5.4 shows SLM phase-screens for different turbulent conditions. It also shows their phase profiles, and correspondent measured focal intensity patterns. For very strong turbulence, represented by a $D/r_0 \geq 20$, the regions undergoing a phase wrap are tightly packed. If the wrapping effect increases, the phase cannot be well resolved by the available pixels on the SLM and the amplitude transmission diminishes [142]. Furthermore, a high number of phase wraps acts as a grating that produces an unwanted artifact with a constant bright central speckle. These two effects are seen in the cases of D/r_0 20 and 40, where the measured focal intensity pattern shows a central intensity spot in all the images. In line with this, the principal limitation of using

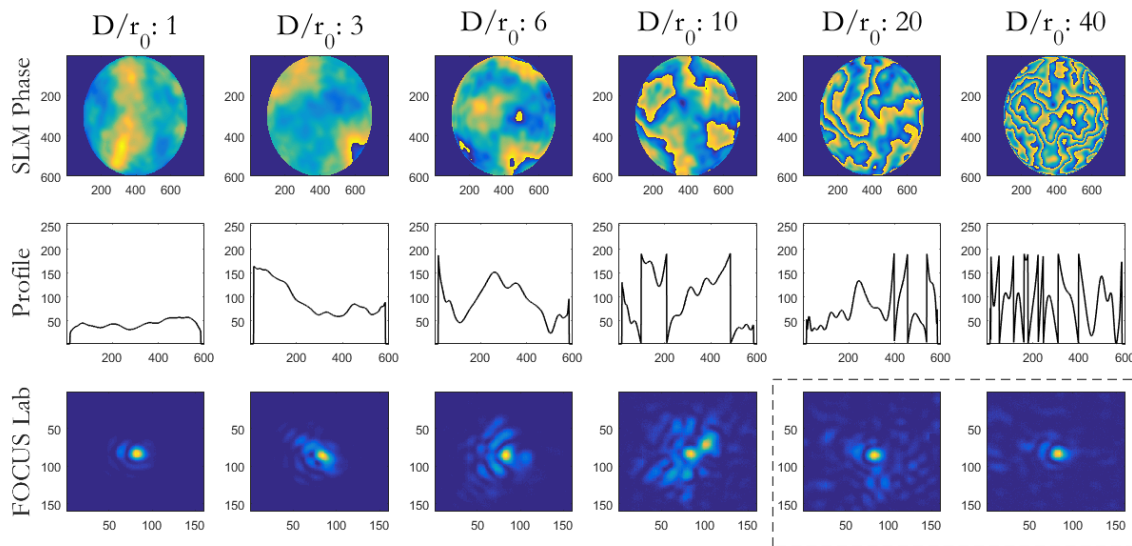


Fig. 5.4: Laboratory examples of SLM phases and their profiles for different turbulent regimes. The measured focal intensity patterns are compared. Higher D/r_0 are not well resolved by the SLM (dashed box), showing a single stable central intensity spot in all tested phase screens.

an SLM to emulate the turbulence is that phase wraps cannot be properly represented by a membrane-based deformable mirror. The membrane cannot reproduce abrupt jumps in the phase and the scenarios under test need to be limited to those with a phase excursion within the span of the SLM. By subtracting the tilt on each generated phase-screen, the number of wraps can be minimized without affecting the phase aberration. As explained in Sec.4.1, tilt compensation only moves the speckle to the center of the image and does not alter the high order distortions targeted by the AO system.

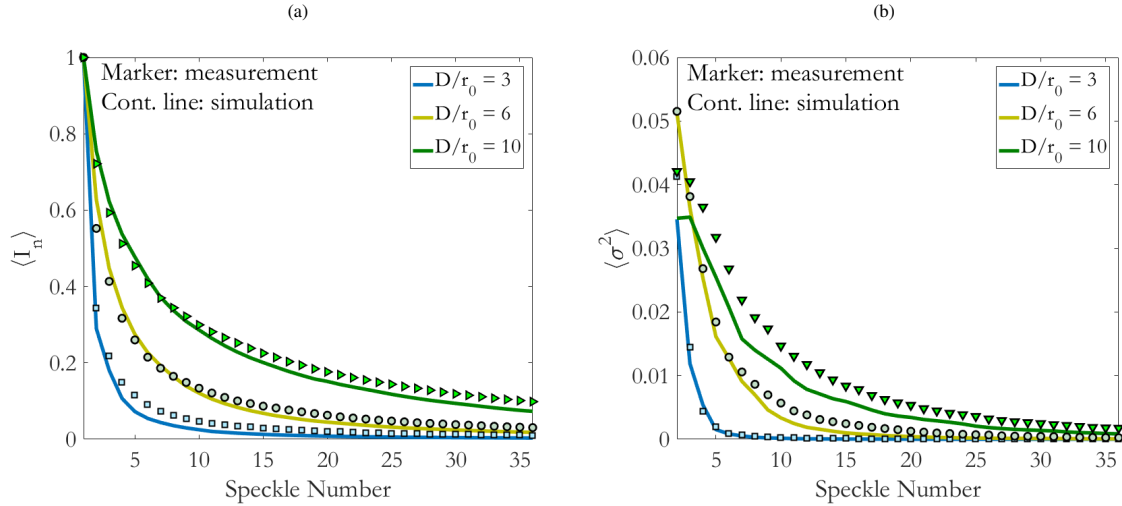


Fig. 5.5: Comparison between simulated (continuous line) and measured (markers) focal speckle patterns. Analysis of the intensity distribution per speckle for different turbulent regimes. (a) Normalized mean intensity per speckle. (b) Mean intensity variance per speckle.

The analysis of Sec. 4.1.1 is performed over simulated and measured focal images to verify the correct generation of the focal intensity pattern. In this analysis, the mean intensity distribution per speckle is calculated. If the mean intensity distribution of the measured speckles follows the same distribution of the simulated patterns, then it can be concluded that the SLM is accurately emulating the turbulent scenario.

For such analysis, a set of 400 phase-screens is created for a $D/r_0 = [3, 6, 10]$. On each scenario, the phase maps are applied to the SLM and images of the focal intensity pattern are acquired. The same phase maps are numerically Fourier transformed to have pairs of simulated and measured images. Each pair of focal images is post-processed. First, the images are normalized to their maximums. Then, the speckles are individualized and classified in descending order based on the total intensity per speckle. Finally, the mean and variance intensity per speckle are plotted. The results in Fig. 5.5 show that the measured focal intensity patterns on each scenario, have speckles of decreasing intensity that closely follow their numerical counterparts.

5.2.2 Tip Tilt Mirror

The TTM hardware was introduced in Sec. 3.1.1. The maximum angular deflection of the TTM mirror φ_{tm} can be calculated with Eq. (3.1). Considering a $D/r_0 = 6$ and a beam diameter $D = 12$ [mm] after the relay R2, a maximum $\varphi_{tm} = 2$ mrad is needed, see Figure 5.6. This range is within the capacity of the TTM, see Table 5.1. For the experiments, the phase screens are generated without the tilt components to minimize phase wrapping. Consequently, the TTM only corrects the remnant system tilt to assure the centering of the speckle pattern in the

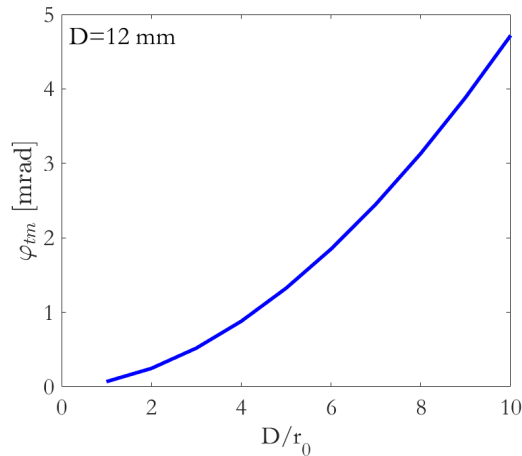


Fig. 5.6: Maximum angular deflection of the TTM mirror for a 12 [mm] beam diameter and different turbulent regimes.

camera sensor, proper illumination of the DM active area, and good alignment with the fiber coupling section. This particular stage does not represent any limitation for the experimental proof of concept.

5.2.3 Deformable Mirror

The working principle of a membrane-based DM was introduced in Sec. 3.1.2. The required stroke of the DM can be calculated with the Eq. (3.6), and compared with the numerical estimation of the peak-to-valley (P2V) phase excursion of a set of phase screens. The phase screens are generated for different turbulent regimes using the single screen phase method detailed in Sec. 2.1.4.

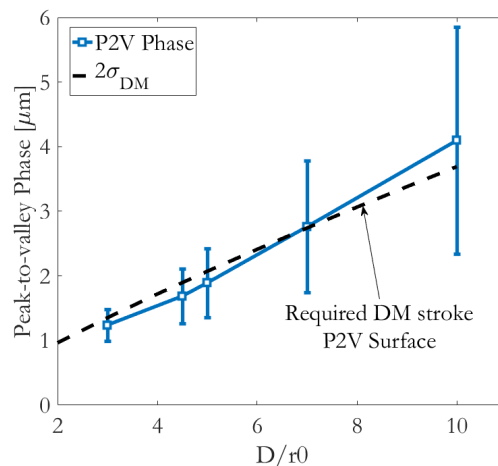


Fig. 5.7: Comparison between the required peak-to-valley (P2V) DM stroke, and the numerical estimation of the P2V phase excursion of a set of phase screens generated for different turbulent regimes.

The results in Fig. 5.7 show good matching between analytical and numerical simulations. As highlighted by K. Morzinski [94], the $2\sigma_{DM}$ is the stroke requirement at the center of the pupil. Other factors like, non-stationarity of phase, inherent curvature of the MEMS, and tip-tilt residuals, further increase the stroke

requirements [143, 144]. The numerical simulation of the P2V phase excursion shows significant variance, which may well push for the selection of DM with higher stroke capacity.

For the particular case of the proposed compensation method, as mentioned in Sec. 4.2.5, a scanning process is required to create the lookup table of all possible plane wave phases. For each plane wave, a DM tilt produces a displacement of the diffraction limited speckle. The camera sensor registers the peak coordinate of the speckle and associates this coordinate with the tilted phase, see Fig. 4.17. This process is constrained by the DM stroke and the number of actuators. In the experimental setup, only a section of 8×8 actuators of the DM is illuminated. This corresponds to a beam diameter of 3.7 mm, highlighted in Fig. 5.8. This figure shows a maximum membrane tilt of $2.6 \mu\text{m}$. Membrane surface tension, associated with actuators outside the illuminated area, limit the maximum deflection. Based on Fig. 5.7, the available stroke may be sufficient to deal with a $D/r_0 = 6$. For higher D/r_0 , speckles tend to separate more. Note that, during the optimization process, the speckles inside the *scanned area* in the camera sensor can be assigned to a plane wave as the tilted phase map is available. The speckles outside this area must be discarded.

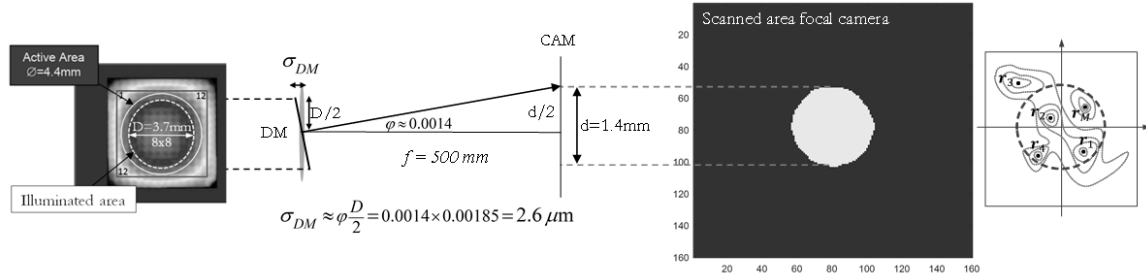


Fig. 5.8: Laboratory measurement of the DM scanning process. Different tilts are applied to the illuminated area of the DM, producing a displacement of the focal speckle. The dimensions of the scanned area define the maximum DM stroke.

5.2.4 Single-mode Fiber coupling

As detailed in Sec. 2.3.4.1, the efficiency of the SMF coupling depends on the good matching between the beam profile in the aperture (focusing lens), and the back propagated fundamental mode of the fiber (Gaussian). The energy of a free-space beam with diameter D_{be} is collected by a lens, which focuses the beam into the core of the fiber. In Fig. 5.9, the focused beam must converge within the cone of acceptance of the fiber, delimited by two times $\alpha \approx \sin^{-1}(\text{NA})$. The numerical aperture (NA) of the fiber is a parameter provided in the fiber datasheet, from which the focal length f of the lens can be approximated as $f = D_{\text{be}}/(2\text{NA})$.

In practice, a more accurate calculation of f is performed with Eq. (5.1), where w_0 is the mode field radius of the fiber, also provided in the fiber datasheet. A commercially available lens is then selected based on the best-matching characteristics considering a slightly large $D \approx 1.5D_{\text{be}}$ to avoid vignetting.

$$f = \frac{\pi w_0 D_{\text{be}}}{2\lambda} \quad (5.1)$$

In a LEO downlink, the Gaussian beam at the satellite position reaches the turbulent layer (20 Km) with a flat intensity profile and it is modeled as a plane wave. The Fourier transform of the wave-front, assuming a flat

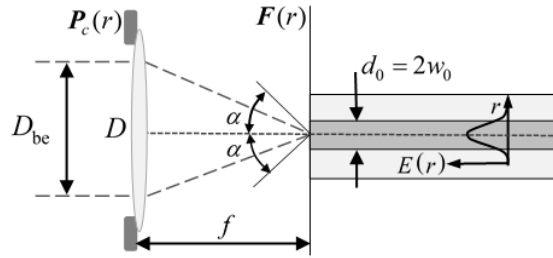


Fig. 5.9: Free-space beam being focused into a single mode fiber.

phase, results in a focal intensity distribution that resembles an airy pattern, Fig. 4.4 (a). The mismatching with the Gaussian fiber mode limits the maximum SMF coupling efficiency to $\eta = 0.814$.

As initially mentioned, in the laboratory experiment the flat beam profile is generated with the collimator. The beam results affected by diffraction due to internal stop rings in the collimator and the polarizer located before the SLM. This results in a distortion of the intensity profile, see Figure 5.10.

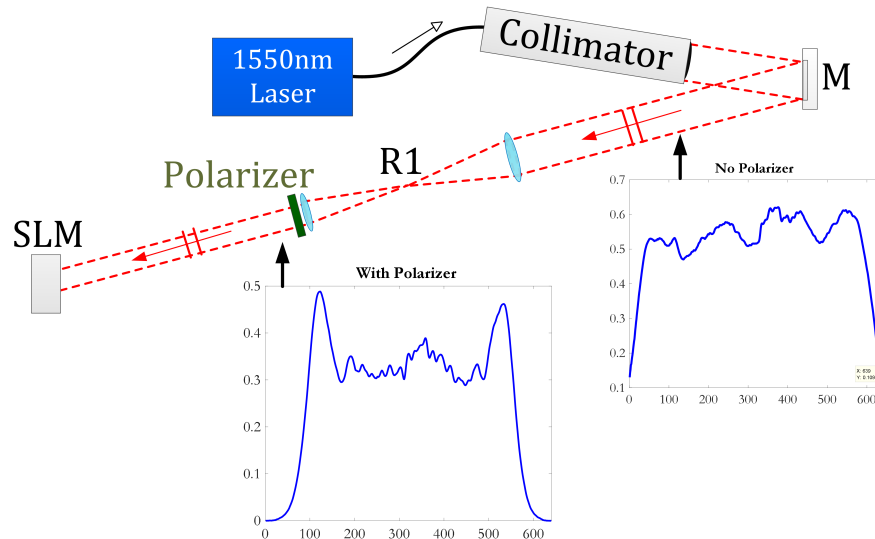


Fig. 5.10: Beam profile before the SLM.

The measured intensity profile of the beam at the entrance pupil of the coupling section and the back propagated simulated Gaussian profile of the fiber mode are shown in Fig. 5.11 (a). Their respective Fourier transform are shown Fig. 5.11 (b). The beam wave-front acquires additional aberration due to the optical components that further alter the profiles of Fig. 5.10. The phase aberration corresponds to a small degree of astigmatism with a peak-to-valley phase excursion of 0.8 radians, shown in the inset of Fig. 5.11 (a).

It is important to highlight that the alterations in the beam intensity profile only reduce the maximum coupling efficiency but do not significantly alter the proof of concept of the method. In a real scenario the beam intensity profile will certainly show worse variations of intensity (scintillation). The measured wave-front is used to estimate the maximum expected coupling efficiency. The calculation is performed with the Eq. (2.104) considering a $w_0 = 5.4 \mu\text{m}$, beam diameter $D_{\text{be}} = 3.7 \text{ mm}$, and the lens focal length equal to $f = 19.5 \text{ [mm]}$.

The estimated SMF coupling efficiency is $\eta = 0.67$. The measured ratio of received optical power in the coupling lens ($f = 19$ mm), and coupled power in the SMF fiber, results in a coupling efficiency $\eta = 0.6$.

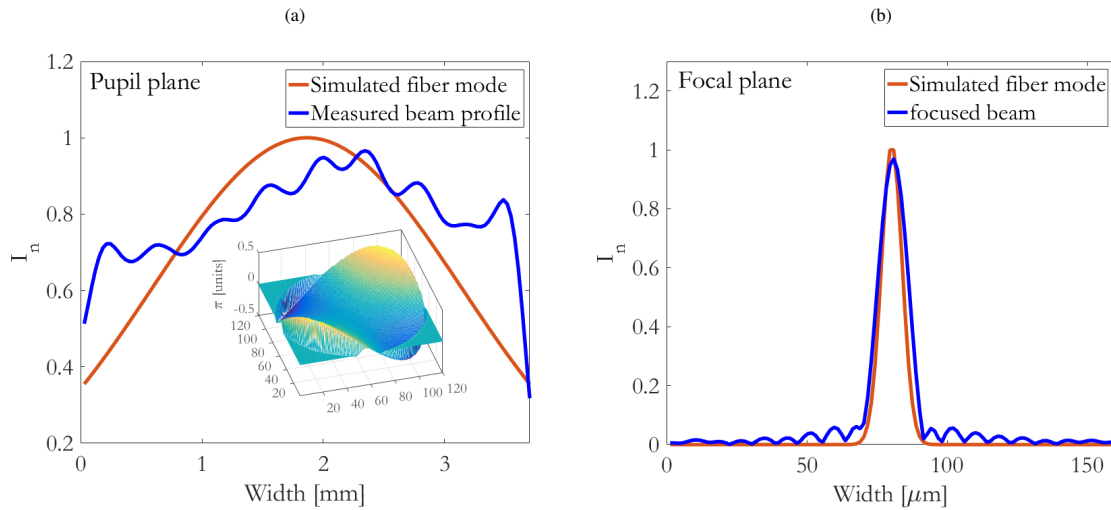


Fig. 5.11: (a) Measured Intensity beam profile and simulated back propagated Gaussian profile of the fiber. (b) Focal intensity profiles.

5.2.5 Avalanche Photodiode

The optimization process is highly dependent on three signal power measurements to find the maximum of a parabolic-fitted curve. Signal noise randomly changes the position of such measures leading to sub-optimum optimizations. Consequently, to know the range of input power for a good performance of the algorithm, the detector needs to be characterized by its electrical signal-to-noise ratio.

In these experiments it is used an InGaAs detector that can adjust its gain between 0 and 70 dB, see Table 5.1, where the gain is set to 60 dB. The optical input power P_{in} can be accurately estimated with the linear relation $P_{\text{in}} = V_{\text{out}}/G_{\text{H}}$, where V_{out} is the measured output voltage in units volt, and $G_{\text{H}} = 1.5 \times 10^6$ [V/A] is the high impedance gain. The SNR is estimated as $\text{SNR} = 20\log_{10}(V_{\text{out}}/N_{\text{RMS}})$, where $N_{\text{RMS}} = 880 \times 10^{-6}$ [μV] is the RMS noise, see Table 5.2.

Figure 5.12 shows the estimated SNR of the APD for different optical input powers. This estimation is confirmed by directly applying an input signal to the APD, and measuring 2.4 million samples at different output voltages. Then, their correspondent mean voltage V_{mean} and standard deviation V_{std} are calculated. The signal-to-noise ratio is approximated as $\text{SNR} = 20\log_{10}(V_{\text{mean}}/V_{\text{std}})$. The results are shown with the markers, closely matching the estimated curve. When the laser beam propagates through the AO system and gets coupled into the SMF fiber, vibrations and small changes in temperature affect the coupled signal, inducing additional signal variations on top of the intrinsic noise. The overall effect is a reduction of the SNR, reaching a plateau around 40 dB. Note that these additional signal variations are not noise, but anyway included in the SNR to have a single metric.

60 dB Settings	Values
Gain (Hi-Z)	$1.5 \times 10^6 \text{ V/A} \mp 5\%$
Bandwidth	25 kHz
Noise (RMS)	880 μV
NEP	$1.76 \times 10^{-12} \text{ W}/\sqrt{\text{Hz}}$
Offset	6 mV (10 mV max)

Table 5.2: APD characteristics for the Thorlabs PDA20CS-EC set to 60 dB gain.

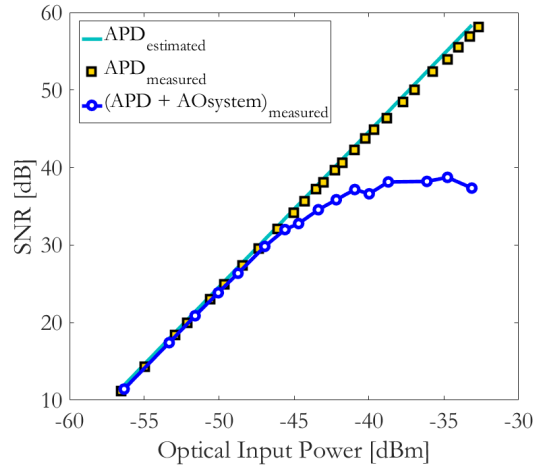


Fig. 5.12: Signal-to-Noise ratio characterization of the APD.

5.2.6 Focal Camera

As previously explained, the camera (CAM1) performs a short-exposure image acquisition required by the algorithm to identify focal intensity speckles. The acquisition time is set to 100 microseconds. Based on the analysis performed in Sec. 4.1.1 and Fig. 4.5, the incident power distributes among the speckles in different ratios depending on the turbulence strength. Hence, the received power must be enough to assure sufficient SNR in the speckle with less intensity.

The focal camera is then characterized by its signal-to-noise ratio for three input powers within its dynamic range. For such characterization, a lens with short focal length $f = 45 \text{ mm}$ is adjusted to produce a single speckle of 6×6 pixels. The ratio between the background noise standard deviation and mean total intensity of the speckle is calculated for 5000 images.

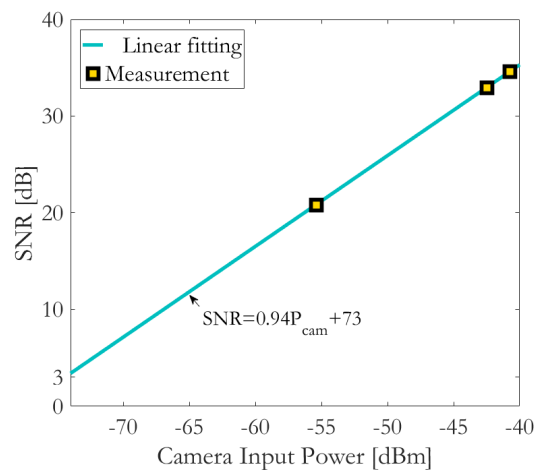


Fig. 5.13: (a) Camera signal-to-noise ratio in function of the input power.

Figure 5.13 shows the camera SNR in function of the received power. The Eq. (5.2) allows the estimation of

the camera SNR for different input powers

$$\text{SNR} = 0.94P_{\text{cam}} + 73, \quad (5.2)$$

where P_{cam} is in dBm units, and the SNR in dB units.

5.3 Channel emulation

The turbulent channel used for the proof of concept is constrained to $D/r_0 \leq 6$ to be within the capacity of the DM and reduce the occurrence of phase wrapping in the SLM. These scenarios are congruent with the expected ones in a LEO downlink operating with a telescope diameter of 40 cm, as shown in Fig. 2.5. The scenario of strong turbulence represented by a $D/r_0 = 10$ is also tested to evaluate the algorithm against phase wrapping, which occurs due to branch points in a real scenario and here are induced by the SLM. Each turbulent scenario considers 600 phase-screens generated with the single screen phase method. Besides the initial verification of the turbulence generation, detailed and validated in Sec. 5.2.1 and Fig. 5.5, an additional verification is performed by comparing the simulated and measured normalized SMF coupling efficiency η_{norm} under turbulence effects.

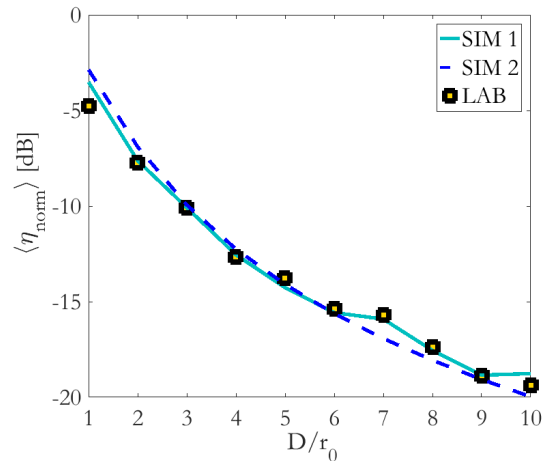


Fig. 5.14: Normalized single-mode fiber coupling efficiency comparison between the laboratory measurements (markers) and the simulations, considering a different set of phase-screens for varying turbulence regimes.

The η_{norm} results from the normalization of the coupled signal by the maximum possible coupled power in the current setup, shown in Sec. 5.2.4. This metric allows a better comparison with the simulation.

Figure 5.14 compares the laboratory measurements of the normalized coupling with the numerical estimation (SIM 1) and (SIM 2) calculated with the Eq. (2.104) and Eq. (2.108), respectively. The good matching of the curves further confirms that the channels are emulated properly.

5.4 Proof of concept

During the compensation process, each phase screen is applied to the SLM, the overall phase wave-front tilt is corrected with the TTM, and the focal image of size 160×160 pixels is acquired. The speckles are detected

using a local maxima algorithm which is fast and efficient [145]. With the identified speckles, the lookup table is used to generate the proper plane waves. Then, the algorithm performs the sequential iterative DM shaping, signal power acquisition, and phase optimization. This process is repeated for all the set of phase screens. For each case, the initial and final coupled power as well as the signal on each iteration and corrected speckle is registered. The experimental results are also compared with simulations where the relevant laboratory constraints like camera noise, optical aberration of the system, APD noise, and DM maximum deflection are included. To validate the method, three main experiments are carried out:

- Evaluation of the behavior of the algorithm for different SNR and varying received signal power
- Overall performance over a range of turbulent scenarios
- Verification of the proposed concept for the dynamic compensation of correlated fields

5.4.1 Algorithm performance under the effect of signal noise

Figure 5.15 (a) depicts the mean SMF coupling efficiency penalty for each corrected speckle in a turbulent scenario with a $D/r_0 = 6$. Here $D = 12$ mm is the beam diameter and $r_0 = 2$ mm indicates the spatial coherence of the wave-front. This ratio is representative of a LEO satellite downlink around 10° elevation when the beam is received with a telescope aperture of $D = 40$ cm [140, 141]. The experimental values (LAB) and the simulation results (SIM) are normalized to the maximum achievable coupled power for comparison. The analysis is performed for values of SNR $\approx [14, 40]$ dB and received powers of -56 dBm and -36 dBm, respectively. This range of received power is selected from Fig. 5.12 and it is representative for multi-gigabit data reception, either working with direct detection or coherent systems [146, 147].

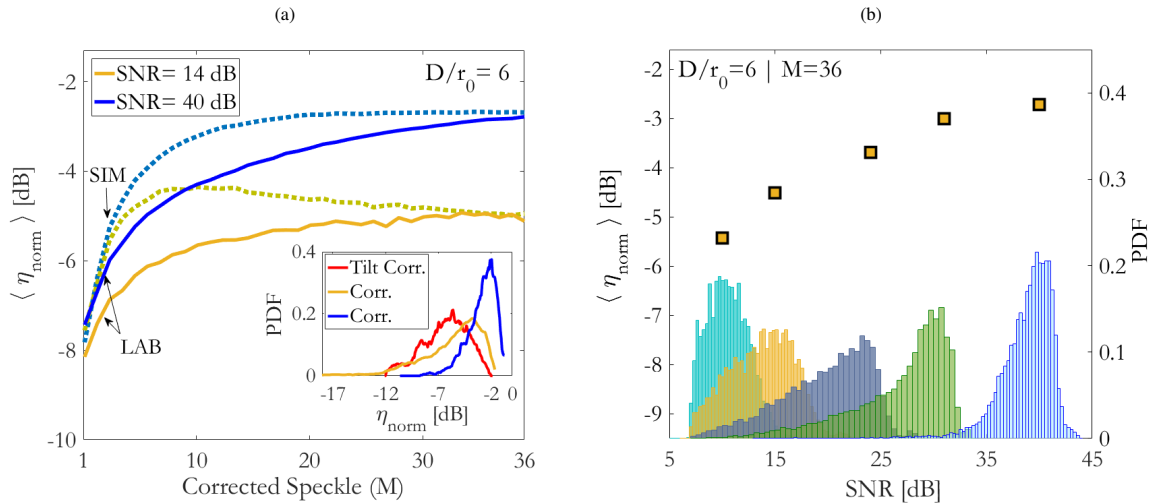


Fig. 5.15: (a) Normalized coupling efficiency vs. number of corrected speckles. The inset shows the PDFs for the final coupling. (b) Evolution of the coupled signal and SNR distribution.

As expected from the numerical analyses, with higher SNR the coupling improves with each corrected speckle, delivering a gain of 4 dB after approximately 58 iterations ($M = 20$). The inset shows the probability

density functions (PDFs) of the final coupled signal, with a reduction in the variance compared with the tilt-corrected cases. While the maximum achievable coupling match closely, a slower growth of the experimental curve is appreciated. It is assumed to be given by a residual tilt in the evolving estimated phase, which is not compensated because the TTM remains static during the correction.

The performance penalty due to the decrease in the SNR is also verified. The system can still provide a gain of 2.5 dB with 58 iterations. Here, as mentioned during the numerical analysis, the noise introduces random deviations in the measured power values used for optimization, affecting the parabolic fitting and leading to sub-optimum phase shift estimations. This effect is prone to impact more in speckles of lower intensity when the SNR is high, limiting the slope of the curve. Also, it can alter the initially estimated phase shift associated with speckles of higher intensity, forcing an earlier saturation. In Fig. 5.15 (b), the evolution of the coupling penalty against the mean SNR is depicted. The right axis is associated with the PDFs of each SNR case, which illustrate the noise distribution when the optical power varies during the iterative process. The right-skewed shape of the PDF of higher SNR is given by the combined effect of APD internal noise and signal variations due to system vibrations. At lower SNRs, the APD internal noise dominates and the distribution approaches to Gaussian.

5.4.2 Overall performance

Figure 5.16 (a) shows the performance of the method in the pre-established optimum range of turbulence. Stronger turbulence is separately tested, limited by the maximum DM stroke of the illuminated area and the resolution of the SLM.

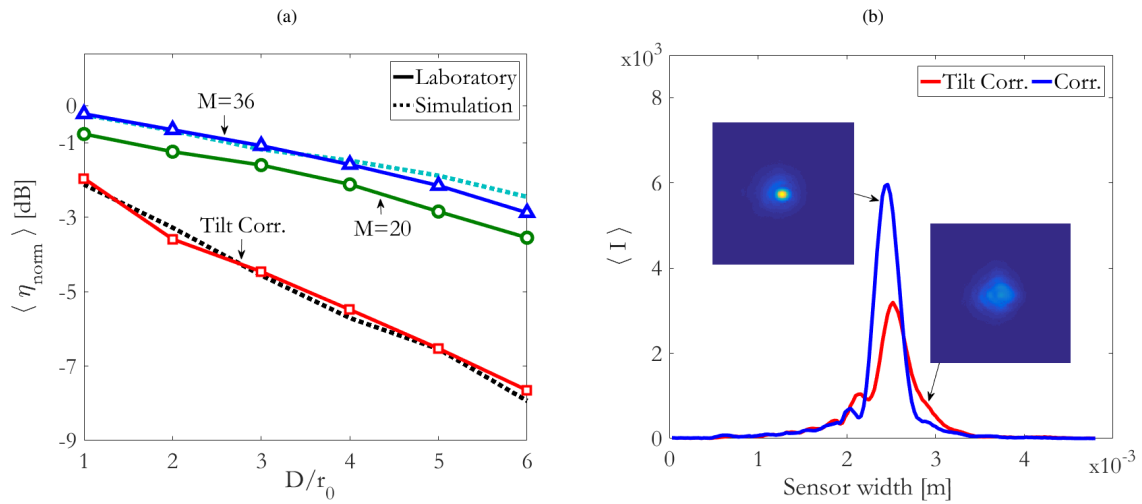


Fig. 5.16: (a) Overall performance for different turbulent scenarios. (b) Ensemble of normalized intensity patterns before and after correction.

The curves show a close matching between the experimental and numerical results alongside the tested scenarios. There is an important improvement in the mean of the signal when the fields are corrected with $M = 36$ (106 iterations) and $M = 20$ (58 iterations). A nearly half-reduction in the number of iterations comes at the expense of a minimum penalty of 0.4 dB in the signal mean. The long-term point spread function for the scenario $D/r_0 = 6$ can be calculated by performing the ensemble of the corrected intensity patterns $\langle I \rangle$ over a

set of $N = 500$ captured focal images [4]. The result is shown in Fig. 5.16 (b) and the calculation is performed before and after the correction of $M = 20$ speckles per field. The insets highlight beam focusing improvement.

In addition, figure. 5.17 shows the improvement in the variance of the signal when the fields are corrected with $M = 36$ and $M = 20$ speckles. The scenarios $D/r_0 = [5, 6]$ are equivalent to a case of a LEO downlink around 10° elevation with $D = 40$ cm, see [140, 141]. Here, the reduction in the number of iterations implies a slight increase in the variance.

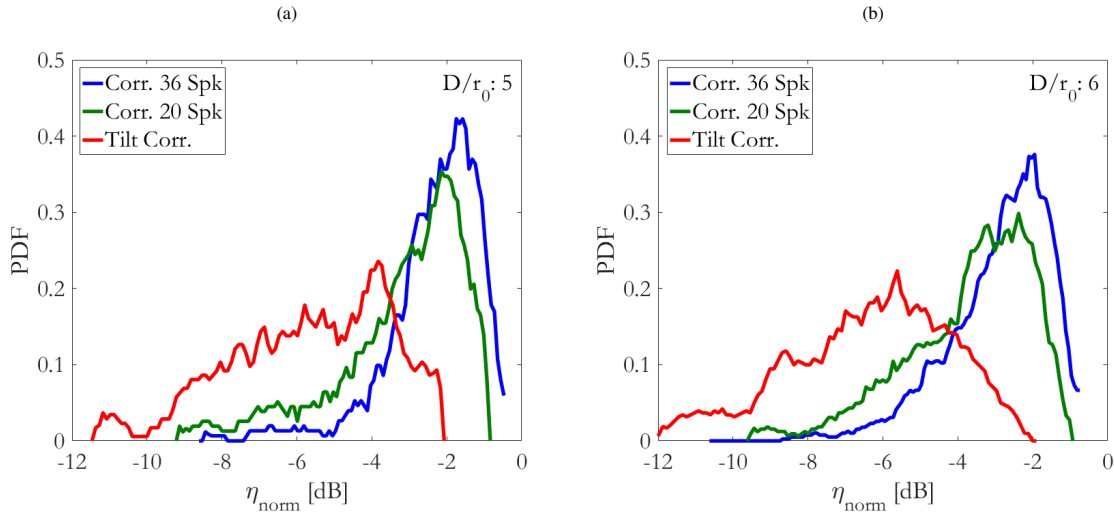


Fig. 5.17: Experimental PDF of the coupling penalty for the scenarios (a) $D/r_0 = 5$ and (b) $D/r_0 = 6$. Comparison between the correction with 36 and 20 speckles.

Overall, the performance shows stability in a wide range of turbulence conditions. The signal gain is increased and the variance gets reduced substantially. The enhancement in the signal quality is achieved with reduced bandwidth utilization.

5.4.3 Algorithm performance under very strong turbulence

The scenario with $D/r_0 = 10$ is tested to evaluate the performance of the algorithm under strong turbulence. This scenario can be associated with LEO downlinks below 10° elevation, as shown in Fig. 2.5 and [146, 147]. As mentioned before, the SLM phase map shows an increment in the number of phase wraps beyond $D/r_0 = 6$, and one must consider that the performance of the correction may suffer deterioration due to the DM limitations facing such abrupt phase jumps. On the other hand, it is of interest to see the degree of improvement in coupling efficiency delivered by this iterative solution knowing that the iterative nature of the algorithm may encounter a good solution, not necessarily the best, to increase the signal power.

Figure. 5.18(a) compares the performance curves for $D/r_0 = [6, 10]$. In the scenario of $D/r_0 = 10$, a signal gain of 4 dB ($M = 30$ corrected speckles) and 3 dB ($M = 20$ or 58 iterations) is obtained. There is a difference in gain between both curves of less than 2 dB, which is larger by 0.7 dB to that of the simulated case in Fig. 4.21. Note that simulations do not include all hardware limitations. The measured PDF's in Fig. 5.18(b) clearly show how the algorithm improves the quality of the signal with respect to the tilt-corrected cases. Centroid-tilt correction under strong turbulence does not deliver much of improvement since the focal energy is sufficiently

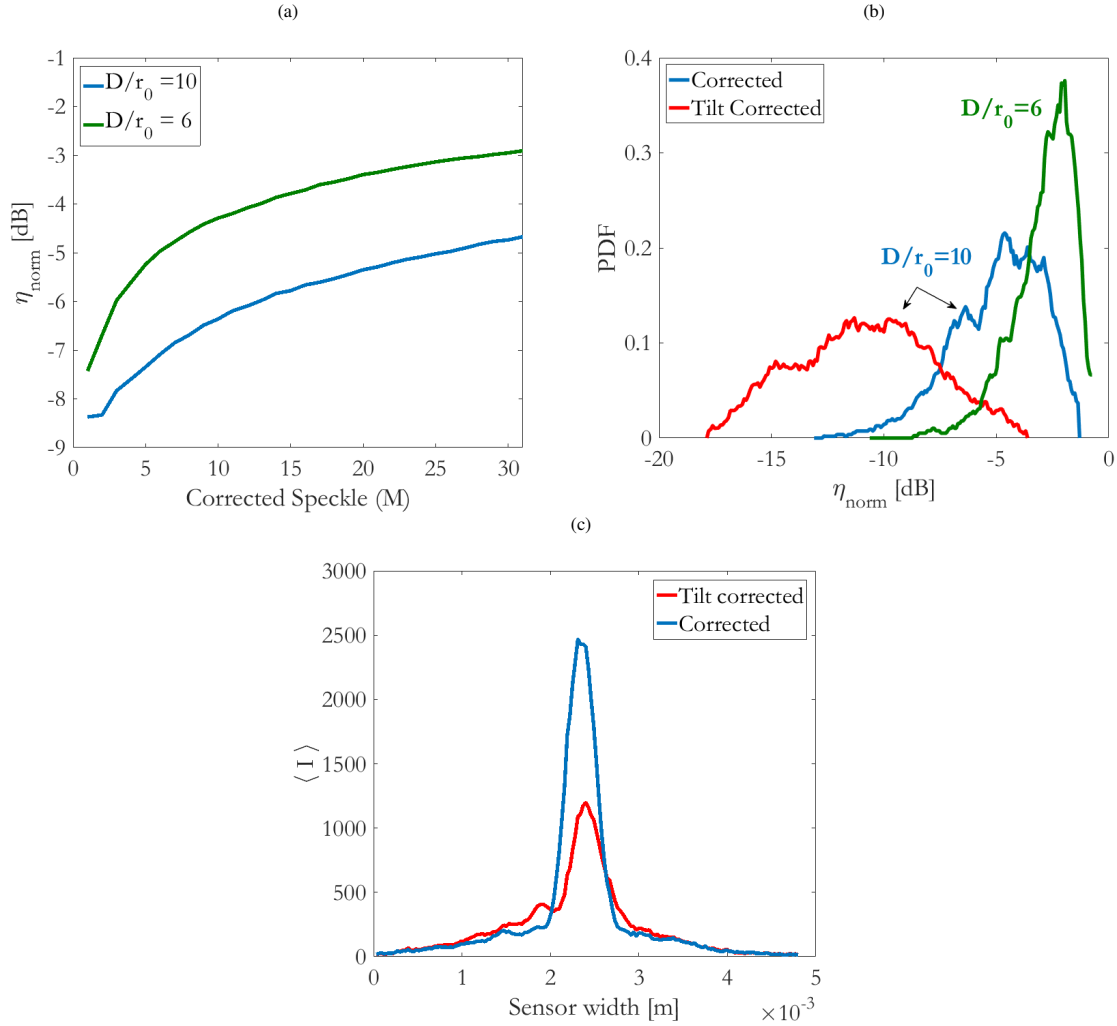


Fig. 5.18: (a) Experimental normalized coupling efficiency versus number of corrected speckles for the scenario $D/r_0 = 10$. Comparison against the curve associated with $D/r_0 = 6$. (b) PDF of the tilt corrected fields and full correction with 36 speckles. (c) Ensemble of normalized intensity patterns before and after correction.

dispersed, reducing the probability of energy at the fiber core position. Still, the variance of the PDF after correction should be reduced to avoid signal fading. The performance of the system and algorithm in the scenario $D/r_0 = 6$ is better as the occurrence of phase wrapping is less probable. Finally, Fig. 5.18(c) shows the normalized ensemble of focal intensity patterns where the algorithm improves the beam energy focusing at the fiber core position. Overall, even though the described limitations, the algorithm proves its capacity of improving the quality of the received signal in scenarios of stronger turbulence.

5.4.4 Correction of correlated fields

This analysis evaluates a preliminary algorithm for the dynamical correction of the speckles originated from correlated pupil fields, as presented in Sec. 4.3.4. This approach compares the changes in each speckle location between subsequent images and decides the phase shift range to be used in the optimization. For minimum changes in the speckle location, a reduced phase shift range is assigned for the optimization of each speckle,

thus, minimizing the power fluctuation in the fiber. For major changes, a larger phase shift range is assigned, increasing the variance of the coupled signal but accelerating the correction. Following this procedure, it is expected to reduce the overall power fluctuations during instantaneous iterations.

A real-time test is not yet possible, but the concept can be evaluated with the use of correlated phase-screens accounting for their coherence time and number of screens involved. The in-house DLR tool Pilab [137], briefly introduced in Sec. 4.3, is used to create correlated fields for a scenario of a LEO downlink at 30° elevation. A total of 300 fields are generated with a mean $D/r_0 = 6$, a $\tau_0 = 2.1$ msec calculated with Eq. (2.26), and transversal wind velocity $V_t = 10$ m/sec. Here, fields are generated and propagated through the turbulent layers every $250 \mu\text{sec}$. Hence, around 9 fields are contained within τ_0 .

The cross-correlation between the generated fields is depicted in Fig 5.19. It is expected around 1 dB loss of correlation if the initial field is corrected with the subsequent 9th realization, and 3 dB loss of correlation with the equivalent 20th realization. From this plot, and for the following experiments, the theoretical $\tau_0 = 2.1$ msec, and $N = 9$ fields are adopted as the threshold limits.

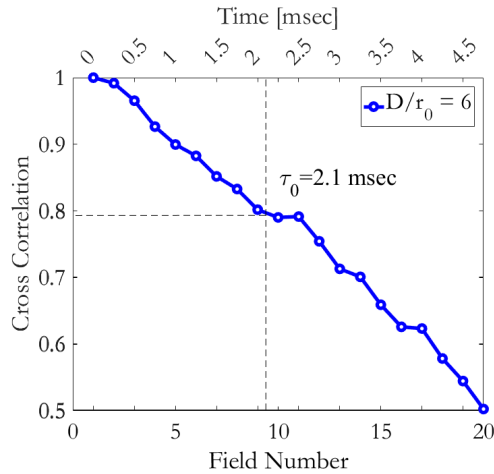


Fig. 5.19: Cross-correlation between pupil phase wave-fronts

For the experiment, the correlated fields are sent to the SLM with a spacing of $N = [3, 6, 9]$ fields, or a time gap $\Delta t = [0.3\tau_0, 0.7\tau_0, \tau_0]$. With this, it is intended to verify the correction performance with increased decorrelation. The results are shown in Fig. 5.20.

Figure 5.20 (a,b) shows the η_{norm} per iteration while the algorithm dynamically corrects 20 speckles per field. Each field is applied to the SLM spaced every 3rd realization, and this separation implies an AO loop time $\text{AO}_{\text{loop}} = 0.3\tau_0$. Here, the AO_{loop} considers the total time required for the compensation of one field. The dotted line shows the η_{norm} of the fields only corrected in tilt. The red plot shows the algorithm performance without the dynamic tracking of the speckles or managing of the phase shift range. Without this dynamic tracking, every single speckle of subsequent fields is optimized using a large phase shift range, resulting in power fluctuations with deep fading at the beginning of each field compensation. Even though each optimized field reaches a satisfactory final state of coupling efficiency, the repetitive fades are unwanted from the perspective of a communication channel. Instead, the blue curve highlights the enhancement in the performance when the algorithm makes use of the information of anterior fields, keeping the η_{norm} within a band gap of -3 dB.

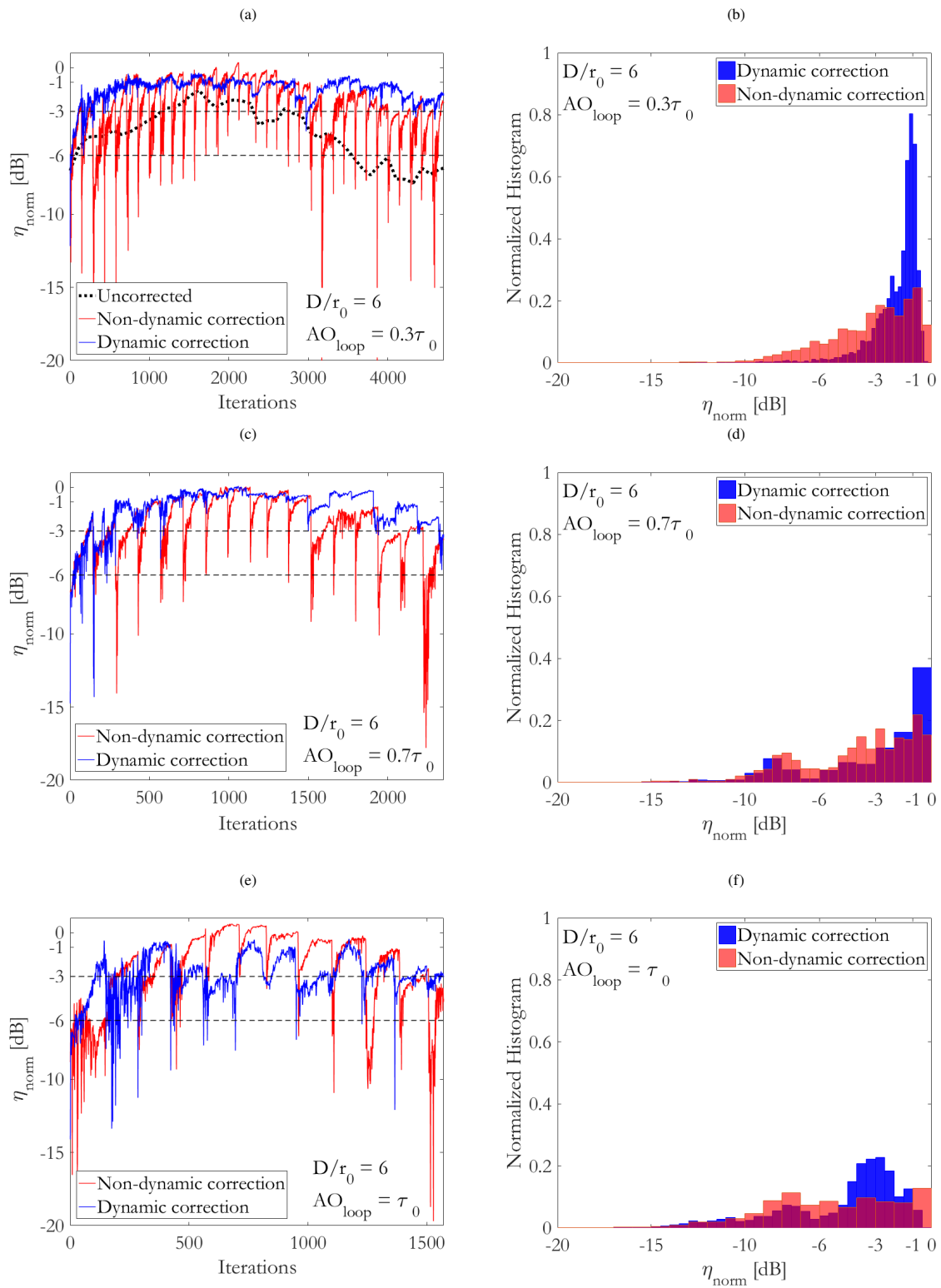


Fig. 5.20: Laboratory performance of the dynamical compensation of correlated fields ($D/r_0 = 6$, $\tau_0 = 2.1$ msec). The correction time per field ΔO_{loop} of the algorithm increases from (a) $\Delta O_{\text{loop}} = 0.3\tau_0$, to (b) $\Delta O_{\text{loop}} = 0.7\tau_0$, and (c) $\Delta O_{\text{loop}} = \tau_0$.

The algorithm also shows a fast recovery when the synchronization is lost ($N_{\text{iter}} \approx 3000$). At this point, the synchronization is recovered within ≈ 60 iterations. The histogram clearly contrasts the improvement in the variance of the coupled signal with and without the dynamic correction of the fields.

The algorithm has a diminished performance against more spaced fields. If the spacing approach to τ_0 , the correction fails. Figure 5.20 (c-f) show this behavior with AO_{loop} approaching to τ_0 , here implemented by increasing the field spacing to 6 and 9 realizations. The longer it takes to correct an initial field, the more the wave-front evolves and thus the focal pattern decorrelates. The increased difference in the speckle locations, force the update of the table of plane waves that needs to be combined and optimized. Hence, each subsequent field is seen as a new field realization that needs to be optimized from the beginning. This result in deep fades and larger variance.

It is evident that this preliminary approach performs better with $\text{AO}_{\text{loop}} \leq \tau_0/2$. As mentioned before, it is important to constrain the power fluctuations within a functional threshold, which can be defined differently based on factors like, receiver sensitivity, modulation formats, the use of FEC, and the turbulent scenario. In addition, the decision criteria for the phase shift assignment in scenarios of stronger turbulence may require the consideration of other factors, like peak intensity changes between speckles.

5.5 Conclusion of the chapter

This chapter has presented the experimental work performed for the proof of concept of the technique. To validate the proposed technique, an emulator of an optical satellite downlink was built in the laboratory. This setup was equipped with an AO system based on a focal camera, as designed in Fig. 6.8. The set of experimental tests were performed with synthetically generated phase-screens, considering uncorrelated and correlated fields. The hardware components were characterized to identify the system limitations on the AO system.

The experiments verify the model and method presented Sec. 4.2. Each distorted field is corrected following the processing steps shown in Fig. 4.16, and the calibration of the system is done as described in Fig. 4.17. The technique improves the mean coupling efficiency and reduces the signal fluctuations in scenarios of weak to strong turbulent regimes. The adaptation process shows that the signal improves with each corrected speckle and that each plane wave phase shift, or the equivalent associated speckle phase, is optimized with three power measurements. This results confirm the assumptions made in chapter 4 and indicate that approximately 60 power measurements (3×20 speckles) are required to correct fields in scenarios of moderate to strong turbulence. There is a difference of less than 0.5 dB respect to the maximum improvement reached after 36 corrected speckles, which match the maximum attainable predicted with the simulations but where experimental curves grow at a slower rate. Several factors may contribute to such behavior, namely, residual tilts after each plane wave compensation, and DM fitting limitations. This point remains open for further experimentation and analysis. Overall, the use of 60 iterations in the tested scenarios reduces by 40% the required number of iterations (≈ 100) of stochastic methods, and this performance may be further improved after refinement of the algorithm and AO system.

The impact of the noise in the overall performance verifies the curves obtained in the numerical analyses. Noise affects the optimization process of each plane wave, deteriorating the correction. With sufficient SNR,

the method delivers around 4 dB gain under strong turbulence. A reduction of 26 dB in the SNR induces a gain penalty, but the algorithm still manages to deliver 2.5 dB of signal improvement. This highlights robustness, which is wanted in FSOC systems. Additionally, it shows the adaptability of the iterative methods as it can adjust to different states of the channel and signal, still performing the correction.

The preliminary concept for the correction of correlated fields behaves as expected. Some unwanted losses of performance indicate that the underlying idea requires more work and refinement, particularly dealing with strong turbulence. One may conceive the use of predictive Kalman-based algorithms or alike methods to introduce robustness in the dynamic correction. Also, the stochastic dynamic correction may also be an option once the initial compensation is achieved. These alternatives are worth to be researched in future works.

The next chapter experimentally tests the proposed AO method in a communication scenario in order to evaluate if the improvement in the quality of the received signal is sufficient to allow multi-gigabit data transmission.

EXPERIMENTAL VALIDATION WITH TRANSMISSION SYSTEM

THIS chapter experimentally evaluates the AO technique in a communication scenario. As introduced in previous chapters, in order to increase the receiver sensitivity and therefore achieve several gigabits data rates, spectrally efficient modulation format like BPSK and QPSK can be used. This modulation schemes are phase-sensitive and require an efficient SMF coupling and wave-front phase correction, especially for LEO downlinks at lower elevations.

In this context, a suitable AO system capable of mitigating the wave-front distortion in all turbulent regimes, and able to stabilize the signal coupled in the SMF, may allow a coherent receiver demodulating and compensating remnant induced signal impairments like atmospheric piston effects and phase noise. To quantify the performance of the AO system regarding the improvement in the communication link affected by turbulence, a coherent QPSK system is integrated into the AO setup. The test involves the transmission of data over the channel affected wave-front phase distortions, measuring the BER before and after the AO compensation. The trials are performed with decorrelated and correlated phase screens following the previous procedures.

This chapter first extends the concepts of QPSK modulation and demodulation, briefly presented in Chapter. 2.2. Then, the setup and main hardware components of the transmission systems are presented. The development of this coherent system is out of the scope of this thesis, thus only the integration and functional aspects of the system is given. The performance is evaluated with curves of BER that are contrasted with theoretical estimations calculated from real SNR values of the acquired SMF power signal. Finally, a discussion of the results is given.

6.1 Coherent QPSK modulation

As introduced in Chapter 2.2, the amplitude and phase modulation of the carrier can be performed with a Mach-Zehnder modulator operating in push-pull or push-push mode, respectively. The combination of these type of modulators allows the implementation of higher order modulation formats, like QPSK. Likewise, as briefly introduced in Sec. 2.2.2.2, a coherent receiver combines the received signal with that of a local oscillator to obtain the in-phase and quadrature signals required to map the detected symbol with the adopted constellation map. The next sections further detail these concepts to give the reader a better overview of the QPSK modulation format employed in the experiments.

6.1.1 QPSK modulator

The IQ-modulator depicted in Fig. 6.1 is used to modulate a carrier signal in QPSK. Following the modulator description of Sec. 2.2.1, this configuration combines two MZM modulators separated in two arms, each one set in push-pull mode to produce an amplitude modulation of its input signal. The output signals $E_I(t)$ and $E_Q(t)$ of the upper/lower MZM are respectively called "In-phase" and "Quadrature" respect to the entrance signal $E_{in}(t)$ of the IQ-modulator, and they are driven by the voltages $U_I(t)$ and $U_Q(t)$ on each MZM. The difference is given by the additional phase modulator in the lower arm, which shifts the entrance signal by $\pi/2$ applying a bias voltage $-U_\pi/2$. The transfer function of the IQ-modulator T_{IQ} can be written as

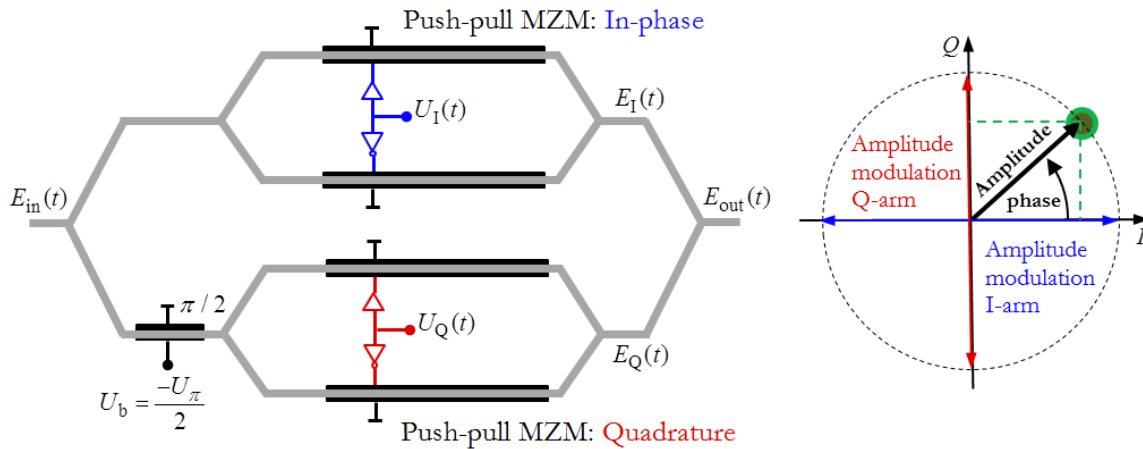


Fig. 6.1: Configuration of an IQ modulator based on two $\pi/2$ phase shifted MZM operating in Push-pull mode.

$$T_{IQ} = \frac{E_{out}(t)}{E_{in}(t)} = \frac{1}{2} \cos\left(\pi \frac{U_I(t)}{2U_\pi}\right) + j \frac{1}{2} \cos\left(\pi \frac{U_Q(t)}{2U_\pi}\right) \quad (6.1)$$

Equation (6.1) shows how the input signal E_{in} of the IQ-modulator can be modulated in different manners by just controlling the amplitude state of the driving MZMs voltages. The QPSK scheme encodes 2 bits on each symbol by setting both arms of the IQ-modulator in the null operating point of the MZM and driving each MZM with a swing voltage of $2U_\pi$.

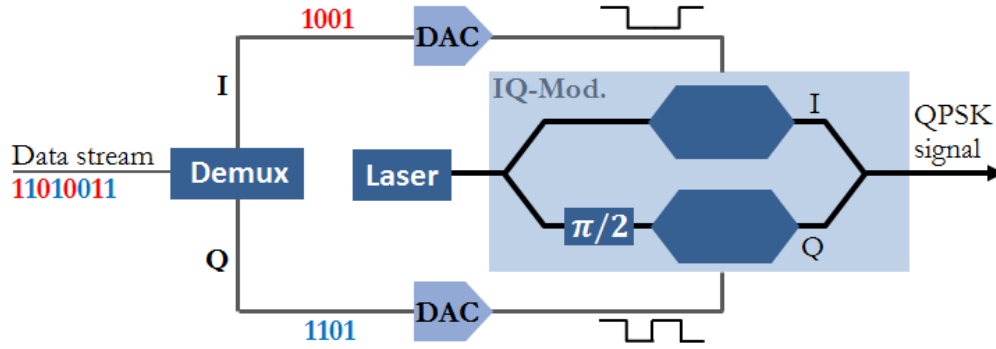


Fig. 6.2: General schematic of an optical transmitter based on the IQ-modulator.

To transmit a digital stream of data, the electrical bit sequence from the DSP in Fig. 2.9 is split by a demultiplexer into the I and Q arms and then converted with a Digital-to-Analog converter (DAC) to a bit-equivalent analog signal. This signal, with the corresponding voltages, drives the MZM to produce the intended constellation. Figure 6.2 shows this process, where the carrier $E_{in}(t)$ in Eq. (2.41) is modulated in QPSK. At this point, the output signal $E_{out}(t)$ can be written as

$$E_{out}(t) = a(t)\sqrt{P_s}\exp(j[w_s t + \phi_s(t) + \phi_{ls}(t)]) \quad (6.2)$$

where, depending on the adopted modulation format, the carrier is modified in amplitude $a(t)$ and in phase $\phi_s(t)$. Figure 6.3 shows the effect of phase and amplitude noise in the constellation diagram, where each symbol constellation becomes less definite and broadens. This phenomenon must be controlled under higher order modulation formats to allow the accurate detection of each symbol. It is important to consider that further alterations of the constellation will occur due to the channel impairments.

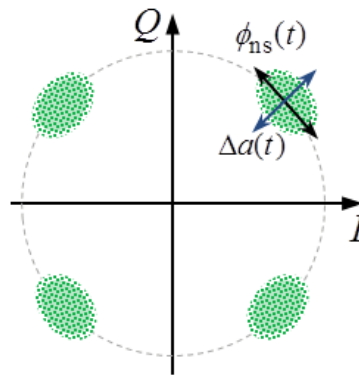


Fig. 6.3: Representation of the effect of the laser phase noise and amplitude in the constellation diagram of a QPSK modulation.

6.1.2 QPSK demodulator

The coherent receiver introduced in Sec. 2.2.2.2 is further detailed, showing the demodulation steps from the input signals Eq. (2.67)-Eq. (2.68) to the output in quadrature signals Eq. (2.69)-Eq. (2.70), here newly repeated.

This receiver is used to demodulate signals encoded with higher order modulation formats. This receiver requires the mixing of the incoming signal with the one of a local oscillator. At this point, it is only considered the modulated carrier signal components in Eq. (2.44) to represent the incoming signal $E_s(t)$

$$E_s(t) = \sqrt{P_s} \exp(j(2\pi\nu_s t + \phi_s(t))), \quad (6.3)$$

and the local oscillator (LO) signal $E_{l_0}(t)$ is described as

$$E_{l_0}(t) = \sqrt{P_{l_0}} \exp(j(2\pi\nu_{l_0} t + \phi_{l_0}(t))) \quad (6.4)$$

where the input signal power P_s , frequency ν_s , and phase $\phi_s(t)$ are combined with their equivalents local oscillator signal power P_{l_0} , frequency ν_{l_0} , and LO phase $\phi_{l_0}(t)$ to reconstruct the constellation of the modulated signal. This process is performed with the help of a so-called 90° -Hybrid and balanced detectors, which discriminates the in-phase $I_I(t)$ and quadrature $I_Q(t)$ signals from $E_s(t)$, see Fig. 6.4. These signals are then amplified with a TIA and further converted into digital signals $V_{I,Q}(n)$ using an ADC. Finally, the discrete signals require additional data processing, involving timing recovery, imbalance compensation, frequency offset compensation, and carrier phase recovery, previous demodulation. This is performed within a Digital Signal Processor (DSP).

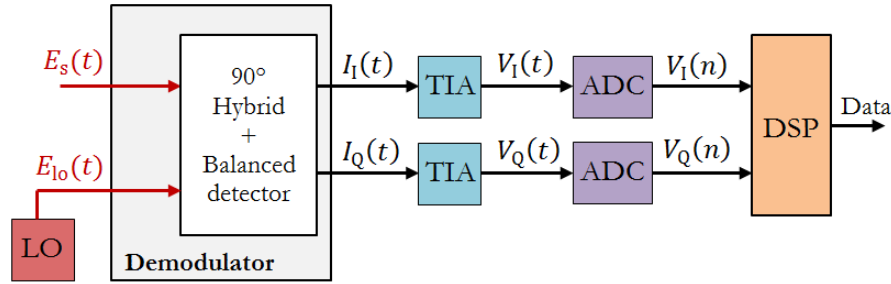


Fig. 6.4: Block diagram of the coherent receiver.

In this receiver, a key section is the 90° -Hybrid and balance detectors. The 90° -Hybrid is an arrangement of four 3dB-couplers that mix $E_s(t)$ with $E_{l_0}(t)$, inducing an additional $\pi/2$ phase shift in one of the split local oscillator signals to allow mixing with the quadrature term of $E_s(t)$, see Fig. 6.5. The output of the 90° -Hybrid are four signal, described by the following equations

$$E_1 = \frac{1}{2} (E_s + E_{l_0}) \quad (6.5)$$

$$E_2 = \frac{1}{2} (E_s - E_{l_0}) \quad (6.6)$$

$$E_3 = \frac{1}{2} (E_s + jE_{l_0}) \quad (6.7)$$

$$E_4 = \frac{1}{2} (E_s - jE_{l_0}) \quad (6.8)$$

In these equations the temporal variable is omitted for mathematical simplification, the $1/2$ factor comes from the half power attenuation of the couplers, and the j indicates the effect of the $\pi/2$ phase shift. These in-phase signals $E_{1,2}$ and quadrature signals $E_{3,4}$ are correspondingly sent to a balance detector, which transforms their

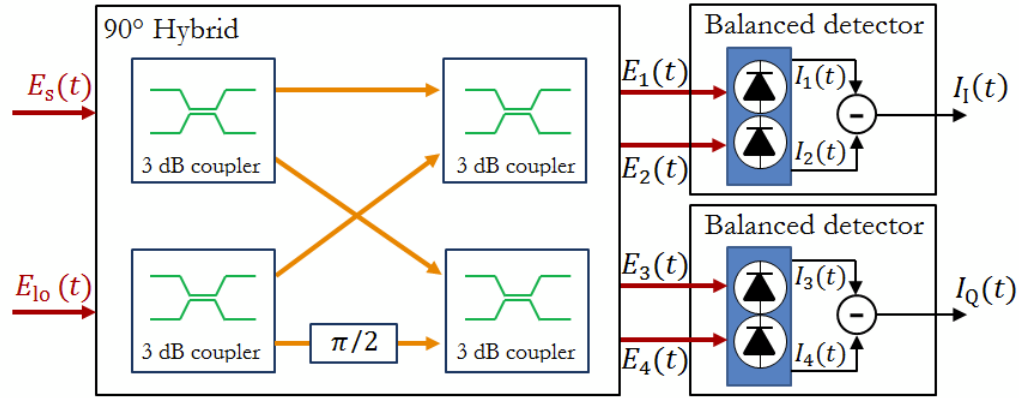


Fig. 6.5: Main blocks of the 90°-hybrid and balanced detectors.

respective optical power into electrical currents and deliver the differential of them. To describe this mixing process, let's start with the output signal current I_1 from one of the diodes of the balance detector

$$\begin{aligned}
 I_1 &= R |E_1|^2 = RE_1 E_1^* = \frac{R}{4} (E_s + E_{lo}) (E_s^* + E_{lo}^*) \\
 &= \frac{R}{4} \left(P_s + P_{lo} + \left[\sqrt{P_s P_{lo}} \exp(j(2\pi\nu_b t + \phi_s - \phi_{lo})) \right] + \left[\sqrt{P_s P_{lo}} \exp(-j(2\pi\nu_b t + \phi_s - \phi_{lo})) \right] \right) \\
 &= \frac{R}{4} \left(P_s + P_{lo} + 2\sqrt{P_s P_{lo}} \cos(2\pi\nu_b t + \phi_s - \phi_{lo}) \right) \quad (6.9)
 \end{aligned}$$

where $\nu_b = \nu_s - \nu_{lo}$ is the beat frequency, a DC term is present from the summation of the signal powers P_s and P_{lo} , and the encoded signal phase is affected by the local oscillator phase as $\phi_s - \phi_{lo}$. Similarly, the output balance detector currents $I_{2,3,4}$ are

$$I_2 = \frac{R}{4} \left(P_s + P_{lo} - 2\sqrt{P_s P_{lo}} \cos(2\pi\nu_b t + \phi_s - \phi_{lo}) \right) \quad (6.10)$$

$$I_3 = \frac{R}{4} \left(P_s + P_{lo} + 2\sqrt{P_s P_{lo}} \sin(2\pi\nu_b t + \phi_s - \phi_{lo}) \right) \quad (6.11)$$

$$I_4 = \frac{R}{4} \left(P_s + P_{lo} - 2\sqrt{P_s P_{lo}} \sin(2\pi\nu_b t + \phi_s - \phi_{lo}) \right) \quad (6.12)$$

Because the balance detector delivers the difference between both generated signal currents, the DC bias is removed and the two output signals are equal to

$$I_I = I_1 - I_2 = R\sqrt{P_s P_{lo}} \cos(2\pi\nu_b t + \phi_s - \phi_{lo}) \quad (6.13)$$

$$I_Q = I_3 - I_4 = R\sqrt{P_s P_{lo}} \sin(2\pi\nu_b t + \phi_s - \phi_{lo}) \quad (6.14)$$

From these equations it is clear that weak received signals can be amplified by increasing the power P_{lo} of the LO signal, which represents one of the most useful characteristics in coherent receivers. With this, the effects of background noise and dark current can be neglected, and since shot noise is directly proportional to the optical power, it dominates over the thermal noise allowing to consider the receiver as shot noise limited. Then, as the

mean optical input power on each diode of the balanced detector is constant, the shot noise produced can be written as

$$\sigma_{\text{sn}}^2 = 2qR \frac{P_{\text{lo}}}{4} \Delta f \quad (6.15)$$

After the balanced detector, the noise produced on each diode is added, leading to

$$\sigma_{\text{sn}}^2 = 2qR \frac{P_{\text{lo}}}{2} \Delta f \quad (6.16)$$

for the in-phase and quadrature signals. After being combined, the signal noise can be written as $n_{\text{sn}} \sim \mathcal{N}(0, \sigma_{\text{sn}}^2)$ with

$$\sigma_{\text{sn}}^2 = 2qRP_{\text{lo}}\Delta f \quad (6.17)$$

Consequently, the total noise n_{AG} will consider only shot noise and laser spontaneous emission noise as

$$n_{\text{AG}} = n_{\text{sn}} + n_{\text{ase}} \quad (6.18)$$

Likewise, combining all phase shifts in one as

$$\phi_{\text{m}}(t) = \phi_{\text{ls}} + \phi_{\text{lo}}(t) + \phi_{\text{pt}}(t), \quad (6.19)$$

and including also the terms representing the atmospheric fading $\alpha_{\text{atm}}(t)$ and transmitter gain G_{a} , the orthogonal signals $I_{\text{I,Q}}$ after the TIA and before the ADC, can be written in a combined manner as

$$V_{\text{RX}}(t) = V_{\text{I}}(t) + jV_{\text{Q}}(t) \quad (6.20)$$

$$V_{\text{RX}}(t) \propto \alpha_{\text{atm}}(t)R\sqrt{P_{\text{s}}P_{\text{lo}}}\exp(j[2\pi\nu_{\text{b}}t + \phi_{\text{s}}(t) - \phi_{\text{m}}(t)]) + n_{\text{AG}}. \quad (6.21)$$

Based on the carrier frequency difference between the LO and carrier signals, there are three main types of coherent reception:

- **Homodyne:** It drives the LO with the exact same frequency and phase of the carrier, thus the beat frequency $\nu_{\text{b}} = \nu_{\text{s}} - \nu_{\text{lo}} = 0$. This down-converts the received signal to a baseband and allow the sampling and signal recovery. An optical phase-locked loop (OPLL) system is used to precisely lock the frequency and phase of both signals, which change in time. The OPLL system is complex to calibrate and tends to lose synchronization in scenarios with strong fading, thus they have been implemented in inter-satellite links where atmospheric effects are non-existent and signal maintains sufficient stability.
- **Heterodyne:** It uses a LO running at a different frequency of the carrier signal, thus the beat frequency down-converts the signal onto an intermediate frequency $\nu_{\text{i}} = \nu_{\text{b}}$. Since the signal has a particular spectrum bandwidth, the ν_{i} has to be at least twice this bandwidth to avoid overlapping.
- **Intradyn:** It runs the LO at a similar frequency of the carrier, but it does not lock it. This results in an unknown digitized ν_{b} and phase offset between the carrier and LO signal. Hence, it requires a DSP to compensate them. This system is being investigated for satellite applications.

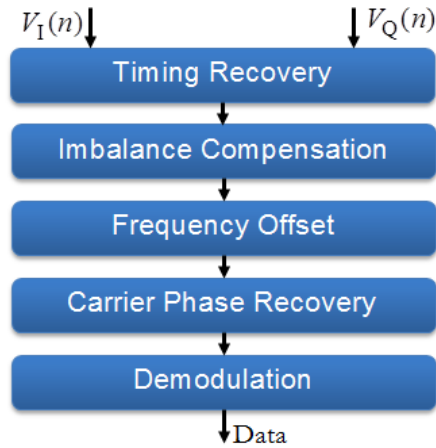


Fig. 6.6: Digital signal processing stages.

After the ADC sampling process, the signal is processed with the DSP and the data is recovered. Details about the involved DSP processes are out of the scope of this work. Here, a broad overview of each main processing stages is given. Once the received signal is demodulated and digitized, the steps shown in Fig. 6.6 are carried out. Figure 6.7 shows the signal after each processing stage.

- **Timing recovery:** This process is necessary for direct and coherent detection. Here, signal sampling must be performed at the right instant during the symbol duration T_s , preferably at its center, avoiding to sample at the transitions. Fluctuations of the ADC clock introduce a drift in the sampling time, which can be compensated using a timing recovery stage in closed-loop and controlling an error metric. This error metric represents the difference between the sampling point respect to the center of the symbol. The DSP timing recovery can be performed with the Gardner algorithm [148], which forces a sample at the center and the transition of the symbol, or with the spectral-based squared timing recovery [149], among others. Figure 6.7 shows how timing recovery improves the sampling process reducing the uncertainty of symbol detection from the received signal (yellow circle).
- **Imbalance compensation:** gain imbalances between the I and Q signals produce a loss of orthogonality which moves the constellation symbols away from the expected positions. This leads to the wrong symbol mapping and errors in the retrieved data. The correction is performed with a filter of the type

$$\begin{bmatrix} I' \\ Q' \end{bmatrix} = \begin{bmatrix} g_1 & 0 \\ g_2 & g_3 \end{bmatrix} \cdot \begin{bmatrix} I \\ Q \end{bmatrix} \quad (6.22)$$

where the coefficients $g_{1,2,3}$ are calculated with algorithms like [150, 151]. Figure 6.7 shows how the imbalance compensation process improves the slight ellipsoid shape after timing recovery.

- **Frequency offset compensation:** this step is compulsory on intradyne receivers as the LO signal runs freely and the frequency and phase offset between the LO and carrier are unknown. Laser frequency fluctuations can be divided in slow static drifts, caused by changes in the environmental conditions (slower than 1 GHz/h), and faster dynamic drifts due to laser oscillations around its fundamental frequency (MHz

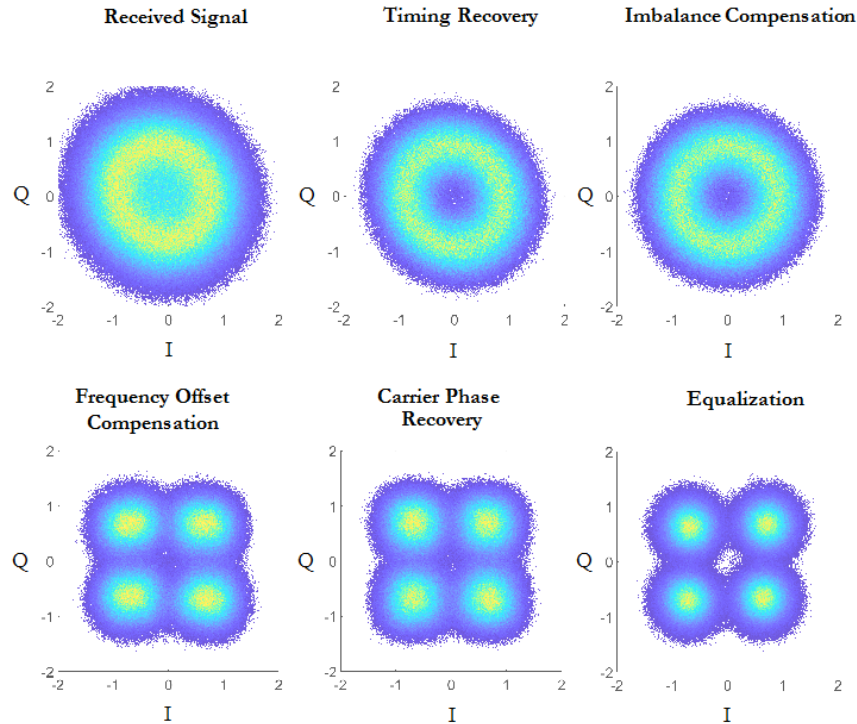


Fig. 6.7: Visualization of the signal after each DSP stage for QPSK demodulation.

range). Again, a digital domain compensation can be used either in the time domain comparing the phase of consecutive symbols [152–154], or in the spectral domain identifying the peak position [155]. Figure 6.7 shows now a clear image of the four symbols.

- **Carrier phase recovery:** This step is also compulsory on intradyne receivers. As introduced in the previous sections, Eq. (6.19), the total phase noise is a compound of phase noises originated in the laser source ϕ_{ls} , local oscillator ϕ_{lo} , atmospheric piston effect ϕ_{pt} , and some residual phase error ϕ_{res} originated during the frequency offset compensation process. These phase variations broaden the symbols so that their relative phase is estimated with errors. This effect is corrected using algorithms like the Viterbi Viterbi, which divides the burst into blocks, averages the phase offset within it, and finally re-shift the block phase [24]. Other algorithms are the blind phase search and the decision-directed digital phase locked loop [156, 157].
- **Equalization:** Inter Symbol Interference (ISI) is seen in the previous step, increasing the probability of wrong symbol detection. The equalizer mitigates the ISI by redistributing the power within the signal, meaning that the signal-to-noise ratio of low power symbols is increased, and the energy of high power symbols is reduced. This process allows an efficient detection of each constellation symbol, improving the BER [158].

After all these processes, the data is recovered by mapping the symbol position with the original symbol modulation map.

6.2 Coherent data communication test

This experiment evaluates the AO system in a communication scenario. The objective is to verify that the improvement in the signal quality is sufficient to allow high throughput data transmissions. The original setup presented in Fig. 5.2 is integrated with a coherent transceiver that modulates the laser carrier in Quadrature Phase Shift Keying (QPSK). The modulation is performed at 40 Gbauds (80 Gbps). Figure. 6.8 shows the system, where the laser carrier is collimated, then the beam wave-front is distorted in phase with the SLM, and the reflected beam is guided through the AO system to be finally coupled into the SMF. The coupled signal is split, sending 90% of the signal to the QPSK demodulator, and 10% to the APD detector.

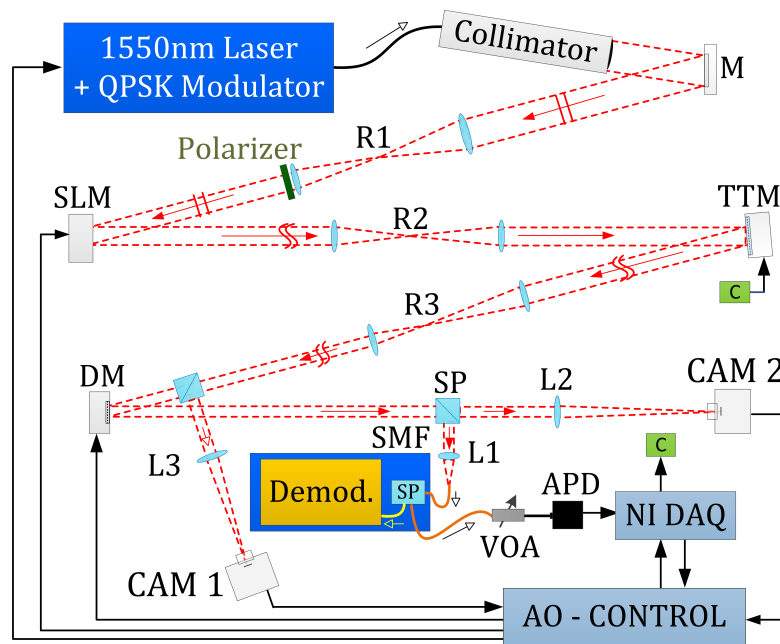


Fig. 6.8: AO setup with integrated coherent transmission system.

6.2.1 Description of the transmission system

The coherent communication system used in the experiment consists of separated modules for the QPSK transmitter and receiver, see Fig. 6.9. In the transmitter, a bit pattern generator (SHF-12163A) with two 40 GHz bandwidth differential outputs generates a non-pulse-shaped pseudo-random bit sequence (PRBS) with a length of $2^7 - 1$ bits. Each differential output feeds a customized optical modulator (IQ-ModBOX IXBlue) that contain two IQ modulators, used for dual polarization. The carrier signal for the modulator is generated internally with a C-band laser source of 25 KHz linewidth and 16 dBm maximum power. The output of the modulator is connected to the AO system that produces a collimated beam that propagates through the AO system until reaching the SMF coupling section. The coupled signal power is then split, sending 10% of the signal to the AO system and 90% to the QPSK receiver. The coherent receiver (Finisar CPRV4225A) consists of two matched 90° -Hybrid with integrated balanced photodetectors (one for each polarization) and four linear trans-impedance amplifiers (TIA); Figure 6.5 shows one single-polarization receiver. The local oscillator signal for the coherent

receiver is generated with an external laser source (Teraxion Purespectrum NLL) of narrow linewidth (<5 KHz) and 10.5 dBm output power. The output of the coherent receiver is then sampled at a rate of 80 GSa/s (Giga samples per second) with a 63 GHz real-time bandwidth Oscilloscope (Keysight DSA-Z-634A Z-series). The bandwidth of the oscilloscope is limited to 80% of the received Baudrate (40 Gbauds \rightarrow 32 GHz). The acquired signals are stored for post-processing where the DSP stages are applied. This system was design by DLR and details can be found in [147, 159].

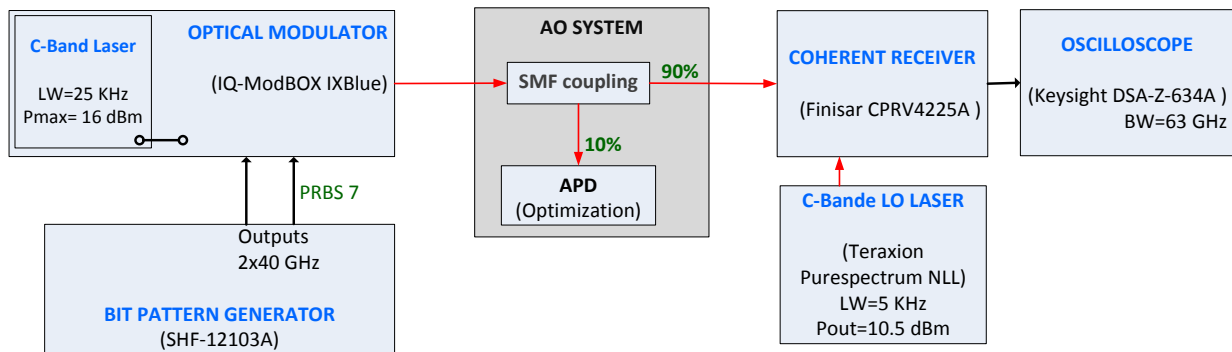


Fig. 6.9: Block diagram of the experimental coherent transmitter and receiver.

6.2.2 Power requirements - Communication vs. AO system

Power efficiency is an important characteristic of an AO system for FSOC. The AO system has to be able to operate with a fraction of the power required by the communication system. Here, the camera must have sufficient signal power to properly detect the speckles that are targeted for correction on each turbulent regime, meaning that each speckle must have enough SNR. Likewise, the APD must also acquire the coupled signal with high SNR to perform the parabolic optimization with a minimum impact of the noise.

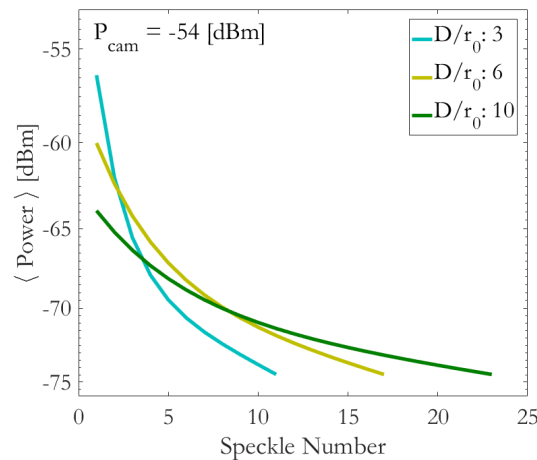


Fig. 6.10: Camera input power distribution between the speckles for different turbulent regimes. The cumulative power of the speckles sum up 80% of the total input power. The minimum input power to assure a 3 dB SNR in the less intense speckle of each scenario is $P_{cam} = -54$ dBm.

The minimum input power of the camera (CAM 1) is defined to have at least 3 dB of SNR in the less intense speckle, see Fig. 5.2. This input power is equal to -75 dBm, obtained from Eq. (5.2) of the camera characterization. As shown in Fig. 4.5, the number of speckles considered to accumulate 80% of the total focal power vary with the turbulence. The Eq. (4.1) allows the estimation of the mean normalized power per speckle for different D/r_0 , thus, the power ratios between speckles can be used to project the power distribution from the less intense speckle to the brightest one, and calculate the total required input power.

Figure 6.10 shows the curves of power distribution among the speckles for three turbulent regimes. The total power contained within the speckles is 80% of the maximum, but distributed differently. The very last speckle on each scenario has a minimum power that assures 3 dB over the camera noise floor. The total power required, independently of the scenarios, sum up $P_{\text{cam}} = -54$ dBm. The SNR per speckle can be directly mapped with the help of Eq. (5.2).

The total power required for the AO system can be estimated by adding P_{cam} and the minimum APD input power for a sufficient optimization process SNR, see Fig. 5.12. Here, the APD input power is set to -46 dBm to have an SNR = 35 dB. Assuming $P_{\text{cam}} = -50$ dBm to increase the SNR of the less intense speckle above 6 dB, the AO system would need a total received power of $P_{\text{AO}} = 35$ nW or -44.2 dBm.

The AO power requirement can be compared with the minimum sensitivity power for different QPSK data rates. From the BER measurements, shown in Fig.6.11 and Fig.6.13, a minimum input power of $P_s = -30$ dBm is required for a BER $\approx 10^{-6}$. The number of photons per bit N_p for the measured data rate $R_b = 80$ Gbps, can be calculated as

$$N_p = \frac{P_s}{R_b E_p}, \quad (6.23)$$

where $E_p = hc/\lambda$, with $h = 6.6 \times 10^{-34}$ [m²kg/s] being the Planck constant, $c = 3 \times 10^8$ [m/s] the velocity of light, and $\lambda = 1550$ [nm] the wavelength of the carrier. The calculation results in $N_p \approx 98$ [ph/bits]. This N_p is typical for coherent receivers [58]. Assuming this number constant for different data rates, the required received power P_{in} for the communication system can be calculated from Eq. (6.23). The results are shown in Table 6.1.

<i>Data Rate</i> <i>QPSK</i>	P_{in} (BER = 10^{-6})	P_{AO}	<i>AO power</i> <i>requirement</i>
1 Gbps	12.5 nW	35 nW	$3P_{\text{in}}$
10 Gbps	125 nW	35 nW	$P_{\text{in}}/4$
40 Gbps	500 nW	35 nW	$P_{\text{in}}/14$
80 Gbps	1 μ W	35 nW	$P_{\text{in}}/29$
100 Gbps	1.25 μ W	35 nW	$P_{\text{in}}/36$

Table 6.1: Comparison between the power requirements of the AO system and the communication system for a QPSK modulation format and BER = 10^{-6} .

This general estimation shows that, for the current test, the AO system needs -15 dB power (15 dB less power) than the communication systems, which indicates good power efficiency. At 10 Gbps this margin drops to -6 dB. Instead, at 1 Gbps the AO system needs around 5 dB more power than the communication system, which makes it power inefficient. Furthermore, adaptive optics may not be needed for receivers working in on-off keying (OOK) at $R_b \leq 10$ Gbps, where free-space detectors can be used. With higher data rates, SMF coupling is required to benefit from the use of optical amplifiers and coherent reception, hence AO is needed.

Generally, an AO system targets a $\text{BER} \approx 10 \times 10^{-3}$, from where Forward Error Correction (FEC) system can provide error-free data transmission. In such a case, the power requirement gap reduces, as shown in Table 6.2. The AO systems needs between -7 dB and -11 dB power than the communication system, operating with data rates between 40 and 100 Gbps, respectively.

<i>Data Rate</i> <i>QPSK</i>	P_{in} ($\text{BER} = 10^{-3}$)	P_{AO}	<i>AO power</i> <i>requirement</i>
1 Gbps	4 nW	35 nW	$9P_{in}$
10 Gbps	40 nW	35 nW	P_{in}
40 Gbps	158 nW	35 nW	$P_{in}/5$
80 Gbps	316 nW	35 nW	$P_{in}/9$
100 Gbps	395 nW	35 nW	$P_{in}/11$

Table 6.2: Comparison between the power requirements of the AO system and the communication system for a QPSK modulation format and $\text{BER} \approx 10^{-3}$. This BER is considered the limit for the error correction system to deliver error-free data transmission.

6.2.3 Evaluation of the AO system in a communication scenario

The AO system is evaluated in a communication scenario by integrating a coherent QPSK transmitter and receiver in the setup. The test is performed over 200 uncorrelated fields generated for the scenarios $D/r_0 = [5, 6]$, which are representatives of a satellite downlink at elevations near 10° with an aperture $D = 40$ cm, see Fig. 2.5. On each case, the coupled signal is measured before and after the correction of 20 speckles (≈ 58 iterations) per field. Concurrently, the mean BER of the received data is measured. For each distorted field, 50 data sequences with 10^6 bits each are generated by a PRBS7 (pseudorandom bit sequence of size $2^7 - 1$). Each data sequence is modulated in the laser carrier in QPSK at 40 Gbaud. In the receiver side, the signal is sampled with an oscilloscope at 80 GSamples/s. Then, the sampled signal is saved for post-processing. The procedure is repeated after each field distortion is corrected with the algorithm.

The post-processed 50 data sequences per field result in a mean BER value, one for the corrected state with the AO system activated (AO ON) and one for the uncorrected state (AO OFF). Both are plotted in Fig. 6.11 (a,c). The results are contrasted against the 40 Gbaud back-to-back reference curve and the ideal shot-noise limited curve (dashed black). The PDF of the BER, when the AO system is set on/off, is shown in Fig. 6.11 (b,d).

The results show a better BER when the AO correction is performed, indicating an increment in the SMF coupled power. For the scenario $D/r_0 = 5$, the speckle correction implies an improvement in the quality of the beam, which increases the coupled power and reduces its variance, improving the BER by three orders of magnitude. For the scenario $D/r_0 = 6$, the slight increment in the variance of the coupled signal is seen as a larger span of the measured BER values (AO OFF). Here, the stroke of the illuminated section of the DM reaches its maximum, limiting the correction capabilities. Nevertheless, signal enhancement is achieved reducing the errors in the data transmission, as shown in the histograms.

To estimate the system performance under stronger turbulent regimes, the curves of BER can be directly calculated from the fiber coupled power measurements performed in the APD of the AO system. Note that after the fiber coupling the signal is split with a 90/10 ratio, but the variance should remain equal to the power signal

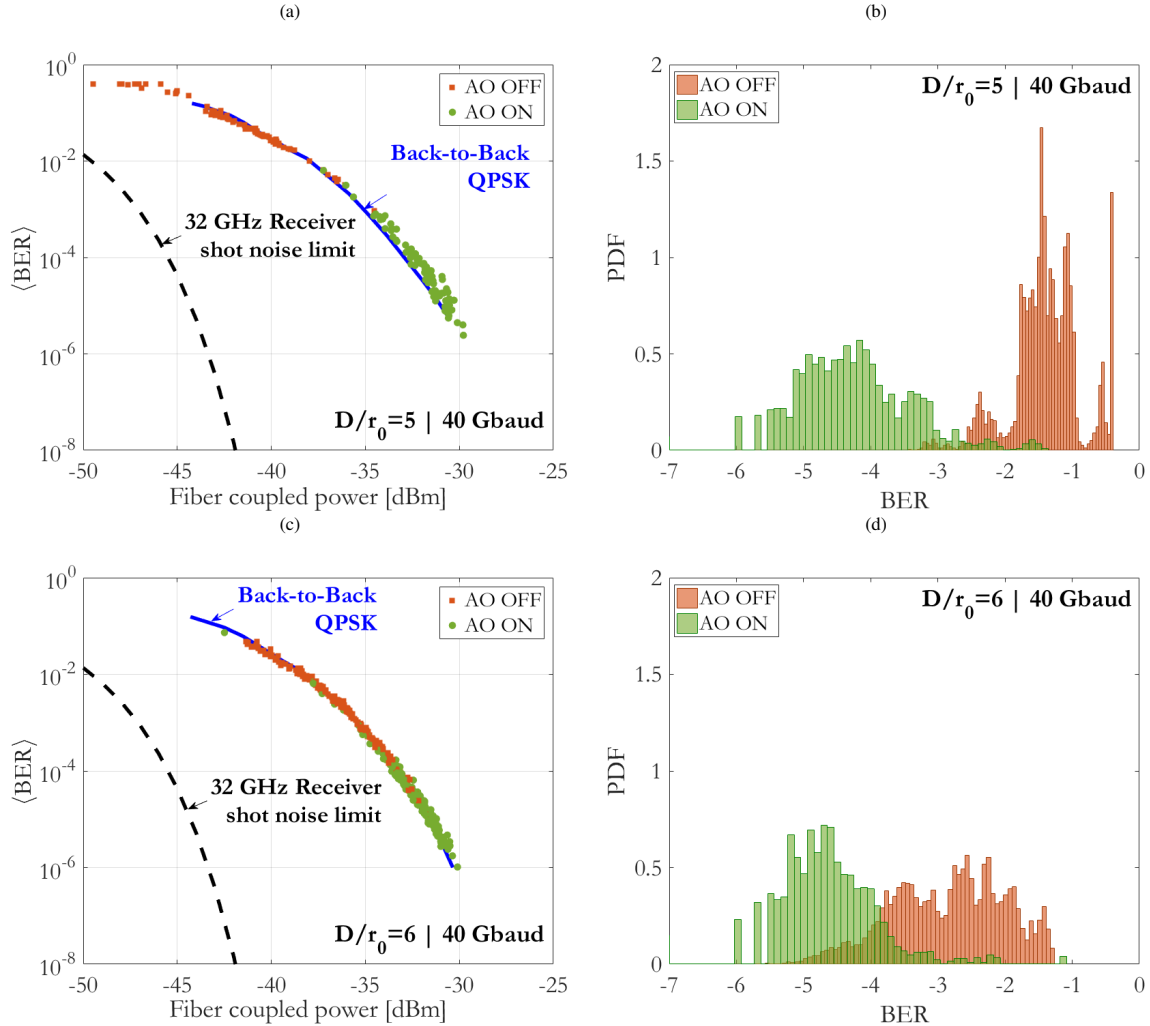


Fig. 6.11: (a) Receiver sensitivity measurement for a 40 Gbaud QPSK data transmission corrected by the AO system. (b) PDF of the BER when the AO system is set on/off. The dashed curve represents the shot-noise limited ideal performance and the dotted curve. The blue curve represents the back-to-back reference of the receiver. The green and red dots are the mean BER calculated after DSP processing of the received 50×10^6 bits per field when the AO system is ON and OFF, respectively.

of the coherent receiver. Considering again the Eq. (2.99)

$$\text{BER}_{(\text{QSPK})} = \frac{1}{2} \text{erfc} \left(\sqrt{\eta_e N_p} \right) \quad (6.24)$$

and recalling Eq. (2.58) with $R = \eta_e q / h\nu = 0.08$ being the responsivity of the coherent receiver (Finisar CPRV4225A), the quantum efficiency η_e can be calculated and used to approximate the signal-to-noise ratio $\text{SNR} = \eta_e N_p$. The number of photon N_p is estimated with Eq. (6.23) and $R_b = 32 \times 10^9$, which is the filter bandwidth of the ADC oscilloscope set to 80% of the 40 Gbauds symbol rate. Figure 6.12 shows the estimated BER curves for $D/r_0 = [3, 5, 10]$ superimposed on Fig. 6.11(a). The BER performance for the scenario $D/r_0 = 5$ closely follows the lower limit BER performance obtained after DSP post-processing in the coherent receiver. One may consider that these power vectors are obtained directly from the optimization signal, thus the influence of the APD shot and thermal noise may reduce the SNR. In the scenario with $D/r_0 = 3$, the AO system can perform better and correct the fields with minimum constraints of the hardware, thus the curve follows the best

case represented by the QPSK back-to-back dotted line. The opposite case is represented by the scenario with $D/r_0 = 10$, where the focal energy is highly dispersed and hardware limitations do not provide that high level of correction, hence the BER curve shows nearly 7 dB penalty for a $\text{BER} = 10^{-6}$.

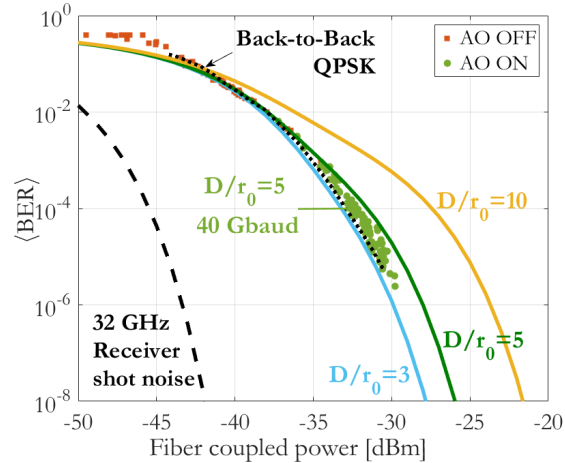


Fig. 6.12: (a) Continues BER curves are calculated with Eq. (2.99) and consider the measured power vectors for the scenarios $D/r_0 = [3, 5, 10]$ assuming constant shot noise. The dashed curve represents the shot-noise limited ideal performance and the dotted curve the back-to-back reference curve of the receiver. The green and red dots are the mean BER calculated after DSP processing of the received 50×10^6 bits per field when the AO system is ON and OFF, respectively.

The same BER analysis of Fig. 6.11(c) is performed with correlated fields in order to verify the BER performance during the iterative optimization, which implies measuring the BER on each iteration. The result is shown in Fig. 6.11. Here, the correlated fields are generated and sent to the SLM with a spacing ($N=4$) or $0.4\tau_0$. In this case, 10^6 bits are sent with each iteration. Each field is corrected with 20 speckles (58 iterations), which means that a total of 58×10^6 bits are considered per optimized field. Only 16 fields are tested, which represents around 5 uncorrelated states. In other words, with a field spacing of $0.4\tau_0$, every second field occurs at $0.8\tau_0$ and it is partially correlated, see Fig. 6.11 (c), and every third field occurs at $1.2\tau_0$ being fully uncorrelated; this means that in 16 fields the transition to an uncorrelated state happens 5 times.

Figure 6.13 (a) shows the BER per iteration during the correction of the fields. Most of the measured BER values tend to be positioned around a $\text{BER} \approx 10^{-5}$. There are also measurements with worse BER, which results from the loss in coupling efficiency during the correction, visualized in Fig. 6.13 (b). Around the iteration number 1000, the algorithm faces a reduction on its performance with a coupling penalty below 3 dB. Later, the signal recovers. The inset shows that this signal deterioration rarely falls below 5 dB.

Overall, it can be seen that the method corrects highly distorted fields with a reduced number of iterations (≈ 58), allowing very high data throughput ($= 80$ Gbps). The signal fluctuations during the optimization of each field do not greatly impact in the mean BER, but the method for the dynamic correction of the fields still requires further improvements. This is a first approach and preliminary test to prove the continuous correction capabilities of the technique, facing correlated fields with realistic temporal evolution.

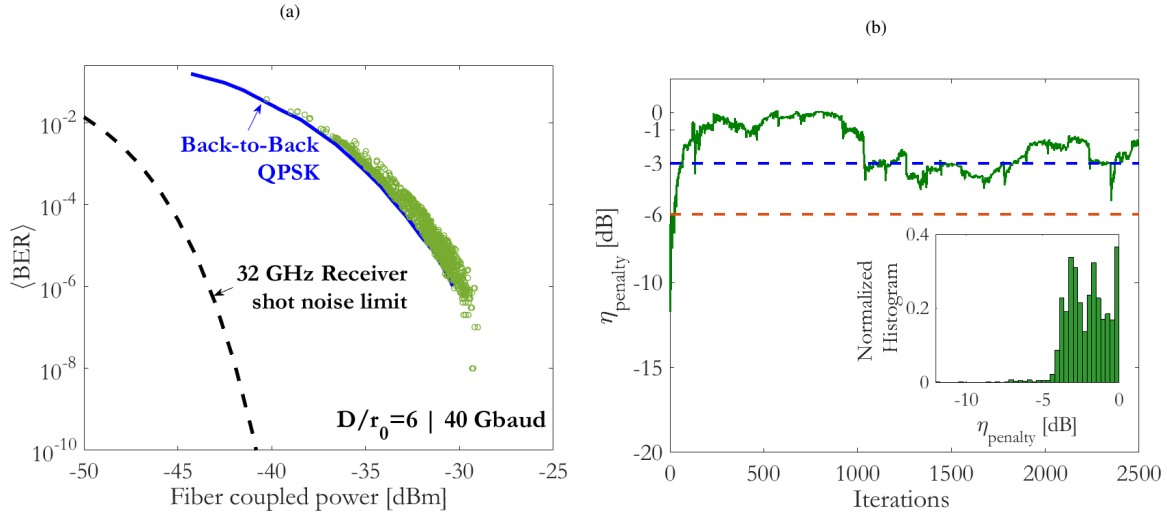


Fig. 6.13: (a) Receiver sensitivity measurement for a 40 Gbaud QPSK data transmission corrected by the AO system ON and considering correlated fields. The data measurement is performed on each iteration. The dashed curve represents the shot-noise limited ideal performance and the blue curve the back-to-back reference of the receiver. The green circles are the mean BER calculated after DSP processing of the received 58×10^6 bits (10^6 bits per iteration) per field. (b) Coupling signal penalty for each iteration of the optimization process. Normalized histogram of the coupling penalty.

6.3 Conclusion of the chapter

This chapter has addressed the final objective of this thesis and validated the AO system in a communication scenario. The main goal was to verify that, in the presence of turbulence, this AO technique can sufficiently correct the induced wave-front distortion allowing a better SMF coupling and improving the BER performance in multi-gigabit transmission.

The experiment involved the integration of a coherent QPSK transmitter and receiver in the AO system, where a set of decorrelated and correlated phase screens were applied to the SLM to induce different levels of phase distortions in the beam wave-front. The analysis with decorrelated fields intended to evaluate the communication performance with the final state of correction of the fields. The mean BER was measured before and after AO correction to quantify the improvement. For the case of correlated fields, the BER measurement was performed on each iteration to evaluate the performance during the correction process and transitions between fields. This test also intended to indirectly verify that the algorithm for dynamic compensation can maintain the signal correction over several fields, and thus the BER performance.

The results indicate that for moderate turbulence $D/r_0 \approx [5, 6]$ the distorted beam can be sufficiently corrected, improving the BER beyond the minimum FEC limit (10^{-3}). Note that the FEC limit is the minimum BER from which Forward-error-correction system can provide error-free transmission. The numerical curves calculated with the experimental power vectors and considering the coherent receiver parameters showed the expected performance under scenarios of strong turbulence, clearly show a good match with the tested $D/r_0 = 5$ case.

It can be concluded that this AO approach improved the coupling efficiency and improved the BER performance. The demonstration was performed using QPSK modulation at 80 Gbit/s and intradyne reception. Future experiments should be oriented towards the prototyping of the concept to test the technique dynamically in real-time, thus to confirm these results.

CONCLUSIONS AND FUTURE WORK

THIS thesis has proposed a new adaptive optics solution for turbulence compensation in satellite laser communications scenarios. The goal was to achieve SMF coupling with sufficient efficiency and signal stability allowing the use of advanced coherent modulation formats to achieve very high data throughput.

7.1 Summary

The motivation of this work was originated by the need of establishing robust laser links from satellites and aircraft to earth ground stations, targeting lasercom applications like earth observation. A particular emphasis was given to the case of LEO downlinks at low elevations ($<30^\circ$). As explained in chapter 1-2, the cumulative effects of the turbulence over long paths induce in the beam wave-front strong amplitude fluctuations, strong phase distortions, and phase singularities, resulting in signal fading affecting the communication performance. When the turbulence distorts the phase-front, the focused light results in spread intensity spots (speckled intensity pattern), and the power fluctuates randomly every millisecond, impairing a stable fiber coupling. Consequently, phase wave-front aberrations are the principal limitation to the use of coherent modulation formats like BPSK and QPSK, which require an efficient single mode fiber (SMF) coupling.

The FSOC community have addressed this problem with the help of standard adaptive optics systems, mostly inherited from astronomy. Due to the severe turbulence conditions in LEO downlinks, such systems have performed with partial success, being truly efficient and allowing gigabit downstream up to moderate turbulence [43–47]. Satellite communications require a robust solution under any turbulence condition, as well as a simple system easy to integrate either in a fixed or transportable optical ground station (OGS).

Under such conditions, an iterative (sensor-less) approach was chosen as a potential solution due to positive characteristics like robustness in all turbulent regimes, hardware simplicity, easiness of integration and calibration, and low cost. The principal limitation was identified in the long convergence time of the iterative process. A standard stochastic iterative method follows a blind optimization of the power coupled in the fiber and thus it requires above 100 iterations to converge, or equivalently AO loops running at 100 KHz or more, definitively non-practical with the state-of-the-art deformable mirrors.

To address this limitation and make possible the use of iterative solutions in FSOC, the proposed AO technique makes use of the existing OGS tracking camera and the power coupled in the fiber, thus adding minimum hardware complexity to the standard sensor-less system designs. The adaptation method operates on each main intensity spot of an acquired focal image (speckled intensity pattern), sequentially updating and optimizing their phases. It can estimate the phase of each speckle in a closed form via the quadratic optimization of the power of the fiber-coupled signal, thus only three power measurements (iterations) are needed per speckle. Consequently, the algorithm does not need to monitor nor to react to the trend of the coupled signal, and just perform the pre-established measurements and optimization steps to assure the correction of the field.

The general objective of this thesis was to validate these claims and prove that these ideas and methods

are technically feasible, also offering a new insight to iterative solutions, and hopefully encouraging new development in the field.

7.2 Conclusions

The conclusions of this thesis follow the initial objectives presented in Sec. 1.5:

- *Regarding the analysis and modeling of the proposed speckle-based compensation method:* The principal limitation of the iterative methods state-of-the-art is related to the working principle of their algorithms, that blindly search for the signal optimization. Such an approach certainly needs too many iterations as there is no predictable connection between the measured focal power and the unknown pupil phase distortion. The model presented in chapter 4 relates both optical planes in a simple manner, linking each main speckle spot of the intensity image with a predefined pupil mode (plane-wave phase). Following basic principles of Fourier optics, a very complex problem is simplified to the search of scalar variables representing the relative phase differences between speckles, or equivalently the best coherent phase matching between plane waves. The proposed model also benefits from the possibility of performing each speckle optimization with just three iterations, allowing each field to be corrected proportionally to the number of speckles selected. Consequently, this approach truly simplifies the search of the best compensation phase, now in a priori well-defined, tractable, and flexible manner.

These combined set of properties makes the technique very attractive for FSO applications. To my knowledge, there is no other method capable of identification of the required number of iterations and a limited set of possible solutions in-advance. The method directly addresses the dispersed energy spots saving time in the process of focusing the focal energy. Furthermore, the method can be adapted to the turbulence conditions or the targeted coupling efficiency by varying the number of corrected intensity speckles, i.e. the number of iterations.

This model also offers the possibility of working directly in the focal plane. As described mathematically in Sec. 4.2.3 and Eq. 4.21, the phase on each speckle spot can be reasonably considered constant. This may allow the use of a segmented DM positioned directly in the focal plane, applying piston phase changes at each speckle position. This approach may benefit from very fast segmented DMs able to reach up to 120 KHz with piston excursions of half wavelength [115], sufficient for the range of phase values related to the phase of a focal speckle.

- *Regarding the numerical analysis of the technique:* The main objective of the numerical analysis was to verify the assumptions of the model and its working principle.

The numerical analyses considered the generation of decorrelated and correlated phase screens, from which pupil complex fields were created and Fourier transformed, thus the speckle patterns needed for the adaptation method were obtained. The algorithm was implemented following the steps described in Fig. 4.16, and the results showed an excellent performance in all turbulent regimes, as depicted in Fig. 4.21. In the particular case of strong turbulence and $D/r_0 = 10$ shown in Fig. 4.19, the technique efficiently addressed the most intense speckles and corrected them with the expected number of iterations, needing

for convergence less than 60 iterations per field. The signal gain was substantial (≈ 10 dB), and the variance was greatly reduced (≈ 7 dB) which is crucial to minimize the fading of the signal and improve the communication performance. The concept was also tested against strong scintillation and branch points by generating phase screens with an in-house software tool developed by the German Aerospace Center (DLR) [137]. The impact of scintillation and phase singularities showed a slight reduction of 2 dB in the signal gain but not much influence in the number of required speckles for correction, which proves that phase distortions are dominant defining the spreading of energy in the focal plane. The impact of signal noise resulted in early saturation of the curves and less overall gain, originated by the errors in optimization due to noisy power measurements used in the quadratic optimization process. It is estimated that a SNR ≈ 50 dB in the measurement of the coupled-signal power is required for near-ideal performance. Different levels of signal-to-noise-ratio of the coupled-signal reduce the maximum coupling efficiency. Simulations show however that the AO system improves the coupling efficiency, working at SNR > 40 dB.

From these results, one can conclude that the numerical evaluation of the technique has validated the assumption of the model. Each speckle can indeed be related to a well-defined plane wave mode in the pupil plane, and its phase can be optimized with three power measurements. Because of this, the method can correct the distorted field with a total number of iterations equal to three times the number of selected speckles. The coupling efficiency shows a steady improvement with each corrected speckle, supporting the assumptions made in Eq. (4.23). The study of the number of required corrected speckles and iterations per turbulent scenario shown Fig. 4.21, and the trend of the coupling efficiency after each correction, support the assumed relation between the speckles and the plane wave modal representation of the wave-front. From the analysis of the optimum number of speckles per turbulent scenario, one can predict $\approx 40\%$ less loop bandwidth requirements in comparison with other stochastic iterative methods.

- *Regarding the experimental evaluation of the adaptation technique:* The main objective in the experimental evaluation of the technique was to confirm the results of the numerical analysis.

In order to perform the experiments, a laboratory setup was built to emulate turbulence phase distortions in satellite downlinks, as it is shown in Fig. 5.2. The algorithm was implemented following the steps described in Fig. 4.16. All hardware involved was characterized to identify the possible limitations and minimize errors in the analyses due to hardware constraints. In line with this, due to limitations on the SLM phase range and the DM excursion and resolution, the optimal operation range of the emulated phases was defined for weak to moderate turbulence between $D/r_0 = 1$ and $D/r_0 = 6$. However, measurements under the equivalent of strong turbulence $D/r_0 = 10$ have also been performed to quantify the impacts of such constraints in the technique and to evaluate the degree of improvement obtained. The preliminary concept for dynamic correction of correlated fields was also evaluated.

The results have validated the model and simulations, confirming the proposed pupil plane wave representation of the focal intensity pattern and the quadratic optimization of the speckles phase. The performance curves have confirmed the predicted trend of the coupling efficiency and the required number of iterations per speckle and field. The receiver noise had the expected impact on the overall performance. However,

the improvement in the coupling efficiency was occurring a slower rate than in the simulations, having a mismatch of approximately 0.5 dB between the experimental coupling efficiency and the simulated one at the evaluated point of 20 corrected speckles (58 iterations). One can conclude that fitting errors in the DM, system vibrations, and non-perfect tilt compensation surely impact the performance of the experiments. The experimental PDFs in Fig. 5.17 showed that the signal variance in scenarios of moderate turbulence was reduced by 3 dB, and the final coupling was enhanced by nearly the same proportion. The scenario of equivalent stronger turbulence $D/r_0 = 10$ in Fig. 5.18 also showed a signal gain of approximately 3 dB with 60 iterations and nearly the same amount of reduction in the variance, noticing an expected penalty in both metrics due to the hardware limitations. The positive aspect of this test is that the algorithm can still deliver an increment in the signal quality, indicating that refinement on the system design may certainly improve these results.

This thesis has also experimentally tested a preliminary approach to the dynamic speckle tracking and correction, presented and briefly analyzed in Sec. 4.3.4. The laboratory tests evaluated this approach with correlated fields in moderate turbulence $D/r_0 = 6$. The results showed a good performance maintaining the correction between field states decorrelated by one-third of the field coherence time $\tau_0/3$, reducing the variance of the coupled signal by approximately 4 dB. On the other hand, this solution may face limitations operating at very fast loop rates or under strong turbulence, requiring frequent re-lock of the distorted phase. Here, this approach is not robust enough, and stochastic methods perform better.

Finally, one can conclude that the technique experimentally works and corrects a wide range of turbulent regimes with a reduced number of iterations. Still, the experiment needs to be improved to further test this concept under $D/r_0 \gg 6$, and more work is required in the control and dynamic correction of the fields.

- *Regarding the experimental validation in a communication scenario:* The final objective of this thesis involved the validation of the AO system in a communication scenario. The main goal was to verify that, in the presence of turbulence, the AO system can sufficiently correct the induced wave-front distortion allowing a better SMF coupling improving multi-gigabit transmission.

For this analysis, a coherent QPSK transmitter and receiver was integrated with the AO system. The tests were performed in a non-real time regime measuring the BER before and after the correction of a turbulent field. The experiment was performed with decorrelated fields testing the performance after the final correction of each field. Additionally, the same test was performed with correlated fields measuring the BER on each iteration. The acquired power vectors were used to estimate the performance under strong turbulence $D/r_0 = 10$ by the use of the theoretical BER formula.

The results under moderate turbulence showed in both cases a clear improvement in the BER of the transmission system after AO correction. It was achieved nearly four orders of magnitude improvement and a BER $\approx 10^{-6}$ for the scenario $D/r_0 = 5$, and around two orders of magnitude better BER in the scenario $D/r_0 = 6$ due to increased signal variance. The estimation under strong turbulence $D/r_0 = 10$ showed the expected penalty, needing 7 dB more power to reach similar performance. Here, the power vector used in the estimation includes the hardware limitations as the signal variance is influenced by

these constraints. The BER test performed with correlated fields, measuring on each iteration, also showed improvements in the BER, maintaining the coupled with minimum fading. Still, as evaluated with decorrelated fields, the technique needs to be improved as the BER results largely span between $\text{BER} = 10^{-3}$ and $\text{BER} = 10^{-6}$ which indicates larger signal variance.

7.3 Future work

Future work should focus on each of the above-described sections improving the model, the numerical simulations, and the experimental tests to finally move towards the prototyping and field test. In addition, the technique should be compared with other alternative methods proposed for FSOC, like multi-aperture transceivers.

Regarding the model, the dynamic correction of the fields needs to be addressed more in detail, either refining the proposed approach, combining it with predictive algorithms, or proposing a suitable alternative able to keep track of the speckle evolution. This must involve parallel processing, where the image acquisition of the camera is performed while the algorithm corrects the field. One may consider alternatives like Kalman-based predictors of the speckle positions, or a combination with Zernike modes to maintain the correction once the initial phase-lock is reached.

Regarding the simulation, the numerical analyses have not evaluated the dynamics of the AO system in terms of loop bandwidth constraints. Future numerical analyses must consider the modeling of the hardware, especially timing constraints of a realistic closed loop, control system, deformable mirror, and camera acquisition. This could help to refine the technique for future lab implementation targeting a real-time working prototype.

About the practical implementation, future developments should focus on the optimization of the optical system, maybe testing mirrors with larger stroke and number of actuators, and also considering segmented DM's. The emulation of the turbulent scenarios (without wrapping effects) may also consider the use of other methods, like digital holography with micromirror arrays [160], or hot-air chambers [161]. In my opinion, a suitable and fully-controllable method, able to represent larger D/r_0 and dynamic turbulent regimes with realistic atmospheric time evolution, should involve a membrane-based deformable mirror. A key point here is that the turbulence emulation must allow reproducibility of the scenario to verify the results. The beam collimation needs to be improved to avoid the interference pattern and obtain a cleaner flat intensity profile, resembling a plane wave arriving from a satellite. This should further enhance the coupling efficiency. Future design must certainly consider the real-time implementation of the method and the study of some of the mentioned alternatives for the dynamic correction of the speckles. A prototype for a real-time implementation must consider the fact that this algorithm can also run in a non-sequential fashion, not studied in this work. The mathematical model clearly shows that the plane waves are uncorrelated, hence they can be optimized independently. Naturally, starting the optimization from a speckle of lower intensity may induce a penalty, but this option can greatly benefit the implementation of the method. Today's DMs have the option of pre-storage of a set of phase maps in the DM driver, which can be addressed at will avoiding the transmission delays. In the calibration process of the method, all the possible phase maps and their three stages alternatives could be stored in the DM driver and accessed on demand based on the speckle position. This approach could be combined with a suitable sensor, replacing the camera, as only the speckle peak coordinate and relative magnitude is needed. To my knowledge, this kind

of sensor solution does not exist, but the general idea should involve a photodetector array receiver with pixel positions electronically mapped to a lookup table of pre-stored phase maps, directly controlling the DM. Hence, all the process could be integrated without the need of running the algorithm in a computer. In my opinion, a real-time working prototype should move in this direction, including the simplification and optimization of the optical system.

New techniques offer alternatives to the traditional AO system design considered in this work. Typically, the receivers consist of a single aperture with a full-size collecting area that fully embraces the phase distortions of the field. Instead, the spatial diversity technique divides the single aperture into smaller sub-apertures whose output are coupled into a fiber, electronically combined, and co-phased [135, 162]. Each sub-aperture only sees a small region of the distorted phase-front, thus, the number of speckles in the focal plane get substantially reduced allowing an easier coupling into the SMF. In coherent reception, this technique facilitates the local oscillator locking with the received signal, reducing the probability of errors in reception [163]. Because this technique performs signal phase compensation electronically, it can achieve very fast loop rates and does not need a DM. On the other hand, the technique needs a high number of channels that increase the complexity in the electrical domain. The speckle-based technique proposed in this thesis should be compared in a common framework, like the capacity of improving in the BER. Both methods can also be compared in terms of complexity and cost of implementation.

Last but not least, the technique proposed in this work shows many new characteristics that may encounter applications in different fields. This method opens the door to possible combinations with other iterative algorithms without the need for adding complex wave-front sensors. Considering more relaxed time constraints, and that the same technique can work with many more intensity points of the speckle image, it can also be used in applications seeking for higher resolution like AO for medicine and spectroscopy, or high power laser in industry. In FSOC the resolution is reduced in favor of time optimization. For example, in a LEO downlink moving from strong to low turbulence conditions, the number of focal speckles vary, and the related algorithm can easily adjust itself reducing the treated modes and iterations depending on the number and strength of the measured intensity spots. Another possible application for FSOC could be AO for pre-compensation in laser communication uplinks. Applications like GEO feederlinks need to sens the aberrations induced by the turbulence in the downlink and pre-distort the uplink beam with the phase-front conjugate, so as the turbulent channel acts as a compensation element. Research in this area is mostly carried out in laboratories [164, 165], where the adopted technique is real-time Hartmann-based systems. An open question remains on the potential use of fast iterative solutions in this application.

THE focus of this Ph.D. dissertation is on free-space laser beam propagation, and the suggestion of adaptive methods and strategies to minimize the adverse effects of atmospheric turbulence on optical communication systems for space-to-ground link applications. The adaptation approach presented in this work is based on the sequential optimization of speckle components and works by iteratively updating individual adaptation phases to maximize coupled power. The method has the attractive property that the phase estimates can be obtained in a closed form from optimizing a quadratic cost function based on power measurements. Our work uses the power of new insights about iterative compensation methods for improving the performance of advance free-space

communication systems and shows how simple concepts can be combined to solve complex communication needs.

REFERENCES

- [1] J. Mikołajczyk, Z. Bielecki, M. Bugajski, J. Piotrowski, J. Wojtas, W. Gawron, D. Szabra, and A. Prokopiuk, "Analysis of free-space optics development," *Metrol. Meas. Syst.*, vol. 24, no. 4, pp. 653–674, 2017.
- [2] G. P. G. P. Agrawal, *Fiber-optic communication systems*. Wiley, 2010.
- [3] S. Bonora, R. Zawadzki, G. Naletto, U. Bortolozzo, and S. Residori, "Devices and Techniques for Sensorless Adaptive Optics," in *Adaptive Optics Progress*, InTech, dec 2012.
- [4] J. W. Goodman, *Speckle Phenomena in Optics: Theory and Applications*. Roberts and Company, 2007.
- [5] Hamamatsu, "Phase spatial light modulator LCOS-SLM," tech. rep., 2012.
- [6] H. Henniger, S. Seyfarth, and E. Diedrich, "Analysis and Comparison of new Downlink Technologies for Earth Observation Satellites," vol. 25, no. 1, pp. 1–11, 2016.
- [7] D. Lee, A. Gray, E. Kang, Haiping Tsou, N. Lay, Wai Fong, D. Fisher, and S. Hoy, "A gigabit-per-second Ka-band demonstration using a reconfigurable FPGA modulator," in *2005 IEEE Aerospace Conference*, pp. 1370–1378, IEEE, 2005.
- [8] M. Toyoshima, "Trends in satellite communications and the role of optical free-space communications," *Journal of Optical Networking*, vol. 4, p. 300, jun 2005.
- [9] D. M. Boroson, "Free-Space Optical Communications Comes of Age," *Photonics Spectra*, 2017.
- [10] J. H. Churnside and K. Shaik, "Atmospheric propagation issues relevant to optical communications," tech. rep., National Oceanic and Atmospheric Administration, Boulder, CO., United States, jan 1989.
- [11] F. Moll and M. Knappek, "Wavelength selection criteria and link availability due to cloud coverage statistics and attenuation affecting satellite, aerial, and downlink scenarios," vol. 6709, p. 670916, International Society for Optics and Photonics, sep 2007.
- [12] J. Horwath, N. Perlot, M. Knappek, and F. Moll, "Experimental verification of optical backhaul links for high-altitude platform networks: Atmospheric turbulence and downlink availability," *International Journal of Satellite Communications and Networking*, vol. 25, pp. 501–528, sep 2007.
- [13] D. Giggenbach, B. Epple, J. Horwath, and F. Moll, "Optical satellite downlinks to optical ground stations and high-altitude platforms," *Lecture Notes in Electrical Engineering*, vol. 16, no. July, pp. 331–349, 2008.
- [14] C. Fuchs and F. Moll, "Ground station network optimization for space-to-ground optical communication links," *IEEE/OSA Journal of Optical Communications and Networking*, vol. 7, no. 12, pp. 1148–1159, 2015.

- [15] H. Weichel, *Laser beam propagation in the atmosphere*. SPIE Optical Engineering Press, 1990.
- [16] M. C. Roggemann and B. Welsh, *Imaging Through Turbulence*. CRC University LLC, 1996.
- [17] H. Kaushal and G. Kaddoum, "Optical Communication in Space: Challenges and Mitigation Techniques," *IEEE Communications Surveys & Tutorials*, vol. 19, no. 1, pp. 57–96, 2017.
- [18] A. N. Kolmogorov, "The Local Structure of Turbulence in Incompressible Viscous Fluid for Very Large Reynolds Numbers."
- [19] D. L. Fried, "Statistics of a Geometric Representation of Wavefront Distortion," *Journal of the Optical Society of America*, vol. 55, no. 11, 1965.
- [20] L. C. Andrews and R. L. Phillips, *Laser Beam Propagation through Random Media second edition*. SPIE, 2005.
- [21] S. K. Sharma, S. Chatzinotas, and P.-D. Arapoglou, *Satellite communications in the 5G era*.
- [22] T. Okoshi, K. Emura, K. Kikuchi, and R. T. Kersten, "Computation of Bit-Error Rate of Various Heterodyne and Coherent-Type Optical Communication Schemes," *Journal of Optical Communications*, vol. 2, pp. 89–96, jan 1981.
- [23] J. Salz, "Modulation and detection for coherent lightwave communications," *IEEE Communications Magazine*, vol. 24, pp. 38–49, jun 1986.
- [24] A. Viterbi, "Nonlinear estimation of PSK-modulated carrier phase with application to burst digital transmission," *IEEE Transactions on Information Theory*, vol. 29, pp. 543–551, jul 1983.
- [25] R. Barrios, *Exponentiated Weibull Fading Channel Model in Free-Space Optical Communications under Atmospheric Turbulence*. PhD thesis, 2013.
- [26] V. Chan, "Coding for the Turbulent Atmospheric Optical Channel," *IEEE Transactions on Communications*, vol. 30, pp. 269–275, jan 1982.
- [27] C. Xu, X. Liu, and X. Wei, "Differential Phase-Shift Keying for High Spectral Efficiency Optical Transmissions," *IEEE Journal of Selected Topics in Quantum Electronics*, vol. 10, pp. 281–293, mar 2004.
- [28] F. Moll and M. Knapek, "Free-space laser communications for satellite downlinks: Measurements of the atmospheric channel," in *62nd International Astronautical Congress*, (Cape Town, SA), pp. 1–9, IAC2011, 2010.
- [29] K. Murphy, D. Burke, N. Devaney, and C. Dainty, "Experimental detection of optical vortices with a Shack-Hartmann wavefront sensor," *Optics Express*, vol. 18, p. 15448, jul 2010.
- [30] D. L. Fried, "Branch point problem in adaptive optics," *Journal of the Optical Society of America A*, vol. 15, p. 2759, oct 1998.

- [31] K. Murphy, R. Mackey, and C. Dainty, "Branch point detection and correction using the branch point potential method," *Proc. SPIE Atmospheric Propagation V*, vol. 6951, no. 695105, pp. 1–10, 2008.
- [32] D. L. Fried, D. J. Link, G. A. Tyler, W. Moretti, T. J. Brennan, R. Q. Fugate, J. D. Barchers, D. L. Fried, D. J. Link, G. A. Tyler, T. J. Moretti, William, Brennan, and R. Q. Figate, "The performance of wavefront sensors in strong scintillation," in *SPIE Adaptive Optical System Technologies II*, vol. 4839, pp. 217–227, SPIE, 2003.
- [33] M. Knappek, *Adaptive Optics for the Mitigation of Atmospheric Effects in Laser Satellite-To-Ground Communications*. Ph.d., Technische Universität München, 2010.
- [34] J. R. Fienup, B. J. Thelen, R. G. Paxman, and D. a. Carrara, "Comparison of phase diversity and curvature wavefront sensing," *Adaptive Optical System Technologies, Proc. SPIE*, vol. 3353, no. March, pp. 930–940, 1998.
- [35] F. Roddier, "Curvature sensing and compensation: a new concept in adaptive optics," *Applied Optics*, vol. 27, p. 1223, apr 1988.
- [36] J. Frank, S. Altmeyer, and G. Wernicke, "Non-interferometric, non-iterative phase retrieval by Green's functions," *Journal of the Optical Society of America A*, vol. 27, p. 2244, oct 2010.
- [37] E. Anzuola, M. Segel, S. Gladysz, and K. Stein, "Performance of wavefront-sensorless adaptive optics using modal and zonal correction," in *SPIE Optics in Atmospheric Propagation and Adaptive Systems XIX* (SPIE, ed.), vol. 10002, (Edinburgh, United Kingdom), p. 100020J, 2016.
- [38] M. Vorontsov, G. Carhart, M. Cohen, and G. Cauwenbergs, "Adaptive optics based on analog parallel stochastic optimization technique," *Conference on Lasers and Electro-Optics (CLEO 2000). Technical Digest. Postconference Edition. TOPS Vol.39 (IEEE Cat. No.00CH37088)*, vol. 17, no. 8, p. 605, 2000.
- [39] H. Ma, C. Fan, P. Zhang, J. Zhang, C. Qiao, and H. Wang, "Adaptive optics correction based on stochastic parallel gradient descent technique under various atmospheric scintillation conditions: Numerical simulation," *Applied Physics B: Lasers and Optics*, vol. 106, no. 4, pp. 939–944, 2012.
- [40] A. K. Majumdar, *Advanced Free Space Optics (FSO)*, vol. 186 of *Springer Series in Optical Sciences*. New York, NY: Springer New York, 2015.
- [41] T. Weyrauch and M. A. Vorontsov, "Free-space laser communications with adaptive optics: Atmospheric compensation experiments," *Journal of Optical and Fiber Communications Reports*, vol. 1, pp. 355–379, dec 2004.
- [42] N. H. Schwartz, N. Védrenne, V. Michau, M.-T. Velluet, and F. Chazallet, "Mitigation of atmospheric effects by adaptive optics for free-space optical communications," in *SPIE Atmospheric Propagation of Electromagnetic Waves III*, vol. 7200, pp. 72000J—1, 2009.

- [43] K. Saucke, C. Seiter, F. Heine, M. Gregory, D. Tröndle, E. Fischer, T. Berkefeld, M. Feriencik, M. Feriencik, I. Richter, and R. Meyer, "The TESAT transportable adaptive optical ground station," in *Free-Space Laser Communication and Atmospheric Propagation XXVIII*, vol. 9739, SPIE, 2016.
- [44] M. Li and M. Cvijetic, "Coherent free space optics communications over the maritime atmosphere with use of adaptive optics for beam wavefront correction," *Applied Optics*, vol. 54, no. 6, p. 1453, 2015.
- [45] M. Li, M. Cvijetic, Y. Takashima, and Z. Yu, "Evaluation of channel capacities of OAM-based FSO link with real-time wavefront correction by adaptive optics," *Optics Express*, vol. 22, no. 25, p. 31337, 2014.
- [46] M. W. Wright, J. F. Morris, J. M. Kovalik, K. S. Andrews, M. J. Abrahamson, and A. Biswas, "Adaptive optics correction into single mode fiber for a low Earth orbiting space to ground optical communication link using the OPALS downlink," *Optics Express*, vol. 23, no. 26, pp. 33705–33712, 2015.
- [47] K. E. Wilson, D. Antsos, L. C. Roberts Jr., S. Piazzolla, L. P. Clare, and A. P. Croonquist, "Development of the Optical Communications Telescope Laboratory: A Laser Communications Relay Demonstration Ground Station," in *International Conference on Space Optical Systems and Applications*, (Ajaccio, Corsica, France), pp. 3–3, ICSOS, 2012.
- [48] D. Giggenbach, "Method for adjusting atmospherically distorted optical wave fronts," 2012.
- [49] M. Muñoz Fuentes, *Adaptive Optics without wave-front sensor using the APHEFIS (Adaptive Optics by Phase Estimation from Focal Intensity Speckles) algorithm*. PhD thesis, Polytechnic University of Catalonia (UPC), 2012.
- [50] S. D. Lord, "NASA Technical Memorandum 103957," 1992.
- [51] J. Haase, "Simulation in the Design Process of Free Space Optical Transmission Systems," in *6th Workshop Optics in Computing Technology*, (Paderborn), pp. 45–53, 2001.
- [52] V. I. Tatarskii, R. A. Silverman, and N. Chako, "Wave Propagation in a Turbulent Medium," *Physics Today*, vol. 14, pp. 46–51, dec 1961.
- [53] F. F. Roddier and Francois, *Adaptive optics in astronomy*. Cambridge University Press, 1999.
- [54] F. Roddier, "The Effects of Atmospheric Turbulence in Optical Astronomy," in *Progress in Optics* (E. Wolf, ed.), vol. 19, pp. 281–376, New York: North-Holland: ELSEVIER, 1981.
- [55] C. Rao, W. Jiang, and N. Ling, "Spatial and temporal characterization of phase fluctuations in non-Kolmogorov atmospheric turbulence," *Journal of Modern Optics*, vol. 47, pp. 1111–1126, may 2000.
- [56] M. Toyoshima, H. Takenaka, and Y. Takayama, "Atmospheric turbulence-induced fading channel model for space-to-ground laser communications links," *Optics Express*, vol. 19, p. 15965, aug 2011.
- [57] F. Moll, "Experimental characterization of intensity scintillation in the LEO downlink," *2015 4th International Workshop on Optical Wireless Communications, IWOW 2015*, vol. 12, no. 4, pp. 31–35, 2015.

- [58] A. K. Majumdar and J. C. Ricklin, *Free-space laser communications : principles and advances*. Springer, 2008.
- [59] L. C. Andrews, R. L. Phillips, and C. Y. Young, *Laser Beam Scintillation with Applications*. SPIE, jul 2001.
- [60] M. A. Al-Habash, L. C. Andrews, and R. L. Phillips, "Mathematical model for the irradiance probability density function of a laser beam propagating through turbulent media," *Optical Engineering*, vol. 40, p. 1554, aug 2001.
- [61] M. Nakagami, "The m-Distribution—A General Formula of Intensity Distribution of Rapid Fading," *Statistical Methods in Radio Wave Propagation*, pp. 3–36, jan 1960.
- [62] J. Horwath, F. David, M. Knappek, and N. Perlot, "Coherent transmission feasibility analysis," vol. 5712, p. 13, International Society for Optics and Photonics, apr 2005.
- [63] J.-M. Conan, G. Rousset, and P.-Y. Madec, "Wave-front temporal spectra in high-resolution imaging through turbulence," *Journal of the Optical Society of America A*, vol. 12, no. 7, p. 1559, 1995.
- [64] R. J. Noll, "Zernike polynomials and atmospheric turbulence," *Journal of the Optical Society of America*, vol. 66, no. 3, pp. 207–11, 1976.
- [65] B. E. A. Saleh and M. C. Teich, *Fundamentals of photonics*. Wiley-Interscience, 2007.
- [66] F. N. H. Robinson and F. N. H., "Noise and fluctuations in electronic devices and circuits," *Oxford, Clarendon Press, 1974. 252 p.*, 1974.
- [67] M. D. Hull, "Electrical Noise. W. R. Bennett. McGraw-Hill, New York. 1960. 280 pp. Diagrams. 77s. 6d.," *Journal of the Royal Aeronautical Society*, vol. 65, p. 442, jun 1961.
- [68] D. K. C. D. K. C. MacDonald, *Noise and fluctuations : an introduction*. Dover Publications, 2006.
- [69] J. B. Johnson, "Thermal Agitation of Electricity in Conductors," *Physical Review*, vol. 32, pp. 97–109, jul 1928.
- [70] H. Nyquist, "Thermal Agitation of Electric Charge in Conductors," *Physical Review*, vol. 32, pp. 110–113, jul 1928.
- [71] B. Goebel, G. J. Foschini, G. Kramer, P. J. Winzer, and R.-J. Essiambre, "Capacity Limits of Optical Fiber Networks," *Journal of Lightwave Technology*, Vol. 28, Issue 4, pp. 662-701, vol. 28, pp. 662–701, feb 2010.
- [72] T. Kaneda, H. Matsumoto, T. Sakurai, and T. Yamaoka, "Excess noise in silicon avalanche photodiodes," *Journal of Applied Physics*, vol. 47, pp. 1605–1607, apr 1976.
- [73] R. K. Tyson, *Introduction to adaptive optics : Robert K. Tyson*. SPIE Press, 2000.

- [74] J. H. Shapiro, "Imaging and optical communication through atmospheric turbulence," pp. 171–222, Springer, Berlin, Heidelberg, 1978.
- [75] M. Abramowitz and I. A. Stegun, *Handbook of mathematical functions, with formulas, graphs, and mathematical tables*,. Dover Publications, 1965.
- [76] W. Freude, R. Schmogrow, B. Nebendahl, M. Winter, A. Josten, D. Hillerkuss, S. Koenig, J. Meyer, M. Dreschmann, M. Huebner, C. Koos, J. Becker, and J. Leuthold, "Quality metrics for optical signals: Eye diagram, Q-factor, OSNR, EVM and BER," in *2012 14th International Conference on Transparent Optical Networks (ICTON)*, pp. 1–4, IEEE, jul 2012.
- [77] T. Y. Elganimi, "Studying the BER performance, power- and bandwidth- efficiency for FSO communication systems under various modulation schemes," in *2013 IEEE Jordan Conference on Applied Electrical Engineering and Computing Technologies (AEECT)*, pp. 1–6, IEEE, dec 2013.
- [78] W. Lim, "BER Analysis of Coherent Free Space Optical Systems with BPSK over Gamma-Gamma Channels," *Journal of the Optical Society of Korea*, Vol. 19, Issue 3, pp. 237-240, vol. 19, pp. 237–240, jun 2015.
- [79] P. Wang, L. Zhang, L. Guo, F. Huang, T. Shang, R. Wang, and Y. Yang, "Average BER of subcarrier intensity modulated free space optical systems over the exponentiated Weibull fading channels," *Optics Express*, vol. 22, p. 20828, aug 2014.
- [80] V. N. Mahajan, "Strehl ratio for primary aberrations: some analytical results for circular and annular pupils: erratum," *Journal of the Optical Society of America A*, vol. 10, no. 9, p. 2092, 2008.
- [81] P. J. Winzer and W. R. Leeb, "Fiber coupling efficiency for random light and its applications to lidar," *Optics Letters*, vol. 23, no. 13, p. 986, 1998.
- [82] Y. Dikmelik and F. M. Davidson, "Fiber-coupling efficiency for free-space optical communication through atmospheric turbulence," *Applied Optics*, vol. 44, p. 4946, aug 2005.
- [83] H. Takenaka, M. Toyoshima, and Y. Takayama, "Experimental verification of fiber-coupling efficiency for satellite-to-ground atmospheric laser downlinks," *Optics Express*, vol. 20, no. 14, p. 15301, 2012.
- [84] M. P. Cagigal and V. F. Canales, "Generalized Fried parameter after adaptive optics partial wave-front compensation," *Journal of the Optical Society of America. A, Optics, image science, and vision*, vol. 17, no. 5, pp. 903–10, 2000.
- [85] C. Ruilier and F. Cassaing, "Coupling of large telescopes and single-mode waveguides: application to stellar interferometry," *Journal of the Optical Society of America A*, vol. 18, p. 143, jan 2001.
- [86] A. Belmonte and J. Khan, "Performance of synchronous optical receivers using atmospheric compensation techniques," *Optics Express*, vol. 16, no. 18, p. 14151, 2008.

- [87] R. J. Sasiela, *Electromagnetic Wave Propagation in Turbulence*. 1000 20th Street, Bellingham, WA 98227-0010 USA: SPIE, may 2007.
- [88] G. Chanan, "Principles of Wavefront Sensing and Reconstruction," *Center for Adaptive Optics (CfAO) Proceedings: Summer School on Adaptive Optics*, pp. 5–40, 2000.
- [89] P.-Y. Madec, "Overview of deformable mirror technologies for adaptive optics and astronomy," no. March, pp. 844705–844718, 2012.
- [90] T. Bifano, S. Cornelissen, and P. Bierden, "Recent advances in high-resolution MEMS DM fabrication and integration," *Proceedings of AMOS*, 2010.
- [91] S. A. Cornelissen, T. G. Bifano, and P. A. Bierden, "MEMS Deformable Mirror Actuators with Enhanced Reliability," 2012.
- [92] K. Shtyrkova, L. Arguello, D. Oesch, D. J. Sanchez, P. Kelly, C. Tewksbury-Christle, and J. Smith, "Experimental analysis of diffraction effects from a segmented MEMS deformable mirror for a closed loop adaptive optics system," vol. 7816, p. 781608, International Society for Optics and Photonics, aug 2010.
- [93] T. Bifano, P. Bierden, and J. Perreault, "Micromachined Deformable Mirrors for Dynamic Wavefront Control,"
- [94] K. Morzinski, B. Macintosh, D. Gavel, and D. Dillon, "Stroke saturation on a MEMS deformable mirror for woofer-tweeter adaptive optics," *Optics Express*, vol. 17, p. 5829, mar 2009.
- [95] D. L. Fried and J. L. Vaughn, "Branch cuts in the phase function," *Applied Optics*, vol. 31, p. 2865, may 1992.
- [96] V. V. Voitsekhovich, D. Kouznetsov, and D. K. Morozov, "Density of turbulence-induced phase dislocations," *Applied Optics*, vol. 37, p. 4525, jul 1998.
- [97] D. L. Fried, "Branch point problem in adaptive optics," *Journal of the Optical Society of America A*, vol. 15, p. 2759, oct 1998.
- [98] G. A. Tyler, "Reconstruction and assessment of the least-squares and slope discrepancy components of the phase.," *Journal of the Optical Society of America. A, Optics, image science, and vision*, vol. 17, pp. 1828–39, oct 2000.
- [99] N. B. Baranova, A. V. Mamaev, N. F. Pilipetsky, V. V. Shkunov, and B. Y. Zel'dovich, "Wave-front dislocations: topological limitations for adaptive systems with phase conjugation," *Journal of the Optical Society of America*, vol. 73, p. 525, may 1983.
- [100] J. D. Barchers, D. L. Fried, and D. J. Link, "Evaluation of the performance of Hartmann sensors in strong scintillation," *Applied Optics*, vol. 41, p. 1012, feb 2002.

- [101] J. H. Shapiro, "Reciprocity of the Turbulent Atmosphere," vol. 61, no. April, pp. 492–495, 1971.
- [102] M. L. Plett, P. R. Barbier, D. W. Rush, P. Polak-Dingels, and B. M. Levine, "Measurement error of a Shack-Hartmann wavefront sensor in strong scintillation conditions," in *Propagation and Imaging through the Atmosphere II*, vol. 3433, (San Diego, CA, United States), pp. 211–220, SPIE, nov 1998.
- [103] M. Soto, E. Acosta, and S. Ríos, "Performance analysis of curvature sensors: optimum positioning of the measurement planes," *Optics Express*, vol. 11, p. 2577, oct 2003.
- [104] R. K. Tyson and B. W. Frazier, *Field Guide to Adaptive Optics, Second Edition*. SPIE, apr 2012.
- [105] R. N. Smartt and W. H. Steel, "Theory and Application of Point-Diffraction Interferometers," *Japanese Journal of Applied Physics*, vol. 14, p. 351, jan 1975.
- [106] J. Glückstad and P. C. Mogensen, "Optimal phase contrast in common-path interferometry," *Applied Optics*, vol. 40, p. 268, jan 2001.
- [107] D. Malacara, "Optical Shop Testing (Wiley Series in Pure and Applied Optics)," 2007.
- [108] T. Weyrauch, M. a. Vorontsov, J. Gowens, and T. G. Bifano, "Fiber coupling with adaptive optics for free-space optical communication," *Spie*, vol. 4489, pp. 177–184, 2002.
- [109] S. Zommer, E. N. Ribak, S. G. Lipson, and J. Adler, "Simulated annealing in ocular adaptive optics," *Optics Letters*, vol. 31, p. 939, apr 2006.
- [110] M. Zakyntinaki and Y. Saridakis, "Stochastic optimization for a tip-tilt adaptive correcting system," *Computer Physics Communications*, vol. 150, pp. 274–292, feb 2003.
- [111] H. Yang and X. Li, "Comparison of several stochastic parallel optimization algorithms for adaptive optics system without a wavefront sensor," *Optics and Laser Technology*, vol. 43, no. 3, pp. 630–635, 2011.
- [112] G. Naletto, F. Frassetto, N. Codogno, E. Grisan, S. Bonora, V. Da Deppo, and A. Ruggeri, "No wavefront sensor adaptive optics system for compensation of primary aberrations by software analysis of a point source image 2 Tests," *Applied Optics*, vol. 46, p. 6427, sep 2007.
- [113] D. Debarre, M. J. Booth, and T. Wilson, "Image based adaptive optics through optimisation of low spatial frequencies," *Optics Express*, vol. 15, p. 8176, jun 2007.
- [114] A. Zepp, M. Segel, E. Anzuola, S. Gladysz, and K. U. Stein, "Optimization of wavefront-sensorless adaptive optics for horizontal laser beam propagation in a realistic turbulence environment," *Laser Communication and Propagation through the Atmosphere and Oceans VI*, no. August 2017, p. 14, 2017.
- [115] Boston Micromachines Corporation, "The Kilo-DM: A high performance wavefront corrector for demanding applications in astronomy, laser communications and long-range imaging."
- [116] R. Köhler, "Speckle interferometry," *Contributions of the Astronomical Observatory Skalnaté Pleso*, vol. 43, no. 3, pp. 229–236, 2014.

- [117] A. Labeyrie, "Attainment of Diffraction Limited Resolution in Large Telescopes by Fourier Analysing Speckle Patterns in Star Images," *Astronomy and Astrophysics*, vol. 6, p. 85, 1970.
- [118] A. W. Lohmann, G. Weigelt, and B. Wirtzner, "Speckle masking in astronomy: triple correlation theory and applications," *Applied Optics*, vol. 22, p. 4028, dec 1983.
- [119] L. P. Murray, J. C. Dainty, and E. Daly, "Wavefront correction through image sharpness maximisation," vol. 5823, p. 40, International Society for Optics and Photonics, jun 2005.
- [120] M. A. Vorontsov, G. W. Carhart, and J. C. Ricklin, "Adaptive phase-distortion correction based on parallel gradient-descent optimization," *Optics Letters*, vol. 22, no. 12, p. 907, 1997.
- [121] R. A. Muller and A. Buffington, "Real-time correction of atmospherically degraded telescope images through image sharpening," *Journal of the Optical Society of America*, vol. 64, p. 1200, sep 1974.
- [122] A. Buffington, F. S. Crawford, R. A. Muller, A. J. Schwemin, and R. G. Smits, "Correction of atmospheric distortion with an image-sharpening telescope*," *Journal of the Optical Society of America*, vol. 67, p. 298, mar 1977.
- [123] J. R. Fienup and J. J. Miller, "Aberration correction by maximizing generalized sharpness metrics.," *Journal of the Optical Society of America. A, Optics, image science, and vision*, vol. 20, pp. 609–20, apr 2003.
- [124] J. Braat, "Polynomial expansion of severely aberrated wave fronts," *Journal of the Optical Society of America A*, vol. 4, p. 643, apr 1987.
- [125] N. Yaitskova and S. Gladysz, "First-order speckle statistics for arbitrary aberration strength," *Journal of the Optical Society of America A*, vol. 28, no. 9, p. 1909, 2011.
- [126] D. Giggenbach, "Deriving an estimate for the Fried parameter in mobile optical transmission scenarios," *Applied Optics*, vol. 50, no. 2, pp. 222–6, 2011.
- [127] J. C. Dainty, M. A. Fiddy, and A. H. Greenway, "On the danger of applying statistical reconstruction in case of missing phase information," in *Image Formation from Coherence Functions in Astronomy*, pp. 95–101, Springer, Dordrecht, 1979.
- [128] A. Walther, "The Question of Phase Retrieval in Optics," *Optica Acta: International Journal of Optics*, vol. 10, no. 1, pp. 41–49, 1963.
- [129] A. H. Greenaway, "Proposal for phase recovery from a single intensity distribution," *Optics Letters*, vol. 1, no. 1, p. 10, 1977.
- [130] Y. M. Bruck and L. G. Sodin, "On the ambiguity of the image reconstruction problem," *Optics Communications*, vol. 30, no. 3, pp. 304–8, 1979.

- [131] R. H. T. Bates, “Uniqueness of solutions to two-dimensional fourier phase problems for localized and positive images,” *Computer Vision, Graphics and Image Processing*, vol. 25, no. 2, pp. 205–217, 1984.
- [132] J. W. Goodman, *Introduction to Fourier Optics*. McGraw-Hill, 1996.
- [133] G. C. Sherman, “Introduction to the angular-spectrum representation of optical fields,” in *Applications of Mathematics in Modern Optics*, vol. 0358, 1982.
- [134] I. Freund and N. Shvartsman, “Structural correlations in Gaussian random wave fields,” *Phys Rev E*, vol. 51, no. 4, pp. 863–868, 1995.
- [135] A. Belmonte and J. M. Kahn, “Sequential optimization of adaptive arrays in coherent laser communications,” *Journal of Lightwave Technology*, vol. 31, no. 9, pp. 1383–1387, 2013.
- [136] N. A. Roddier, “Atmospheric wavefront simulation using Zernike polynomials,” *Optical Engineering*, vol. 29, no. 10, 1990.
- [137] R. Jüngling, “Simulation gerichteter Ausbreitung optischer Wellen in turbulenter Atmosphäre,” 2001.
- [138] J. Horwath, N. Perlot, D. Giggenbach, and R. Jungling, “Numerical simulations of beam propagation through optical turbulence for high-altitude platform crosslinks,” p. 243, jun 2004.
- [139] N. Perlot, J. Horwath, and R. Juengling, “Modeling wind in simulations of atmospheric optical propagation,” vol. 5712, p. 140, International Society for Optics and Photonics, apr 2005.
- [140] D. Giggenbach, P. Becker, R. Mata-Calvo, C. Fuchs, Z. Sodnik, and I. Zayer, “Lunar Optical Communications Link (LOCL): Measurements of Received Power Fluctuations and Wavefront Quality,” in *International Conference on Space Optical Systems and Applications*, (Kobe, Japan), ICSOS, 2014.
- [141] N. Perlot, M. Knappek, D. Giggenbach, J. Horwath, M. Brechtelsbauer, Y. Takayama, and T. Jono, “Results of the optical downlink experiment KIODO from OICETS satellite to optical ground station Oberpfaffenhofen (OGS-OP),” in *Free-Space Laser Communication Technologies XIX and Atmospheric Propagation of Electromagnetic Waves*, vol. 6457, (San Jose, California), pp. 645704–8, SPIE, 2007.
- [142] I. a. Litvin, L. Burger, M. P. D. Gama, A. Mathye, and A. Forbes, “Laser beam shaping limitations for laboratory simulation of turbulence using a phase-only spatial light modulator,” *Proc. SPIE*, vol. 6663, pp. 66630R–1, 2007.
- [143] R. Conan, “Mean-square residual error of a wavefront after propagation through atmospheric turbulence and after correction with Zernike polynomials,” *Journal of the Optical Society of America A*, vol. 25, p. 526, feb 2008.
- [144] J.-F. Lavigne and J.-P. Véran, “Woofers-tweeters control in an adaptive optics system using a Fourier reconstructor,” *Journal of the Optical Society of America A*, vol. 25, p. 2271, sep 2008.
- [145] A. Natan, “2D fast peak finder.” <http://web.stanford.edu/~natan/#cod>.

- [146] D. Giggenbach, E. Lutz, J. Poliak, R. Mata-Calvo, and C. Fuchs, "A High-throughput Satellite System for Serving whole Europe with Fast Internet Service, Employing Optical Feeder Links," *Broadband Coverage in Germany. 9th ITG Symposium. Berlin*, pp. 1–7, 2015.
- [147] P. Conroy, J. Surof, J. Poliak, and R. M. Calvo, "Demonstration of 40 GBaud intradyne transmission through worst-case atmospheric turbulence conditions for geostationary satellite uplink," *Appl. Opt.*, vol. 57, no. 18, pp. 5095–5101, 2018.
- [148] F. Gardner, "A BPSK/QPSK Timing-Error Detector for Sampled Receivers," *IEEE Transactions on Communications*, vol. 34, pp. 423–429, may 1986.
- [149] M. Oerder and H. Meyr, "Digital filter and square timing recovery," *IEEE Transactions on Communications*, vol. 36, pp. 605–612, may 1988.
- [150] I. Fatadin, S. J. Savory, and D. Ives, "Compensation of Quadrature Imbalance in an Optical QPSK Coherent Receiver," *IEEE Photonics Technology Letters*, vol. 20, pp. 1733–1735, oct 2008.
- [151] T. Nakagawa, M. Matsui, and K. Araki, "Gain/phase imbalance compensation for multi-band quadrature receivers," in *IEEE 60th Vehicular Technology Conference, 2004. VTC2004-Fall. 2004*, vol. 3, pp. 2034–2037, IEEE.
- [152] S. Tretter, "Estimating the frequency of a noisy sinusoid by linear regression (Corresp.)," *IEEE Transactions on Information Theory*, vol. 31, pp. 832–835, nov 1985.
- [153] S. Kay, "A fast and accurate single frequency estimator," *IEEE Transactions on Acoustics, Speech, and Signal Processing*, vol. 37, no. 12, pp. 1987–1990, 1989.
- [154] A. Leven, N. Kaneda, U.-V. Koc, and Y.-K. Chen, "Frequency Estimation in Intradyne Reception," *IEEE Photonics Technology Letters*, vol. 19, pp. 366–368, mar 2007.
- [155] D. Rife and R. Boorstyn, "Single tone parameter estimation from discrete-time observations," *IEEE Transactions on Information Theory*, vol. 20, pp. 591–598, sep 1974.
- [156] T. Pfau, S. Hoffmann, and R. Noe, "Hardware-Efficient Coherent Digital Receiver Concept With Feed-forward Carrier Recovery for M-QAM Constellations," *Journal of Lightwave Technology*, vol. 27, pp. 989–999, apr 2009.
- [157] I. P. Kaminow, T. Li, and A. E. Willner, *Optical fiber telecommunications V. B. Systems and networks*. Academic Press, 2008.
- [158] D. N. Godard, "Self-Recovering Equalization and Carrier Tracking," *IEEE transactions on communications*, vol. 28, no. 11, pp. 1867–1875, 1980.
- [159] J. Surof, J. Poliak, and R. Mata-Calvo, "Demonstration of intradyne BPSK optical free-space transmission in representative atmospheric turbulence conditions for geostationary uplink channel," *Optics Letters*, vol. 42, no. 11, pp. 2173–2176, 2017.

- [160] E. Anzuola and A. Belmonte, "Generation of atmospheric wavefronts using binary micromirror arrays," *Applied Optics*, vol. 55, p. 3039, apr 2016.
- [161] H. Gamo and A. K. Majumdar, "Atmospheric turbulence chamber for optical transmission experiment: characterization by thermal method," *Applied Optics*, vol. 17, p. 3755, dec 1978.
- [162] A. Belmonte and J. M. Kahn, "Field Conjugation Adaptive Arrays in Free-Space Coherent Laser Communications," *Journal of Optical Communications and Networking*, vol. 3, no. 11, p. 830, 2011.
- [163] A. Belmonte and J. M. Kahn, "Capacity of coherent free-space optical links using diversity-combining techniques," *Optics Express*, vol. 17, p. 12601, jul 2009.
- [164] R. Berlich, A. Brady, N. Leonhard, A. Kamm, C. Reinlein, and T. Kopf, "Transportable system for in-field testing of adaptive optical pre-compensation for optical feeder links," in *International Conference on Space Optics — ICSO 2016* (N. Karafolas, B. Cugny, and Z. Sodnik, eds.), vol. 10562, p. 231, SPIE, sep 2017.
- [165] N. Leonhard, R. Berlich, S. Minardi, A. Barth, S. Mauch, J. Mocchi, M. Goy, M. Appelfelder, E. Beckert, and C. Reinlein, "Real-time adaptive optics testbed to investigate point-ahead angle in pre-compensation of Earth-to-GEO optical communication," *Optics Express*, vol. 24, p. 13157, jun 2016.